MECHANISMS AND CONDITIONS OF DEFORMATION IN QUARTZITES FROM THE CANTABRIAN AND WEST ASTURIAN-LEONESE ZONES, NORTH SPAIN

VOLUME I

T.G. Blenkinsop

A Thesis submitted for the degree of Doctor of Philosophy

University of Keele

1987

ACKNOWLEDGEMENTS

The principal acknowledgements, for their consistent encouragement and advice, are due to the academic staff at Keele, Liverpool and London Universities, including Professor N.J.Kusznir, Drs.E.H.Rutter, G.Rowbotham, M.Norton, and above all, Dr.R.G.Park. The assistance of Dr.A.Pérez-Estaún, Dr.C.Brime, F.Mart, and several other colleagues at the University of Oviedo has been almost equally imortant. The members of the technical staff in all departments at Keele are warmly thanked, and the good humour, patience, and toil of Karen Harrison during the typing is much appreciated. Finally, friends at Lask Edge and family support can not be justly acknowledged.

CONTENTS

VOLUME I

VOLUME II

ABSTRACT

Deformation mechanisms and conditions have been studied, principally in Ordovician quartzites, from the Cantabrian and West Asturian-Leonese zones, north Spain. The quartzites have been strongly deformed at shallow crustal levels during the Variscan orogeny. In the external Cantabrian zone, the dominant mechanism was **cataclasis**, which occurred both pervasively around large-scale folds by shear on a network of bedding-normal fractures, and as localised deformation along large faults. **Solution transfer** was confined to grain boundaries. **Grain boundary sliding** operated in sandstones with porous microstructures, which deformed by small-scale chevron folds. This contrast in deformation modes is shown to be a consequence of different initial microstructures.

In the West-Asturian Leonese zone (towards the internal part of the orogen), solution transfer extended along stylolites, and progressively increasing amounts of **crystal plasticity** became the fold accommodating mechanism. This can be followed by an increase in the intracrystalline extinction angle as grain boundary migration and sub-grain rotation contributed to further dynamic recrystallisation. The late stages of deformation were cataclastic. In all examples of cataclasis, fractures clustered together to form deformation zones of high density fracturing: this is an inherent part of the deformation mechanism, which is interpretted as a localisation phenomenon in response to changed material properties.

The changes in mechanisms from the external to internal parts of the orogen correlate with an increase in temperature from 0-250^{0} to

311 - 411^{0}. Effective confining pressures were from 30 to 75 MPa. and differential stresses from 50 to 300 MPa. These conditions of deformation are linked with the deformation modes to define nine **deformation facies** ; the sequence of facies, the **deformation path**, is plotted for the four localities studied in detail, and it is suggested that the study area can be subdivided into four sub-areas, each characterised by one path.

CHAPTER 1

INTRODUCTION

1.1 AIMS, OBJECTIVES AND RELEVANCE OF THIS STUDY

1.2 STUDY AREA

1.3 STRUCTURE OF THESIS

1.4 SYMBOLS AND UNITS

1.1 AIMS, OBJECTIVES AND RELEVANCE OF THIS STUDY

Recent studies in structural geology within the upper levels of the crust have emphasised kinematic aspects, leading to a new detailed understanding of thrust systems in compressional regimes, and extensional tectonics. The ideas generated, conveniently called 'thin skinned tectonics', have found widespread use and have been of particular benefit in hydrocarbon exploration. However, there has been a corresponding shortage in work on stress systems and deformation mechanisms in such environments, and it is these areas of research, when integrated with the strain-based approaches, that should provide a substantial further advance.

Another imbalance can be detected between the comprehensive knowledge of rock mechanics from experiments such as conventional triaxial testing, creep tests, fault gouge rheology, indentation tests, and sub-critical crack growth, which can relate closely to these conditions of natural deformation, and its application to field observations and examples, although this has been attempted for example by Engelder (1974), Brock and Engelder (1977), McEwen (1981), and House and Gray (1982). One of the central difficulties is the question of whether the small-scale laboratory tests may be extrapolated to crustal deformation; Hadizadeh and Rutter (1982) have posed this question, and it has been addressed by Blenkinsop and Rutter (1986). Only by establishing natural **conditions** of deformation accurately, and by proving similar **mechanisms** of deformation between experiments and nature, can the rock mechanics data be confidently applied to real examples.

Theoretical approaches to shallow-level deformation have attempted to explain empirical rock mechanics results, such as strength criteria, creep laws or sub-critical crack growth in terms of fundamental processes: this has been the aim of Griffith theory and its many derivatives as well as fracture mechanics theory. Theories have also been developed to apply

directly to rocks, such as localisation and instability theory (Rudnicki and Rice (1975), Aydin and Johnson (1983), Latham (1985a,b)) minimum work theories (Oertel (1965), Reches (1978) and fracture mechanics theory (e.g. Rudnicki (1980), Das and Scholz (1981)). The testing of these theories requires both more experimental data and perhaps more urgently, an understanding of natural deformation mechanisms. It is from two of these theories (localisation and minimum work) that a radically new view of cataclasis has started to emerge. This is challenging conventional views of faulting which remain essentially within Andersonian terms for most geologists.

The aim of this study is to attempt to meet some of the need to complement strictly geometrical approaches, to provide data for the application of rock mechanics experiments, to test theories of cataclasis, and to examine the new view of cataclasis. The objectives to meet this aim are to:

(1) Describe mechanisms and modes of deformation in a range of upper crustal environments from field examples.

(2) Describe as quantitatively as possible the texture, structures and microstructures characteristic of each mechanism.

(3) Deduce as quantitatively as possible the conditions of temperature, confining pressure and differential stress under which the mechanisms operated.

(4) Deduce the major factors that determine type of deformation mechanism.

The scope of the study was originally designed to include a variety of lithologies. Most attention has been given to quartzites because microstructure could then be held as a constant in a variety of environments to examine the role of other variables. The field area, the Cantabrian and West-Asturian-Leonese zones, N.W. Spain offers a good exposure of a pure quartzite deformed under conditions from lowest grade to

mid-greenschist facies.

The study also has a wider relevance to other problems than referred to above:

i) **Shallow level seismicity.** The quartzites are intensely deformed and therefore may preserve structures from both seismic events and aseismic creep. The identification of diagnostic seismic structures is important to understanding seismicity and seismic risk assessment.

ii) **Neotectonics.** Cataclastic features have been widely used to deduce neotectonic kinematics and even crustal stress levels (e.g. Bevan and Hancock 1986). However their interpretation is speculative and requires establishing on a firm basis from field studies.

iii) **Models of Crustal Scale Deformation.** Computer models such as those of Kusznir and Park (1982, 1984) rely on failure criteria from rock mechanics data and conventionally refer to a 'brittle-ductile' transition. This study should bring some insights into the reality of the modelling.

iv) **Permeability and Mineral Potential.** The type of deformation studied has already been identified as important in the evolution of hydrocarbon resources (e.g. Pittman 1981) through its control on permeability.

v) **Regional Geology.** Some aspects of the regional geology of the Cantabrian and West Asturian Leonese zones are considered during the study.

1.2 STUDY AREA

This study has been made on quartzites from the Cantabrian and West Asturian-Leonese zones (C.Z. and W.A.L.Z.) of the Ibero-Armorican Arc, N.W. Spain, a major C shaped structural feature that can be traced from north Spain into northern France, and represents part of the Variscan orogenic belt. In Spain, the Ibero-Armorican Arc can be subdivided from east to west, and externally to internally, into the C.Z., and the W.A.L.Z. separated by the Narcea antiform, and the Galician-Castillian zone in the

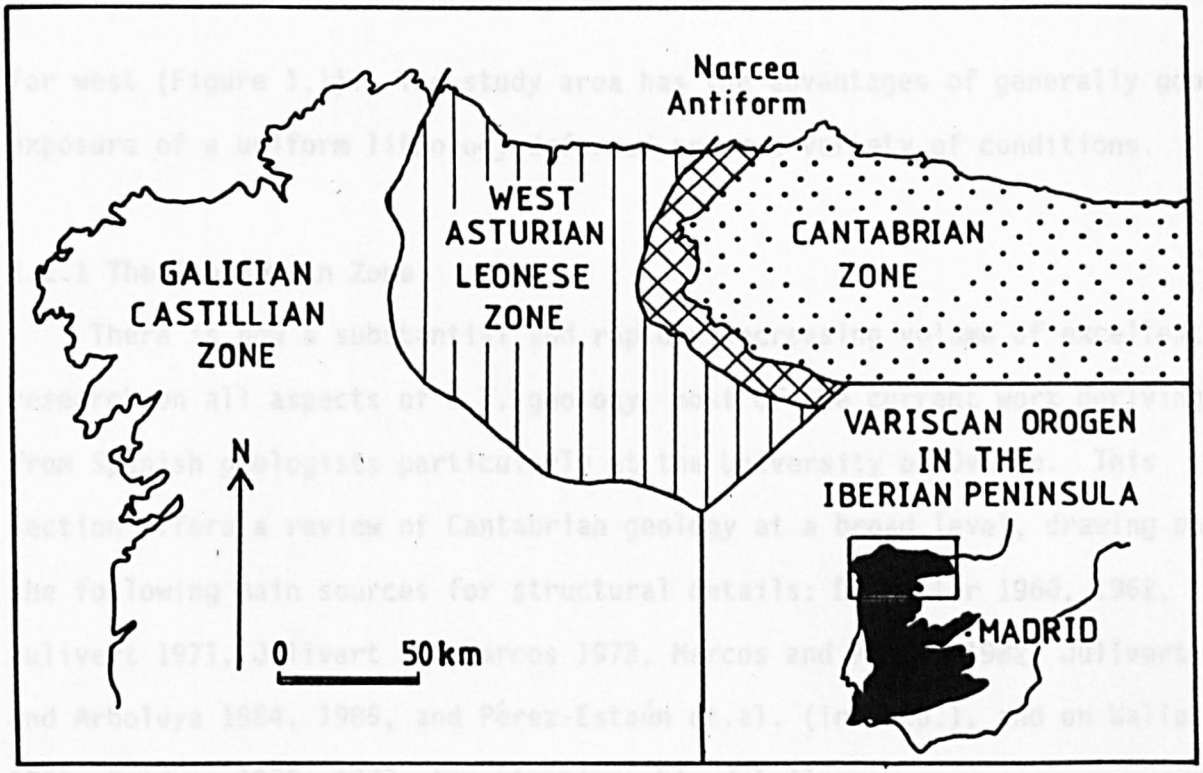

FIGURE 1.1
The Ibero-Armorican Arc, North Spain.

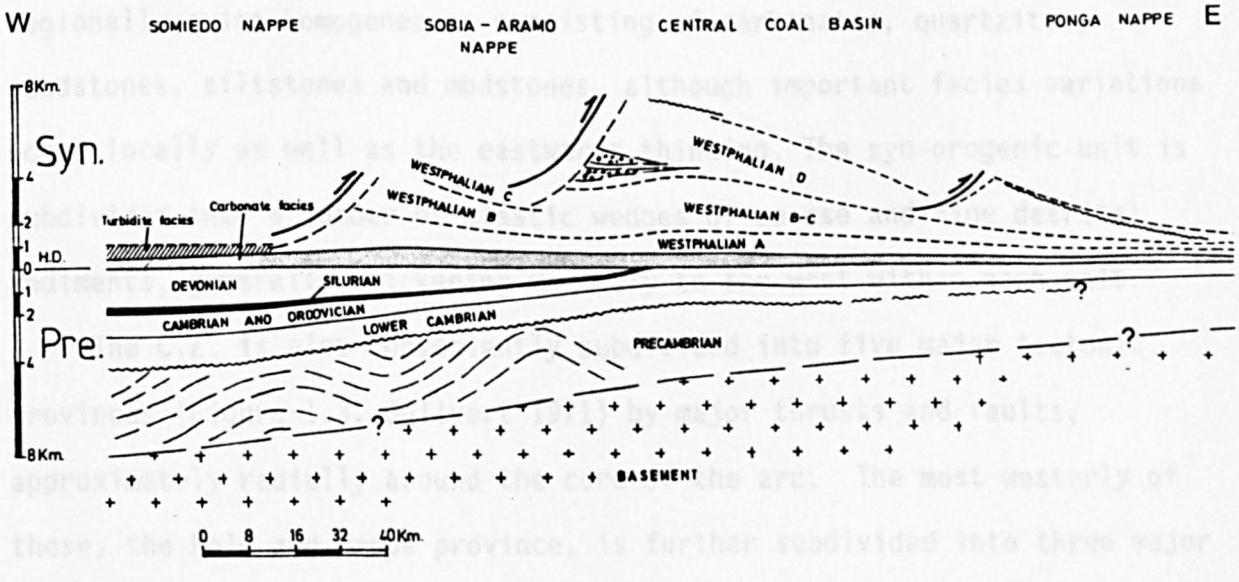

FIGURE 1.2
Palinspastic reconstruction of the Cantabrian Zone, Marcos and Pulgar (1972), showing the preorogenic and synorogenic teconostratigraphic units.

far west (Figure 1.1). The study area has the advantages of generally good exposure of a uniform lithology deformed under a variety of conditions.

1.2.1 The Cantabrian Zone

There is now a substantial and rapidly increasing volume of excellent research on all aspects of C.Z. geology, most of the current work deriving from Spanish geologists particularly at the University of Oviedo. This section offers a review of Cantabrian geology at a broad level, drawing on the following main sources for structural details: De Sitter 1960, 1962, Julivert 1971, Julivert and Marcos 1973, Marcos and Pulgar 1982, Julivert and Arboleya 1984, 1986, and Pérez-Estaún et.al. (in prep.), and on Wallace 1972, Baldwin 1976, 1977, for stratigraphic details.

The C.Z. consists of a 3-4km thick sequence of lower Palaeozoic continental-shelf sediments, which can be subdivided following Marcos and Pulgar (1982) into two tectono-stratigraphic units at the Devonian-Carboniferous boundary: a pre-orogenic wedge thickening to the west, and a syn-orogenic unit (Figure 1.2). The pre-orogenic unit is regionally quite homogeneous, consisting of cárbonates, quartzites, sandstones, siltstones and mudstones, although important facies variations occur locally as well as the eastwards thinning. The syn-orogenic unit is subdivided into a number of clastic wedges of coarse and fine detrital sediments, generally thickening markedly to the west within each unit.

The C.Z. is also conveniently subdivided into five major tectonic provinces (Figure 1.3, Julivert 1971) by major thrusts and faults, approximately radially around the core of the arc. The most westerly of these, the Fold and Nappe province, is further subdivided into three major units (Esla, Sobia-Bodon, and Someido-Correcilla) and these units into smaller thrust sheets (e.g. Correcilla, Rozo, Pozo and Bregon within the Someido-Correcilla Unit). The boundaries between the units and thrust sheets are thrusts with a general decollement within the Ordovician Láncara

FIGURE 1.3

Tectonic Provinces, Units and Thrust Sheets of the Cantabrian Zone (After Julivert 1971), with sampling localities indicated.

WEST ASTURIAN LEONESE ZONE

NARCEA ANTIFORM

CANTABRIAN ZONE

N

Cabo de Peñas

Punta Vidrias

Gijon

Ventaniella Fault

Rb.

•Oviedo

Bl.

T.

L.S.

L

Ri.

E.

Leon Line

Villamanin

Bd.

G.

R.

C.

P.

B.

Sabero

Gordon Line

Cremenes

Luna Lake

Bernesga Valley

0 10 20km

NARCEA ANTIFORM

PreCambrian Core and Lower Palaeozoic

FOLD AND NAPPE PROVINCE

UNITS

Somiedo-Correcilla

Sobia-Bodon

Esla

THRUST SHEETS

Bl. Belmonte Tm. Tameza

R. Rozo P. Pozo

C. Correcilla B. Bregon

Bd. Bodon

CENTRAL COAL BASIN

Carboniferous

PONGA NAPPE PROVINCE

THRUST SHEETS

L. Laviana

Ri. Rioseco

Rb. Ribadesella

E. Espinaredo

PICOS DE EUROPA PROVINCE

PISUERGA CARRION PROVINCE

THRUST

STRIKE SLIP FAULT

OTHER FAULT

ANTICLINE SYNCLINE ARCHED FOLDS

ANTICLINE SYNCLINE RADIAL FOLDS

Formation, but decollement also occurs at stratigraphically lower horizons (the Cambrian Herrería Formation) and at higher levels (the Devonian Santa Lucía Formation at the base of the Carboniferous, (Vegamián), and intra-Stephanian (Julivert and Arboleya, 1984). Field areas and samples in this study came from the south and north of the Somiedo-Correcilla unit at Cremenes, the Bernesga Valley, Luna Lake, Punta Vidrias and Cabo de Peñas (Figure 1.3).

Pérez-Estaún et al. (in prep.) have recently summarised some of the characteristics of the C.Z. thrust units, but also emphasised the considerable structural variety. They compare the overall outcrop of the units to the leaves of a camera Iris; that is, a curved wedge shape, opening towards the outside of the arc. Thrusts are characterised by ramp and flat staircase geometries, with important lateral as well as frontal ramps which may cut through all or only part of the stratigraphy. Imbrication is common but highly variable in amount; duplexes and out-of-sequence thrusts are observed. Very dense imbrication creates tectonic windows, for example at Rio Color and Rio Monasterio within the Ponga nappe. The thrust style is therefore one typical of 'thin skinned' tectonics.

Thrust transport directions can be established by the use of lateral ramps (e.g. Butler 1982), cut-off lines, and folds. These are summarised in Julivert and Arboleya (1986). The Esla unit, and the southern part of the Somiedo-Correcilla unit had a N.E. transport direction. In the west of the latter unit, the direction became due east. A similar NE direction is inferred for the Sobia-Bodon thrust sheet, while the Central Coal basin moved in this direction in the south, but more towards the east further north. The Ponga nappe movement was towards the east or southeast, and the Picos de Europa as a whole moved due south. These patterns can be described overall as radially inwards towards a relatively autochthonous core of the arc in the Pisuerga Carrion province. Julivert and Arboleya propose an

elegant model in which the curving transport directions observed within the Somiedo-Correcilla, Sobia-Bodon and Central Coal basin nappes are due to rotational emplacement about a hinge point in the north corner of the nappes. Rotation of the nappe sheets generated a swing in strike of transport directions. In this model, the hinged edge of the thrust sheet dies out into a fold pair; the curved trace of the thrust front eventually becomes a strike-slip fault. Transport amounts are more difficult to estimate. Alonso (1987) estimates 90 km cumulative displacement on the thrust sheets of the Esla nappe, and about 65km accumulated displacement is given for deformation within the Ponga Province by Pérez-Estaún et al. (in prep.) and 35km within the Picos de Europa Province.

Emplacement mechanisms have been considered by Julivert and Arboleya (1986) and Pérez-Estaún et al. (in prep.). The former authors show clearly that, from the wedge shape of the pre-orogenic units thickening to the west, an imposed shear stress of 6MPa at 7km could produce movement on a weak decollement level. Gravitational gliding could only occur in the front of the orogen: there is, for example, evidence from olistrostromes of this process in the Pisuerga-Carrion province. The latter authors agree that crustal compression is the essential driving force related to the processes of orogeny in the internal zone.

An equally important aspect of deformation within some parts of the Cantabrian zone is the large scale folding. Conventionally, two systems of folds have been recognised in the C.Z.: an 'arched' set parallel to the strike of the arc, and a 'radial' set about the arc core. These are evident in Figure 1.3, and have been subject to three separate interpretations. Julivert and Marcos (1973) considered the two sets to have occurred sequentially, the radial set post-dating and refolding the arched set to generate fold interference structures, and also that both fold sets post-dated thrusts, although they did point out that this did not imply three separate deformation phases, since the events occurred

diachronously across the whole C.Z. The 'radial' fold set was related to the convergence of the thrust units towards the centre of the arc as a response to the space problem. More recently, Julivert and Arboleya (1984) incorporated generation of the arched folds into their model for rotational nappe emplacement as a consequence of shortening perpendicular to one edge of the rotating, curved nappe, and also considered that the propagation of the thrusts was preceded by the development of the folds, which were eventually cut by the thrust; this is the 'ductile bead' model. Finally, Pérez-Estaún et al. (in prep.) and Alonso (1987) have linked not only arched or longitudinal folds to thrusts, but also many instances of radial folding, which are considered to be due to geometrically necessary folding over lateral ramps. Tightening of longitudinal folds leading to overturning has been a consequence of continued displacement over frontal ramps, and both sets of folds have been tightened by the late southward movement of the Picos de Europa. Which structures have been amplified depends on their orientation with respect to this movement: longitudinal folds and thrusts have been tightened in the south, and radial structures in the Central Coal basin and Ponga provinces, since these are the structures perpendicular to the S-directed movement in each place. Successively more recent views of the folds have therefore reduced the difference between different deformation phases in favour of a progressive evolution; the latest synthesis has the advantage of overcoming the space problem generated in the core of the C.Z. by simultaneous convergence of all thrust units.

The timing of the deformation and thrust sequence can be well constrained by the stratigraphy of the synorogenic deposits within each unit. Absence of Westphalian A deposits in the Somiedo-Correcilla Unit suggests that deformation was well established here by this time - also witnessed by the presence of Namurian olistrostromes formed ahead of the thrust front in the Sobia Gordon unit. This unit has Westphalian A-C

deposits in a wedge shape thickening towards the west: it was the next to move. In the Central Coal basin and Ponga nappes, the synorogenic deposits reach Westphalian D, with coarse fluviatile conglomeratic facies. The last Province to move was the Picos de Europa: southwards movement began in the Kasimovian (Marquinez, in Pérez-Estaún et al. (in prep.) and was responsible for folding of upper Westphalian D deposits lying uncomformably over the Esla thrust during Stephanian A times. The whole deformation lasted throughout the Westphalian, spreading clockwise around from the Esla Nappe to the Somiedo Correcilla unit, Sobia Gordon unit, Central Coal basin, Ponga nappe and finally the Picos de Europa province. The synorogenic wedges have been interpreted as fillings of the foredeep trough migrating ahead of the growing stack of nappes by Marcos and Pulgar (1982): their view of this occurring in an east-to-west direction is probably oversimplified in view of the above account. Areal balancing of the C.Z. by Julivert and Arboleya (1986) suggests an areal reduction of 45-50%.

Palaeomagnetic techniques have been applied to the C.Z. with considerable success (Ries et al. 1980, Peroud and Bonhommet 1981, Bonhommet et al. 1981, Perroud et al. 1984) to constrain rotational motions and to reconstruct the arc. The total present curvature of the arc from thrust traces, bedding, and fold axial traces has been measured as 165^{o} or 150^{o} by Ries et al. (1980) and Perroud and Bonhommet (1981) respectively. 110^{o} or 80^{o} of curvature is calculated from the palaeomagnetic data, indicating that 55^{o} or 70^{o} of the arcs' curvature was primary (pre-tectonic). Julivert and Arboleya (1984), have factorised the tectonic curvature into 60^{o} (or 40^{o}) due to rotational nappe emplacement, and 50^{o} (or 40^{o}) due to tightening of radial folds.

In addition to the pervasive thrusting and folding of the C.Z., there are a number of other important regional faults that require comment.

a) The Leon line. An E-W line can be drawn at the base of the Sobia Gordon unit (Figure 1.3) separating two structural and stratigraphic

provinces in which there is a contrast in the pre-orogenic sedimentation, known as the Asturides to the north of the line and the Leonides to the south. The main difference between the two areas is that the Devonian is largely absent from the Asturides, where upper Devonian is uncomformable on Ordovician or Cambrian rocks. Kullman and Schonenberg (1979) have argued that this is a tectonic control on stratigraphy; during the Devonian, uplift of the Asturides led to erosion while the Leonides accumulated thick shelf sediments. Subsequently, the Asturides also subsided, accumulating manganese shales in the Westphalian while the Leonides have clastic orogenic sediments derived from the inception of thrusting. They also refer to the possibility that igneous activity has been localised along the Leon line. However, Marcos (1979) argued that the contrast between deep water, 'Asturian-Leonese' facies in the south and shallow water 'Palantine' facies in the north across the line was due to tectonic telescoping of an originally widespread regional facies change, using as evidence the existence of equally large facies contrasts within a single province (the Pisuerga-Carrion Province). He suggests that the fault is a sinistral strike-slip feature related to nappe emplacement, and the same role is implicit in Julivert and Arboleya's model for rotational nappe emplacement. The fault was certainly active in the Variscan orogeny; Marcos suggests a phase of strike slip from the Namurian to Westphalian, followed by vertical movement in the Stephanian. This may also be an effect of the southward movement of the Picos de Europa. The long lived history and length of the fault lead naturally to the speculation that a deep, fundamental lineament may be involved.

b) The Sabero Gordon line. A second E-W line has been described within the Somiedo Correcilla Unit (Figure 1.3). This too has had an important influence on sedimentation and was active during the Westphalian thrusting of the Somiedo-Correcilla Nappe. During the Stephanian, small intramontane basins formed along the line at Sabero, Matallana and

Magdalena, and later coalesced to form a single basin. The earlier importance of the line is shown by the formation of a reef in the Mid-Devonian Portilla limestone where the line crosses the Luna Lake.

c) The Ventaniella Fault. A major strike-slip fault crosses the Ponga nappe and Central Coal basin in a NW direction (Figure 1.3). In post-Westphalian times, a minimum of 6km dextral movement has occurred,, and the fault has been active at least until the Tertiary. Marcos (1979) divides the movement history of the Ventaniella Fault into a Permian dextral strike-slip episode, and a Tertiary normal episode. In the Pisuerga-Carrion province, the fault dies out to be replaced by a number of splays.

d) The Narcea antiform. The N.A. in the far West comprises a large antiformal structure of Precambrian schists which are uncomformably overlain by the Cambrian Herrería sandstone. They are deformed and inverted in Precambrian times (Pérez-Estaún, 1973) as well as taking on a cleavage sympathetically with the Palaeozoic rocks.

Since none of the major thrusts appear at the surface again to the west of their present outcrop, it can be inferred that they must ramp from much deeper levels somewhere beneath the Narcea antiform. This has been termed a 'zone of deep faulting' by Julivert (Julivert 1971) and has given rise to the suggestion that the whole vast structure can be viewed as an antiform generated on a large scale in association with the deep- to shallow-level ramping of the decollement (E.H. Rutter, personal communication).

Although the metamorphic conditions of the Narcea antiform indicate slightly lower crustal levels than the rest of the Cantabrian zone, the Narcea schists clearly do not represent the crustal basement. The lack of any such crystalline basement indicates that shortening has occurred at shallow levels and/or relatively small displacements throughout the Cantabrian zone.

1.2.2 The West Asturian-Leonese Zone

The W.A.L.Z. has also been studied extensively by the Oviedo workers: the main source remains the seminal work by Marcos (1973), more recent work added by Bastida and Pulgar (1978), Bastida (1981), Bastida, Martinez-Catalan and Pulgar (1986).

Lithostratigraphically, the W.A.L.Z. also consists of a thick sequence of Lower Palaeozoic meta-sediments, equivalent to the pre-orogenic wedge of the C.Z., resting on similar late Proterozoic clastics. The sediments are shallow-water marine sandstones, siltstones, slates, quartzites, limestones and a deeper-water turbidite facies, of Cambrian-Ordovician age, with a thin covering of Silurian and even lower Devonian in the west. Marcos has shown that the cumulative thickness increases from similar values to the C.Z. in the east (3km) to a maximum of over 6km in the central W.A.L.Z., before decreasing again to 2km in the west.

The W.A.L.Z. is defined by a basal thrust (Allende Thrust) or unconformity on Precambrian rocks of the Narcea antiform in the east, and by the Vivero fault between it and the Central Iberian zone or Galician-Castillian zone in the far west of Spain, a crystalline province of gneisses, granites, and migmatites including allochthonous mafic and ultramafic bodies at eclogite-granulite facies, some with an ophiolitic nature (Figure 1.4). The Vivero fault may have a downthrow to the west of 10km. Three tectonic domains are distinguished within the W.A.L.Z.: the Navia domain to the east, which is subdivided into approximately equal east and west domains at the Barayo thrust by Marcos, the Mondoñedo domain in the west, separated by the Mondoñedo Basal thrust, and the Sierra del Caurel-Truchas or Caurel domain in the south. The field areas and samples come from coastal exposures in the north of both halves of the Navia domain (Figure 1.4). Although there are substantial differences between domains, the W.A.L.Z. can be treated as one unit on a broad scale.

All domains are cut by large thrusts which extend for long distances

FIGURE 1.4

Tectonic Domains of the West Asturian-Leonese Zone. (After Marcos 1973, Bastida, Martinez-Catalan and Pulgar 1986), with sampling localities indicated.

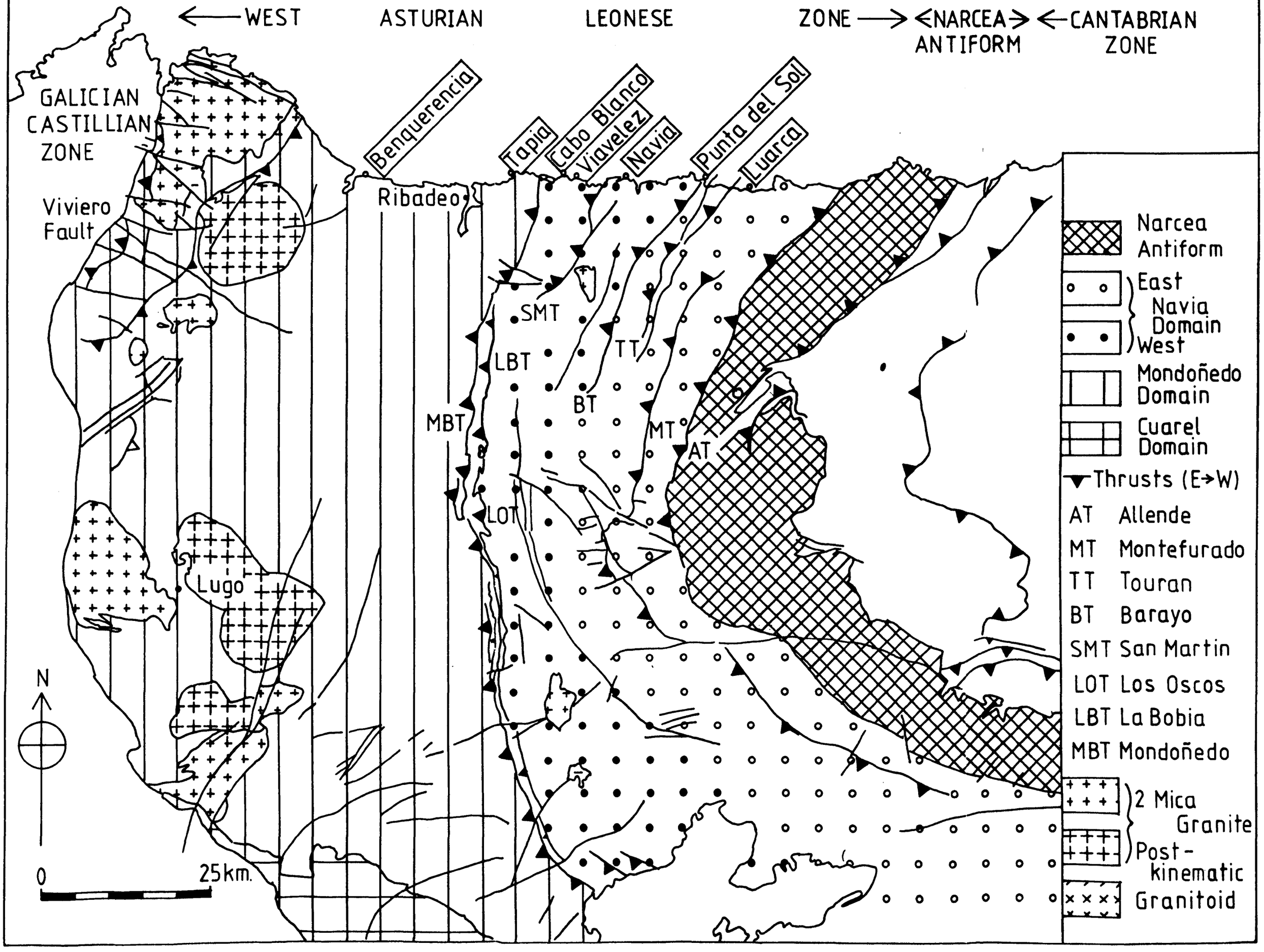
WEST
ASTURIAN
LEONESE
ZONE
NARCEA ANTIFORM
CANTABRIAN ZONE
GALICIAN CASTILLIAN ZONE
Viviero Fault
Benquerencia
Ribadeo
Tapia
Cabo Blanco
Viavelez
Navia
Punta del Sol
Luarca
SMT
LBT
TT
BT
MBT
MT
AT
LOT
Lugo
N
0
25km.
Narcea Antiform
East Navia Domain
West
Mondoñedo Domain
Cuarel Domain
Thrusts (E→W)
AT Allende
MT Montefurado
TT Touran
BT Barayo
SMT San Martin
LOT Los Oscos
LBT La Bobia
MBT Mondoñedo
2 Mica Granite
Post-kinematic Granitoid

parallel to the strike of the Asturian arc (over 100km), including the Allende, Montefurado, Touran, Barayo, San Martin, Bobia, Los Oscos, Basal Mondoñedo, Villaodrid and Recende thrusts from east to west (Figure 1.4). Transport directions are taken as approximately normal to the strike of the thrusts; displacements are not known in much detail, except for the Mondoñedo Basal thrust (M.B.T.), which has a minimum displacement of 40km. Some thrusts juxtapose domains of different stratigraphy; this has been taken to indicate large displacements by Marcos (1973). The M.B.T. is a zone between 200m and 3km wide of intense deformation, in which small-scale east-verging isoclinal asymmetric folds are developed, often with sheath geometries, and an intense schistosity or crenulation cleavage. Mylonites and phyllonites are present as well as cataclastic features: the thrust has the characteristics of a major shear zone showing different levels of exposure.

The thrusts generally have a sub-vertical attitude at outcrop; this is ascribed to later folding, which is certainly evident in the convoluted trace of the Los Oscos thrust, but it is noteworthy that the thrusts of the Navia domain are much more linear features.

Four sets of folds are developed throughout the W.A.L.Z. The most pervasive are recumbent, tight-isoclinal, east-verging structures described as F1 by Marcos (1973) and Bastida et al. (1986). The fold axes plunge gently to the north or south. The axial traces of the larger folds extend parallel to the thrusts for up to 100km along strike. Minor folds of this set are also seen with limbs several hundred metres long but more commonly 10 metres. Bastida (1981) has shown how the interlimb angle of these minor F1 folds reduces from 40^{o} to 20^{o} in a westerly direction across the W.A.L.Z., and that they formed initially as trains of rounded buckle folds which tightened to become chevron in style by flattening. The shortening calculated therefore increases from 36% to 69% in the same direction. A slaty cleavage or schistosity develops with these folds, generating an

intersection lineation parallel to the fold axis, and there is also a stretching lineation perpendicular to strike.

The second set of folds (F2) is confined to the Mondoñedo Basal thrust as described above, while the third set (F3), affecting the whole zone are upright, open folds which refolded F1, F2, and thrust planes, homoaxial with F1. An axial planar (S3) cleavage is developed as well as sub-horizontal kink bands and both intersection and stretching lineations parallel to the F3 axes. Marcos (1979) has shown that the S3 cleavage is sub-vertical or steeply dipping to the east in the Navia province, while the kink bands are sub-horizontal; the two maintain a fairly constant dihedral angle of 35-60^{o}, which, together with their complementary senses of shear, he has interpreted as indicating that the two features formed as a conjugate set. Interference fold patterns are seen between F1 and F3 folds in the Mondoñedo Nappe: these are of type 3 (Ramsay 1967) ("continuously converging or diverging forms") in which the angle between the fold axes (α) is 0^{o}, and the angle between the pole to the first axial surface and the second fold axis (β) is 0^{o} or small. An interesting observation is the lack of interference structures in the whole of the Navia unit; this has been explained in two alternative, but equivalent ways, firstly by Marcos (1973) and subsequently by Bastida et al. (1986). The former explanation is that F1 folds in the Navia province had moderately inclined axial surfaces; the superimposition of upright, homoaxial folds therefore caused very little refolding (almost none on the subvertical inverted limb) since the two fold axes were parallel (α=0^{o}), and the axial planes were separated by a small angle (β approached 90^{o}). The latter view, that refolding is not evident because the dihedral angle of F1 folds is larger in the east, is a similar way of seeing this; both the dip of the axial surface of F1 and the dihedral angle decrease to the west.

A fourth set of folds which affect the W.A.L.Z. is quite evident from the interference structures in both the Mondoñedo and Navia domains: these

are very large-scale gentle flexures with axial traces perpendicular to strike, which cause the outcrop of the Villayon anticline, for example, to appear as an elongate dome due to gentle N and S plunges at either end of the fold axis. These obvious type 1, "eggbox" interference patterns bear similarity to the radial folds of the C.Z., and it can be suggested that they played a similar role in accommodating late tightening of the Asturian arc by allowing uplift above converging lower crust. In this way, the stretching lineations and other evidence of strike-parallel extension is compatible with folding perpendicular to strike.

The whole W.A.L.Z. is at a metamorphic grade of chlorite zone or greater, increasing to the west up to silliminite and locally andalusite and kyanite in the Mondoñedo Nappe. Bastida et al. (1986) have shown that the isograds cut D1 and D2 structures but are distorted by D3, though their detailed disposition is complex because medium-pressure, low-pressure and retrogressive episodes can be distinguished - the last being confined to the Mondoñedo Basal thrust.

Within the Mondoñedo domain, there are abundant granitic rocks which can be classed into synkinematic biotite granitoids, part of the calcalkaline series, two-mica hydrated granites and post-kinematic, calcalkaline granitoids (Bastida et al. 1986). The synkinematic and two-mica granites were intruded after the first deformation but before shearing of the M.B.T. and had local metamorphic effects. Several outcrops of granitoid occur in the Navia domain including the Los Ancares, Boal, and Salave and Porcia granitoids (Figure 1.4). The first two are two-mica granites, and the third is a post-kinematic granitoid.

According to Bastida et al., all granites are deformed by F3 folds but Marcos shows evidence of porphyorblasts overgrowing the S3 crenulation from the Los Ancares granite, and deduces from its similarity to the Boal granite that both of them post-date D3. Small outcrops of granite occur in the Narcea antiform and even in the northwest of the C.Z.

In the absence of synorogenic sediments, dating of deformation in the W.A.L.Z. relies on extrapolation from outside the domain. There are sediments at least as old as Stephanian B-C strongly deformed by the D3 phase in the Caurel Domain; they may be Viséan, suggesting a 'Bretonic' age for D1. This is supported by dates of 349 +/- 10MA for deformed granites in Galicia; other syn-kinematic granite ages from that area have been given ages from 315 to 323 +/- 10 (Viséan-Namurian). The first deformation is therefore probably at least as old as Viséan.

Marcos (1973) has given evidence that the D2 thrusting phase in the W.A.L.Z. can be correlated with thrust movement in the C.Z. The first movements have been dated as early Westphalian (Westphalian A) in the C.Z. (as described above): it is probable that D2 is therefore also early Westphalian. This is slightly earlier than the Westphalian B date given by Marcos (1973) following more recent evidence of earliest Westphalian deformation in the C.Z. A similar correlation has been established between late folding in the C.Z. and D3 in the W.A.L.Z., which can therefore be dated as early Stephanian. The Los Ancares and Boal granites have ages of 300MA: if they are truly post-D3, this gives an upper limit of the Westphalian C-D boundary to the last deformation. The ages of deformation in the W.A.L.Z. are therefore probably Viséan - Westphalian D, equivalent to part of the range deduced for the C.Z., although the earliest deformation is not well constrained.

1.2.3 The Plate Tectonic Context of the Ibero-Armorican Arc

On the largest scale, the Variscan Orogeny in Europe must relate to the convergence of Laurasia and Gondwanaland. Perroud et al. (1984) have recently used palaeomagnetic data to suggest that during the Silurian-Devonian Armorica (including S. Britain, France and Spain) moved northwards ahead of Gondwana to which it was adjacent in mid-latitudes of the southern hemisphere during the Ordovician. Europe was assembled by

coalescence of Armorica, Baltica and Laurentia by the end of the Devonian; the Carboniferous orogeny represents the arrival of Gondwana which these authors imply provided the energy for lithospheric deformation of the Hercynian basement responsible for closure of the Ibero-Armorican arc. In this view, Armorica formed a "single coherent tectonic element" during most of Palaeozoic time.

To what extent this large scale model can be reconciled with that of Le Fort (1979) is unclear; the latter gives a satisfactory account for the major features of the Ibero-Armorican arc by invoking closure of an intra-Armorican ocean, followed by Matte and Burg (1981).

Lower Palaeozoic sediments of the Ibero-Armorican Arc were deposited originally in a continuous arc-shaped basin, which subsequently opened to form a small ocean on the site of the present Bay of Biscay, on the basis of the similar lower Palaeozoic sediments across the whole of Armorica, and gravity data which show the same pattern on both sides of the arc and correlate with isopachs of the Palaeozoic sediments. The arc was therefore partly a pre-tectonic configuration, as deduced by the palaeomagnetic data. At some stage in the mid-lower Palaeozoic, rifting produced an ocean basin on the site of the present Bay of Biscay, which closed on a north-dipping subduction zone during the Devonian; the evidence for this subduction, in the form of paired metamorphic belts, the anatectic granites of Brittany with dates of 370-380MA, and truncation of the pre-tectonic arc by linear features of gravity, magnetic and historical seismicity, is much more clear than similar suggestions made for a subduction zone north of Brittany somewhere in the English Channel, and is generally accepted as part of the Varsican story. Continental collision between the Iberian microplate and Armorica occurred from Namurian to Westphalian times, correlating with the tightening of the Asturian arc (the late southward movement of the Picos de Europa) and the emplacement of leucogranitic intrusions with ages of 300-300MA.

To the north of the Iberian segment of the Ibero-Armorican arc therefore, there is reasonable evidence for oceanic closure and continental collision that can be related to some tectonic events described in the W.A.L.Z. and C.Z. The situation to the west is not so clear; here there seems to be evidence for ocean closure and collision but with an essentially E-W convergence. The Cabo-Ortegal complex in the GalicianCastillian zone, a high grade complex of mafic/ultramafic rocks, has been interpreted as a nappe, partly ophiolitic, obducted towards the east southeast over a melange of continental Palaeozoic metasediments by several workers (e.g. Bayer and Matte, 1979). These authors extended this interpretation to similar arrangements of high-grade mafic and ultramafic rocks over Palaeozoic schists in Brittany and the Massif Central. The Mondoñedo Basal Thrust is interpreted as the upper levels of an 'intracontinental megashear' by Bastida et al. (1986) with the same direction of convergence, and they also suggest a second megashear which isolates a wedge of continental crust seen as the Ollo de Sapo anticlinorium to the west of the W.A.L.Z. If this links with the M.B.T. megashear, it forms a continental duplex. The Cabo-Ortegal complex and the megashears therefore suggest oceanic subduction and continental collision to the west of the Ibero-Armorican Arc and this view of a sharply convex, continuous convergence zone is also given by Badham (1982). However, it is difficult to reconcile the E-W directed convergence seen in the west with the NE-SW convergence in the northern part of the arc. One solution may be that the former occurred slightly earlier, during the earliest Carboniferous, and subsequently a change in plate motions towards the second convergence direction occurred during the Westphalian. This suggestion is made more plausible by the clockwise, sequential thrust emplacement directions inferred for the C.Z. in 1.2.1.

However, Haworth and Le Fort (1979) cast some doubt on the possibility of a plate boundary to the west by their correlation of Hercynian

structures across an 'Avalon' structural entity in Atlantic Canada between the Charlie Fracture Zone and the Collector Anomaly. Structural trends in the Canadian area, defined by mafic intrusions, match those of the Ibero-Armorican arc, while the South Armorican Shear Zone is supposed to connect with the Charlie Fracture Zone, and some faults in Spain with the Collector Anomaly. The authors do point out differences in crustal structure across the Atlantic (more mafic intrusions are found in the west), which, they suggest, may have localised the opening of the Atlantic.

In summary, a continuous plate boundary around the exterior of Iberia and between Iberia and Brittany is considered most probable, although closure may have been diachronous (earlier in the west) and the extent of ocean subducted on the site of the present Bay of Biscay may have been small.

1.3 STRUCTURE OF THESIS

Following this introduction to the field areas, the next chapter is a review of cataclasis as a deformation mechanism in the field, experiment and theory, limited to a consideration only of those aspects relevant to this study,and emphasising recent approaches. The concepts of brittleness, ductility, the brittle-ductile transition and cataclastic flow are reviewed, and finally some of the most common cataclastic features are defined. In Chapter 3, possible methods of study are reviewed. The choice made here is justified and the methods are evaluated for precision and error. Illite crystallinity, however, is reserved for a separate chapter (4), because some general conclusions about the technique resulting from this study are also presented. Chapters 5 to 8 give in detail observations on the four main field areas, the Bernesga Valley, Punta Vidrias, Luarca and Punta del Sol (Figure 1.3 and 1.4). Each is subdivided into the following sections: Stratigraphy and Lithology, Macrostructures,

Mesostructures, Microstructures, Illite Crystallinity and Synthesis. The three sections dealing with the structure are each concluded by a discussion. Both regional implications and the relevance of the literature review are considered in these chapters. Finally Chapter 9 compares the deformation mechanisms and conditions described in the area chapters to reach some conclusions about low-grade deformation mechanisms, modes, and conditions, finishing by summarising the specific conclusions and recommending future research. The Appendices contain the majority of microstructural data used, and some of the computer programmes written. All Figures and Plates appear in the text immediately following the first reference to them, but they do not have page numbers.

1.4 SYMBOLS AND UNITS

1.4.1 Symbols

Because of the great variety of symbols used, and a desire to maintain the author's usage where possible, symbols are defined as required in Chapter 2 independently of the remainder of the thesis, for which the following scheme is used, in which the symbols are given in approximately the order in which they appear in Chapter 3. Within equations, multiplication signs are generally implicit.

a) General Symbols

G.M. - Geometric Mean

H.M. - Harmonic Mean

A.M. - Arithmetic Mean

A.S.D. - Arithmetic Standard deviation

G.S.D. - Geometric Standard Deviation

V - Variance

$Q_{1,2,3}$ - Upper, Median and Lower Quartziles

SK - Skewness

n, N - Number of items/samples, defined as necessary

a,b,c - Lengths defined as necessary

θ - Angle, defined as necessary

R - Correlation Coefficient

ER - Error

Σ - Sum of Series, 1 to n

Π - Products of series, 1 to n

$\sigma_{1,2,3}$ - Principal Stresses

τ - Shear Stress

T - Temperature

< > - Crystallographic Zone Axis

b) Fractures and Microfractures

S - Fracture Spacing

F - Fracture Frequency

$D\ m^{-1}$ - Mesofracture Density

Dmm^{-2} - Microfracture Density/mm^2

Dmm^{-1} - Microfracture Density/mm

DG^{-1} - Microfracture Density/Grain

V - Unit Volume

S_V - Crack Surface/unit volume

FV - Field of View

ε - Dimensionless Crack Parameter

Af - Anisotropy in microfracture frequency

c) Grain Size

AR - Grain Area/Equivalent Sphere Area

L,l - Linear Intercept

r - Number of Intercepts/unit length

D - Equivalent Sphere Diameter

C - Class Interval

L.C. - Lower Limit of Smallest Class

F - Fabric (G.M.L.X/G.M.L.Z.)

d) Strain

$\lambda_{1,2,3}$ - Principal Quadratic Elongation

i,s,f - Postscripts for initial, strain, final values

R - Ellipse Axial Ratio

ϕ - Angle between ellipse long axis and reference direction

$E_{1,2,3}$ - Principal Natural (Logarithmic) Strains

α - Stretch

γ - Shear

f,g,h - Components of Matrix Representation of an Ellipse

c_{ij} - Components of Matrix Representation of an Ellipsoid

ρ - Owen's goodness of fit parameter

L - Number of Fryplot Origins

M - Total number of points on a Fryplot

N - Number of points in source data file

O - Overlap parameter of Fryplot

R - Fryplot Circle Radius

ISYMM - Lisle's Symmetry Test Parameter

ν - Lodes Parameter

k - Logarithmic Flinn Parameter, (Ellipsoid Shape Factor)

γ - Natural Octahedral Shear Strain

E_s - Natural Shear Strain

e) Fracture Mechanics

G - Strain Energy Release Rate/Crack Extension Force

Γ - Fracture Toughness

K - Stress Intensity Factor

I,II,III - Subscripts for Crack Mode

o,s,c,d - Subscripts for Threshold, Static, Critical, Dynamic Values

v - Crack velocity

U_m - Mechanical Energy

U_s - Surface Energy

1.4.2 Units

The following units are used exclusively

Lengths - metre (m), millimetre (mm), micrometre μ

Stress - Megapascals (MPa) = $1x10^6 N/m^2$=100b=0.1kb

Temperature - Degrees Centigrade (^oc)

CHAPTER 2

REVIEW AND DEFINITIONS

2.1 REVIEW OF STUDIES OF NATURAL CATACLASTIC DEFORMATION

2.2 REVIEW OF EXPERIMENTAL WORK

2.3 REVIEW OF THEORETICAL STUDIES OF CATACLASIS

2.4 REVIEW OF THE CONCEPTS AND DEFINITIONS OF BRITTLENESS, DUCTILITY, THE BRITTLE-DUCTILE TRANSITION, AND CATACLASTIC FLOW

2.5 FRACTURE, FAULT AND FOLD ROCK NOMENCLATURE

2.1 REVIEW OF STUDIES OF NATURAL CATACLASTIC DEFORMATION

Compared with the amount of experimental and theoretical work, the volume of literature on natural cataclastis is relatively small. Four main themes can be distinguished in these studies: cataclasis and folding, cataclasis and faulting, the nature of regional fracture systems and, as a rather specialised category, the surface morphology of fractures, or fractography. Studies have been made on all scales, with slightly more emphasis on meso- and macroscale features, but the most successful integrate evidence from the entire range of scales.

2.1.1. Cataclasis and Folding

a) **Fracture Orientations.** The early observations of Stearns (1964, 1968a, b) and Price (1966) remain the most fundamental. Both authors report the existence of a characteristic 'assemblage' of two to three sets of fractures: two sets are conjugate inter-secting in an acute angle of 60^{o} or less, with the third set, if present, bisecting the conjugate pair. Throughout the literature this assemblage is assumed to have formed in an ideal Andersonian orientation to the principal stress: the two conjugate fractures are thus shear and hybrid fractures intersecting in the intermediate principal stress direction (σ_2) with the maximum principal stress (σ_1), perpendicular to the line of intersection in the acute angle and the least principal stress (σ_3) in the obtuse angle. The third fracture set is interpreted as a tension fracture formed perpendicular to σ_3. It is well worth emphasising at this early stage that while the orientation of genuine conjugate fractures can give the relative directions of the principal stresses, not only may the fractures bear no relationship to subsequent stress systems, but the likelihood of rotation during folding means that no information about the initial absolute orientation of the stress system can be inferred on the basis of the fracture sets alone.

Also Mohr-Coulomb theory prohibits the formation of both extension and shear (or hybrid) fractures in the same stress conditions.

This assemblage is found in four orientations relative to the fold axis. Unfortunately these relations are usually described in coordinates of the inferred stress system, but this is undesirable for the reasons just given. The observations can be described in purely geometrical terms by the orientations of two lines, λ_1, and λ_2, relative to the bedding and fold axis (b). λ_1 is the acute bisector of the conjugate fractures, and λ_2 is their line of intersection (Figure 2.1). (In the ideal Andersonian system, λ_1 and λ_2 would correspond to the maximum and intermediate principal stresses σ_1 and σ_2).

Assemblage 1. λ_1 perpendicular to b, λ_2 perpendicular to bedding. Fractures in the plane bisecting the conjugate pair are also described as ac joints. All fractures of this set are perpendicular to bedding (Figure 2.1a).

Assemblage 2. λ_1 parallel to b, λ_2 perpendicular to bedding. Fractures in the bisecting plane are also referred to as bc, longitudinal or radial joints, and all fractures of this set are perpendicular to bedding (Figure 2.1b).

Assemblage 3. λ_1 perpendicular to bedding, λ_2 parallel to b. The plane bisecting the conjugate set has the same orientation as the plane in assemblage 2. Fractures of this set are all perpendicular or sub-perpendicular to bedding (Figure 2.1c).

Assemblage 4. λ_1 parallel to bedding, λ_2 parallel to b. Such fractures with shear displacements have been called inner arc thrusts (Ramsay 1967). All these features are sub-parallel to bedding.

Fractures of all these orientations have been described by Stearns (1964, 1968) from the Teton anticline, Montana. Assemblage 1 is more densely developed than 2, and assemblage 3 is defined only locally. Assemblage 4 is found below assemblage 3.

FIGURE 2.1

Observed orientations of fractures with respect to folds, after Stearns (1968). λ_1 is the acute bisector of the conjugate set, λ_2 is their lines of intersection, and b is the fold axis.

a) Assemblage 1
b) Assemblage 2
c) Assemblage 3
d) Assemblage 4

FIGURE 2.2

Hancock's classification of fractures (e.g. 1985).

a) Fractures in ab
b) Fractures in bc
c) Fractures in ac
d) Conjugate hol fractures enclosing an acute angle about a.
e) Conjugate hol fractures enclosing an acute angle about c.
f) Conjugate okl fractures enclosing an acute angle about b.
g) Conjugate okl fractures enclosing an acute angle about c.
h) Conjugate hko fractures enclosing an acute angle about b.
i) Conjugate hko fractures enclosing an acute angle about a.

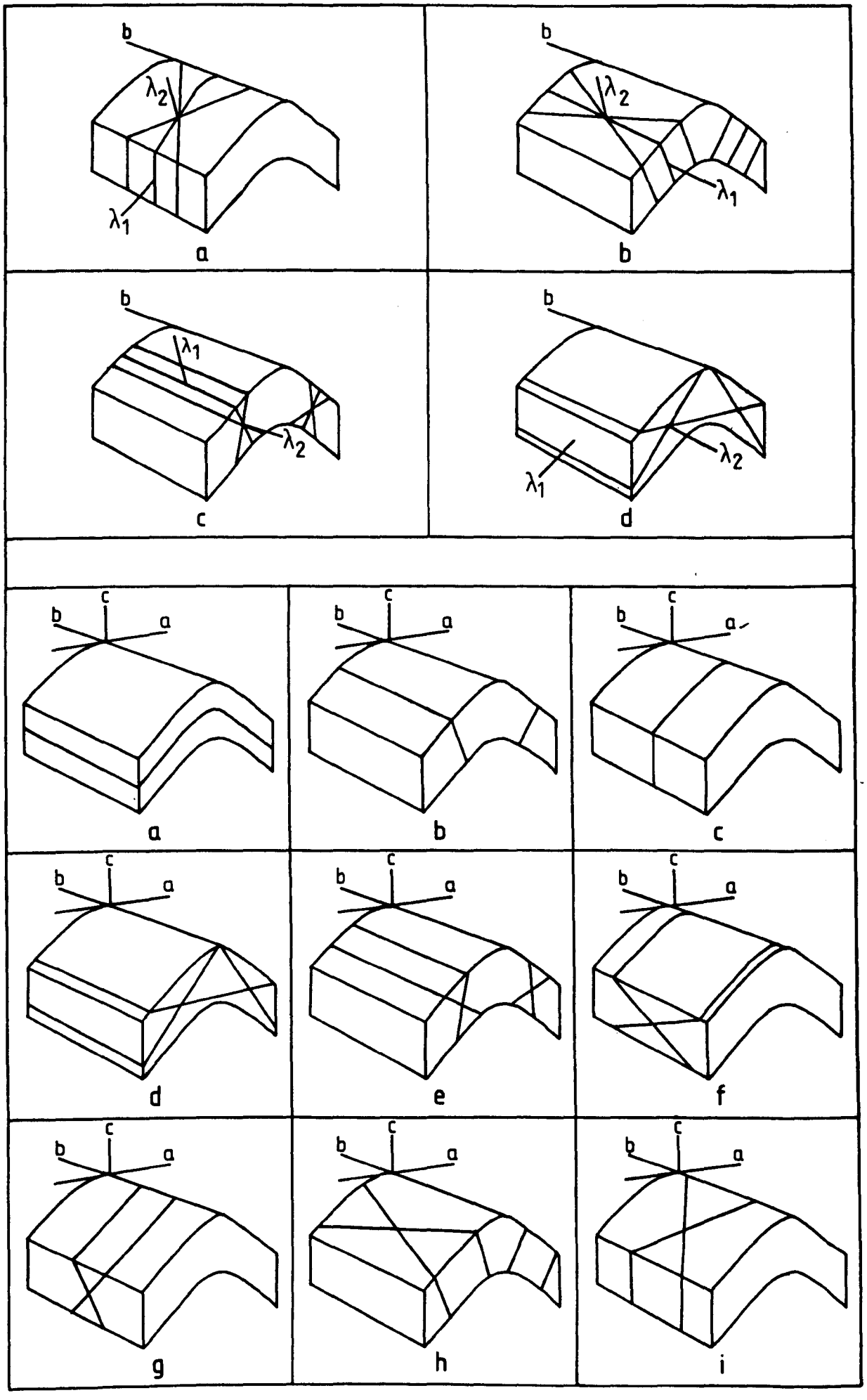
b
λ2
λ1
a
b
λ2
λ1
b
c
λ1
λ2
c
b
λ1
λ2
d
c
b
a
a
c
b
a
b
c
b
a
c
d
c
b
a
e
c
b
a
f
c
b
a
g
c
b
a
h
c
b
a
i

The same geometries are described, but more comprehensively by Hancock's classification of fractures around folds (Hancock et al., 1982, Hancock, 1985). The reference frame is taken as the fabric cross abc, with b parallel to the fold axis, ab the plane of bedding, and c the bedding normal. Fractures are described by their intercepts (hkl) on the abc axes, in a similar fashion to the Miller Indices of crystal planes (Figure 2.2). The four assemblages above of Stearns can be described exactly by this classification, which has the advantage that fractures bisecting the acute angle of a conjugate set do not have the genetic link to that set implicit in the Stearns system of assemblages. Fractures of most of these orientations have been described by Hancock et al. (1982) from the Variscan orogen of S.W. Wales, and Turner (1986) has also described some of such fractures from a Tertiary molasse basin in the Spanish Pyrenees.

Two important points are revealed by Figures 2.1 and 2.2. Firstly, fractures can be considered more generally as normal or at a high angle to bedding (Figure 2.1 a,b, and c, and Figure 2.2 b,c,e,g,h,i), or parallel or sub-parallel to bedding (Figure 2.1 d, Figure 2.2 a,d,f). Secondly, the majority of fractures belong to the first group, those perpendicular or sub-perpendicular to bedding.

Descriptive accounts of fracture orientations around folds which do not introduce schemes of classification such as those in Figures 2.1 and 2.2 have the merit of not imposing an artificial symmetry on the observations. A good early example is the account by Harris et al. (1960) of fracture orientations around two open domes in Wyoming. The authors identify one dominant set of bedding perpendicular fractures at most positions around the fold, with a second subordinate set in places. They show that the orientation of the dominant set is consistent throughout each limb of the fold but changes on opposite sides. In the hinge, both sets are developed. The dominant sets are interpreted as conjugate fracture, "initially determined by the regional stresses... in turn modified in trend

and concentration by the local compressional structural elements." It is not clear whether the authors mean a modification by rotation or by the formation of the dominant set in a different direction ab initio, and either possibility is admissable from their data.

McQuillan (1973) has some interesting observations on fracture sets and orientations in the Asmari formation of S.W. Iran. Bedding perpendicular fractures may occur in up to ten sets, all related to a single tectonism, although most stations show two dominant sets and others less well developed. The overall regional picture is of a dominant direction of fracturing in the bc plane (hoo fractures) which McQuillan interprets as radial fractures reactivated due to tensile stresses on the outer arc of a fold deforming by tangential longitudinal strain. In common with the earlier study by Harris et al., the results of fracture orientations are difficult to interpret because they are presented in two dimensions as rose diagrams.

Orientations of 'microfaults' were measured around a gentle drape fold in the Wingate sandstone above a vertical, dip-slip basement fault in Colorado (Jamison and Stearns, 1982). Two conjugate sets of microfaults were observed but the accurately measured orientations do not coincide with any of those in Figures 2.1 or 2.2. In Hancock's classification, they are hkl fractures, enclosing acute angles of 20-40^{o} about c and 20^{o} about b, or a combination of Stearns's assemblages 2 and 3. Although there are two sets with opposing displacements, their orientations form a spread within a small circle of 30^{o}, and one set is usually dominant: as the basement fault is approached, on the upthrown side, this changes from the sense sympathetic to the basement fault (sinistral) to the antithetic sense. The orientations of the microfaults change as the basement fracture is approached and the beds flex: the cluster of microfault poles rotates to maintain an approximately normal relationship to the bedding.

Winsor (1985) measured fracture orientations on a large steeply

plunging anticline in the Mount Isa District, Australia, over an area of approximately 100km^2. A pattern of steeply dipping faults with a radial orientation about the fold axis was observed. To test how well these could be described as bc features, the predicted bc orientation was constructed from the fold axis and local bedding plane. The observations matched this pattern well.

The accommodation of any three-dimensional strain by fracturing has been studied from field examples by Bruhn and Pavis (1981), Aydin and Reches (1982) and several examples therein, Underhill and Woodcock (1985) and speculated on by Oertel (1965). In these examples it was shown that at least three sets of fractures developed simultaneously with deformation, none in conjugate pairs.

b) Fracture Densities. The work of Harris et al. referred to above is much more useful for its account of fracture density measurements, evaluated by number of fractures per square yard. The influence of bed thickness and lithology are carefully allowed for by 'thickness' and 'lithology' factors, used to reduce all measurements to a datum value. The thickness factors are derived from a simple inverse relationship observed between density and bed-thickness. Lithology factors are calculated by comparing densities in different lithologies at the same structural position, corrected for bed thickness. The final calculated densities show, reasonably clearly, an increase of two to three in areas of maximum bed curvature, although there seem also to be spurious areas of increased fracture density. One possible criticism of this study is the assumption that the same inverse relationship applies to all thickness/density data: this is certainly not demonstrated.

Fracture densities specifically around folds have been reported by Stearns (1968), who showed the dominant influence of lithology in determining the fracture spacing. This increased from 2.9m^{-1} to 20.7m^{-1} for the sequence of lithologies: limestone-calcite cemented

sandstone-quartz cemented sandstone-dolomite-quartzite, and Stearns compared this to the same sequence of decreasing ductilities obtained from triaxial experiments. On the Teton Anticline, localised zones of high intensity fracturing, with a spacing of 18m parallel to the anticlinal axis were recorded. He noted that the hinge areas of a fold at Rattlesnake Mountain, Wyoming, showed dense fracturing and also showed the importance of bed thickness in determining fracture densities. Quite contradictory results emerged from McQuillan's study. He found that fracture frequency (measured per metre along a line normal to the fracture set) was effectively constant in beds of given thickness and lithology, irrespective of structure. An inverse logarithmic relationship between density and bed thickness was shown.

In the Jamison and Stearns study, a detailed map of microfault densities over the drape fold had increasing fracture density with proximity to the basement fault and the drape fold hinge in the upthrown side only, which correlated with, and caused a decrease in permeability. In the downthrown side, moderate fracture densities occurred at the synclinal flexure, some distance from the basement fault. A second exposure also showed high densities adjacent to the basement fault and fold hinge in the upthrown side, but generally lower densities throughout the structure. The higher fracture densities are firstly correlated with hinge regions of folds. However, important effects are also due to lithology, explaining the contrast between the up and downthrown patterns (since the lower half of the Wingate sandstone, with the high fracture densities, does not outcrop in the downthrown side) and to localisation. This is considered to explain the overall low densities of the second exposure, where "within these cover intervals, there are scattered exposures of highly microfaulted and rubbleized bedrock." The localisation also is confined to certain units.

The influence of lithology on fracture densities in a general context

has been addressed by many other studies and will not be considered here (e.g. Price 1966, see Pohn 1981 for a summary of references). Likewise, several different relationships have been proposed between fracture density and bed thickness, most of which can be approximated by an inverse relationship between frequency and thickness (equivalent to a linear relationship between separation and thickness). Ladeira and Price (1981) showed that this held for a variety of lithologies (each with a different constant of proportionality) up to a maximum bed thickness beyond which fracture separation was constant. A hypothesis to account for this was the change from traction-controlled fracture spacing in thin beds to permeability-controlled hydrofracture in thicker beds, in which a constant fracture spacing, necessary to maintain the hydraulic gradient for hydrofracture, is predicted.

(c) Fracture and Fold Dating. The characteristic and common relationship between fractures and fold orientations, shown in Figures 2.1 and 2.2, is often considered as evidence that the two are contemporaneous and formed in the same stress field, particularly when an appropriate and simple stress geometry can be deduced, for example from Figure 2.1 a, d and Figure 2.2 a, c, d, g, i, in which the maximum principal stress deduced from the conjugate fractures is perpendicular to the fold axis, or Figure 2.2 b, which might indicate a minimum principal stress normal to the fold axis, appropriate to tangential longitudinal strain in the outer arc of a beam. However, this is not sufficient proof of contemporaneity of formation, since identical stress fields may have been applied at different times or even continuously over a long time interval; nor of stress field homogeneity, since fold axes do not necessarily form perpendicular to the maximum principal stress. A similar point has been made by Price (1966, p.153) with regard to joints normal to bedding: this orientation can be predicted both by tectonic stress before folding, and by those following uplift. They are therefore insufficient evidence in themselves for

relative dating of fractures and folding. While Price suggested that many joints are post-folding, McQuillan strongly advocated the idea that fractures formed before bedding (in the case of the Asmari limestone, by 'shockwaves' soon after deposition of sediments, in orientations determined by the morphology of the depositional surface and the physical properties of the bed). In his review, he cited the studies of Parker (1942), Hodgson (1961) and Cook and Johnson (1970) as further evidence for his case.

None of these studies considered diagnostic evidence for relative dating of folding and fracturing: there are at least three good indications that fracturing may pre-date or accompany folding. Firstly, rotation of fractures with bedding continuously around tight to isoclinal fold hinges cannot be considered to be a consequence of post-fold stress concentration in a folded layer. Secondly, folding of individual fracture planes, has been shown for example by Blenkinsop (1982) for inner arc thrusts and Winsor (1985) for b-c joints. Fracture densities can provide evidence for the synchroneity of fracturing and folding. As previously mentioned, Harris et al. (1960), Stearns (1968b) and Jamison and Stearns (1982b) for example, have all shown an increase in fracture densities near hinge regions of folds.

(d) Deformation Mechanisms. The idea that displacement on fractures is the major deformation mechanism allowing natural folding has a thin, discontinuous history in the literature. The first detailed exposition can be attributed to Stearns (1968a), in which, drawing on experimental rock mechanics analogies, a clear and explicit definition of cataclastic flow is given (see Section 2.2.2), and the examples of the phenomenon in Mesozoic sandstones near Fruta, Colorado, the Teton anticline and the fold at Rattlesnake Mountain are quoted. Stearns uses negative evidence that cataclastic flow is the deformation mechanism: there is no plastic deformation and no volume change; and claims that every large fold in dolomites or quartzites at low confining pressures is an example of large

scale cataclasis. The next important contribution was in McQuillan's (1973) study. As well as relating the regionally dominant fracture set to the stresses within the fold, he also explicitly regarded the fracture as the fold accommodation mechanism: "Fold formation results from the summation of small adjustments between the limestone blocks..."

After this strong start, very little appears until the Jamison and Stearns study in 1982. As well as giving a description of the 'microfault' orientations and densities in the drape fold, the microstructure of the microfaults is described, and the deformation mechanisms are inferred. The microfault planes themselves are 0.3mm-wide zones of cohesive, compact material. Porosity and grain size are reduced as the microfault is approached, and the percentage of grains with undulatory extinction rises to a maximum at the margins. This is interpreted as the effect of microcracking on the crystal lattice, as opposed to crystal plasticity, because of the low confining pressure (25MPa) and temperature ($80^{o}C$). The decrease in undulatory extinction into the microfaults follows from the comminution of the strained grains into their constituent, relatively strain-free, parts. With further strain, the single microfaults develop into an anastomosing network forming a shear zone which progressively widens by the addition of more microfaults. (This is identical to the growth of deformation zones from deformation bands (Aydin and Johnson, 1983) discussed in 2.1.2). The study concludes with a calculation of bulk strain due to microfaults (assuming plane strain) which shows that this correlates well with microfault density. The combined evidence of the rotation of the microfaults, the deformation mechanisms appropriate to the deformation conditions, and the strain dependent microfault density allow the firm conclusion to be drawn that microfaulting accommodated the folding.

The potential importance of cataclastically accommodated folding was also stressed at this time by Hadizadeh and Rutter (1982) from field

evidence in the Central Appenines of Italy, the Cantabrian Zone, and the Ord and Kishorn Nappes of S.W. Skye, Scotland. In all these examples, 'distributed cracking' enclosing intact blocks of material with dimensions of several tens of millimetres are observed around folds. However, in this study, the dominance of cataclasis is not conclusively shown, and no details are given of its mechanism.

A more detailed study of the Ord Thrust Sheet was made by the author (1982, Blenkinsop and Rutter 1986). Samples of the Cambrian Pipe rock quartzite were taken from around a large fold. The microstructural evolution with progressive strain is described by a sequence from intact rock to protobreccia (the 'distributed cracking' of Hadizadeh and Rutter 1982), breccia, and ultrabreccia. Initially, a pervasive network of intragranular extension microcracks formed throughout the rock by impingement between grains at contacts. These linked together to form small shear faults with a matrix of cement and grain fragments. Further strain localised on a few large breccia zones in which fluid flow was concentrated, depositing cement and iron oxides. The microcrack densities in unsheared fragments increased constantly, but average lengths remained consistently less than the grain size. A good preferred orientation of microcracks exists in the first three stages. Within the matrix of the shear faults, the proportion of matrix to grain fragments increased to over 75%, at which point an ultrabreccia was developed locally in the breccia zones. Protobreccias are distributed around the hinge area of the fold, while the breccias and ultrabreccias occur only on large zones approximately perpendicular to the fold axis (ac, or hoo, Hancock's terminology). It is shown that no crystal plasticity accompanied this process, which probably occurred at less than 200^{0}C at a maximum depth of 7km (confining pressure 175MPa). Although this study is a quite comprehensive account of the microstructural deformation its major weakness is a failure to examine closely the relationship of the micro- and

meso-scale features to the geometry of the fold. No shear fault densities or orientations were measured.

It is, nevertheless, the study of deformation mechanisms in detail which provides the compelling evidence for the importance of cataclasis in folding. A good example is the study of a sandstone of the Tuscarora Formation in the hinge of chevron fold in central Pennsylvania by Narahara and Wiltschko (1986). The single sample, measuring approximately half a metre, was analysed by making thin sections of almost the entire area. A variety of deformation structures are reported, the most important of which are fractures. Minor faults of small indeterminate offset occur sub-parallel to the bedding on the inner arc and sub-perpendicular on the outer arc. Two major faults have the classic orientation and displacement of inner arc thrusts (Figure 2.1 d). Extension fractures, either open, well-healed or fibrous with extremely microfractured and elongated grains, are sub-perpendicular to bedding. Deformation lamellae are found within both fractured and unfractured zones, and are used to deduce that σ_1 is parallel to bedding in most places, except on the outer arc where it is at a high angle to bedding, and that σ_2 and σ_3 were in the bc plane. Minor amounts of pressure solution and strain due to intracrystalline plasticity occurred. An attempt was made to unstrain the fold using the measured offsets on the major faults and the extension in the outer arc: restoring these values to zero achieved only 40^0 of the total 100^0 necessary.

The deformation mechanisms deduced from these observations began with a phase of intracrystalline plasticity, recorded by the deformation lamellae, with principal stresses concentrated along the bedding plane. Subsequently, during buckling, most lamellae were passively rotated to maintain their layer-parallel stress directions. A neutral surface developed, outside which some additional deformation lamellae were formed, together with the outer arc extension fractures. On the inner arc, major and minor faulting occurred. The remaining strain, after allowing for the

major faulting, must have been accommodated by either grain boundary sliding or movement on the minor faults, neither of which can be quantified. It is concluded that the overall mechanism was the displacement of relatively rigid blocks along a number of faults - exactly the type of cataclastic flow first envisaged by Stearns and described by Rutter. The minimum effective confining pressure is considered to be 120MPa, and the temperature 190^{o}C.

e) Conclusion. The following general points can be abstracted from the selected reviews of cataclasis and folding. Firstly, there is a common geometrical association of fractures with folds formed in shallow-level environments. These relationships are best summarised by classifying fractures into a larger, bedding-normal group, and a less numerous, bedding sub-parallel group. Secondly, early studies analysed fractures exclusively in terms of assemblages or idealised conjugate sets in a qualitative way, and inferred synchronous fold and fracture formation on the basis of the geometrical relationships. The latter inference is not theoretically justified, and more quantitative analyses of fracture orientations show that the description of fractures in terms of simple conjugate pairs may be inadequate: several sets may form simultaneously. Thirdly, the importance of fractures which form before or during folding can be demonstrated where these can be shown to be folded, either as individual fracture surfaces or as fracture sets, continuously around acute angles in tight folds, and by the association of high fracture densities with high-strain areas of folds. However, fracture densities are also very profoundly influenced by three other factors: lithology, bed thickness, and the phenomenon of zoning. Lastly, detailed studies of deformation mechanisms in folds can give good evidence of the importance of cataclasis as a fold accommodation mechanism.

2.1.2 Cataclasis and Faulting

There is obviously a larger volume of literature on this subject, due to its wider appreciation, than on the previous section. Only a few more recent examples will be reviewed, chosen because of their importance to general aspects of cataclasis.

a) Fracture Orientations. The relation of minor fractures to major fault planes has been studied extensively in the field and theoretically. Both conjugate minor fractures and minor fractures sympathetic to the sense of major fault movement ('splay' or 'second-order' fault, Price, 1966) are known from field examples. Stearns (1964) reported conjugate macrofractures intersecting in an acute angle which was bisected by a major thrust plane under the Teton anticline. Engelder (1974) described a single set of microfractures intersecting a major fault at angles of 29-41^{o} in a line perpendicular to the displacement direction, with a conjugate sense of displacement. Brock and Engelder (1977) found a random pattern of microfractures 100m below the Muddy Mountain Overthrust, Nevada, due to the rigid body rotations accompanying the grain-scale cataclasis. In the 2m below the thrust, most macrofractures are subparallel to the thrust plane, although in detail their results show a spread of planes intersecting the thrust in the movement direction but with angles up to 90^{o}. These fractures are interpreted as a conjugate set to the main thrust. In the hangingwall, there is no macrofracture preferred orientation. House and Gray (1982), also examining fractures in dolomite around a thrust plane (the Saltville Thrust) report two conjugate sets for 20m above the fault plane, with the acute bisectrix perpendicular to the fault. In the fault zone itself, fractures are parallel to the fault and at an acute angle with the same sense of shear. Hancock and Barka (1985) report the existence of minor, dilatant fractures intersecting a Quaternary normal fault in W. Turkey, perpendicular to the fault plane and slip direction. They term these "comb fissures".

Probably the most widely used nomenclature today for minor fractures derives from the observations of Tchalenko (1970) on shear zones; these have been comprehensively summarised recently by Rutter et al. (1986). Minor fractures, such as those just described, with the same sense of displacement but making an acute angle of 10-20^{0} with the major fault margin, are referred to as Reidel Shears (R1), and those with a conjugate sense of shear, intersecting the fault margin at 75-80^{0} are conjugate Reidels (R2). Field examples of Reidel and Conjugate Reidels are particularly abundant from studies of strike-slip fault zones (e.g. Reading 1980). Fractures along which no displacement can be seen, but with the same orientation relative to a major fault, are described as pinnate joints, fringe joints or f-joints (e.g. Price 1966, Hancock 1985). A third type of fracture described from the same environment is exactly parallel to the fault margin with the same sense of shear: these have been termed Y shears, and correspond to those describe by House and Gray (1982) in the Saltville Thurst zone. Reidels and Y shears have also been described from the Tarskavaig thrust gouge, in the Moine thrust zone, Scotland, by the author (Blenkinsop 1982). A fourth fracture is the P shear, making an obtuse angle with the shear direction and often sub-parallel to a foliation in fault gouges: however it can also be demonstrated that synthetic shear displacements have occurred in this direction. This very brief account indicates that almost every combination of parallel, sub-parallel, sub-perpendicular, perpendicular, synthetic and antithetic minor fracture may be associated with a major fault plane.

b) Fracture Densities. Fracture densities in relation to faults have been investigated extensively in three studies by Wheeler (1980), Wheeler and Dixon (1980) and Pohn (1981). The first author detected an increased joint density over the Petersburg Cross-strike Structural Discontinuity (C.S.D.) in the Appalachian Overthrust Belt, in conglomerates, sandstones, siltstones and shales and through 0.8km of topographic relief. The

increase occurred irrespective of dip or lithology. A doubling of 'Joint Intensity' was reported by Wheeler and Dixon (1980) over the Petersburg Lineament. An investigation with a similar objective by Pohn (1981) analysed joint spacing separately in two joint sets, which showed a different pattern over the study area (the Appalachians in Pennsylvania). Lithology had an important effect on both sets but bed thickness did not. The proximity of thrust faults correlated with a **maximum** joint spacing, i.e. low joint intensity in the NW-SE joints, while those of a NE-SW orientation had a **maximum** joint spacing over tear faults. In an interesting discussion following this publication, Wheeler suggests that the combination of spacing measurements from both joint sets would give a parameter more similar to his joint intensity: this may resolve the apparent contradiction between his results, which suggested a **decreased** fracture spacing over large faults and those of Pohn. However, the pattern observed by Pohn persists for the combined measurements, and Pohn proposes that the relief of uplift strain on the major fault itself may **increase** the fracture spacing in its immediate vicinity. There is no necessity for his results to compare directly with those of Wheeler and Dixon because the major faults in each case are of a different nature.

Brock and Engelder (op.cit.) also measured variation in fracture densities with distance from the Muddy Mountain Overthrust: the microfracture index (Number of microfractures/m) in the footwall increases towards the thrust, showing a higher rate of increase in the last metre. The macrofracture index also increases from $4m^{-1}$ to $16m^{-1}$ in the penultimate metre below the thrust, but no relationship between macrofracture density and distance was detected in the hangingwall. Deformation along the Saltville Thrust (House and Gray, op.cit.) is concentrated in the dolomites of the hangingwall only: fracture 'spacings' decreased from 2200 to $600m^{-1}$ in the first metre. It therefore appears that fracture densities may show strong relationships to major faults, with

both positive and negative correlations, depending on the type of fault and scale of fracture. Asymmetry of cataclasic deformation between hanging and footwalls is usual.

c) Deformation Mechanisms and Fractures in Sandstones and Quartzites

The detailed study of cataclastic deformation mechanisms on faults has again suffered from the over-emphasis of experimental and theoretical work compared with field studies. This has been emphasised by Sibson (e.g. 1977), and resulted in his indispensable classification of fault rocks, and the appreciation of the significance of veins that are commonly associated with faults. This led to the proposal of the hydrothermal pumping mechanism (Sibson et al. 1975) and more recently to his analysis of the relationship between seismicity, fault plane geometry, and fluid flow (Sibson 1985, 1986).

Fundamental observations were also made by Engelder (1974) and Brock and Engelder (1977), from the Aztec sandstone under the Muddy Mountain overthrust, and the Mesa Rica sandstones over the Bonita Fault. In the first example, the zone of cataclasis extends 75m below the thrust, in which the grain size and sorting decrease to within 1m of the thrust, and then decrease more rapidly within the last metre. Bedding is destroyed and leached, and the sandstone is indurated due to compaction and welding of quartz grains by pressure solution. Just below the planar thrust contact, the gouge, 3-300mm thick, consists of more than 70% of fragments less than 100μm, and has a granular or foliated texture. In the overthrust sheet, there are shattered breccia zones of localised deformation, up to 200m above the thrust plane, characterised by red veins of granulated material around clasts of 0.1-0.5mm, coloured by the iron leached from the footwall. The study concludes that the initial deformation by cataclasis created the 75m cataclastic zone. High pore fluid pressures cannot have existed at this stage due to the cataclasis. Subsequently induration hardened the cataclasite, and so further slip was confined to the gouge zone.

Several features of this description are common to other recent accounts of cataclastic features in sandstones. The central element in all these is a mesoscopic fracture which usually has a shear displacement. This is described by Engelder (1974), Brock and Engelder (1977), and House and Gray (1982) as a 'microfracture', by Aydin (1978), Aydin and Johnson (1978, 1983) as a 'deformation band', by Jamison (1978) simply as a 'fracture' and by Pittman (1981) as a 'granulation seam'. It is also demonstrably the same feature reported by several authors in the previous section describing cataclastic aspects of folding: the 'microfaults' of Jamison and Stearns (1982), both the 'major and minor' faults of Narahara and Wiltschko (1986), 'faults' in Underhill and Woodcock (1985), and the 'shear faults' of Blenkinsop and Rutter (1986). Although there is a variety of names which differ particularly in regard to the specification of scale, the feature is clearly very similar in each account, and is probably the same as most of the other fractures around folds mentioned in the above, e.g. 'macrofractures' of Stearns (1968), 'shear and hybrid joints', and 'mesofractures' of Hancock (1985) and Price (1966) but these do not give adequate microscopic descriptions for detailed comparisons. Four characteristics can be identified as common to all these, summarised in Table 2.1.

i) Scale. Widths are described as variable in the range 0-5mm, and lengths generally 0-100mm but up to 100m (Aydin and Johnson 1983).

ii) Displacement. All these features have shear displacements varying from 1 to 30 mm. The smaller displacements are not visible in hand specimen, and can only be seen by matching grains across the faults. In other cases, grains cannot be matched across faults indicating that sections are not parallel to the displacement direction (e.g. Narahara and Wiltschko 1986), or that larger displacements have occurred.

CATACLASTIC FEATURE		SHEAR FRACTURE	MICROFAULTS	DEFORMATION BAND	GRANULATION SEAM	SHEAR ZONE	SHEAR FAULTS	FAULTS	MINOR FAULTS	MAJOR FAULTS
		Engelder (1974) Brock and Engelder (1977)	Jamison (1978) Jamison & Stearns (1982)	Aydin (1978) Aydin & Johnson (1978,1983)	Pittman (1981)	House & Grey (1982)	Blenkinsop (1982) Blenkinsop & Rutter (1986)	Underhill & Woodcock (1985)	Narahara & Wittschko (1986)	Narahara & Wittschko (1986)
WIDTH (mm)			0.3	1.0	Several	Several	1-4		0.005-0.2	0.5-2
LENGTH (mm)				10^4-10^5			Few 10's		0.5-0.25	40-75
DISPLACEMENT (mm)			0.2-5.0	Few 10's	Several		Several	<10	>0.5	13,24
GRAIN SIZE(mm)	UNSHEARED	0.25	0.17			0.2	0.2			
	MATRIX	0.05	0.03			<0.01				
SORTING IN MATRIX		Reduced				Increased		Reduced		
POROSITY %	UNSHEARED		20	25	25					
	MATRIX		5	6-10	2.8					
LITHOLOGY		Aztec Sandstone	Wingate Sandstone	Navajo, Entrada Sandstone	Simpson Group	Dolomite	Cambrian Quartzite	Permo Triassic Aedian Sands	Tuscarora Formation	Tuscarora Formation
MICROCRACKS		√	√		√	√	√		√	
TEMPERATURE (°c)			80			<250	<200		190	
CONFINING PRESSURE (MPa)		125	25			125-200	175		120	
DIFFERENTIAL STRESS (MPA)		30				130	150-250			
ZONING			Anastomosing Microfaults Intervals of rubbleized bedrock	Zones of Deformation Bands		Several sliding surfaces, shatter zones	Breccia Zones	Fault Zones & Slip Surfaces		
FURTHER LOCALISATION				Slip Surface			Ultra Breccia			
OTHER FEATURES		Microcracks Randomly Orientated			3-D Pods of unsheared rock, 300mm			Quadrimodal Fault Orientations		

TABLE 2.1
Summary of microstructural characteristics of shear faults

iii) Grain Size and Porosity Reduction. The porosity and grain size reduction reported by Brock and Engelder (1978) over the whole proto-cataclasite area beneath the Muddy Mountain Overthrust, responsible for its induration, is repeated on individual faults within the matrix. Jamison and Stearns report additionally that the zone of porosity reduction is twice as wide as the zone of reduced grain size. Porosity reductions of between two and fourfold are common, and grain sizes in the matrix are less than 0.01mm. An interesting difference between Brock and Engelder and House and Gray is that sorting decreases for the former into the fault as a fine grained fraction is created, while the generation of matrix in the latter study increases the sorting as a uniform smaller grain size is formed. Sorting also decreases within Underhill and Woodcock' s faults. This presumably reflects the different degrees of sorting in the host rock. Several authors refer to the fine grained, low porosity material within the fault as 'gouge'. However, following Sibson's (1977) classification of fault rocks, the very cohesive nature of the material (which often gives it greater resistance to weathering than the host rock) prohibits the use of this term, especially since the cohesion at the time of deformation cannot be deduced and in the models of Aydin and Johnson (1983), is assumed to be considerable. Hence the material within the fault is referred to as 'shear matrix'.

iv) Microcracks. Three of the studies in Table 2.1. report the existence of intragranular extension microcracks. As mentioned in the previous section, these were deduced by Jamison and Stearns (1982) from the optical strain features of quartz grains adjacent to the fault. The other two studies explicitly identify the microcracks with the use of cathodoluminescence (C.L.). Jamison (1978) notes that one difference between the natural studies and experimental failure is the lack of microcracks. It is likely that in view of the difficulty of detecting such cracks optically (Blenkinsop and Rutter, 1986) most if not all of the

deformation was accompanied by microcracking, and indeed this is implicit in the observation that angular grain fragments are present in the shear matrix.

A fair consensus is also reached about processes involved in the fault formation. Essentially these are the same as described by Jamison and Stearns (1982) and Blenkinsop and Rutter (1986). An initial period of microcracking, probably by grain to grain impingement, occurs although it is not clear whether this is homogeneously distributed throughout the rock. The fault forms and widens by additional microcracking: Jamison and Stearns showed that the density of microcracks increased towards the fault, and Blenkinsop and Rutter that microcrack densities increased with strain. Pittman (1981) identified overgrowths within the matrix by their crystal faces, which had an inverse relationship with the amount of 'granulated quartz', and presumably were separated from the intact grains by microcracks. The fragmentation of grains clearly causes porosity reduction by mechanical compaction, but an important additional mechanism is the deposition of a fine grained cement. This was also identified by Pittman, and described in detail by Stel (1981) from a microcrack infilling in a granite cataclasite. Diagnostic microstructures for the growth of such a cement were given, including the non-luminescing nature of the cement in C.L. Blenkinsop and Rutter inferred that much of the shear matrix may be such a cement and suggested a cyclic history of shearing and cementation. A further mechanism of induration found by Brock and Engelder was compaction and welding of grains by pressure solution.

The influence of lithology on microstructural processes has received some speculative attention, e.g. Pittman 1981, Blenkinsop and Rutter 1986, but scarcely any study based on natural examples. Jamison and Stearns (1982) report that in very fine-grained, low-porosity calcite-cemented sandstones, the fault matrix is calcite, and single microfaults with displacements of several tens of millimetres develop at a lower density,

with few anastomosing faults.

d) Zoning. Most of the studies in Table 2.1 document at least one further stage in the development of shear faults. This can be described generally as zoning, and involves the formation of a larger-order feature described by Engelder as a 'braided shear fracture', by Jamison and Stearns as 'anastomosing microfaults', by Aydin and Johnson as 'deformation zones', by House and Gray as 'several sliding surfaces', by Underhill and Woodcock as 'fault zones', and by Blenkinsop and Rutter as 'breccia zones'. These features all have in common a particularly dense development of the single shear faults, often in an anastomosing pattern. The thickness of these larger-order features depends on the number of individual faults which comprise them, and likewise their total displacement is simply the sum of the individual components. The best described are the deformation zones of Aydin and Johnson (1983), consisting of 10 to 100 deformation bands with a total displacement of 20-300mm and a thickness of up to 500mm. It is clear that the zones in every case form by the lateral addition of faults or bands. Blenkinsop and Rutter (1986) show that the evolution of the breccia zones from a protobreccia is a large scale analogue of the development of shear faults from extension microcracks. The orientation of the breccia zones, and of the deformation zones, is parallel to the shear faults or bands of which they are composed. In the case of deformation zones, there are usually two sets of orientations intersecting in 60^{o} for strike slip faults and four in dip and oblique slip faults, but only a single rather diffuse set of breccia zones was observed.

A final stage of deformation reported in these two studies is the formation of 'slip surfaces' and 'ultrabreccias'. Within deformation bands, quite discrete, discontinuous surfaces with well developed striations occur, with large displacements, and total porosity reduction over a width of 0.05mm. Ultrabreccias, where the proportion of fragments reduces to less than 75%, occur locally within breccia zones and may also

have striations on discrete surfaces. Possibly the Muddy Mountain thrust plane and the Saltville thrust plane may be comparable in representing a very thin surface of completely discontinuous strain. Underhill and Woodcock also report slip surfaces.

The last aspect of cataclasis in fault zones considered here is the relationship between 'gouge' or shear matrix thickness and fault displacement. The existence of such a relationship has been the subject of controversy and the discussion in Blenkinsop and Rutter (1986), referring to field evidence of Robertson (1982, 1983) and Jamison and Stearns (1982), can be supplemented by Engelder's (1974) observation that the gouge thickness is unrelated to displacement on the Muddy Mountain Overthrust and the Bonita fault, to reach the same conclusion that the relationship has yet to be convincingly demonstrated.

2.1.3 Regional Fracture Systems

Fracture systems on a large scale have been studied too extensively in the field for a completely comprehensive review. Therefore a few examples have been chosen to demonstrate the point that a great variety of interpretations have been given to regional fracture systems.

Possibly the simplest starting point are studies in a neotectonic context, where fractures can be related to measured or inferred stress systems. An example is Scheidegger's (1983) analysis of fracture and physiographic patterns in Alberta. Joint measurements show two dominant, vertical, sets intersecting at angles only slightly less than 90^0. By fitting a 'Dimroth-Watson' probability density function to each set, the best fit orientation for the set was determined. The joint sets were interpreted as conjugate fractures from which a maximum principal stress direction was inferred as the bisector of the enclosed acute angle. This showed a rather heterogeneous pattern which Scheidegger described as a turning from E-W to NE-SW from north to south over the study area, or

normal to the Rocky Mountain front. Breakout logs in the area also give a NE-SW direction for σ_1, prompting Scheidegger to ascribe the conjugate joint set to the contemporary stress field. There are a number of serious weaknesses with this study: in particular, no field descriptions of the joint sets are given to check whether they are contemporary and have shear displacements; furthermore they can only have formed as hybrid joints at the surface with σ_3 tensile, since σ_2 is zero: no evidence of this restrictive condition is given. Nevertheless, the principal of relating fractures to stress fields is illustrated.

S. England and N. France were the areas of a study with a similar objective by Bevan and Hancock (1986). Five types of fracture were identified, using 75 stations, including single vertical extension joints, conjugate sets of steeply inclined hybrid joints, conjugate sets of vertical hybrid joints, conjugate sets of steeply inclined shear joints, and conjugate sets of normal mesofaults. All these give a common NE-SW, horizontal direction of σ_3 on a generalised map, and can be dated as Neogene. A similar orientation is deduced from Landsat images of the area, which is also perpendicular to the direction of maximum principal stress determined from in-situ stress measurements and fault plane solutions in Europe and S.W. England (summarised in Blenkinsop et al. 1986).

In relating all five types of fracture to a common stress system, two problems are raised: firstly, extension, hybrid and shear joints cannot form simultaneously with the same relative stress magnitudes, and secondly that vertical conjugate shear joints imply a vertical direction of σ_2 while steeply inclined conjugate shears, hybrid shears, and normal faults, imply a horizontal direction for σ_2. These difficulties can be resolved by invoking a changed stress system in response to the earlier formation of one set of fractures, by the formation of different sets of fractures at various depths of burial, or by the possibility of tectonic fluctuation in the values of stresses. All these should leave some imprint of age

relationships between the fracture sets.

Changes in superimposed stress systems are well documented in regional fracture patterns. For example, a system of NE-SW post-Pliocene joints in the Arabian Platform record a phase of lateral extension in the Arabian foreland, simultaneous with NE-SW shortening in the Zagros thrust-fold belt. But these joints are superimposed on an older Mesozoic-Palaeogene system indicating extension, parallel to the Arabian arch, caused by the peripheral bulge induced by the emplacement of the Ophiolite nappes (Hancock 1985).

Three studies have shown that microfractures may also have a regionally systematic orientation: the most recent (Lespinasse and Pecher, 1986) identified a sequence of three stress systems in granite in the Massif Central, France. Data from the preferred orientation of microcracks, revealed as fluid inclusion trails in thin section, give three populations of vertical microcracks. Unlike the sometimes irreconcilable stress systems deduced from fractures, microcracks give a unique orientation for σ_3 and the σ_1-σ_2 plane since they form perpendicular to σ_3. They are therefore a useful palaeostress indicator. The palaeostress fields were deduced from the Etchecopar et al. method (1981) using fault plane and slickenside lineation orientations, which gave three directions for the maximum principal stress at each of the six stations, all with a vertical intermediate stress. The three directions can be dated from field evidence, and correspond with the three populations of microcracks, giving the azimuth of the maximum principal stress as 020^0 in the Viséan-Stephanian, 150^0 in the Stephanian-Autunian, and 080^0 in post-Jurassic times. As a final corroboration that the microcracks reflect genuinely different stress generations, they can also be distinguished by inclusion chemistry, which implies the same conclusion as the field data, that the 020^0 stress system predates the other two.

Some of the most intensively and extensively studied regional joints

are those of the Appalachian Plateau. In a comprehensive review paper, Engelder (1985) again emphasizes the theme of the multiple nature of fracture systems, even from an area which has experienced only one major orogenic cycle. It is likely that this very detailed analysis is possible because all the joints referred to are vertical, and assumed to have formed as extension fractures, conferring them with the same advantages as microcracks in terms of stress analysis. Engelder first proposes an elegant genetic classification of four joint types, and then gives evidence that at least three are present in the Appalachian plateau on the basis of their chronology and a somewhat idealised tectonic cycle. Hydraulic joints are formed during burial, due to excess pore fluid pressures developed as a consequence only of burial: as such they cannot form at depths less than .5km. Tectonic joints need to be distinguished, because, although also formed under high fluid pressure, the additional tectonic stress allows this to occur at depths of less than 3km. Unloading joints form during uplift in response to a tensile stress which can develop given the plane strain boundary conditions of the model. Both types of burial and unloading joints will have orientations determined by the prevailing stress field. This tensile stress also generates the final type of joint, the release joint; it is distinguished because, unlike the other joints, its orientation is determined by a fabric. Joint chronology can be established sometimes on the basis of abutting relationships, and from the relative timing of cleavage: on this basis, the earliest set of joints formed normal to and synchronously with the cleavage, and must be tectonic joints. Later sets of joints have the same cross-strike orientation, and strike-parallel orientations: the relative chronology of these cannot be given from abutting relationships, but since they are later than the tectonic joints, the cross-strike joints are taken to be unloading joints, and the strike-parallel joints as release joints, with an orientation controlled by cleavage. No hydraulic joints formed because the depth of burial was

insufficient.

Several criteria for the recognition of a hydraulic fracture mechanism are suggested by Engelder: fractures should propagate in siltstones before shales; early fractures in siltstones should stop at shale-siltstone interfaces; later joints from shales may penetrate siltstones; and joints in thick shale beds should have a greater vertical extent than joints in interdigitating shale-siltstone beds. All these are observed, but these characteristics do not apply to the cross-strike joints that post-date the earliest set: since they seem to have no lithological bias, they probably formed without a high pore-fluid pressure, according with their interpretation as unloading joints.

A set of ENE joints can be distinguished from both these unloading joints and the earlier tectonic joints. These joints also characterise well cores in the area of depths less than 500m. (Below this, joints of the cross-strike orientation are encountered). This direction is also the direction of the contemporary stress field, and magnitudes of the least principal stress measured in a borehole and extrapolated to the surface suggest that it becomes tensile and decreases below the tensile strength of the local rocks at 200m. These additional pieces of evidence are strong support that the latest joint set is an unloading joint formed in the present-day stress field.

A point made clearly by Engelder's study is that fractures may form at many stages during orogeny. As previously mentioned, this contrasts with the view of Price (1966) who doubted that early formed joints would survive burial and compaction. However, Fitches at al. (1986) have recently described a whole suite of small-scale structures from the Welsh basin that formed during burial but survived later regional deformation. The most important of these are bedding-parallel veins of quartz and dolomite, and minor thrusts with small displacements. There are also three bedding-normal features: two comprise sets of perpendicular veins occurring as single

veins, in groups comprising several veins spaced at intervals of 100mm or more, and in dense arrays, and the third comprises vein breccias that formed after the diagenetic growth of chlorite-white mica stacks, but before the regional cleavage and folding. Hydraulic fracturing is considered to be responsible for these features which would be either 'hydraulic' or 'tectonic' in Engelder's terminology, but the depth of burial is unknown. However, the authors suggest that such early formed structures may be widespread in sedimentary basins, and have been overlooked because they are assumed to be related to later folding and faulting. Even earlier shear deformation, of completely unconsolidated sediments, has been described recently by Jones and Addis (1986).

This review suggests that regional fracture systems may be complex and that dating of fracture sets is difficult. A common problem seems to be the existence of multiple sets of fractures, which do not appear to show clearly separable ages, yet which cannot be ascribed to a single stress system using conventional Andersonian or Mohr-Coulomb-type failure criteria (e.g. Bevan and Hancock 1986). Another aspect of this problem is the distinction between shear, extension and hybrid joints: where there is no evidence of macroscopic displacement, the application of these terms based solely on geometrical relationships assumes again that conventional failure criteria operate. These conclusions point strongly towards the cataclastic theories based on bulk strain described in Section 2.1.3. Microscopic examination may indicate that distinction of fractures on the basis of displacement is inadequate, even in the case of extension microcracks, some of which have shear displacements and others of which are pure Mode I fractures (Lespinasse and Pecher 1986). Finally, fractures may form at all stages of a sediment's history and be preserved through subsequent deformation: indeed they have a high preservation potential because they can be preferentially reactivated (as shown, for example, by Hancock (1964) for fractures in S.W. Dyfed, and justified theoretically by Price (1966)).

2.1.4 Fractography of Natural Fractures

Five main features have been described from field examples (Figure 2.3); some of these have also been interpreted on the field evidence, as described below.

i) Plume Structure. This has also been referred to as Herringbone or Feather structure, or Hackle marks, but the use of the latter two terms in other contexts is confusing. These first markings have been subdivided by Bahat and Engelder (1984) into

S (straight)-type plumes, consisting of crescentic shoulders or barbs disposed symmetrically about an axis, which is commonly along the centre of a bed. Ramsay (1986) has shown that these may be described almost perfectly by a logarithmic curve.

C (curved)-type plumes, consisting of wavy barbs radiating from an initiation point.

Rhythmic C-type plumes, consisting of cycles of fans of C-type plumes with fan perimeters convex towards the initiation point of each cycle.

Plume structure may terminate at the bedding surface, or become en-echelon fractures either continuously or discontinuously (Bahat 1986), at a shoulder.

ii) Rib Structure. Also known as Augen and Arrest Lines. These are convex ridges with sawtooth cross-sections on which plume structure may develop (e.g. the rhythmic C-type plume of Bahat and Engelder 1984). They may have a perfectly parabolic geometry (Ramsay 1986).

iii) En-Echelon Fractures. These have also been called Fringe or f-joints, Feather Fractures and Pinnate Fractures. They develop as shorter fractures at acute angles of 0-25^{o} to a main fracture face, which may have both C-type and S-type plume structures themselves, and form along either side of the central part of the main fracture. The geometry of en-echelon fractures has been defined by Nicholson and Pollard (1985) and is shown in Figure 2.3d. In a very detailed description of such fractures in chalk

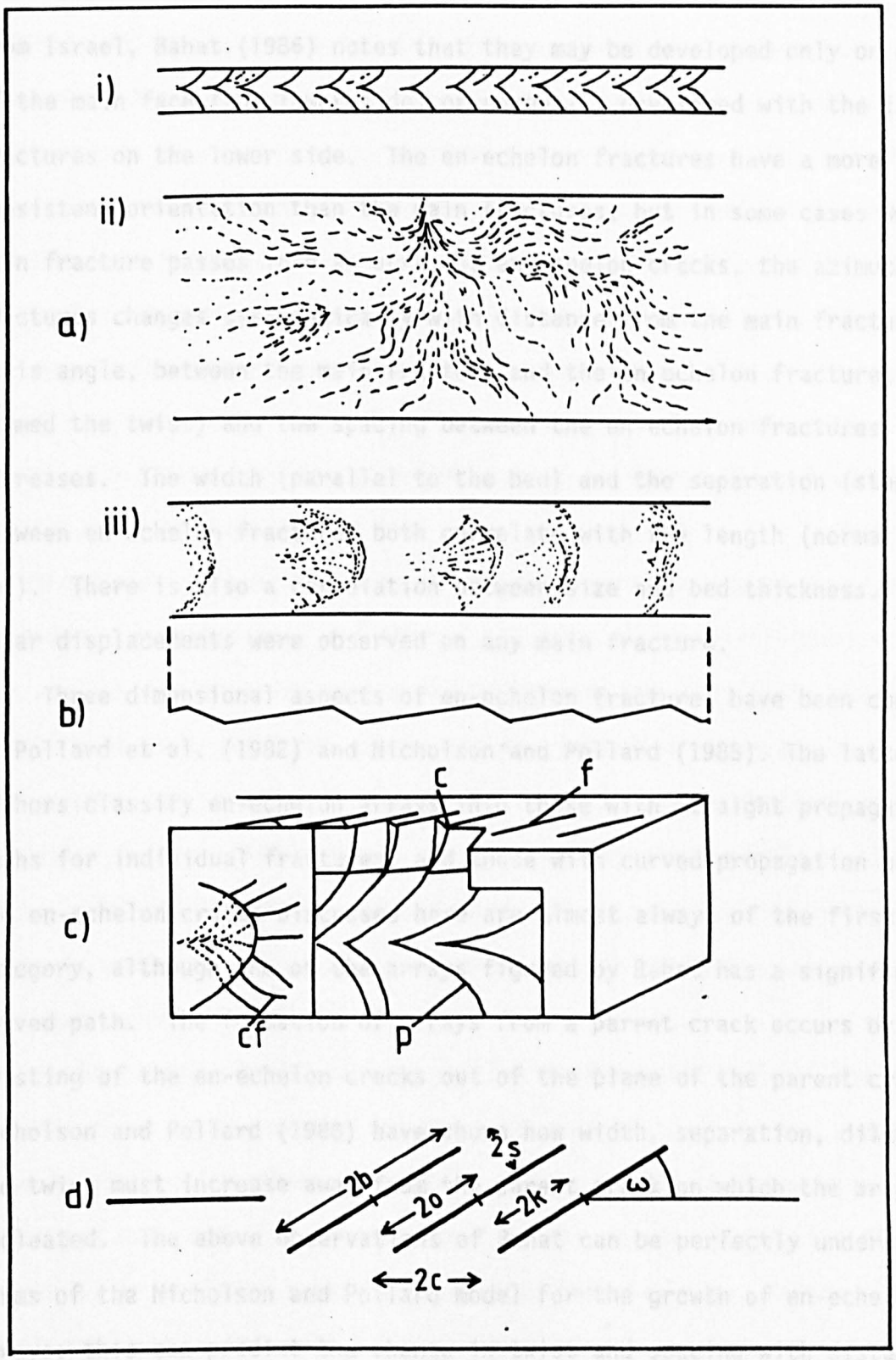

FIGURE 2.3

Fracture Surface Features. After Hodgson (1961), Price (1966), Bahat and Engelder (1984), Nicholson and Pollard (1985), Ramsay (1986).

a) Plume Structure. (i) S-type plume (ii) C-type plume. (iii)Rythmic-C-type planes.

b) Rib Structure; profile view of bed in (iii) above, on which rhythmic-C-type plumes are developed.

c) Relationship of Plumes (P), en-echelon fractures (f), cross joints (c), and conchoidal fringe joints (c.f.).

d) Geometry of en-echelon fractures. 2b = Crack Width. 2o = Crack Overlap. 2k = Center spacing parallel to cracks. 2c = Center spacing parallel to array. 2s = Separation. ω = Twist Angle

from Israel, Bahat (1986) notes that they may be developed only on one side of the main face (the lower side) or unequally developed with the larger fractures on the lower side. The en-echelon fractures have a more consistent orientation than the main fractures, but in some cases where the main fracture passes into an array of en-echelon cracks, the azimuth of the fractures changes systematically with distance from the main fracture tip (this angle, between the main fracture and the en-echelon fracture, is termed the twist) and the spacing between the en-echelon fractures increases. The width (parallel to the bed) and the separation (step) between en-echelon fractures both correlate with the length (normal to the bed). There is also a correlation between size and bed thickness. No shear displacements were observed on any main fracture.

Three dimensional aspects of en-echelon fractures have been considered by Pollard et al. (1982) and Nicholson and Pollard (1985). The latter authors classify en-echelon arrays into those with straight propagation paths for individual fractures, and those with curved propagation paths. The en-echelon cracks discussed here are almost always of the first category, although one of the arrays figured by Bahat has a significantly curved path. The formation of arrays from a parent crack occurs by twisting of the en-echelon cracks out of the plane of the parent crack, and Nicholson and Pollard (1985) have shown how width, separation, dilatation and twist must increase away from the parent crack on which the array has nucleated. The above observations of Bahat can be perfectly understood in terms of the Nicholson and Pollard model for the growth of en-echelon arrays: this can predict the change in twist and spacing with distance from the crack tip, and the correlations between width and separation with length by considering that Bahat was sampling a range in the development of en-echelon arrays, due to samples which had reached different final stages (controlled by bed thickness), and to sections of various stages through a developing array.

iv) Cross Joints. Abbreviated to c-joints, these link en-echelon fractures. Nicholson and Pollard's observations are equally relevant to the formation of cross-joints: for straight propagation paths, dilation of en-echelon fractures necessitates bending intervening bridges: eventually these fail to form cross fractures (see Nicholson and Pollard 1985 fig.1).

(v) Conchoidal Fringe Joints. Ramsay (1986) has identified a further type of fringe joint, termed by him a 'Conchoidal Fringe Joint'. This forms radially in advance of a convex rib structure: if plume structure is present, the conchoidal fringe joints appear to extend their trajectories into the area in front of the rib.

vi) Lineations. Linear features on fracture surfaces may be described as striations, wear grooves, and fibres. These are commonly asymmetrical, with small steps at their ends perpendicular to the lineation; where the direction of shear is known, these may be classified as incongruous if the steps oppose the shear, or congruous otherwise. Wear striations and oblique stylolites (slickolites) are both incongruous: rarely the former can be attributed to the ploughing action of a tool but in many cases their origin is unclear. Fibres growing on a fracture plane are congruous and have been described fully by Ramsay (1980).

Field evidence has been used in the interpretation of all the above features. One of the central problems is whether they can be associated uniquely with any displacement modes. Parker (1942) observed plume structures most commonly on cross-fold joints of the Appalachian Plateau and rarely on strike joints: he classified these as shear joints. Engelder (1985) referred to the same joints as exclusively extension fractures, with Mode I opening, since there was no shear offset of fossil markers, surface morphology of the fractures was bilaterally symmetrical, on the basis of abutting relationships, and an inferred low deviatoric stress during propagation. Roberts (1961) and Syme-Gash (1971), however, agree with Parker that cross-field joints with plume structures are shear joints, and

Hancock (1985) suggests that the association of en-echelon fractures with plume structure indicates shear failure because this association has a geometry comparable with second order fractures in fault or shear zones. Nicholson and Pollard (see below) indicate quite firmly that the en-echelon fractures form perpendicular to the least principal stress, and that such fully developed fractures remote from the effects of the major fracture will give an unequivocal direction for the least principal stress. If the mature en-echelon fractures are at an acute angle to the main fracture, this must imply a shear stress along the latter, a conclusion also reached by Ramsay (1986).

However, Bahat (1979), Engelder (1974) and Bahat (1986), in addition to Engelder (1985) associate plume structures with Mode I fractures. Bahat (1986) observed no mesoscopic shear displacements on the main fractures that show plume structures and assumed that they are tensile fractures. But there is a 31^{0} change in azimuth of main fractures over a distance of 400m; if as shown in his figure 10, there is to be a common direction of maximum horizontal compression in the bisector of this spread, then opposite shear stresses must have existed on the main fractures at either extreme. (The fractures may have originated in Mode I given a heterogeneous stress field).

There is no dissension that en-echelon fractures are Mode I, and form in response to a local tensile stress perpendicular to the plane of individual fractures. However, Nicholson and Pollard have suggested that where the en-echelon fractures are consistently oriented and at a sufficient distance from the parent crack tip, the straight part of the crack wall gives a good indication of the remote applied stress. In this case, too, there must be a shear stress on the main fracture, although 'remote' needs to apply only on the scale of the en-echelon fractures. Bahat, for example, deduces from conjugate vein arrays that the direction of least principal stress on the largest scale is different from that

operating within the shear zones generating the en-echelon fractures. These give a very unusual configuration of tension in the small acute angle between the shear zones.

Bahat's insistence that both the en-echelon and main fracture planes (which both show plume structure) are formed in tension, forces him to divorce the stress field responsible for each. The main fracture planes are considered to form first in response to a NNE compression; regional unloading of this is considered to give the NNE tension which then forms the conjugate sets of en-echelon fractures. In support of a separate origin for the latter, he demonstrates from the initiation points of C-type plumes on the en-echelon fractures that they do in fact nucleate from a point at some distance from the main fracture, and grow both towards and away from it.

In view of the very common association of en-echelon fractures with plume structure on a main fracture, a hypothesis involving two quite different remote stress states seems improbable. Furthermore, growth of en-echelon fractures from the main fracture plane, rather than from a remote position, can be confirmed as a general case by analogy with fractography in ceramics. This discussion indicates that there are four difficulties in resolving the shear or tension origin of fracture topography. Firstly, that criteria used to identify displacement modes independently of surface features are inadequate: it is probably insufficient to cite lack of mesoscopic shear displacement as definitive of Mode I opening. Secondly, the influence of lithology must be accounted for: Bahat, for example, states that plume and en-echelon structures were confined to certain beds, while Engelder notes that no plume structures were observed on shale beds, which had only arrest lines. Such differences could also affect the displacement mode. Thirdly, the interaction between the remote and fracture stress fields must be considered. Remote stress fields will certainly be distorted at the tip of a parent fracture, where

en-echelon fractures are formed. Lastly and perhaps most importantly, there does not necessarily have to be a unique association between these features and the crack opening mode: fractography of ceramics suggests that crack dynamics have an essential role to play (Section 2.2.3).

Engelder (1985) has used the type of plume structure to deduce the dynamics of fracture opening. Rythmic C-type plumes in siltstones are considered to indicate cyclic propagation, caused by release and build up of effective stress, the fluid perhaps being recharged from an adjacent shale. S-type plumes on thin siltstones within shales indicate, from lack of arrest lines, that rupture was 'massive' - i.e. over lengths of 50m. This can be taken to indicate that, if fluids were necessary for fracturing, they must be available from source at the fracture tip, because it is unlikely that they could be transported along the fracture at a speed equal to the fracture propagation. This inference does not allow for the possibility of sub-critical crack growth discussed in section 2.2.3.

2.2 REVIEW OF EXPERIMENTAL WORK

Not even a significant fraction of the literature on experimental cataclastic deformation could be comprehensively reviewed. Five topics have been selected because of their relevance to the remainder of this study: Microstructural Observations From Experiments, Creep Laws, Subcritical Crack Growth Experiments, Gouge tests, and Fractography. Even within these fields, only a few of the total publications are chosen, with an emphasis on the most recent.

2.2.1 Microstructural Observations from Experiments

Three fundamental processes occur in cataclastic experiments: microcracking, shear and tensile faulting. The sequence from microcracking to failure by shear or tensile faulting makes these useful categories by

which to analyse the subject.

a) Microcracking. A comprehensive review by Kranz (1983) is an essential basis for this subject. Microcracks are classified into **grain boundary cracks** (which may be coincident or non-coincident with the actual grain boundary), **intracrystalline cracks, intercrystalline cracks, and cleavage cracks.** An alternative classification is presented in section 2.5.1. By far the most common microcracking mode in experimentally induced cracks is Mode I. Such tensile microcracks are referred to as 'axial' and observed in nearly all experiments with any component of cataclasis as a deformation mechanism, including confined experiments up to the highest pressures. It is therefore necessary to determine how tensile stress fields can exist in such conditions. In the following section, seven **microcrack mechanisms** are identified that control tensile failure. The mechanisms treat details of the stress field with varying degrees of formality, but each of them describes the reason for propagation of a microcrack in a particular situation. The classification is similar to that of Kranz (1983) with some modifications, and includes references to Atkinson's (1982) classification. In the latter, dynamic and subcritical mechanisms were distinguished: the following makes no such division because it has not been made in triaxial experiments.

i) Impingement-Induced Microcracks. (These correspond with Kranz's 'stress concentation at boundaries'). The formation of microcracks perpendicular to σ_3 in tensile stress fields developed by impingement of grains was shown using photoelastic techniques by Gallagher et al. (1974). The six basic patterns are shown in Figure 2.4, depending on the boundary loads, packing arrangement, size sorting, and grain shape. Borg et al. (1960) observed extension fractures with a strong preferred orientation perpendicular to σ_3 when deforming loose sand. An increasing number assumed this orientation with strain. These are highly likely to be impingement microcracks. Although McEwen (1981) modelled pebble conglomerates, the results of his

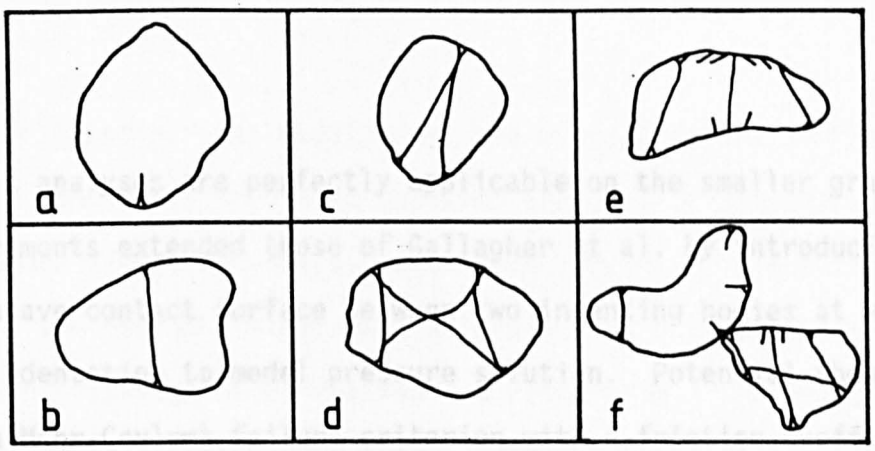

FIGURE 2.4

Impingement Induced Microcracks

Six microcrack patterns deduced from photoelastic models by Gallagher et al. (1974)

a) Single Load c) Triple Load e) Beam-like load
b) Double Load d) Quadruple Load f) Combined load

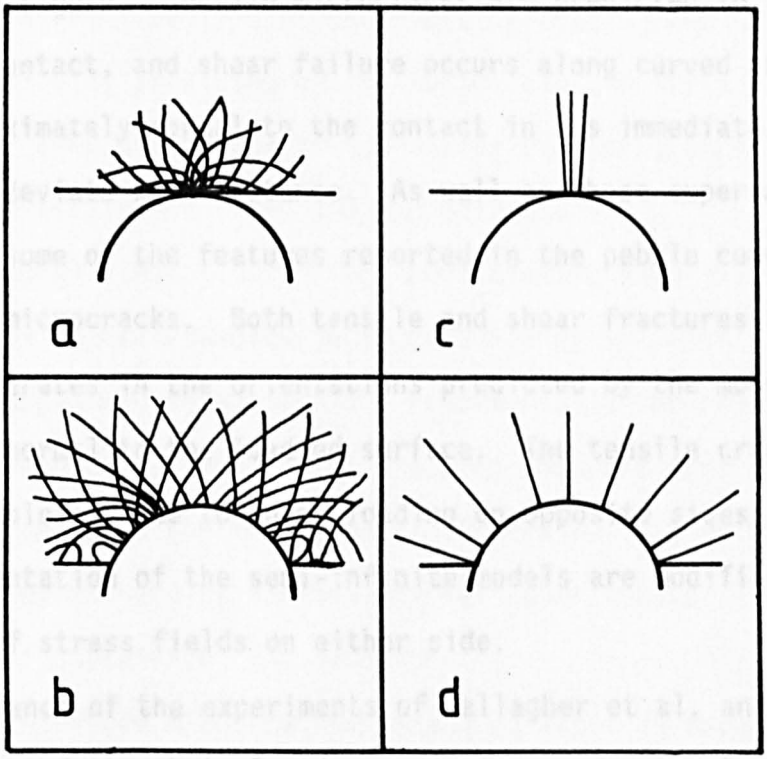

FIGURE 2.5

Potential shear planes (assuming μ=0.5) (a,b), and trajectories of σ_1 (c,d), at initial contact (a,c) and after an indentation of 0.36 x R, the radius of the indenter (b,d). (McEwen, 1981).

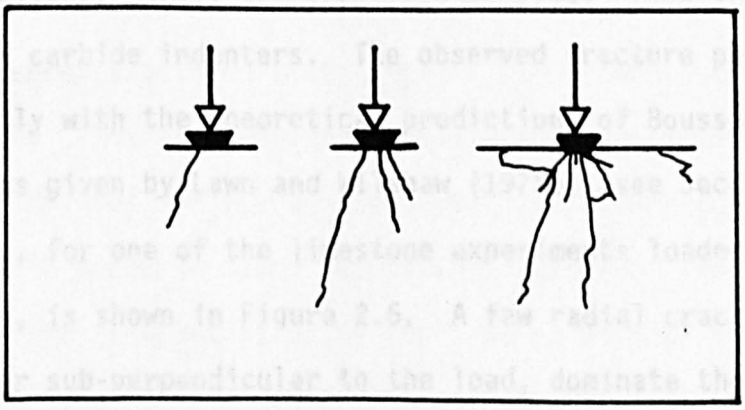

FIGURE 2.6

Indentation Fracture Patterns in limestone under a truncated wedge (after Lindquist et al. 1984).

photoelastic analyses are perfectly applicable on the smaller grain scale. These experiments extended those of Gallagher et al. by introducing a convexo-concave contact surface between two indenting bodies at various depths of indentation to model pressure solution. Potential shear planes (assuming a Mohr-Coulomb failure criterion with a friction coefficient of 0.5), and trajectories of σ_1 are shown for the initial contact and an indentation of 0.36 times the indenter radius in Figure 2.5. The patterns for smaller indentation depths are exactly intermediate between the two end members in the figure. Tensile microcracks are predicted to form normal to the indenter contact, and shear failure occurs along curved trajectories that are approximately normal to the contact in its immediate vicinity, but progressively deviate with distance. As well as these experimental observations, some of the features reported in the pebble conglomerates may well apply to microcracks. Both tensile and shear fractures are observed in the conglomerates in the orientations predicted by the models i.e. +/- 25-30^{o} of the normal to the loaded surface. The tensile cracks may cross the pebble completely due to point loading on opposite sides, in which case the ideal orientation of the semi-infinite models are modified by the interference of stress fields on either side.

The relevance of the experiments of Gallagher et al. and McEwen depend on a comparison of the photoelastic predictions and natural patterns of fracture, but Lindquist et al. (1984) induced indentation fractures in samples of limestone, marble and granite with wedge - and truncated wedge - shaped tungsten carbide indenters. The observed fracture patterns could be compared directly with the theoretical predictions of Boussinesq and Hertzian indents given by Lawn and Wilshaw (1975b) (see Section 2.3.1). A typical pattern, for one of the limestone experiments loaded by the truncated wedge, is shown in Figure 2.6. A few radial cracks, perpendicular or sub-perpendicular to the load, dominate the deformation of both types of indenter, with a variable zone of crushed material under the

indenter. This pattern was modified by the microstructure of the samples: straight and continuous cracks in the fine grained, (grain size less than 0.007mm), dense limestone contrast with more irregular, discontinuous fractures in the medium grained marble (grain size 0.27mm) where grain boundaries and cleavage have affected the crack path. The medium grained granite (0.37mm grain) developed a few cracks at first, like the two calcareous rocks, but subsequently these multiplied into lower-angled shorter cracks; in this case, the grain diameter is comparable with the flat wedge. All types of Kranz's crack interactions (see below) were observed. The general pattern of the radial cracks agreed well with the simple elastic fields predicted by the Boussinesq and Hertzian configurations, even though the transgranular fractures were often strongly influenced by pre-existing flaws and microstructure.

The successful simulations of the photoelastic experiments, and the behaviour of the natural samples in indentation experiments, indicate that impingement-induced microcracking is a fundamentally important mechanism, and probably accounts for much axial cracking observed experimentally and in nature; for example, the impingement microcracks in quartz grains loaded by small, hard pyrite grains observed by Hallbauer, Wagner and Cook (1973) during triaxial compression of a sandstone.

ii) Shear Fault-Induced Microcracks. Kranz called this mechanism 'grain rotation and translation'. It was identified experimentally by Friedman and Logan (1970), who called intragranular microfractures that were found exclusively within 5-10 grain diameters of shear faults, parallel to σ_1, 'microscopic feather fractures (m.f.f.s)'. They do not occur adjacent to an incipient shear, and are therefore clearly shear related. Conrad and Friedman (1976) defined m.f.f.s as microfractures occurring only within grains adjacent to a fault, dying out rapidly away from the fault and statistically close to or parallel to the applied direction of σ_1 (Figure 2.7a). Experiments on pre-cut sandstone showed that the fractures

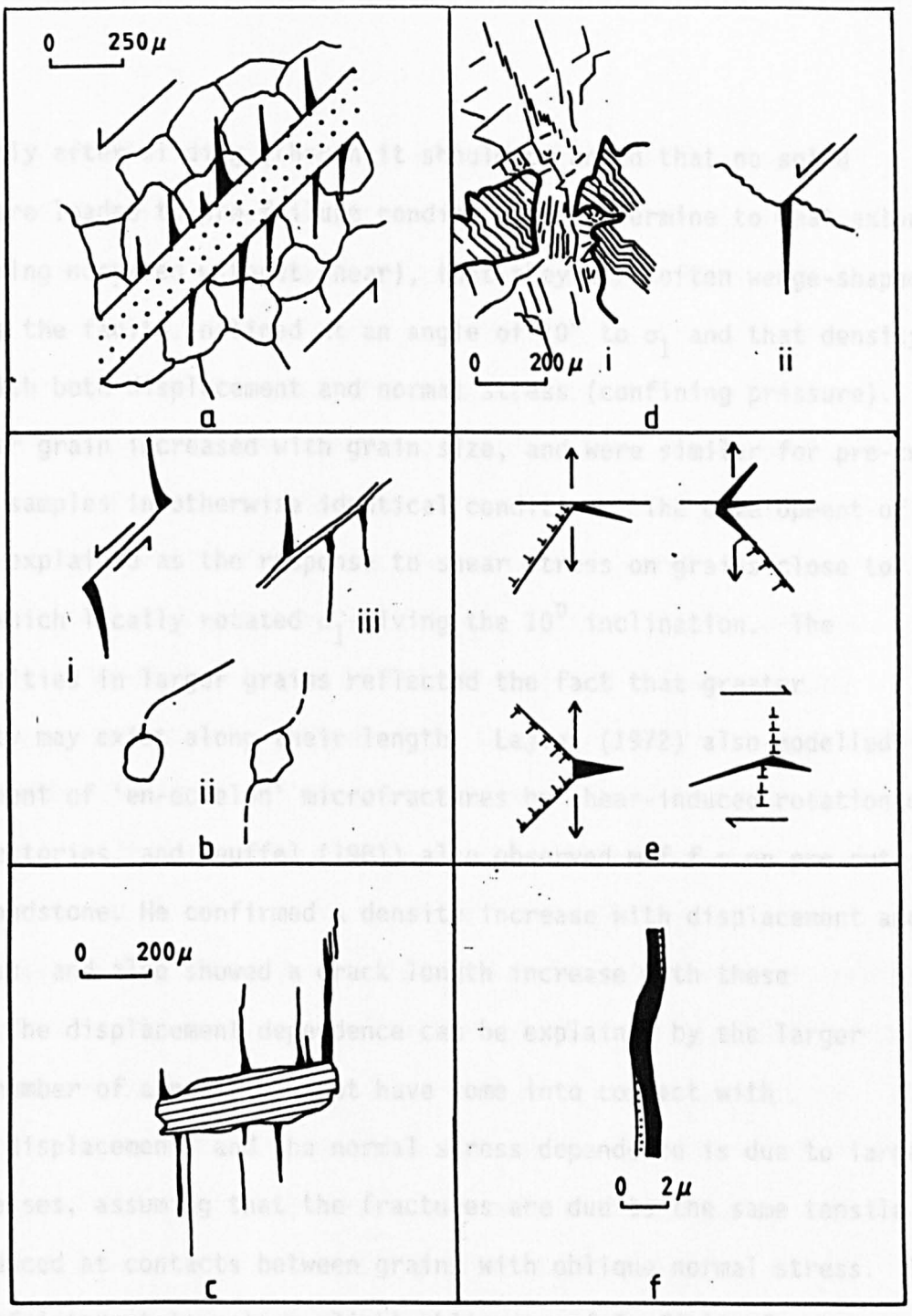

FIGURE 2.7

Mechanisms of Microcrack Formation. In all diagrams except e, the maximum principal stress, σ_1, is vertical.

a) Shear-Induced Microcracks (Microscopic feather fractures (m.f.f.s))
b) Flaw Induced Microcracks. i, iii) Tapponnier and Brace (1976), ii) Kranz (1980).
c) Elastic-Mismatch Induced Microcracks. Tapponnier and Brace (1976) developed at interface between mica (ruled ornament) and quartz.
d) Plastic mismatch Induced Microcracks. i) Wong and Beigel (1985): Zone of intense microcracking in plagioclase developed between kinked biotite grains (ruled ornament). ii) Olson and Peng (1976). Crack develops at the intersection between a lamellae and grain boundary.
e) Plasticity-Induced Microcracks; four alternative models of crack formation due to dislocation pile-ups at an obstacle. Dislocations represented by T symbols. Lawn and Wilshaw (1975a).
f) Pre-existing-Flaw Induced Microcracks. Tapponnier and Brace (1976). A previously formed and cemented crack is reopened.

developed only after sliding (though it should be noted that no solid specimens were loaded to pre-failure conditions to determine to what extent microfracturing occurred without shear), that they were often wedge-shaped, open towards the fault, inclined at an angle of 10^0 to σ_1 and that density increased with both displacement and normal stress (confining pressure). Densities per grain increased with grain size, and were similar for pre-cut and faulted samples in otherwise identical conditions. The development of m.f.f.s was explained as the response to shear stress on grains close to the fault, which locally rotated σ_1 giving the 10^0 inclination. The greater densities in larger grains reflected the fact that greater heterogeneity may exist along their length. Lajtai (1972) also modelled the development of 'en-echelon' microfractures by shear-induced rotation of stress trajectories, and Teuffel (1981) also observed m.f.f.s on pre-cut Cocconino sandstone. He confirmed a density increase with displacement and normal stress, and also showed a crack length increase with these parameters. The displacement dependence can be explained by the larger cumulative number of asperities that have come into contact with progressive displacement, and the normal stress dependence is due to larger induced stresses, assuming that the fractures are due to the same tensile stresses induced at contacts between grains with oblique normal stress. It is however of interest to note a slight obliquity of Teuffel's fractures to the remote direction of σ_1, in the opposite sense to that of Conrad and Friedman.

Returning to the observations of McEwen, a number of tensile fractures were observed in his specimens to be exclusively associated with slickensided surfaces between pebbles in contact. McEwen attributed these to fractures, formed during sliding between the surfaces, reorientating the local direction of σ_1 (by an amount which depends on the coefficient of sliding friction) in the same way as suggested by Conrad and Friedman.

iii) Flaw-Induced Microcracks ('stress concentrations at cavities' - Kranz). The tensile stress concentrations induced by flaws (pores, grain boundaries, or original microcracks in compression) have been appreciated for a long time and indeed formed the basis of the traditional Griffith failure criterion. A useful classification of natural flaws is given in Brace et al. (1966) and Sprunt and Brace (1974). Theoretical solutions to the stress around a crack are described in section 2.3.1(a), but there has been little experimental reference to the process in rocks. The idealised process was figured in Tapponnier and Brace's important early work on microcracking in Westerly Granite (1976) (Figure 2.7b); however, such microcracking was relatively uncommon from their observations. Brace and Bombolakis (1963) describe a classic experiment to determine empirically the development of a pre-existing crack in uniaxial compression: in order to follow the course of the crack, it was artificially grown by cutting a slot to follow the trajectory of maximum tensile stress, rendered visible by photoelasticity. The well known result of stressing an inclined crack is growth in a curved path towards the direction of applied compression. This experiment was of fundamental importance because the problem of the progressive growth of the crack was not yet solved theoretically. Growth of a crack from shear on an inclined flaw is exactly analogous to the development of microscopic feather fractures, or shear induced fractures adjacent to a fault plane: the flaw or fault can be modelled as an inclusion with various properties. Flaw-induced microcracks are distinguished from shear-induced microcracks in this classification simply on the basis of the nature of the 'inclusion' - in the former case, it is a microscopic flaw, while in the latter it is a mesoscopic shear plane which has been created by pre-cutting or shear failure.

In a recent contribution to the theory of an experiment on microcracking mechanisms, Hori and Nemat-Nasser (1985) give a definitive model for progressive microcrack growth and of microcrack interaction

(section 2.3.1(a)), improving on their earlier (1982) approximate results. They illustrate their theory with experiments using resin with pre-existing cracks to follow the process of crack growth. The final course of the crack confirms the curved paths 'grown' by Brace and Bombalakis, and matches closely, but not exactly, the theoretical solution. Individual cracks in figure 2.8d show the observed path. The experiments also confirm another important theoretical result: in the slightest lateral tension, crack growth becomes unstable after a critical crack length, but remains stable (i.e. requires an increase of stress to increase crack length) at a finite length for lateral compression. Also as predicted, larger flaws grow at lower stresses until in unconfined experiments, axial splitting and failure results. Further results of these experiments are given in the next section.

iv) **Elastic Mismatch-Induced Microcracks.** One of the best accounts of microcracks nucleated at the interface between two minerals due to unequal elastic responses across a coherent boundary is again that of Tapponier and Brace (1976). In the case of Westerly Granite, quartz grains were heavily cracked along boundaries with biotite (Figure 2.7c). Elastic mismatches also occurred in San Marcos Gabbro at low confining pressures in plagioclase adjacent to cleaved biotite (Wong and Biegel 1985).

v) **Plastic Mismatch-Induced Microcracks.** These include both the twin-induced and kink band and deformation lamellae-induced microcrack mechanisms of Kranz. Where plasticity is localised in one area, microcracks may be initiated due to the strain incompatibility. This is reported by Wong and Biegel (1985) for plagioclase in areas adjacent to kinked biotite in the San Marcos Gabbro at higher confining pressures, where "incipient localised zones made up of comminuted plagioclase blocks" formed (Figure 2.7d). Biotite was therefore of fundamental importance in the microcracking mechanism of both San Marcos Gabbro and Westerly Granite, although comprising only 12% and 5% of the two rocks respectively. Clearly

any form of intracrystalline glide or creep, (e.g. twinning, deformation lamellae or plastic flow), as well as kinking, has the potential to generate mismatches: this may account for the frequently observed microcracking of feldspar porphyroclasts surrounded by deformed quartz grains in quartzofeldspathic mylonites (e.g. Evans and White 1984). The general microcracking due to plasticity or grain boundary sliding is referred to as cleavage 3 or Brittle Intergranular Fracture 3 (B.I.F.3) by Atkinson (1982).

Plastic mismatches may also occur within single phases and single grains due to stress concentrations at dislocation pile ups. Where stress concentration is due to plasticity in this more restrictive sense, Atkinson calls it cleavage 2 (B.I.F.2). Four possible models are summarised by Lawn and Wilshaw (1975a) and shown in Figure 2.7e. The microcrack may be initiated entirely within the grain, along the grain boundary or within an adjacent grain. Hallbauer, Wagner and Cook (1973) observed microcracks in quartz grains isolated from possible impingement by a phyllosilicate matrix. These were considered to be such intragranular plasticity-induced microcracks but the possibility of elastic mismatch stresses also exists. Plasticity-induced microcracking is thought to be largely responsible for 'semibrittle' behaviour, and is discussed at length in Carter and Kirby (1978). They show that asymmetrically formed kink bands must generate a strain incompatibility, and illustrate fractures along kink bands in naturally deformed enstatite, and normal to the kink bands in experimentally deformed quartz. Arrays of edge dislocations, observed as deformation lamellae, also generate tensile fractures in both experimentally and naturally deformed quartz. Intersections of conjugate slip systems, the generation of sessile dislocations by the intersection of non-conjugate slip systems, and grain boundaries may all provide appropriate obstacles for plastic induced mismatches.

vi) Cleavage-Induced Microcracks. The overwhelming importance of cleavage in controlling microcracks in biotite (e.g. Wong and Biegel, 1985, Fig.8), and also in plagioclase is well known. Although the weak cleavage of quartz is often dismissed as unimportant in microcracking, there are several studies that show not only that there is a large anisotropy in fracture toughness or critical crack extension force along certain planes in quartz, but also that this is a significant factor in experimentally fractured quartz. Cleavage has been reported on many planes in quartz. The table gives the known directions in generally accepted order of ease:

Rhombohedral +	r	$(10\bar{1}1)$
Rhombohedral -	z	$(01\bar{1}1)$
Prism 1st Order	m	$(10\bar{1}0)$
Basal Pinacoid	c	(0001)
Prism 2nd Order	a	$(11\bar{2}0)$
Trigonal Dipyramid 2nd Order	s	$(11\bar{2}1)$
Trigonal Trapezoedron	x	$(61\bar{6}1)$

Three early studies illustrate the importance of cleavage surfaces in the fracture of quartz. Borg and Maxwell (1956) deformed loose Asbury Park sand at temperatures of 270-320^{o}C in a variety of solutions with confining pressures of 79-110MPa and an applied stress of 179-220MPa. They identified the fracture surfaces of 244 grains, which are given below as percentages:

r and z	(10T1) and (01T1)	44%
m	(10T0)	10%
a	$(11\bar{2}0)$	4%
s	$(11\bar{2}1)$	4%
z	$(11\bar{2}2)$	2%
c	(0001)	1%
d	(10T2)	3%
Unidentified		32%

These figures however cannot be taken directly to imply the relative importance of cleavage directions in fracture, since Borg and Maxwell also showed that specimens inherited a weak grain shape and crystallographic

orientation consisting of a c-axis great circle normal to the σ_1 direction when initially packed into the apparatus. Thus crystallographic planes perpendicular to the c-axis would be more likely to fracture. However, the weakness of the initial orientation and the lack of (0001) fracture surfaces does give some indication that r, z and m planes are favoured fracture planes, and the concentration of fracture surfaces on these planes is greater than would be predicted simply from the superimposition of axial cracks on weakly orientated grains. They also observe an increase in numbers of grains with deformation lamellae from 3 to 10%, with poles at 41-80^0 to σ_1, and a weak tendency to form in the [1120] zone. Bloss (1957) analysed crushed fragments from single specimens of quartz at room temperature and 700^{0}C. No quantitative data were collected, but Bloss showed that r and z cleavages, followed by m, were most abundant, that s and x cleavages probably occurred, and that c cleavage was present. In high quartz, a greater proportion of grains had a cleavage parallel to r. Borg et al. (1960) carried out similar experiments on St. Peter sand, and again found that fractures were formed preferentially paralle to r and z, the same temperatures, confining pressures of 50-200MPa and ultimate strengths of 43-490MPa. No deformation lamellae were observed.

There have been three attempts to quantify the fast crack-growth resistance in single crystals of quartz for different directions. Brace and Walsh (1962) measured the surface energy, γ in a simple Double Cantilever Beam test on four crystallographic directions. Atkinson (1979) reports values of the critical stress intensity factor, K_{Ic} for two directions of crack propagation on a face for quartz using a double torsion test, and Hartley and Wilshaw (1973) using the same test method as Brace and Walsh, report the critical crack extension force, G_L for the r direction. Using the equivalence of K_{Ic} and G_c (Section 2.3.1i), all three results are summarised below in units of Jm^{-2}, appropriate to G.

Face	Direction	$G_c(Jm^{-2})$			
		Brace & Walsh	Hartley & Wilshaw Synthetic α Quartz	Atkinson Synthetic α Quartz	
r (10T1)		0.41	11.5		
z (T011)		0.5			
a (T120)		0.76			
a	r				20.08
a	z				14.52
m (10T0)		1.030			

Hartley and Wilshaw also tested various quartz orientations with Hertzian indents. It is not yet possible to deduce an exact expression to relate the load at fracture (Pc) to K_{Ic} or G_c in a Hertzian indent, but the value of Pc can be taken as proportional to either. Cone cracks form approximately perpendicular to the surface tested; results of Pc are given below for three surfaces normalised to the value of the (0001) face (P(0001)):

Force of Indent	Pc/P (0001)	Possible Crack Surface
c (0001)	1	m or a
m (T100)	0.56	c
a (TT20)	0.33	c

Hartley and Wilshaw ascribed this anisotropy to the Poisson's ratio, since they considered that surface energy for quartz "is essentially independent of orientation".

The reason for the very much lower values of G_c reported by Brace and Walsh has been discussed by Hartley and Wilshaw, who think that a consistent underestimate was introduced in the former's experiments due to the large ratio of crack to specimen length. A further complicating factor is that G_c is highly sensitive to the type of quartz: Norton and Atkinson report that their synthetic quartz was half the strength of natural quartz. Hartley and Wilshaw were able to increase dramatically the strength of synthetic quartz by annealing. Thus the results given in the table are unlikely to be strictly comparable. However, all the experimental results, with the exception of the indentation experiments, indicate that there is at least a two-fold anisotropy in G_c for quartz, and that the faces

arranged in order of increasing G_c are r, z, a and m. This correlates with the atomic structure of quartz, in which the r and z planes have the least number of bonds/unit length, with r slightly 'smoother' than z, followed by the a and m planes. The difference between r and z planes reported by Brace and Walsh is within experimental error and was dismissed as insignificant by them; however there is a crystallographic difference which would favour fracture on the r planes. The reason for the apparently anomalous values obtained from indentation experiments may be due to the fact that the crack surface of a cone crack is not a single crystallographic plane. Norton and Atkinson's results illustrate that the anisotropy exists between different directions even within a single plane.

The results of the crushing and critical crack extension force experiments correspond well to suggest that r and z planes are approximately half as strong as m or a planes. Some cleavage studies have detected a greater ease of fracture on r over z, and this is also suggested by the Brace and Walsh experiments as detailed above, but it was proposed that misidentification of the two planes due to twinning may be responsible. The crushing experiments indicate that m may be weaker than a; but Brace and Walsh's results give the reverse order. The second important conclusion that can be drawn from the experiments is that cleavage fracture is likely to be an important process in naturally deformed quartz, but no studies of naturally deformed quartz have addressed this question.

vii) Pre-existing Flaws. Both Tapponnier and Brace and Wong and Biegel emphasise the importance of re-fracturing of pre-existing microcracks. Indeed, the pre-existing crack density in one of the latter's undeformed samples was 2 to 3 times greater than any of the measured densities in the deformed samples. Both partial and complete healed and sealed cracks, and open cracks, were present in the undeformed sample; in the pre-failure stages, this was the most important microcrack mechanism. The authors argue

from the isotropic distribution of the pre-existing flaws that they are primarily thermal cracks. They are considered to be at least as important as cleavage in controlling the overall microcracking process. This is Atkinson's Cleavage 1 (or B.I.F.1) category, which he asserts dominates the first 20km of the crust.

Another plane of inherent weakness is the grain boundary. Tapponnier and Brace (1976) observe that most grain boundaries were almost continuously cracked at failure (Figure 2.7f). Dunn et al. (1973) show that grain boundary cracking followed axial cracking in a variety of sandstones. In Hadizadeh's well-cemented ('Type I') category, an initial phase of distributed grain-boundary cracking preceded axial cracking (in Oughtisbridge Ganister). The weakness of grain boundaries, even when these are overgrown by optically continuous quartz cements, is apparent in the 'granulation seams' studied by Pittman (1981). He identifies overgrowths by their facetted edges as a major component of the matrix in the granulation seams, and shows that their abundance correlates inversely with the proportion of granulated quartz, suggesting that much of the latter was formed by destruction of the overgrowths.

It is quite evident from the experiments quoted that the multiplicity of microcracking mechanisms is a real feature of cataclastic deformation, and not a question of interpretation. The control of these mechanisms of the failure conditions by these mechanisms, and the influence of initial microstructure, are topics of great importance to cataclasis.

A number of studies have examined the change of microcrack characteristics through failure. These are first described through the failure sequence at constant confining pressure, and subsequently the effect of confining pressure itself is mentioned.

A universally reported effect is the increase in microcrack density in the pre-failure phase: for example, Westerly Granite microcrack densities doubled (Tapponier and Brace 1976), while during creep of Barre Granite,

increases of 400% occurred (Kranz 1979). The rate of microcracking increases substantially at high percentages of peak stress: Hallbauer, Wagner and Cook (1973) report an increase in the number of microcracks by a factor of 7 in an argillaceous quartzite, on raising the stress from 0.8 to 0.9 of the ultimate strength, and crack area of the San Marcos Gabbro increased by 5 between 80 and 93% of peak stress (Wong and Biegel 1985). This behaviour correlates with pre-failure dilatancy, and volumetric calculations indicate that microcracking accounts adequately for dilatancy (e.g. Brace et al. 1966, Hallbauer, Wagner and Cook 1973). Change in microcrack mechanism through failure has been mentioned briefly in the previous section. An observation made by both Hadley (1976) and Tapponnier and Brace (1976) for Westerly Granite, and Kranz (1979a) for Barre Granite, and Wong and Biegel (1985) for San Marcos Gabbro is that the earliest microcracks are pre-existing microcracks, grain boundaries and cleavages. Hadizadeh (1980) also observed the formation of a network of grain boundary cracks in Oughtisbridge Ganister with a cellular pattern as the first stage of failure. Subsequently, axial intragranular cracks develop in Westerly Granite, mostly due to elastic mismatches, and it is the loosening of the microstructure in Oughtisbridge Ganister that allows impingement-induced axial cracks to develop. However, in both the high- and low-porosity sandstones studied by Dunn et al. (1973), the axial cracks are considered to pre-date grain boundary fractures, and a similar sequence is implicit in the Peng and Johnson (1972) model of beam-buckling failure in Chelmsford Granite.

By the peak stress, however, axial cracks are forming in all samples and continue to do so in the post-peak region. After a shear surface has been created, shear fault-induced microcracks ('m.f.f.s') may form and continue to increase in density with displacement.

Accompanying these changes in microcrack mechanism through failure are also changes in microcrack orientations and shapes. A tendency for a

tighter preferred orientation of microcrack planes perpendicular to σ_3 was observed, for example, by Borg et al. in their experiments on loose St. Peter sand, and by Kranz (1979a) for Barre Granite. This could be due to the change in microcrack mechanism from pre-existing flaws to impingement-induced microcracks, and due to closure of cracks at high angles of σ_1. In the creep experiments on Barre Granite, crack aspect ratio (width/length) decreased with time, but crack width remained constant; the crack length clearly increased. This caused the cracks to link and change from intra- to intergranular. A similar lengthening of cracks with strain was observed by Hadizadeh for the Oughtisbridge Ganister.

Many of these textural changes through failure are similar to the effects of confining pressure. Crack densities at failure have been shown to increase by an order of magnitude with confining pressure by Hadizadeh and the increased dilatancy with confining pressure in Kranz's experiments could be attributed to a threefold increase in crack density with change in confining pressure from 1 to 100MPa. The data from Wong and Biegel support this trend with the exception of one high density sample at low confining pressure. Shear fault induced microcracks also increase in density with confining pressure (Friedman and Logan 1970, Conrad and Freidman 1976, Teuf el 1981).

Hadizadeh also shows that microcrack length increases with confining pressure and the same effect is implied by Wong and Biegel's observation on the San Marcos Gabbro that arrays of en-echelon fractures may propagate along sub-parallel paths without interacting in their confined experiments. These long microcracks contrast with the intragranular cracks, restricted to single grains (intragranular sensu strictu) observed in the unconfined experiments. However, orientations tend to show an opposite effect to that generally observed with proportion of peak stress. Cracks become orientated at lower angles to σ_1 (Kranz 1983). Wong and Biegel (1985) show

that anisotropy in crack density reduces with confining pressure and they speculate that at a specific pressure, no anistropy would exist, referring to this istropically distributed microcracking as cataclastic flow.

The influence of microstructure on microcrack mechanism is investigated by Dunn et al. (1973). They found an inverse power-law relationship between strength and porosity in a variety of sandstones and quartzites, with or without calcite cement. For both high- and low-porosity rocks without calcite cement, the failure sequence involved firstly axial microcracks, probably impingement-induced, which 'unlock' ends of ready-to-fail grain boundaries subsequently at the point of failure. The high-porosity, low-strength rocks generated a wide zone of cataclasite, with little grain fracturing, compared to the low-porosity, high-strength rocks. Rocks with a calcite cement, however, underwent an initial phase of intracrystalline twinning and gliding, accompanied by some axial (plastic mismatch induced) cracking, before a through-going fracture propagated leading to stable sliding. Hadizadeh (1980) emphasises the importance of microstructure by classifying failure into two types. Well cemented, interlocking, low porosity microstructures are described as Type 1, and include the Oughtisbridge Ganister that he studied. In these rocks, stress distribution is initially homogeneous, and impingement, cavity, elastic and plastic mismatch mechanisms are all suppressed in favour of shear-mode grain boundary cracking until the microstructure is loosened sufficiently for impingement-induced microcracks. Poorly cemented, high-porosity polyphase rocks belong to the type 2 category. Initial stress distribution is markedly inhomogeneous; impingement, cavity, elastic and plastic mismatch-induced mechanisms may all operate from early in the stress history to generate intragranular axial cracks, with cross-linking along subordinate grain-boundary cracks before, during or after formation. Pennant Sandstone, and Tennessee Sandstone are given as examples of such a microstructure and Blenkinsop and Rutter (1986) suggest that the Cambrian

Pipe rock quartzite of N.W. Scotland had a similar microstructure at the time of deformation, as well as all the sandstones listed in Table 2.1. (Simpson Group, Wingate Sandstone, Navajo and Entrada Sandstones). The argillaceous sandstone deformed by Hallbauer, Wagner and Cook, consisting of quartz and muscovite in a matrix of fine-grained sericite, pyrophyllite and quartz, with a matrix: quartz ratio of 1:3, is clearly a type 2 microstructure. This category might be extended to include rocks with high densities of pre-existing cracks and minerals with very easy cleavages, in which intracrystalline cracking would be important from early in the loading history. Therefore Westerly Granite and San Marcos Gabbro may both have this microstructure, and the immediate small-scale heterogeneity of the stress field is evident from the importance of cleavage and pre-existing flaw-induced microcracks in these specimens, although they have very low porosities. The classification into types 1 and 2 is thus essentially based on the homogeneity of the initial stress distribution, which controls the sequence of microcrack mechanisms and microcrack types.

One aspect of the early stages of experimental cataclasis which has received almost no attention since first mentioned by Borg and Maxwell (1956) is the production of both grain shape and c-axis fabrics in quartz. Grain shape fabrics consisting of long axes perpendicular to σ_1 were produced by packing of cylinders of loose Asbury Park sand prior to deformation, and a similar pattern of c axes was observed in both fractured and unfractured grains, but unfortunately the extent to which this happened during the experiments was not determined. In similar experiments on St. Peter sand, Borg et al. (1960) detected a grain-shape fabric parallel to the stretching direction only in extension. They list as possible mechanisms: grain rotation, modification of grain shape by fracturing, selective destruction of grains with certain orientations, and the production of new fragments with a shape fabric, but conclude that grain rotation is the most significant. Optic axis fabrics were unchanged by

uniform compression of the sands, but differentially compressed specimens developed a weak girdle at 30^{o} to the principal shortening (and σ_1) direction. In extension, the primary fabric was rotated with the grains, confirming the mechanism proposed for the production of the grain shape fabric. The authors conclude "... It is quite clear that both dimensional and crystallographic reorientations of quartz can result from a cataclastic deformation without recrystallization". This important experimental result could well apply to weakly-cemented, naturally deformed rocks.

b) Shear Failure. All experimental studies have identified the shear failure mechanism in confined conditions as the linking of microcracks, and several linking mechanisms have been suggested. Peng and Johnson (1972) propose that axial cracks in the Chelmsford Granite became linked when individual beams, bounded by axial cracks, buckled at a critical 'fibre strain', allowing the first through-going fault plane to form (Figure 2.8a). Hallbauer, Wagner and Cook's (1973) diagrams show an exactly similar sequence of axial cracks becoming cross-linked along the fault plane in a quartzite. This linking mechanism can be contrasted with the behaviour of Oughtisbridge Ganister described by Hadizadeh (1980), in which, as noted above, grain boundary cracks formed first, to be linked by axial cracks. The grain boundary cracks formed in a network with a cellular pattern, which defined the position of the final shear fault along the junction between cells (Figure 2.8b).

A third type of linking mechanism is the direct interaction of microcrack stress fields. Such interactions are classified into 'en-echelon' and 'en passant' by Kranz (1979b) (Figure 2.8c, I and II). The former occurred between two straight, sub-parallel cracks, which were linked by a third straight crack. When two en-echelon cracks are at an acute angle to the maximum compressive stress, they may link by a third crack with both tensile and shear components of displacement, though this type of crack is rare (Figure 2.8c, I). More common is the situation of

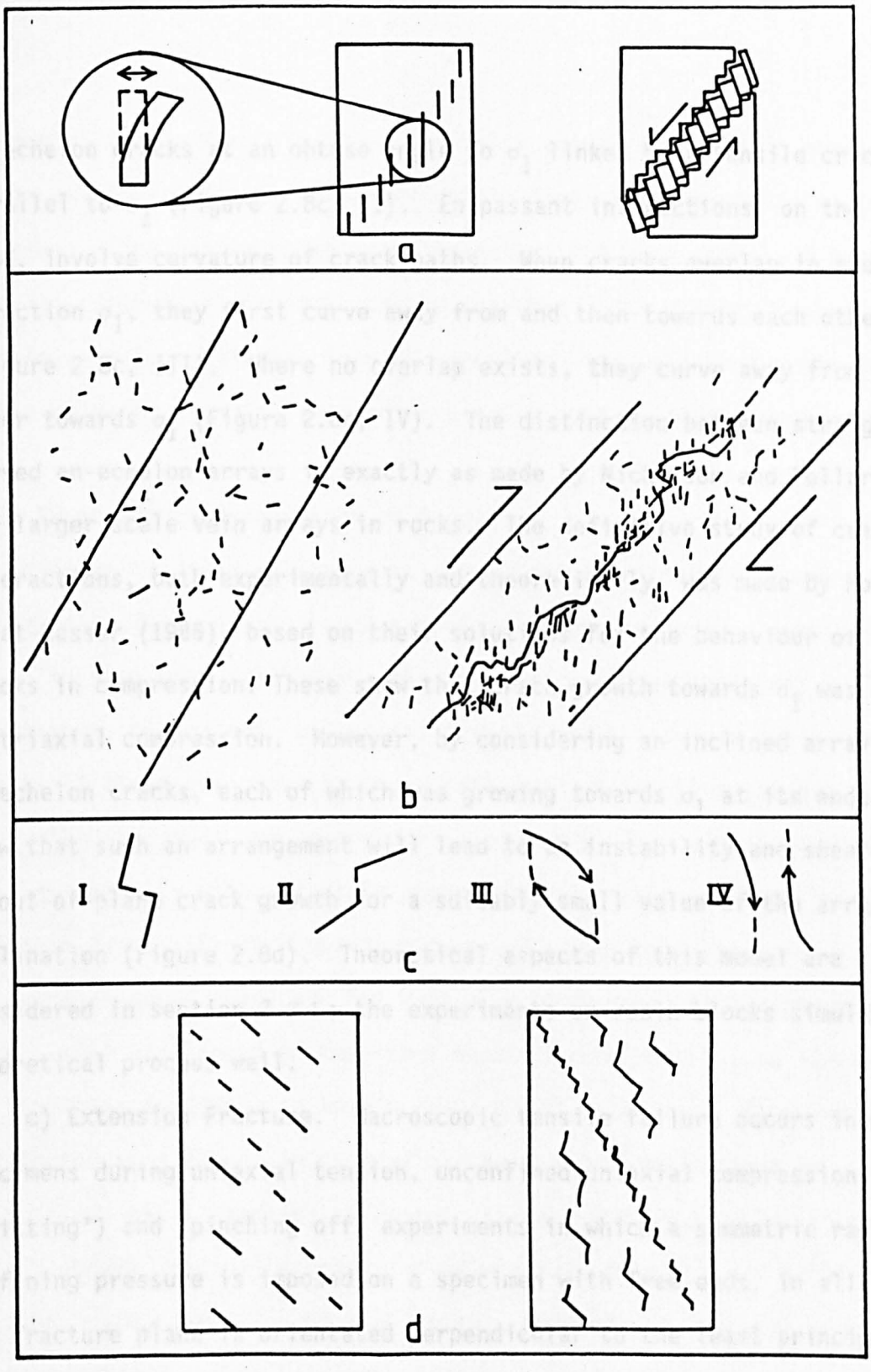

FIGURE 2.8

Shear Failure Mechanisms

a) Beam buckling model (Peng and Johnson 1972)
b) Network of Grain boundary cracks, linked by axial cracks (Hadizadeh 1980).
c) Microcrack interactions (Kranz 1979)
   I), II) En-Echelon
   III), IV) En Passant
   In I) and IV), microcracks are orientated at less than 45^{o} to σ_1.
   In II) and III), microcracks are orientated at greater than 45^{o} to σ_1
d) Interaction of a row of en-echelon flaws (Hori and Nemat-Nasser (1985)).

en-echelon cracks at an obtuse angle to σ_1 linked by a tensile crack parallel to σ_1 (Figure 2.8c, II). En passant interactions, on the other hand, involve curvature of crack paths. When cracks overlap in the direction σ_1, they first curve away from and then towards each other (Figure 2.8c, III). Where no overlap exists, they curve away from each other towards σ_1 (Figure 2.8c, IV). The distinction between straight and curved en-echelon arrays is exactly as made by Nicholson and Pollard (1985) for larger scale vein arrays in rocks. The definitive study of crack interactions, both experimentally and theoretically, was made by Hori and Nemat-Nasser (1985), based on their solutions for the behaviour of isolated cracks in compression. These show that crack growth towards σ_1 was stable in triaxial compression. However, by considering an inclined array of en-echelon cracks, each of which was growing towards σ_1 at its ends, they show that such an arrangement will lead to an instability and shear failure by out-of-plane crack growth for a suitably small value of the array inclination (Figure 2.8d). Theoretical aspects of this model are considered in section 2.3.1 ; the experiments on resin blocks simulate the theoretical process well.

c) Extension Fracture. Macroscopic tensile failure occurs in many specimens during uniaxial tension, unconfined uniaxial compression ('axial splitting') and 'pinching off' experiments in which a symmetric radial confining pressure is imposed on a specimen with free ends. In all cases the fracture plane is orientated perpendicular to the least principal stress, and the origin of extension fractures during compression can be easily understood as a response to local tensile stress fields around flaws in the absence of a fluid pressure (section 2.3.1) or as simple or hybrid extension fractures due to an internal pore-fluid pressure (hydrofracture). The unstable propagation of flaws beyond a critical crack length in unconfined uniaxial compression was shown by the experiments of Hori and Nemat-Naser referred to above. In practice, tensile stresses may be

introduced by elastic mismatches between specimen and loading machine, or by the use of lubricants which generate a local fluid pressure at the interface. The better these are eliminated, the more closely a true uniaxial compressive strength can be measured. The difficulties of performing a true uniaxial tension experiment are such that determination of the uniaxial tensile strength is usually done by an indirect means.

2.2.2 Experimental Deformation of Gouges

Because of their relevance to the behaviour of faults, experimental deformation of gouges has concentrated on gouge rheology. Seven important variables have been identified: strain rate, water and moisture content, temperature, mineralogy, thickness, surface roughness, and grain size. The effects of these variables on the coefficient of friction between rock faces without gouges are reviewed in Paterson (1978). The following review deals essentially with the fault gouges during stable sliding.

i) Strain Rate. Strain rates have generally been considered to have no influence on gouge rheology, but Rutter and Mainprice (1978) and Rutter and White (1979) have shown an important weakening in pre-faulted samples of wet Tennessee Sandstone at strain rates of 10^{-6}-$10^{-1}s^{-1}$. These were interpreted as a change in deformation mechanism from dominantly sub-critical axial cracking at faster strain rates to a cyclic process of grain boundary sliding accommodated by pressure solution and axial cracking, rate controlled by the former. Rutter's theoretical model for pressure solution grain boundary sliding was introduced in the earlier paper and shown to give a good agreement with experimental results: in the second paper, mica beards grown in the shear direction, and facetted quartz overgrowths, were optical evidence of the diffusion deformation mechanisms. Extrapolating to 'geological' conditions gives strain rates of $10^{-12}s^{-1}$ and stresses of 10MPa at 300^{0}C. Even 'dry' samples showed a small reduction of strength at slower strain rates, possibly due to some influence of

sub-critical crack growth. These results were obtained from pre-faulted samples in a triaxial apparatus rather than the more usual direct shear of simulated gouges, but they are of great importance because of their long time scale and slow strain rates.

Dietrich (1981) also reported strain rate effects on simulated fault gouge derived from crushed and sieved Westerly Granite. Changing the velocity caused both a transient and a residual change in gouge strength. Initially, an increase in velocity is followed by a strength increase, but this decays with time. The net strength change may be positive or negative, depending on the relative magnitude of the transient and long-term components. A further strain-rate effect noticed was strengthening following a 'hold' period; the change in coefficient of friction was proportional to the length of the hold. These two experimental results are of significance in interpreting other gouge rheology experiments and indicates that they may not be simply extrapolated to geological conditions.

ii) Water and Moisture Content. Both pore pressure effects and stress corrosion have been shown by Rutter (1979) to be important in the rheology of kaolinite fault gouges. Logan et al. (1981) and Summers and Byerlee (1977) attribute low shear strength of hydrated clays to a 'pseudo pore pressure' effect, which reduces the effective normal stress. The stress corrosion effects of water for pre-faulted samples of Tennessee Sandstone, accounting for the small reduction of strength with strain rate, have been mentioned above, together with the much more important weakening due to pressure solution.

iii) Temperature. It was the observation of Logan et al. (1981) that strengths of natural fault gouge from the San Andreas fault zone, bentonite, and chlorite, increased dramatically from 25^{o}C to 300^{o}C, that led to the pseudo pore pressure hypothesis above, since this is the temperature range in which dehydration of interlayer water occurs in

smectites. The net effect of temperature increases on pressure solution in Rutter's flow law is to produce some weakening at lower values; however the activation enthalpy is low. Temperature rise should also produce some weakening in gouges where reaction rate controlled subcritical crack growth is the dominant deformation mechanism (Region I of the V-K_I curve, section 2.3.1).

iv) **Mineralogy.** The effects of mineralogy on a polyphase natural fault gouge from the San Andreas fault zone were studied by Logan et al (1981) by examining the behaviour of the three main constituents: quartz, montmorillonite, and chlorite. At 25^{o}C, the natural gouge had two thirds of the strength of pure quartz, roughly the same strength as pure chlorite and a much greater strength than pure montmorillonite. At 300^{o}C, the only difference in these relative strengths was that the natural gouge had a similar strength to pure quartz. These results were interpreted as indicating that quartz had very little influence on the strength of the gouge, which was controlled by chlorite (only 10-15% of the modal composition). Also, the chlorite (and gouge) had high shear strengths (200MPa at 150MPa confining pressure, T=300^{o}C) from which the authors conclude that clays do not act as a low-strength material in gouges under these conditions (similar values were reported by Rutter for kaolinite).

v) **Gouge Thickness.** Three experiments have shown that thickness of fault gouge (t) developed on pre-cut surfaces increases with displacement (d) (Jackson and Dunn, 1974, Engelder 1974, Teuf el 1981), and Robertson (1983) has incorporated the first two in his data compiled from natural faults. Three d-t relationships are summarised below:

Engelder	1974	d = 8t	Coconino Sandstone
Teuffel	1981	d = 22t+2	Coconino Sandstone
Robertson	1983	d = 100t	Various

Dietrich (1981) also showed qualitatively that thicker gouge layers had lower strengths of stable sliding.

A mechanical explanation for this can be found in Rutter (1976), who

showed that kaolinite 'gouges' work-hardened. Thicker gouges were weaker because the work-hardening spread through the gouge during deformation.

vi) Surface Roughness. The effect of surface roughness on rheology was investigated by Dietrich (1981), who ground pre-cut blocks of Westerly Granite to various polishes before loading artificial gouge consisting of the crushed granite between blocks. The coefficient of friction for stable sliding increased with surface roughness; the rougher surfaces enhanced development of Reidel shears and spread deformation throughout the gouge, in comparison with the development of concentrated shears at the gouge-rock contact where this was smooth.

vii) Grain Size. Various original grain sizes were tested by Dietrich in the same experiments; with quite a profound effect on residual strengths. Three size fractions were tested: the 125-250μ fraction, all particles less than 250μ, and all less than 85μ. Residual strengths increased in that order, or there was an increase in strength with proportion of fine gouge. The greatest reduction of grain size during sliding occurred in the thinnest gouges with the roughest surfaces.

Dietrich's observations on the effect of gouge thickness, surface roughness, and grain size on strength, can be linked with the above observations on the effects of thickness and roughness on comminution to suggest that a fundamental relationship exists between grain size (and hence the comminution process) and strength. Engelder (1974) was able to derive experimentally an inverse exponential relationship between median grain size and displacement which was qualitatively similar to the cataclastic grain size reduction noted in the field. He also noted that, as in the field, sorting became poorer.

Stable sliding gouge rheologies appear to be divided into those that exhibit long term strain hardening and those that are perfectly plastic. Among the former are kaolinite gouges at 20°C (Rutter 1976), San Andreas gouge at 25°C, bentonite at 25°, and chlorite at less than 450°C (Logan et

al 1981). Perfect plasticity occurred in Westerly Granite gouge (Dietrich 1981), chlorite at 450^{o}C and pre-cut Coconino Sandstone (Teuf el 1981). Strain hardening mechanisms have not been identified in any of these studies, but it has been suggested that localization on discrete sliding surfaces (Reidel shears) is a strain softening mechanism during stick-slip oscillations in San Andreas gouge.

The factors affecting the transition to stick slip have been summarised by Paterson (1978), and include lithology, surface roughness, development of gouge, normal stress, temperature, strain rate, and fabric.

2.2.3 Fractography

Fractography is a versatile and widespread technique in ceramic studies, where it has been successfully applied to deducing fracture stress, fracture velocity, and details of both sub-critical and fast crack growth (e.g. Bansal 1977, Quakenbush and Frechette 1978). The possibility of applying it to geological materials was suggested by Norton and Atkinson (1981), who conducted some successful experiments showing that quartz behaved in some respects like ceramics and glass, and that certain features of experimental quartz fracture surfaces could actually be used to deduce fracture stress. Considerably more experimental data are needed before a reliable palaeopiezomoter could be created, taking into account variables such as temperature, grain size and moisture content.

However a review of the ceramic literature suggests that fractography may be useful in another way. One of the outstanding problems of using recent experimental work on stress corrosion is whether such a mechanism has actually been operative in rocks deformed in the crust. Various stages in the growth of a crack by stress corrosion in glass appear to leave distinctive crack morphologies. If any parallel can be shown with natural quartz fracture surfaces, then the way might be open to resolving the question of the importance of stress corrosion in the crust.

The fractography of fast and slow crack growth in glass and quartz is now summarised and the implications drawn for natural fracture surfaces.

a) **Dynamic Crack Morphology in Glass and Ceramics.** A typical glass fracture surface can be divided into three regions which surround the initiation point of the crack concentrically: the **'mirror'**, a flat highly polished surface, the **'mist'**, a rough broken surface, and the **'hackle'**, consisting of many intersecting planes (Figure 2.9). The mist is an enigmatic feature which cannot be precisely defined: the scale of surface irregularities seems to decrease in a continuum until the smooth surface of the mirror is attained. Thus the mirror/mist boundary is arbitrary depending on the resolution of the examining system. The mist/hackle boundary is usually better defined, though in detail it is somewhat irregular.

Empirically it has been shown (Bansal 1977) that the mirror radius, r, is related to the fracture stress σ_f by a constant A, the 'mirror constant', in the following expression:

$$\sigma_f \; r^{1/2} = A \qquad 2.1$$

Due to the gradational nature of the mirror/mist boundary, some arbitrary criterion must be used to define r. Such 'mirror formulae' also work for the mist/hackle boundary. Johnson and Holloway (1966) produce a more general version of this formula in which Z_p was substituted for σ_f, being the normal tensile stress at any point on the fracture surface before failure, and r was the distance from the flaw to that point. They were able to predict the shape of the mirror area from stress analysis of more complex stress systems.

The mirror formula obviously has a close similarity to the fracture mechanics formula relating stress at failure to the initial crack length, c, by the stress intensity factor K_{Ic}:

$$\sigma_f \; c^{1/2} = BK_{Ic}$$

FIGURE 2.9

Dynamic crack morphology in glass.

FIGURE 2.10

Sub-critical crack morphology in glass (after Quakenbush and Frechette 1978, Varner and Frechette 1971, Michalske and Frechette 1980). The top part of the diagram shows a V-K graph for the crack growth, marked by Wallner lines on the surface of a glass slide shown immediately below. The crack curvature changes from positive (concave towards the origin) in Region I to convex in Region II, and reverses to concave again in Region III. In Region II, a distinctive set of bands 0.05mm long, enveloped by a parabolic crack, are developed, shown in detail in the enlargement. They form when the centre part of the crack is arrested due to lack of water access, while the outside of the crack continues to advance subcritically (stage a, 1, 2, 3). Eventually stress is concentrated sufficiently on the external part of the crack to cause dynamic propagation to a new position (stage b) when the process is repeated (stage c). The lower part of the diagram shows Michalske and Frechette's observation and interpretation of a 'cavitation scarp'. Water retards the crack advance along the H_2O V-K curve until the crack front breaks free with a sudden increase in crack velocity (on the air V-K curve). A 'cavitation scarp' marks this jump.

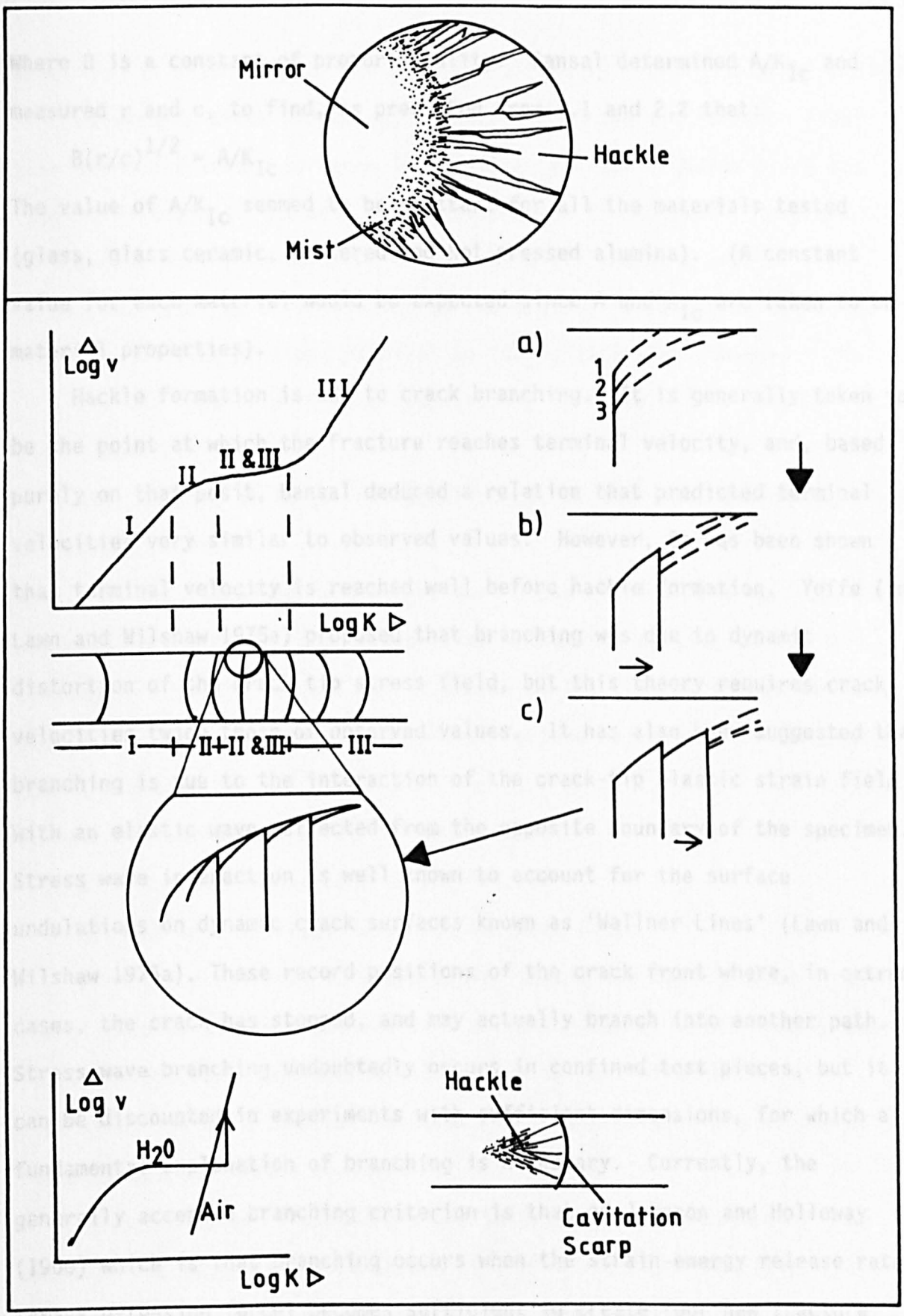
Mirror
Hackle
Mist
Log v
III
II
II &III
I
Log K
a)
1
2
3
b)
c)
I
II+II &III
III
Log v
H2O
Air
Log K
Hackle
Cavitation
Scarp

Where B is a constant of proportionality. Bansal determined A/K_{Ic} and measured r and c, to find, as predicted from 2.1 and 2.2 that:

$$B(r/c)^{1/2} = A/K_{Ic}$$

The value of A/K_{Ic} seemed to be constant for all the materials tested (glass, glass ceramic, sintered and hot pressed alumina). (A constant value for each material would be expected since A and K_{Ic} are taken to be material properties).

Hackle formation is due to crack branching. It is generally taken to be the point at which the fracture reaches terminal velocity, and, based purely on that posit, Bansal deduced a relation that predicted terminal velocities very similar to observed values. However, it has been shown that terminal velocity is reached well before hackle formation. Yoffe (in Lawn and Wilshaw 1975a) proposed that branching was due to dynamic distortion of the crack tip stress field, but this theory requires crack velocities twice those of observed values. It has also been suggested that branching is due to the interaction of the crack-tip elastic strain field with an elastic wave reflected from the opposite boundary of the specimen. Stress wave interaction is well known to account for the surface undulations on dynamic crack surfaces known as 'Wallner Lines' (Lawn and Wilshaw 1975a). These record positions of the crack front where, in extreme cases, the crack has stopped, and may actually branch into another path. Stress wave branching undoubtedly occurs in confined test pieces, but it can be discounted in experiments with sufficient dimensions, for which a fundamental explanation of branching is necessary. Currently, the generally accepted branching criterion is that of Johnson and Holloway (1966) which is that branching occurs when the strain-energy release rate (crack extension force) becomes sufficient to create four new fracture surfaces: a simple extension of the Griffith energy balance criterion for growth of a single crack. This criterion predicts the mirror formula correctly, but the significance of mist formation (microscopic crack

branching in which only one crack path is finally chosen) is still unclear.

b) Dynamic Crack Morphology In Quartz. Norton and Atkinson (1981) have studied fracture surfaces in dynamically cracked quartz along two crystal directions. As well as describing the fractography, they are able to deduce a mirror formula for quartz which fit the data well.

a) Fracture surface perpendicular to the c-axis. Three areas are noted:

I. An area of steps parallel to the initial flaw boundary.

II. An area of very fine steps. This is taken as the 'mirror' in their formula.

III. An area of larger hexagonal steps, 10-15μ wide, exploiting r and z cleavage planes.

Area I is considered to be produced during sub-critical propagation, during which the crack front compromised between its initial shape and r or z cleavage. Areas II and III were taken to be the same as the mirror and hackle of a glass fracture, the only difference being the influence of the quartz cleavage.

b) Fracture surface parallel to the m plane

I. A planar zone, used as the 'Mirror'.

II. An area of steps 100μ wide on rhomb faces.

From these results, it would appear that a dynamically grown crack in quartz should, at the point where it becomes dynamic, show a planar or finely stepped area followed by a fracture surface of much larger crystallographically controlled steps, if it has grown along either of the two orientations tested above.

c) Sub-Critical Crack Morphology In Glass. Some features of slow crack growth in glass are described by Varner and Frechette (1971), and a comprehensive description is made by Quakenbush and Frechette (1978). In these experiments, glass slides were cracked at constant stress in a conventional double cantilever beam test. The position of the crack front was marked by natural or induced Wallner lines and the exact shape of the

crack front could be correlated precisely with its position on a graph of velocity vs stress intensity factor (V/K_I) as a crack grew sub-critically through regions I, II and III (see section 2.3.1b). The results of crack curvature are illustrated in figure 2.10 where the position of the crack front shown in the slide corresponds with its position on the graph. The crack front in region I has positive curvature (convex towards the origin) because the specimen has a higher compliance at the edges of the slide: the crack curves to equalise the stress distribution and maintains constant velocity. In region II where the rate of growth is no longer stress dependent, a negative curvature develops to allow more time for the corrosion agent to reach the central part of the crack, which is further from the supply than the edges. Although the stress is now concentrated on the crack edges, they do not accelerate any further because the growth is not stress dependent. Eventually the stress intensity factor rises on the central portion of the crack sufficiently to cause it to enter region III: the crack front splits into three parts, the outer two growing by region II and the inner by region III processes. When the entire crack front is in region III, it again has a positive curvature.

The detailed way in which the crack advances while in the mixed region stage is reported by Varner and Frechette (1971). The outside of the crack advances with the inner part stationary until stress is built up to advance the inner part by region III processes. This sort of 'stick-slip' oscillation leaves a series of distinctive marks on the fracture surface (Figure 2.10) and has a fascinating geological analogy: it is similar to the barrier mechanism proposed by Das and Scholz (1981) in which a dynamically propagating crack stops at a barrier when the value of the static stress intensity factor K_S is less than the value of the critical stress intensity factor K_D, generating delayed multiple events (section 2.3.1).

A rather different set of features in the same part of the V/K_I curve

was observed by Michalske and Frechette (1980) (Figure 2.10). From a mirror surface while the crack is in region II, the fracture surface developed hackles before leaving a sharp line as the crack suddenly increased velocity and entered region III. These slides were deformed under water, and the explanation for the sudden jump in crack velocity is that water in fact retards the crack growth as K_I increases beyond the value expected for a crack at this velocity in dry air. At a critical point, the crack breaks free of the water, forming the sharp line which is called the 'cavitation scarp', and jumps to the new velocity appropriate to the large value of K_I. The retarding effect of the water may be manifested in the formation of the hackle marks, which may develop around sites of local cavitation leaving dry spots on the advancing crack front. These then absorb energy by creating hackles until a cavitation bubble can spread across the whole crack front, liberating it from water.

In summary, slow crack growth in glass may form a similar variety of features to fast growth, including mirrors and hackles. However, diagnostic of a crack accelerating through regions I, II and III of the V/K_I curve would be reversal of crack curvature, sporadic advance of the crack front, and production of a cavitation scarp.

d) Sub-Critical Crack Morphology in Quartz. There are few observations of the fractography of slow cracks in quartz. Scholz (1972) found that the fracture surface of cracks grown sub-critically consisted of equally-spaced narrow ridges less than 0.1mm wide. The only difference between these and surfaces of fast cracks was that the latter were spaced more widely (0.2mm). Scholz attributed the markings which were on surfaces both parallel to <c> (i.e. prisms) and <a> (prism or basal pinacoid), to the oscillation between region II and III behaviour reported by Varner and Frechette, but made no mention of the possibility of cleavage control.

Martin and Durham (1975) illustrate a fracture surface grown at four different stresses, all by slow crack growth. At each point where the

stress is changed, there is a distinct band, which they suggest is due to a slight alteration in crack direction. Between these points, the surface is ridged exactly like Scholz's specimens. The crack grew on a basal plane (0001), and the ridges are seen as teeth with directions parallel to r and z: they are clearly r-z cleavage steps, with a spacing of 50μ. On surfaces normal to the basal plane, the only markings are random ridges and valleys parallel to the direction of propagation. The only other observation on slow crack morphology is the inference made by Norton and Atkinson (1979) that the area around the initial flaw in cracks grown on a basal plane, (consisting of steps approximately parallel to the flaw boundary) was generated by slow crack growth. These are directly comparable with the features on Martin and Durham's basal plane, and the lack of such features on planes parallel to m in Norton and Atkinson's study is exactly similar to the smoothness of such planes in Martin and Durham's.

Quartz fracture surfaces in slow crack growth seem to be characterised by narrow ridges on basal planes but no markings on prism planes. These ridges are to be 50-100μ wide and may very well be r-z cleavage steps. The variation in spacing illustrated by Martin and Durham's photographs hints that it may be an interesting parameter to measure, perhaps even correlating with crack velocity or stress.

e) Fractography of Rocks. Few studies have been made of experimental fracture surfaces in rocks, which are considerably more complex due to polycrystallinity. Some detailed observations were made by Swanson (1980) on Westerly Granite, in which Mode I fracture surfaces were examined from specimens cracked in the double torsion technique. An important difference emerges between the macroscopic fracture surface at sub-critical crack velocities and wet environments and dynamic fracture surfaces. This is quantified by the **transgranular/intergranular** (T/I) ratio, where 'transgranular' includes the 'intragranular' fractures of this study (section 2.5.1). The overall T/I ratio for sub-critical crack growth was

0.6 compared to 1.2 for dynamic crack growth, but the enhancement of transgranular fractures in fast crack growth was uneven among the components of the granite: it is a factor of five in quartz, two in plagioclase and biotite, and little in microcline.

Under the Scanning Electron Microscope, transgranular fractures have cleavage steps or conchoidal morphology, whereas intergranular fractures appear as smooth surfaces with grain boundary cavities. The cleavage steps coalesce along their length in the direction of crack propagation to give a 'river pattern', in which the crack movement is 'upstream'. Using this criterion, Swanson figures one grain in which cracks have propagated towards each other from opposite sides of the grain. A crack-pore interaction of the type figured in 2.6b is observed in a dynamically cracked specimen. Two further contrasts noted between the dynamic and slow crack morphologies was the presence of linear, parallel secondary fractures "which are suggestive of Wallner lines" on the dynamic fracture surface, and the greater separation of grains along boundaries in the sub-critical fracture surface.

Meredith (1983) reports changes in Mode I fracture features of Westerly Granite and Black Gabbro under sub-critical conditions with temperature and water vapour pressure. Both rocks develop oblique microcracks at the higher temperatures which are considered to be thermal. In addition the Westerly Granite showed a change from predominantly transgranular to much more frequent grain-boundary cracking with increase in water vapour pressure at 300^{o}C. The Black Gabbro showed transgranular cracking in all conditions, but temperatures of 300^{o}C promoted the formation of smaller cleavage steps. Both water-vapour pressure and temperature in general increase crack velocity, but the velocity of the specimens cannot be compared since the point on the V-K_I curve where the specimens were examined is unknown.

Finally, Cox and Atkinson (1983) give descriptions of dynamic, Mode

III fracture surfaces in Carrara Marble, Westerly Granite, Black Gabbro and Tennessee Sandstone. In the first three cases, a clear distinction could be made between Mode I fracture surfaces and those observed. Irregular intragranular cracking is much more common in Mode III, producing a smoother overall crack surface with fewer asperities. Quartz and even calcite exhibits hackle marks and there is a lack of cleavage fracture in other minerals. In Tennessee Sandstone, however, phyllosilicate in the matrix and grain boundary cracks around quartz are important in Mode III.

f) Discussion. This review indicates firstly that dynamic crack surfaces in quartz have the potential to form palaeopiezometers by analogy with mirror formulae in glass, although the hackles are cleavage controlled in quartz. Norton and Atkinson's speculation that a small area of steps parallel to the flaw boundary immediately adjacent to the initial flaw represents sub-critical crack propagation, is strengthened by Quakenbush and Frechette's observation that crack curvature in region I of the $V\text{-}K_I$ curve tends to equalise stress distribution.

Slow crack growth in glass and ceramics leaves diagnostic features when the crack moves from one region of the V/K_I curve to another. At the transition from region I to region II, crack curvature changes from positive to negative. At the transition from region II to III, crack curvature reverses back to positive and a distinctive suite of marks are generated as parts of the crack front enter region III, sometimes sporadically. When the whole crack front enters region III in the presence of water, a cavitation scarp is formed. The fractography of slow crack growth in quartz is not well known, but seems to consist of evenly spaced r-z cleavage steps 50-100μ wide on basal planes and smooth surfaces on prism planes. This correlates exceedingly well with known data on quartz cleavage and critical crack extension force. Cleavage studies indicate that cleavages exist on r, z and m planes but only very weakly indeed on basal planes. Critical crack extension measurements confirm the ease of

parting on r and z. Thus a crack propagating on a basal plane is likely to exploit the easier r-z planes even if they are not in the ideal orientation for purely tensile displacements, while a crack on an m plane will remain in this plane, which has a weak natural cleavage, rather than seeking the slightly easier but unfavourably orientated r-z planes. There is also the suggestion by Martin and Durham that m planes may show ridges marking transitions between region II and III behaviour.

The presence of r-z steps is not diagnostic of slow crack gowth in quartz, but their scale and the absence of a 'mirror' may distinguish sub-critical from fast crack growth. By analogy with glass, changes in crack curvature could also be used to identify transitions to and from region II V-K_I behaviour.

2.2.4 Crack Sealing, Healing and Cementation

The occurrence of cemented microcracks in natural cataclastically deformed rocks is well documented, particularly by studies using cathodoluminescence (e.g. Sprunt and Nur 1979, Stel 1981, Blenkinsop and Rutter 1986) and the importance of pre-existing cemented microcracks in the cracking process has been emphasised from experimental studies by, for example Tapponnier and Brace (1976), and Wong and Biegel (1985). Crack healing is distinguished by the local derivation and transport of the filling material compared to the distant source of precipites bearing fluids in crack sealing (Simmons and Richter 1976). 'Cementation' may be used to describe either process.

Some recent experimental studies by Smith and Evans (1984) detail the most important aspects of healing in quartz. Synthetic single crystals of quartz were thermally cracked and subsequently annealed under 200MPa confining pressure at various temperatures and with various initial concentrations of SiO_2 in added pore fluid. Crack healing was observed at the higher temperatures, leaving arrays of bubbles and tubes on the

original crack surface. The process evidently works in retreat from the crack tip to leave a 'bubble plane' which has features that correlate with the former fractography. Cylinders and bubble trains are parallel to the c-axis on prism faces, and parallel to steps in the original fracture or conchoidal morphologies on other surfaces.

The healing rate was evaluated by measuring the healed length after various times. No healing was observed in the absence of pore fluid or temperatures of 200^{o}C. The healing rate is a function of temperature and initial SiO_2 concentration (the rate increases with degree of undersaturation), and other important variables are likely to be crack width and water concentration. Several lines of evidence suggest that the diffusion path must be through the fluid or at the fluid-solid interface. The influence of initial SiO_2 concentration is interpreted as due to a "reaction enhanced crack sealing" mechanism, but it is estimated that fluids probably become saturated rapidly. The importance of these experiments lies in the extremely rapid rates of healing observed: for example, at 400^{o}C, crack lengths of 300-600μ were healed in only 48 hours. The implication of these rates has been considered by Blenkinsop and Rutter (1986), who suggest that crack healing is a possible work hardening mechanism for the production of distributed shear failure in the Cambrian quartzites of the Moine Thrust zone. A further interesting speculation from these experiments is that healed microcracks may preserve information about original fracture morphology. Among the several other experiments on crack healing, it is worth mentioning the work of Maxwell (1960) for his early appreciation of the rapidity of healing: at temperatures of 308-312^{o}C, pore fluid pressures of 90MPa and confining pressure of 207MPa (designed to simulate a depth of 8500m), fractures were completely healed in 8 hours from a 2% NaOH solution saturated with silicilic acid.

2.3 REVIEW OF THEORETICAL STUDIES OF CATACLASIS

Theories of cataclasis can be conveniently divided into those which are time independent and those which consider time dependent behaviour. There is much common to both groups, particularly the fundamentals of fracture mechanics: this will be considered with the first group. The scope of this review will be limited to recent developments so will not consider except in passim classic Mohr-Coulomb theory.

2.3.1 Time Independent Theories

Three types of theory are identified: Mechanistic, Localisation and Minimum Work.

a) Mechanistic Theories. In the first type, the detailed mechanisms of cataclasis are taken as a starting point and an attempt is made to model them from theoretical principles. The essential stages of failure from both observations of natural behaviour and experiments (Sections 2.1.1 and 2.1.2) are fracture initiation, fracture propagation and fracture interaction. Initiation involves nucleation and formation of cracks; the latter deals with crack growth whilst still within the influence of the nucleus (Lawn and Wilshaw 1975a). Initiation is not often considered in a geological context: 'Griffith Flaws' are assumed to exist. This can be justified by an examination of the mechanisms of fracture initiation from material science literature. Starting with an intact, flaw-free sample, Lawn and Wilshaw (1975a) show that from principles of indentation fracture that contact damage by a particle of radius one micron is sufficient to create a flaw in a brittle solid under an applied load of only one Newton. Maximum tensile stress, (σ_m), under an indenter is given by

$$\sigma_m = 1/2\ (1-2\nu)\ p_0$$

where ν is the Poisson's ratio and $p_o = P/\pi a^2$, with P the applied pressure and a the radius of contact circle. They also relate a to P and the radius of the indenter, R by an expression of the form

$$a \propto (PR)^{1/3}$$

Substituting this into the previous formula gives:

$$\sigma_m \propto P/(PR)^{2/3}$$

So that at constant σ_m, $R \propto P^{1/2}$. Therefore the critical radius to generate a tensile crack depends on the applied pressure via a square root: very modest pressures for even quite large indentations would create cracks. Almost any geological material would be sufficiently heterogeneous naturally on this scale to provide such indenters. Further mechanisms suggested by Lawn and Wilshaw for introducing stress-raising heterogeneities include chemical reactions, devitrification, diffusion and thermal rupture of bonds. Cleavage would play an essential role in many minerals.

In semibrittle solids, where obstacles prevent dislocation movement, cracks may nucleate to relieve the stress concentration at a dislocation pile-up. Such obstacles might be grain or twin boundaries. Non-brittle solids would require void coalescence of such nucleated cracks to allow a crack to form. Again in geological materials it is not difficult to imagine the existence of sufficient obstacles.

The stability of the nucleated crack governs the formation stage: Lawn and Wilshaw show that even in the absence of pre-existing nucleii, the stress required for stability is similar to that required for nucleation; thus the two stages of initiation (nucleation and formation) can occur at the lowest levels of stress. Furthermore, any process of initiation or propagation is generally non-reversible: in semi-brittle solids, natural plastic strains are trapped if stress is released, while in brittle solids, crack-wedging occurs firstly at an atomic level by absorption of contaminants onto the newly created crack surface, and also by movement of

adjacent particals into voids, and by the creation of a crack system morphology which may not allow the return of the crack walls to their unopened position. (It may also guide them back however). This principal of non-reversibility means that damage will accumulate and that geological materials are likely anyway to contain pre-existing cracks.

The solution to the problem of crack propagation has given rise to some of the most important theories of cataclastic failure, including Griffith theory and all subsequent modifications (e.g. McClintock and Walsh (1962), Murrell (1963), Fairhurst (1964) and Murrell and Digby (1970)), and to the whole field of fracture mechanics. The essential problem is to calculate the stresses developed around the crack on the application of a remote stress, for which two approaches have been adopted, depending on the geometry of the crack assumed. The first model assumes an elliptical crack, and was developed by Inglis (1913), Griffith (1924) and those authors above. The solution for the tangential stress σ_t in a biaxial stress field σ_1, σ_2, in elliptical coordinates ξ and η for a crack at an angle β to σ_2 is (Jaeger and Cook 1979): (Figure 2.11)

$$\sigma_t = \frac{(\sigma_1+\sigma_2)\ \sinh 2\xi_0+(\sigma_1-\sigma_2)[\exp 2\xi_0\ \cos 2(\beta-\eta)\ -\cos 2\beta]}{\cosh\ 2\xi_0\ -\ \cos 2\beta}$$

Two particularly useful solutions to this is for a crack orientated at β=o to σ_2: (i.e. axial orientation) in uniaxial compression:

$$\sigma_t = -\sigma_2 \qquad 2.3$$

And in triaxial compression, a crack with length c and width b at $\beta=\pi/2$

$$\sigma_t = \sigma_2\ (2c/b+1)\ -\ \sigma_1 \qquad 2.4$$

The second model treats the crack as flat with a sharp tip (e.g. Lawn and Wilshaw (1975a)), and gives a versatile solution for the stress field around the crack in each of the three modes of crack propagation of the general form, in the coordinates of Figure 2.11:

$$\sigma_{ij} = K(2\pi r)^{-1/2}\ fij(\theta)$$

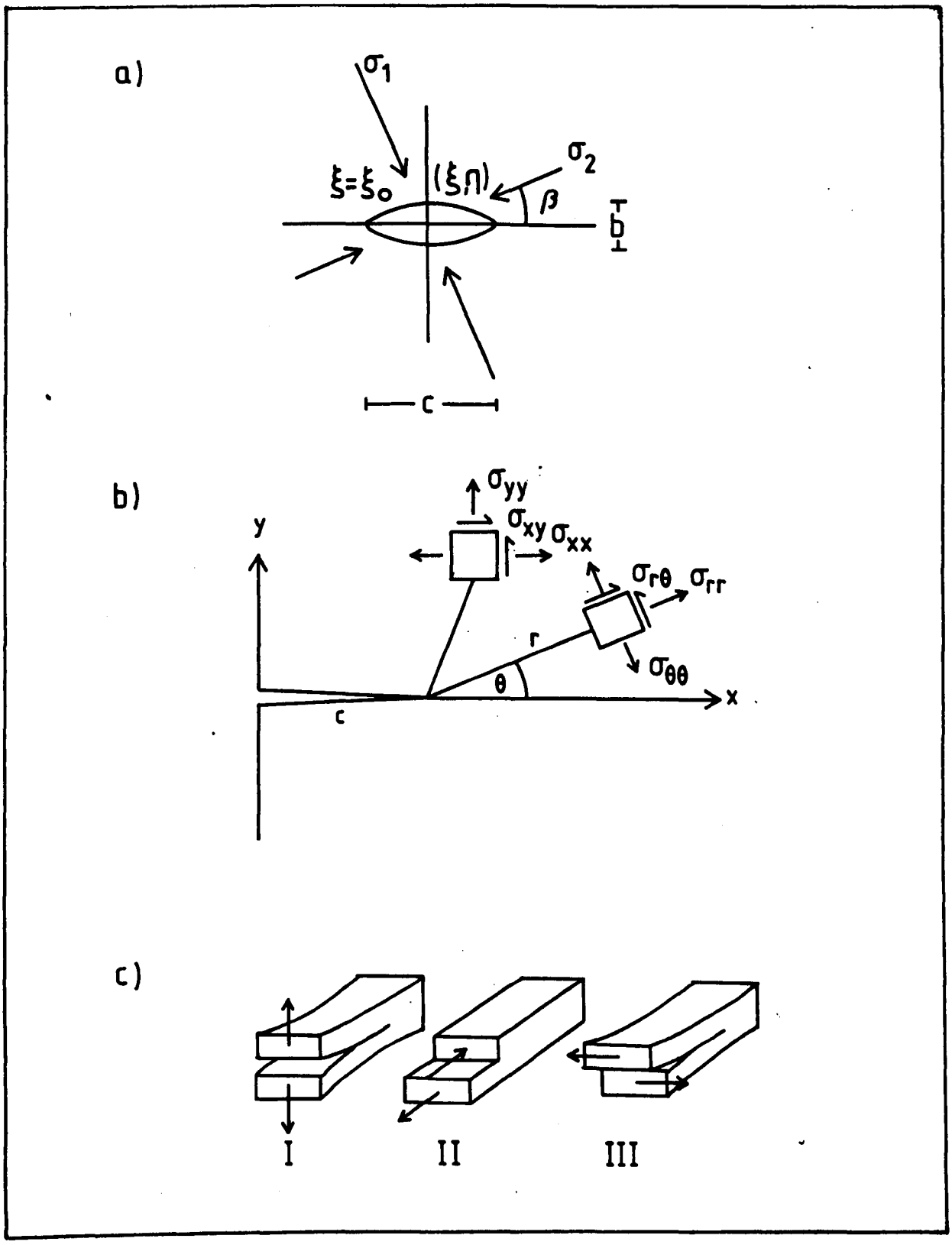

FIGURE 2.11

a) Elliptical Coordinates for the Inglis Solution to the stress field around a fracture (Jaeger & Cook, 1979).

b) Cartesian and Polar Coordinates for the Fracture Mechanics solution to the stress field around a fracture (Lawn & Wilshaw, 1975a).

c) Modes of Fracture (Lawn & Wilshaw, 1975a).

The stress is thus specified by K, the Stress Intensity Factor, describing the intensity of the field around the crack, and its distribution, described by radial factor $r^{-1/2}$ and a more complex function of θ which depends on the propagation mode (Figure 2.11). The stress intensity factor depends on the loading geometry, the crack length, and the applied stress (σ_L) for uniform loading at a remote distance from the crack:

$$\begin{aligned} K_I &= (\sigma_{yy})_L (\pi c)^{1/2} \\ K_{II} &= (\sigma_{xy})_L (\pi c)^{1/2} \\ K_{III} &= (\sigma_{zy})_L (\pi c)^{1/2} \end{aligned} \qquad 2.5$$

For other uniform loading systems, an additional factor m is introduced which depends on the loading geometry, to allow, for example, for edge effects or curved cracks. K can also be calculated for specific examples of non-uniform loading that are useful in different types of test. A crucial difference between the sharp slit and the elliptical crack models is that the former predicts no tensile stress anywhere around the crack in the absence of a tensile load normal to the crack (see above equations for Stress Intensity Factor K_I). By contrast, the elliptical crack has local tensile stresses in both uniaxial and biaxial compression.

Two useful properties of the above formulation are that the stress intensity factors for a given mode of crack propagation are additive, and that they can be related to the strain energy release rate,

$G = du_m/dc$ (U_m = mechanical energy):

Plane Stress: $G = K_I^2/E + K_{II}^2/E + K_{III}^2(1+\nu)$ 2.6

Plane Strain: $G = K_I^2(1-\nu^2)/E + K_{II}^2(1-\nu^2)/E + K_{III}^2(1+\nu)/E$

Two loading geometries of particular relevance to the development of impingement-induced microcracks are the Boussinesq field below a sharp indentor, and the Hertzian field due to a spherical indenter. The fracture mechanics formulations for the strain energy release rate, G, are (Lawn and Wilshaw 1975b):

$$G \propto \underbrace{\frac{P\,2\pi^4 H}{(1-\nu^2)(1-2\nu^2)^2\,\beta E c}}_{\text{Boussinesq}} \qquad G \propto \underbrace{\frac{P^2 k(\nu)}{E c^2}}_{\text{Hertz}}$$

where P is the applied load, H the hardness number, β a constant due to loading geometry, and $k(\nu)$ is an empirically calibrated function of ν. Solutions to the stress fields using the crack extension criterion predict the development of tensile cracks as shown in Figure 2.12.

Given these descriptions of the stress around either the elliptical or the flat crack, it is possible to deduce the failure criteria for brittle solids from Griffith's postulate that a crack will extend when the total energy change with crack length is negative or constant. The energy change is due to the release of mechanical energy U_m and the energy necessary to create new fracture surfaces, U_s. The Griffith energy balance is thus $dU = dU_m + dU_s < 0$. By definition, $-dU_m/dc = G$, the crack extension force and $dU_s/dc = 2\gamma$, the surface tension force

From which it follows that $G = 2\gamma = K^2/E$ (plane stress)

$= K^2(1-\nu^2)/E$ (plane strain)

The conventional Griffith failure criterion can thus be expressed in a fracture mechanics formulation as a critical value of the stress intensity parameter. This can be shown by substituting the expression for $K_I = \sigma_L(\pi c)^{1/2}$ into the above, which yields the classical Griffith result:

$$\sigma = (2E\gamma/\pi c)^{1/2}$$

From this, all the conventional Griffith and modified Griiffth failure criteria can be deduced (e.g. Jaeger and Cook 1979).

As mentioned above, one apparent drawback of the flat crack, fracture mechanics approach is that equation 2.5 predicts infinite stress (and strain) at the crack tip itself. In fact, this is a necessary description of the problem as formulated so far (Lawn and Wilshaw 1975a) since the actual breaking of the bonds at the crack tip violates the assumption of elasticity (in which there is no ultimate strength of a solid). The bond-breaking process should therefore be considered as an additional part of the Griffith energy balance, and this can be done by postulating the existence of a small zone ahead of the crack tip in which non-linear forces

FIGURE 2.12

Fracture planes predicted from

a) Boussinesq (sharp indenter)
c) Hertzian (spherical indenter) stress fields

FIGURE 2.13

a) Propagation of pre-existing flaw (Hori and Nemat-Nasser 1985)
b) Interaction of a row of pre-existing flaws to give shear failure (Hori and Nemat-Nasser 1985)

FIGURE 2.14

General form of the crack velocity (v) versus stress intensity factor (k) diagram. The effects of Temperature (for $T>100^0c$) and water, H_2O, are shown qualitatively. K_o = Threshold Stress Intensity Factor.
K_c^o = Critical Stress Intensity Factor.

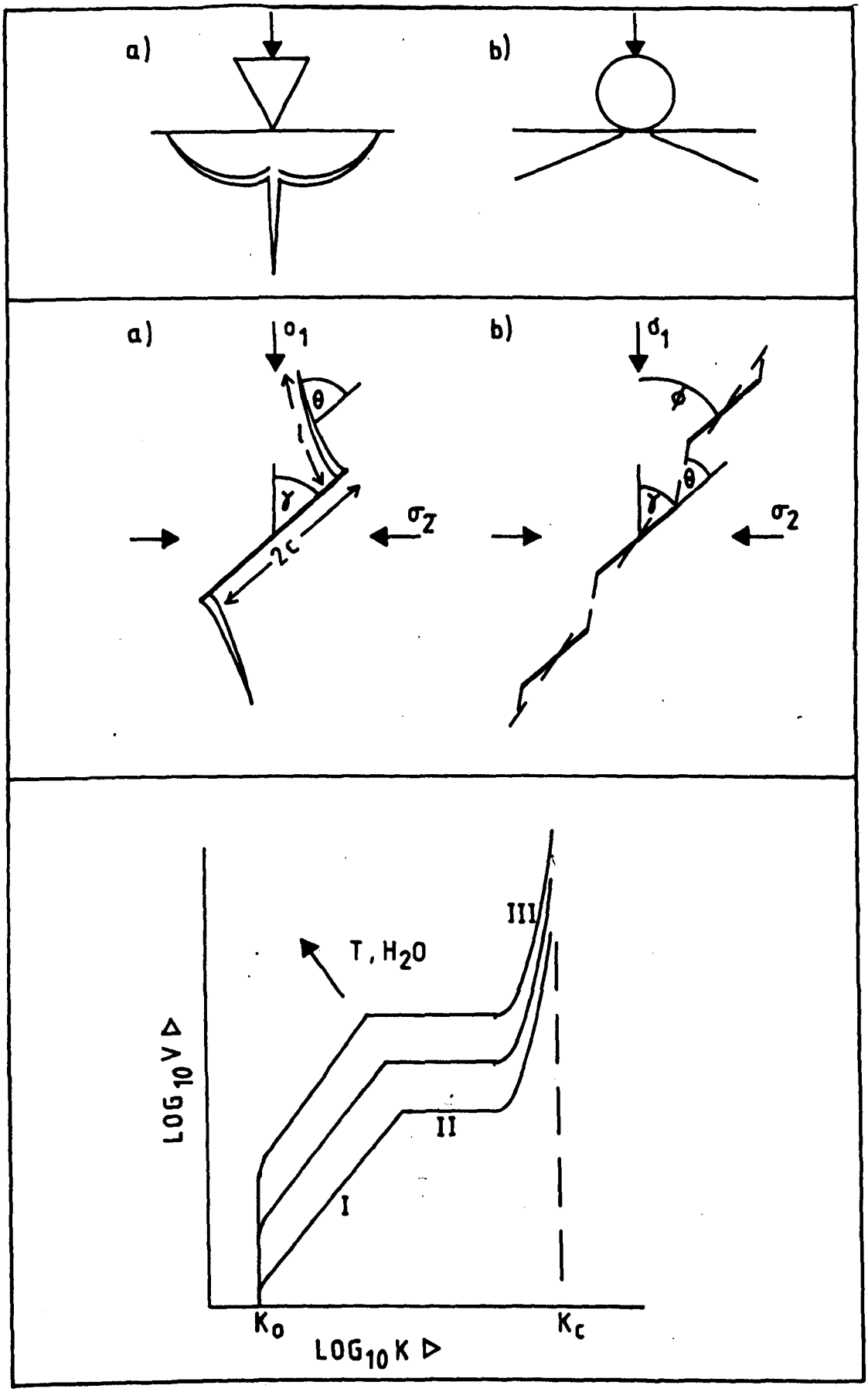
a)
b)
a)
σ_1
θ
γ
σ_2
2c
b)
σ_1
φ
θ
γ
σ_2
III
T, H_2O
II
I
$LOG_{10}V$ ▷
K_o
K_c
$LOG_{10}K$ ▷

are expended in breaking bonds. The additional energy involved is incorporated in the energy balance in the form of a new parameter Γ, the fracture toughness, to replace the surface energy term γ_0. The Energy balance condition is now:

$$G = 2\Gamma$$

This analysis is valid provided that the size of the non-linear zone is much smaller than the length of the crack i.e. it does not affect the elastic stress system as a whole: this condition or assumption is called the 'small scale zone approximation' (Lawn and Wilshaw 1975a) or small scale yielding (Rice 1968). More detailed analyses can relate the critical crack extension force to the displacement on the crack if some function of the cohesive forces ahead of the tip with distance is postulated: these are the 'cohesive force' models (see Rudnicki 1980 for basic principles). The existence of such a non-linear zone ahead of the crack tip is known experimentally from ceramics and metals, where it is referred to as a 'process zone', and more recently has been given geological reality by its detection in quartzite (Swanson 1981) and granite (Peck 1983).

In his wedge loading of Sioux Quartzite, Swanson detected acoustic emissions from in front of the propagating crack: these could be considered as the manifestation of non-linear forces in a process zone. Peck, using the double torsion test on Westerly Granite, observed the process zone as a region of greater microcrack density under the S.E.M. It was also characterised by abundant transgranular microcracks and a preferred orientation of the microcracks parallel to the main crack. The process zone was rendered visible optically by immersing specimens in water: a more permeable zone, 5-10 times the width of the zone observed in the Scanning Electron Microscope (S.E.M.) was revealed. The greater width of the zone was attributed to finer intergranular cracks not visible in the S.E.M. The size of the zone increased with water in the test environment and with crack velocity.

The fundamental understanding of shear failure derives from the experimental work outlined in 2.1.2, which indicates that shears form by interaction of Mode I fractures. A number of theories have attempted to model this interaction, with or without considering also the prior stage of individual fracture propagation. One of the earliest was that of Peng and Johnson (1972) who proposed that shear failure would occur when individual 'fibres' of intact rock, bound on either side by extension microcracks, were buckled to a critical value of 'fibre strain'. The theory gave an excellent fit to the experimental data, compared to strengths predicted by Coulomb and Modified Griffith theory, which were too high. A much more complex model was formulated in fracture mechanics terms by Costin (1983), treating both the propagation and interaction stages of microcracking. It is useful to summarise the main features of this model to illustrate the fracture mechanics approach. The assumptions, apart from those of linear elasticity, are that cracks are penny-shaped, of radius a, and initially isolated. Local tensile stresses are assumed to develop by impingement with the same orientation as the deviatoric stresses, and to be relieved as the crack grows, but the size of the tensile region also increases with load. The postulate that local tensile stresses develop in proportion to the deviatoric stresses, is a satisfactory way of overcoming the drawback of the sharp crack model that no tensile stresses are predicted in the absence of a tensile load, and receives some justification from the elliptical crack stress field solution, which suggests that tensile stress on the crack surface is proportional to the deviatoric stress (equation 2.4). The K_I stress intensity factor, combining both hydrostatic and deviatoric components for these assumptions, is:

$$K_I = 2(\pi)^{-1/2} a^{1/2} (\sigma_{kk}/z + (S_i - S_o a/d_o) F(\tau))$$

Where S_i is the tensile deviatoric stress, S_o and d_o are material properties and $F(\gamma)$ is a factor combining the proportionality of local tensile stress to remote deviatoric stress, and an orientation factor to account for a distribution of crack orientations belonging to a single set of cracks. This equation is generalised to three sets of cracks, each parallel to a principal stress plane, and gives a surface in stress representing the condition for crack growth.

Crack interaction is presumed to cause failure when cracks reach a critical length. Since less favourably orientated cracks are activated with increased stress, this also has an effect on the failure criterion, which is given as an extra stress dependent term. Finally, a constitutive equation relating stress and strain is deduced. Strain is due to elastic deformation of matrix, and opening of cracks. Change in Young's Modulus with crack length is allowed for, and crack dilation is taken to be proportional to a^3 and the local tensile stress. The model parameters are deduced from Westerly Granite data, and used to calculate theoretical stress-strain curves: the agreement with experiment is good. Time dependent aspects are also considered. The derivation of this model shows how complex a mechanistically based theory must be to account for all the variables involved.

It is the work of Hori and Nemat-Nasser (1985) that provides the most comprehensive theoretical analysis of crack growth and interaction. None of the theories of isolated crack growth so far considered have treated the problem of the progressive growth of the crack, which gave the experiments of Brace and Bombolakis such importance. However, Hori and Nemat-Nasser produce a fracture mechanics analysis and solution not only of this problem, but also of the interaction of microcracks leading to shear failure. It is apposite to summarise the treatment and results. For isolated crack growth, a flaw length 2c, orientated at γ to σ_1, is assumed to have both cohesive and frictional resistance to shear; tensile cracks

are growing from both ends with length l (Figure 2.13), making an angle θ with the flaw. With remote applied stresses σ_1 and σ_2, the stress functions are solved to give the normalised compression $\sigma_1 (\pi c)^{1/2}/K_c$ as a function of normalised crack length l/c for various values of cohesion and coefficient of friction on the flaw, for various values of σ_1/σ_2, and the relation between normalised stress intensity factor and θ and γ, and the calculated crack paths. The most important results of the analysis are that after a critical length l/c (approximately 1.0) in even the slightest tensile value of σ_2, crack growth becomes unstable (the normalised compression decreaseswith l/c). This is a plausible model for axial splitting of unconfined specimens in which radial tensile stresses of 4-8% of σ_1 are commonly induced by the mismatch in elastic properties between test specimens and machine or inserts.

In compression, crack growth is entirely stable, i.e. requires an increase in load to extend the crack. The existence of tensile stresses in both uniaxial and triaxial compression at the flaw tip has already been demonstrated by the elliptical crack stress field calculations given above; but the conventional fracture mechanics approach (flat crack model) cannot solve for the crack tip stress field. This is qualitatively as seen in experiments, in which the crack grows towards σ_1 and stabilises. The computed crack paths agree fairly well with observed profiles. The model has great flexibility: either, or both, cohesion and frictional resistance on the flaw can be set to zero, with the surprising result that a flaw with no cohesion (but friction) behaves very similarly to a cohesive flaw with no friction.

To model shear failure, the interactions between cracks in an array of parallel flaws with individual angles γ and overall angle ϕ to σ_1, and spacing d (Figure 2.13). The results show that axial compression at first increases with l/c for all values of ϕ; i.e. crack growth is stable. However, at lower values of ϕ, it drops to a minimum, indicating that the

cracks interact unstably. The stress is calculated as a function of ϕ for various values of γ: the optimum value of γ is that which gives the lowest stress, and this position on the stress vs ϕ curve also gives the optimal value of ϕ, the fault angle. The ultimate strength can be calculated as a function of flaw size and spacing for various confining pressures. Two further assumptions are necessary at this stage. Firstly, there is an inherent variety of flaw size and spacing, with a greater abundance of smaller flaws. Secondly, there are maximum and minimum flaw sizes. Both of these seem reasonable approximations of rock microstructures. This allows calculation of these parameters and the fault angle for any confining pressure. The predicted form of the ultimate strength/confining pressure curve is an initial non-linear part, in which the size of active flaws decreases with confining pressure, followed by a linear part in which the active flaws are all of the minimum size. By adjusting the parameters to fit the ultimate strength vs confining curve for Westerly Granite and Darley Dale Sandstones a very good fit can be achieved to the whole curve and reasonable models of the fault angle are also given for the same parameters. In general, the fault angle ϕ and the flaw angle γ are different, suggesting a failure plane consisting of oblique cracks linked by axial cracks. This has great similarities to the failure sequence described in Oughtisbridge Ganister (Type 1 microstructure) by Hadizadeh, in which the grain boundary cracks formed early, allowing subsequent axial cracking. It may equally well apply to type 2 microstructures in which grain boundary cracks corresponding to flaws already exist, and generate axial cracks by the mechanism described. The second part of the model, describing the interaction of a row of oblique flaws connected to axial microcracks, is relevant to any microstructure that has this feature, even if the axial cracks grew initially by other mechanisms such as impingement, or elastic or plastic mismatches. The experimental observations referred to in Section 2.2.2 suggest that such a microstructure is common to all

shear failure.

As a brief addendum, it is worth mentioning the idea of Rutter (1981) that tensile failure could, in some conditions, occur normal to σ_1 and parallel to σ_3. A sample with large anisotropies in uniaxial tensile strengths, T_1 in the direction σ_1 and T_3 in the direction σ_3 could fail in tension under four conditions (Figure 2.15). (All stresses and strengths are given as compression positive).

i) $T_3 > T_1$, Figure 2.15a. Tensile failure always occurs first normal to the weaker σ_3 direction.

ii) $T_3 < T_1$, $\sigma_1 - \sigma_3 > T_1 - T_3$, Figure 2.15b. Tensile failure again always occurs normal to σ_3 because σ_1 is not low enough to cause tensile failure in spite of the anisotropy in strength.

iii) $T_3 < T_1$, $\sigma_1 - \sigma_3 << T_1 - T_3$, Figure 2.15c. In this case, the condition for failure normal to σ_1, i.e. in the σ_3 direction, is reached before failure in the more usual σ_1 direction. Rutter has suggested that quartz veins parallel to cleavage in slates, which have high anisotropies, may form in this way.

iv) $T_3 < T_1$, $\sigma_1 - \sigma_3 < T_1 - T_3$, Figure 2.15. An additional possibility, not originally considered by Rutter, is suggested here. In this case it is possible to develop tensile failure normal to σ_1 and hybrid failure at a low angle to σ_3 simultaneously in a somewhat similar fashion to Sibson et al.'s (1975) model for contemporaneous tensile and shear failure along a fault during seismic pumping.

b) Localisation theories of cataclastic deformation. These were initiated by the work of Rudnicki and Rice (1975) who used a continuum mechanics approach to define the conditions under which an instability could develop. These were summarised and applied to structures observed in the Entrada and Navajo sandstones by Aydin and Johnson (1983). The theory is for a material deforming both elastically and inelastically with the stress/strain relation given as a function of the total strain, and

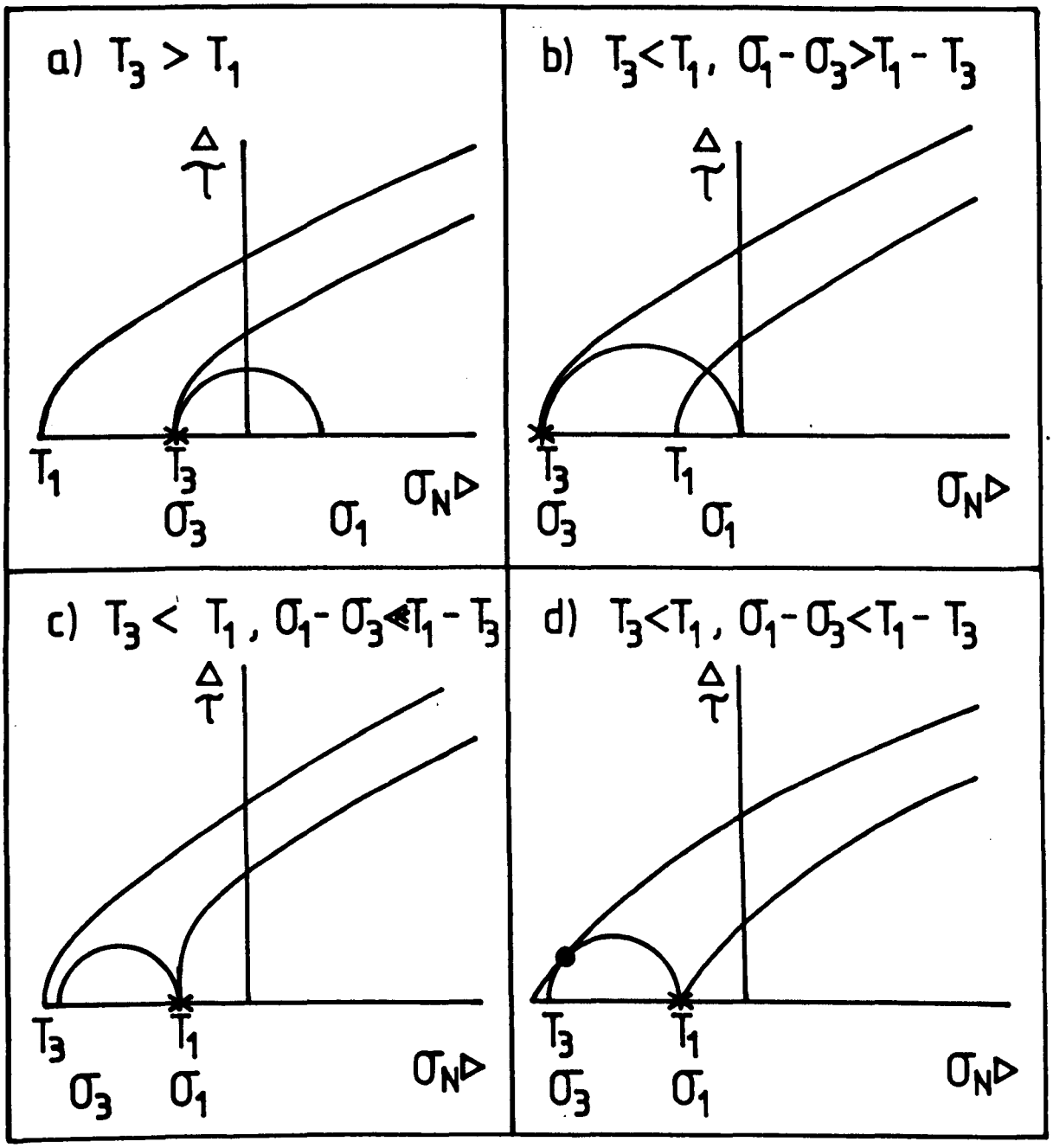

FIGURE 2.15

Conditions for Tensile Failure in samples with large anisotropies in uniaxial tensile strength, T_1 and T_3.

a) and b) Tensile Failure normal to σ_3

c) Tensile Failure normal to σ_1

d) Tensile Failure normal to σ_1 and simultaneous hybrid failure at a low angle to σ_3

× = Tensile Failure

● = Hybrid Failure

investigates whether it is possible, and under what conditions, for localisation to occur. Localisation is simply a difference in strain rate between a band and the matrix, and the importance of the theory is that it predicts that such conditions may occur depending on the following parameters:

- Dilatancy Factor (relation between volume change and inelastic shear strain).
- Inelastic Bulk Modulus (relation between volume change and change in deviatoric stress).
- Coefficient of Friction.
- Elastic Moduli (shear and bulk moduli).

At localisation, the model predicts that the plane of localisation contains σ_2 and will be orientated at less than 45^0 to σ_1: in other words, conjugate planes of localisation should form in a typical Andersonian orientation relative to the principal stresses.

A further feature of the model that is not part of conventional plastic theory is that localisation may occur in either strain hardening or strain softening. Aydin and Johnson investigate the effects of the dilatancy factor, the state of stress, and the inelastic volume change on the value of the hardening modulus at localisation (critical hardening modulus). This increases as the dilatancy factor becomes more negative, and may become positive for many states of stress with negative dilatancy factors: localisation may thus occur during strain hardening. They also show that inelastic volume change will increase the critical hardening modulus for negative dilatancy factors, and decrease it for positive dilatancy factors.

Applying these concepts to the formation of deformation bands, it is shown that, with a small negative value of dilatancy factor implied by the decrease in porosity within the bands, the critical hardening modulus at the inception of banding is likely to have been positive: the bands may

have formed at or before peak stress. Once formed, the dilatancy factor would become positive, and the inelastic bulk modulus would increase: this would lead to strain hardening within the bands and spread of deformation to other bands.

The development of slip surfaces can be understood by extension of the same model. In this case, the condition for a 'runaway instability' is sought: within the localised zone, velocities are allowed to become infinite. Stress within the inclusion becomes too great to be accommodated with the result that a discontinuity develops. The process is similar to the unloading of a 'soft' testing machine (equivalent to the elastic strain in the rock matrix) into a stiff triaxial specimen of catastrophic failure.

Conditions for instability in a homogeneously deforming medium were also investigated by Latham (1985a & b). The elastic-plastic rheology in this model differs from that of Aydin and Johnson in that only strain hardening is allowed, the material is incompressible, and consists of multilayers of different elastic and plastic properties, across which the interfaces are coherent. Plane strain boundary conditions are imposed. The plastic component is defined by hardening exponent m relating the strain energy density to the strain, and is also approximately equal to the ratio of two moduli M and L which are proportional to the shear and bulk modulus respectively. The analysis by Latham follows that of Biot (1965) with the inclusion of a bending resistance term. It proceeds by solving differential equations for the function ϕ defining the displacement field, where ϕ is given as a function of $x \pm \xi y$. The parameter ξ ("characteristic") thus describes directions of lines parallel to which simple shear (non-uniform displacement fields) may occur. It emerges that two types of instability are possible: **first kind instability**, which in the absence of bending resistance, has a dominant characteristic direction 0^0, can be interpreted as the formation of buckles, and **second kind instability**, with a dominant characteristic direction of $0\text{-}45^0$, interpreted

as the formation of kink bands or localised shearing. The theory investigates the effect of the two moduli M and L, the stress and the fractional thickness of each type of layer on the type of instability. The importance of Latham's 1985a contribution is that introducing the bending resistance term indicates that the two types of instability are not separated by the simple criterion M/L=0.5 as in the Biot analysis, but by a function which includes terms related to the makeup of the multilayer as well as the properties of its constituent layers. It is thus possible to have a smooth transition between the first and second kind instabilities, with buckling and oblique localised shearing as the end members, depending on the variables above.

Latham summarises the effects of these variables by referring to the ratio M/L as the **induced** anisotropy (also equal to m, the degree of non-linearity in the power law), and the contrast in properties between layers as the **intrinsic** anistropy. To make a very superficial summary, high intrinsic anisotropies favour active over passive internal buckling and kinking over shearing. High induced anisotropies favour shearing over passive buckling and kinking over active buckling. The importance of this work to cataclasis lies in the suggestion that as in the Rudnicki and Rice model, faulting is a possible interpretation of the response of a rock mass to the development of an instability or 'localisation': a discontinuity in the strain field. The Latham model suggests that such a second kind instability will occur in preference to buckling in conditions of low intrinsic anisotropy (low contrast in properties between layers, and few layers) and high induced anisotropy (highly non linear plastic behaviour). The Rudnicki and Rice criterion for localisation is in fact the same as the condition for Biots' second kind instability, when plane strain incompressible materials are considered.

The value of these insights is tempered by some difficulties in geological interpretation. Firstly, the model deals only with the

conditions of inception of the instability: nothing is predicted about their development with strain, though this may be less of a drawback for faulting than buckling or kinking. The model thus does not account, for example, for the formation of deformation zones. There are also several difficulties in matching the material properties of the model with known rock rheologies. The highly non-linear behaviour is not characteristic of low temperature deformation, but Latham has suggested that pressure-sensitive mechanisms such as microcracking and frictional sliding may be adequate physical processes. Two serious weaknesses of the model, compared to that of Rudnicki and Rice and Aydin and Johnson, are the lack of the possibility of strain softening, and especially important for the porous rocks of the latter study, the assumption of incompressibility. Finally, one prediction of the model which seems particularly irreconcilable with the field and laboratory evidence, is the formation of shear surfaces at angles of 45^{o} or more to the shortening direction for a range of induced anisotropies between 0.5 and 0.1 (Latham 1985a, Fig.11) and low bending coefficients. Acute angles of shear are however predicted for smaller anisotropies, and high bending coefficients.

Both the 'localisation' theories of cataclasis are important because they focus attention on the effects of material properties on faulting and the microstructural processes which may cause them. Microstructural observations from naturally deformed cataclastic rocks are needed to complement the experimental observations to render these models more realistic.

c) Minimum Work Theories. These are described by Reches (1983) as 'slip models', and have been proposed by Oertel; (1965), Reches (1978), and Reches (1983). All these theories have two parts in common: firstly, it is shown that multiple sets of faults can accommodate a general strain as the sole deformation mechanism, by analogy with the theory first established for slip systems in crystal plasticity (Taylor 1938). The assumption of

constant volume is implicit in the restriction of deformation mechanism to fault slip. In the second part, an expression for the resistance to slip on an individual fault plane is assumed. This is transformed into a relationship between principal stresses for slip, known as a 'slip criterion'. The stresses and orientations of faults which will move to satisfy the criterion of minimum work or work rate can then be evaluated. The major differences between the three basic models (due to Oertel (1965), Reches (1978) and Reches (1983)) lie in the expression for resistance to slip chosen in the second part of the analysis. The conditions for the accommodation of strain by faulting in the first part are identical in all theories: they are next summarised following and expanding on Reches (1978).

The general deformation tensor D for three dimensional infinitesimal strain is

$$\begin{bmatrix} D_{11} & D_{12} & D_{13} \\ D_{21} & D_{22} & D_{23} \\ D_{31} & D_{32} & D_{33} \end{bmatrix} = \begin{bmatrix} E_{11} & E_{12} & E_{13} \\ E_{21} & E_{22} & E_{23} \\ E_{31} & E_{32} & E_{33} \end{bmatrix} + \begin{bmatrix} 0 & -R_{12} & R_{13} \\ R_{12} & 0 & -R_{23} \\ -R_{13} & R_{23} & 0 \end{bmatrix}$$

$$D_{ij} \qquad E_{ij} \qquad R_{ij}$$

This asymmetric second-order tensor is divided into a symmetric part, reprsenting a strain (E) and a skew-symmetric part, defining a rigid body rotation (R). The number of independent components of D depends on the strain state. A completely general strain requires all nine components for specification. At constant volume $E_{11} = -(E_{22}+E_{33})$, so there are only 8 independent components (5 strains, 3 rotations). If the boundary conditions do not impose any rotational constraints, there are only 5 independent (strain) components in the deformation matrix.

The total deformation due to simple shear on a number of slip systems is simply the sum of the contributions of each system. The minimum number of slip systems required to solve for the slip in each is equal to the number of independent components of the deformation tensor specified (Reches 1978). On a large scale, shear on a number of parallel faults

results in homogeneous simple shear in the same way that homogeneous strain results from the glide of dislocations. Due to the choice of co-ordinate system, a single slip direction on a fault plane is resolved into two perpendicular components in each of two slip systems. Each fault set therefore represents two slip systems.

From the above it is possible to deduce the minimum number of slip systems (S), and therefore fault planes (F) required to accommodate various specifications of strain. The relationship can be expressed as

$F = S/2$ for even values of S

$F = S/2+1$ for odd values of S

The value of F and S for various specifications of strain are shown in Table 2.2.

Oertel's theory was developed to explain his observations that four families of faults formed during experimental deformation of clay. As Table 2.2. shows, this is the minimum sufficient number to accommodate a general irrotational, constant-volume strain. The analysis is for a viscous fluid, and therefore uses strain and work rates rather than strains and work in Reches' approach. In the second part of the analysis, the stress required for fault movement is factorised into frictional, viscous drag and 'interference' components. The latter arises because two slip systems generally interfere with each other: the slip systems can act without interference only if they intersect in the movement direction of one of them. The total work rate is the sum of the frictional, viscous and interference work rates; this is minimised with respect to slip.

The solution implies that faults will not form in the directions of maximum resolved shear stress due to the anisotropy introduced by their mutual interference, the size of which depends on the magnitude of the relative contributions of the frictional, viscous and interference work rates. The dominance of the latter term explains why the minimum number of possible fault families forms: it minimises the total work rate. Oertel was

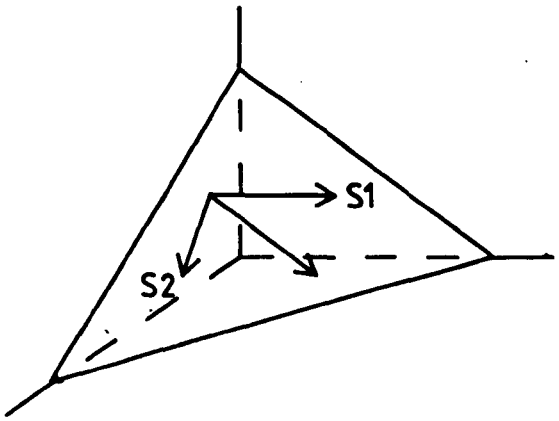

$F = S/2$ for even S

$F = S/2 + 1$ for odd S

STRAIN		ROTATION		DEFORMATION	SLIPSTMS.	FAULTS
State Specified	E	Value Specified	R	D = E + R	S	F
General	6	√	3	9	9	5
General	6	×	0	6	6	3
Constant Volume	5	√	3	8	8	4
Constant Volume	5	×	0	5	5	3

TABLE 2.2

Number of Slip Systems (S) and Faults (F) required for various specifications of the deformation tensor (D) in terms of strain components (E) and rotations (R).

able to calculate the three contributions to the shearing stress for his experiments: the results confirm the importance of the interference term, and the theory is matched well to the results.

In Reches' early work, an elastic analysis is used with the simple slip condition that shear stress must be constant, and work done (or 'dissipation'), calculated by shear stress multiplied by strain, is minimised. The orientation of such faults for various states of strain are calculated: these are symmetrical about the principal strain axes. Four sets of faults with orthorhombic symmetry about the principal strain axes and equal shear strains are predicted for a general state of strain: only for values of $k(=E_2/E_1)$ $\pm\infty$, -1 or 0, i.e. plane strain, are two sets of faults given.

Subsequently, Reches (1983) introduces the more sophisticated slip condition that shear stress on the fault is equal to a cohesive term and a frictional term dependent on the normal stress. The resulting slip criterion (relationship between the stresses necessary to accommodate a given strain) is distinguished from a failure criterion, which is the stress relationship necessary for fault initiation. This distinction is not made in Oertel's work because of the fluid properties assumed, which allow an infinite number of slip systems to be active before faulting occurs. For a strict interpretation of the Reches model, it is therefore necessary to assume that fault systems in appropriate orientations already exist within the deforming body. It can be pointed out that although the assumed form of the resistance to slip is identical to the Coulomb law, the constants are for a pre-existing fault and not for the Coulomb failure criterion: the two differ most fundamentally in the inclusion of the strain ratio in the former. In an addition to the earlier analysis, Reches (1983) calculates the stress ratio which minimises the stress difference and that which minimises the dissipation, as well as those which minimises the elastic strain energy of distortion, for various states of

strain. The results showed that all three are minimised at the same stress ratio in the presence of a small confining pressure. This stress ratio was either $\sigma_1=\sigma_2$ for $E_{11}>>E_{22}$ or $\sigma_2=\sigma_3$ for $0>E_{11}/E_{22}>-0.5$.
The orientations of these 'preferred faults' which minimised the dissipation and stress difference, are calculated as a function of the coefficient of friction and the strain ratio. Finally, in a companion paper with Dietrich, Reches carried out some truly triaxial experiments in which some observed fault orientations correlated with the experimental strains in the way predicted by the theory, and all predicted and observed stress levels agreed well. Field examples of multiple fault sets were also quoted.

The three minimum work theories described consider constant volume irrotational strain, and predict the formation of four faults with orthorhombic symmetry about the principal strain (and stress) axes. The first part of the theory points out that general strains may be accommodated by faulting and represents a new approach to the subject. Multiple fracture sets are often observed in the field, where, following the early approaches of Stearns (1964), Price (1966) and others, they are interpreted as successive generations of conventional Andersonian conjugate or extension fractures. However, the frequent difficulty of unambiguous dating is a serious problem in such schemes, which is resolved entirely in the minimum work theories which suggest that multiple shear fractures may operate simultaneously to accommodate general strains.

2.3.2 Time Dependent Theories

Traditionally, time dependent aspects of cataclasis have fallen into the study of creep behaviour, but recently with the application of fracture mechanics, both theory and experiment have concentrated on the area of stress corrosion, sub-critical or slow crack growth. It is a natural speculation that both are the same phenomenon. Traditional creep laws,

which are simply empirical fitsto experimental data, are not considered here (for reviews see Cruden (1971), Carter and Kirby (1978), Carter et al (1981)).

a) Creep Theories. One of the first creep theories as opposed to the descriptions of creep referred to above, was due to Scholz (1968). The essence of the theory is that creep is due to microfractures, which is supported by observation. This is also the basis of all subsequent theory and data interpretation. The model assumes that local stresses are inhomogeneous and described by a probability density function which is itself a function of the mean stress. Failure occurs on small regions at a critical value of local stress. The time to failure, allowing for slow crack growth, is described by an exponential function of stress and given an Arrhenius temperature dependence. Additional assumptions are that failure of each region contributes a constant strain, that each region acts independently, and that it fails once only, implying that the number of failures decreases exponentially with time. The final creep law has the form

$$\Delta = A\,\sigma^{-n}\,\log t$$

where Δ is the volumetric strain, A incorporates the exponential dependence of slow crack growth on stress, the strain contributed by each individual region, and the form of the stress distribution, and t is time. This logarithmic expression is a familiar form of creep law for transient creep, and Scholtz in fact developed the theory by allowing each failure to contribute an increasing amount of strain with time, and made the suggestion that secondary creep could be explained by the model if successive episodes of fracture were allowed. Cruden (1971), using data from 48 creep experiments has shown that the power-law formulation for the creep rate-time relationship isasignificantly better fit than the alternative exponential law. The Scholz logarithmic creep law deduced above can be derived from such a power-law formulation when the time

exponent is -1. Kranz (1979a) criticises Scholtz's theory for the postulate of single episodes of failure in independent regions. Tertiary creep is considered to occur when microcracks begin to interact.

Cruden's (1971, 1974) theories of creep developed along similar lines: creep displacement was considered to be due to propagation of microcracks which initially grow slowly to a critical length. The decrease in strain rate with time is a consequence of the reduction in number of growing sub-critical cracks as they become stabilised in the axial orientation. Tertiary creep is likewise considered to be due to crack interaction, which occurs at a critical crack density. If each microcrack contributes the same amount of strain, then the onset of tertiary creep at the critical crack density should occur at constant strain for a given initial crack length distribution. In this theory, the strain has a power-law relationship to time of the form

$$E = A\,\sigma^{n}\,t^{B}$$

It is shown that the stress dependence of strain rate is well described by the above law for experimental data. A further assumption, that time to onset of tertiary creep is a constant proportion of time to failure, is necessary to match the data (which give time to failure) with the theory, which strictly gives only time to the onset of tertiary creep.

b) Subcritical crack growth. This has recently been studied intensively by experiment in theory and given geological interpretations (e.g. Anderson and Grew 1977, Das and Scholz 1981, Atkinson 1982, Meredith 1983). An appropriate way in which to begin a brief summary of the relevant results is the crack velocity versus stress intensity factor diagram (V-K_I) which is shown in a generalised form in Figure 2.14. This diagram is deduced from experiments in which the velocity of a mode I crack is measured at various stress intensities (K_I), and applies to a range of geological materials (quartz, granite, andesite, basalt, calcite, oil shale, and sapphire) as well as glass. The relationship falls into three

parts:

REGION I. Velocity is highly sensitive to K_I, water concentration and temperature. K_0 is the threshold stress intensity factor required for any crack growth; crack growth at extremely slow rates in Novaculite (Atkinson 1980) have caused speculation that no such limit may exist although theoretical calculations by Atkinson (in Meredith,1983) suggest a value of $K_0 = 0.2\ K_{Ic}$ in quartz.

REGION II. Velocity is dependent on water concentration&temperature but not K_I.

REGION III. Velocity increases extremely rapidly with K_I until at the critical stress intensity factor K_{Ic}, the crack growth becomes dynamic.

Almost all experiments have been carried out in Region I, but a comprehensive theory to explain subcritical crack growth should account for the entire shape of the curve. Five mechanisms of sub-critical crack growth have been proposed: stress corrosion, dissolution, diffusion, ion exchange and microplasticity (Meredith 1983). Although there is evidence for all processes in various materials under different conditions, stress corrosion, a general term for environmentally influenced, stress driven, thermally activated, chemical reaction allowing breakage of bonds, is considered to be the dominant mechanism for geological materials in upper crustal conditions. Details of the chemical reaction involved have been studied experimentally leading to the conclusion that hydrolysis of the Si-O-Si bond is probably responsible for the weakening. This process has been modelled theoretically by Wiederhorn and Bolz (1970) to give the following expression for reaction rate V:

$$V=V_0 \exp (-Q + \beta K_I)/RT$$

where V_0 is a constant, Q is the activation enthalpy for the reaction, and β is a constant incorporating the activation volume. The reaction rate is therefore assumed to control the crack velocity, and this exponential law gives a perfectly adequate fit to the data in Region I of the V-K_I diagram.

However, it does not satisfactorily account for region II or III behaviour.

Lawn and Wilshaw (1975a) allow for an additional process, the transport of reactive species to the crack tip. Crack velocity is rate controlled in this model by the slower of the two processes, transport or reaction. For the former, the crack velocity V_t is given by:

$$V_t = ubP/NM\ (2\pi m\ kT)^{1/2}$$

where U is an attenuation factor decreasing with crack length, b is lattice spacing normal to the crack, P is the vapour pressure, N is the number of molecules reacting with one bond, M is the surface density of cracked bonds, and m is the molecular mass. The important feature of this expression is that there is no dependence on the stress intensity factor: it can therefore model Region III of the V-K_I curve.

The reaction-rate controlled crack velocity is given by, in simplified form:

$$V_r = C(P)^{N/2} \exp\ (-Q+\beta\ K_I^2)/RT$$

where C and β_1 are constants. This formulation is very similar to the Weiderhorn and Bolz equation, and can also fit the Region I data well. Alternative theories for the V-K_I curve have been proposed by Thompson (1980), in which evaporation of atoms from crack surfaces and tips is responsible for stress corrosion, and by Brown (1979), who proposed a model based on steady state multibarrier kinetics.

The success of the two-stage Lawn and Wilshaw model has led to its use in the standard interpretation of V-K_I curves: Region I is considered to be reaction-rate controlled, and Region II to be transport-rate controlled. The processes occurring in Region III are thermally activated, and unlike Regions I or II, unaffected by water concentration in glass/water systems, but affected by the liquid in which the water is dissolved (Meredith 1983). Weiderhorn and Bolz (1970) suggests that the activation volume at the crack tip may be important, and Atkinson and Meredith (1981) suggest that the chemical environment controlling crack growth is determined by the inherent

chemistry of the cracked material.

Although the Lawn and Wilshaw model gives a good account of the V-K_I curve, the earliest mathematical description was given by Charles (1958) in the form of a power law, and continues to be used more widely than the exponential form of the former model. The Charles Law can be simplified to;

$$V = V_o \exp(-Q/RT)\, K_I^n$$

where V_o and n are constants; n is the subcritical crack growth or stress corrosion index. Atkinson (1982) points out that the experimental data has such large scatter that either exponential or power law formulations provide equally good fits; but Meredith (1983) shows that data for alumina and soda-lime glass are fitted significantly better by a power-law. There are two other major advantages in the power-law formulation, besides its more widespread use: firstly, it can describe all three regions of the V-K_I curve with appropriate modifications of the parameters, and secondly, it has a similar form to the power-law creep-rate equations, shown by Cruden to be better than exponential equations.

Some attempts have been made to use the fracture mechanics and stress corrosion approaches to modelling crustal processes. One of the best but largely unaccredited is due to Rudnicki (1980). After outlining the fundamentals of fracture mechanics as in 2.3.1.5, he introduces the J-integral (due to Rice, 1968) which is simply a method of calculating the crack extension force allowing for a finite size of non-linearity ahead of the propagating crack. For a small scale yielding (small process zone), the J-integral is equal to the crack extension force as previously defined. It can also deal with time dependent effects, but so far such a development has yet to be applied in a geological situation. This is a potentially powerful modification to fracture mechanics, because it can characterise systems with a large process zone that defy the basic assumptions of the simple fracture mechanics theory, and which may apply in the earth's crust

and even in laboratory testing of materials with large grain sizes (Swanson 1981).

The size of the non-linear zone, R, can be evaluated from

$$R = 9/16\ \pi\ \mu\ \sigma'\ [\Delta\sigma\ (1-\nu)]^{-1}$$

where μ is the coefficient of friction, σ' is the displacement, $\Delta\sigma$ is the stress drop, and ν Poisson's ratio. For representative crustal values of $\mu=2x10_4$MPa, $\nu=0.3$, and $\Delta=10$MPa, this simplifies to

$$R = 4.42 \times 10^3 \times \sigma'$$

Estimates of R of between 1 and 100mm are derived from experimental data, and it is suggested that large faults may have very large values for the process zone. Rudniki also compiles values of the critical crack extension force for seismic faulting: these give results varying from 1 to $10^8 Jm^{-2}$, but generally greatly exceed those from laboratory measurements.

This paper also contains an application of fracture mechanics in earthquake faulting which heralds the important model of Das and Scholz (1981). Time-dependent effects are considered to be due to a visco-elastic rheology in which the compliance (M_∞) over long times is much greater than the instantaneous elastic compliance (M_0). From equation 2.6, the value of the stress intensity factor for seismic movement K_c is:

$$K_c = (G_c/M_0)^{1/2}$$

where G_c is the critical crack extension force, while for aseismic fault creep, K is K_S:

$$K_S = (G_c/M_\infty)^{1/2}$$

Three conditions can be envisaged:

1. $K < K_0$: no faulting
2. $K_0 < K < K_c$: seismic creep
3. $K = K_c$: seismic faulting

The use of long- and short-term values of M is exactly equivalent to the use of threshold and critical values in sub-critical crack growth; indeed, subcritical crack growth is a very reasonable interpretation of the viscous part of the rheology, as made explicit below. The paper also derives an energy release equation from fracture mechanics and considers rather superficially the effect of fluids. The more comprehensive theory of Das and Scholz (1981) explains many features of earthquake faults by treating them as subcritically propagating Mode II and III cracks. The theory extends Rudnicki's approach by dividing the deformation into a nucleation and stopping phase. This means that in addition to the stress intensity factors of K_0 and K_c which are the usual threshold and critical values respectively, K_D, K_s, are defined as the dynamic, and static values. After nucleation, the rupture continues with dynamic stress intensity factor K_D until reaching a barrier. Five possible scenarios are envisaged:

1. $K_s<K_0$. The earthquake stops finally.
2. $K_D<K_c<K_s$. The earthquake stops, propagates critically through the barrier, and restarts, giving a multiple event with a short delay time.
3. $K_0<K_s<K_c$. The earthquake stops, propagates through the barrier subcritically, and restarts, generating a delayed multiple event.
4. $K_0<K_s<K_c$, with K_s changing to a value less than K_0. In this case, the barrier increases in strength; subcritical propagation begins and then stops, giving post-seismic rupture growth.
5. $K_0<K<K_c$. The earthquake stops, but locally growth occurs through barriers to generate aftershocks.

The mathematical analysis takes the definition of stress intensity factor

$$K = Y\Delta\tau(C)^{1/2}$$

with Y a constant for loading geometry, $\Delta\tau$ the stress drop and c the crack radius, and combines it with the Charles Law description of the V-K_I curve:

$$K = K_0 (C/C_0)^{1/n}$$

where K_0 and C_0 are the values of K and crack velocity (C) at time t=0 as the crack nucleates. Meredith (1983) points out that it is reasonable to extrapolate the V-K_I curve law to shear mode cracks since the process of stress corrosion should be the same in both cases. Results of the analysis show that the predicted precursory creep curve agrees well with observations showing a very steep increase immediately prior to failure, and that data from a pair of delayed multiple events, when used to calculate a stress corrosion index, give a result within a factor of 2 of the Atkinson (1979) value for quartz in water.

Other theoretical uses of stress corrosion theory have been made in the fields of magmatic intrusion, hydrofracture propagation for both in-situ stress measurements and geothermal reservoir engineering, and lunar seismicity (e.g. Anderson and Grew 1977, Atkinson 1982).

2.4 A REVIEW OF THE CONCEPTS AND DEFINITIONS OF BRITTLENESS, DUCTILITY, THE BRITTLE-DUCTILE TRANSITION AND CATACLASTIC FLOW

Even a cursory inspection of geological literature reveals that the words of the title have been subjected to a bewildering variety of definitions, and very often used without any clear definition at all, although they are some of the most frequently applied terms in rock deformation. This confusion can be traced to the dichotomy between laboratory (and materials science) - based and field-based approaches to deformation: unfortunately, this is a difficult gap which is not often successfully bridged. The problem falls into three areas; the question of defining "brittle," "semi-brittle," and "ductile," the definition of the "brittle-ductile transition", which may be used in a unique sense without

reference to the previous terms, and, lastly, definitions of "cataclastic flow". This offers a brief review of some of the more common definitions that have been used, and concludes with some suggestions for standardising the use of these terms. That the problem is not merely one of semantics emerges from the insight that an important aspect of rock deformation is being widely overlooked through the restrictions imposed by the use of these words.

2.4.1 The Description of Deformation

Some generally accepted definitions of other fundamental material properties are now given to provide a basis on which to proceed. Five aspects of deformation must be clearly distinguished, and depend on scale. Scale can loosely be defined as macro (greater than outcrop, i.e. >10m), meso (outcrop, i.e. 1cm-10m) or micro (miscroscopic, i.e. <1cm).

a) Deformation Mechanism. The mechanism by which strain is accommodated at a microscopic scale. This is the most fundamental aspect of a rock's behaviour because ultimately deformation on all scales must involve a microstructural mechanism. There are three classes of **deformation mechanisms: cataclasis, intracystalline plasticity, and diffusive mass transfer. Cataclasis** is deformation by fracturing and sliding. **Intracrystalline plasticity** is deformation by movements of dislocations (glide and climb). **Diffusive mass transfer** is deformation by diffusion of vacancies, atoms, molecules or ions in the solid, liquid, dissolved or gas phases. Deformation Mechanisms have also been classified into **elastico-frictional** (cataclastic) or **quasi-plastic** (crystal plasticity and diffusive mass transfer) by Sibson (1977). These mechanisms can occur in any combination and in general different mechanisms will dominate throughout the tectonic history of the rock.

b) Deformation State. A complete specification of deformation includes the three elements of translation, distortion or strain, and

rotation. At some scale, all strain is heterogeneous; however, it is often useful to consider deformation as homogeneous. Therefore, strain can be described as localised, discrete, non-pervasive, heterogeneous, or non-localised, pervasive or homogeneous, provided that the scale is specified.

Heterogeneous deformation can be subdivided into continuous or discontinuous deformation. Since all deformation except pure elasticity is discontinuous at some scale, continuity is also a highly scale-sensitive description, but one to which great significance has been attached for interpreting field observations in terms of deformation mechanisms. An example of continuous, heterogeneous deformation is the "ductile" shear zone.

c) Strain Rate Distribution. All the above descriptions may be applied to the spatial variation of strain rates. The relation between deformation and strain-rate distribution must be clarified. A discontinuous deformation necessarily implies a discontinuous strain rate distribution (velocity field). However, it is possible to have a discontinuous strain rate distribution, with continuous deformation. As an example, although a fault is often defined in terms of a discontinuous displacement field, the theories of Ode (1960) ("Faulting as a velocity discontinuity in plastic deformation"), Rudnicki and Rice (1975) see faulting as a **velocity** discontinuity without necessarily the additional **displacement** discontinuity.

d) Stress-Strain Relationship. A good range of well defined words exists to describe nearly every possible aspect of the relationship between stress (σ) and strain (ε). (Unless otherwise noted, stress will be taken as both mean and deviatoric, and strain both bulk and shear).

Elastic - Linear σ-ε relationship.

Plastic (Inelastic) - Non-linear σ-ε relationship.

Dilatancy - Difference between elastic and inelastic volumetric

strain.

Failure - Sudden drop in stress.

Peak or Ultimate Strength - Maximum differential stress at failure.

Residual Strength - Differential stress after failure.

Yield - Abrupt decrease in gradient of σ-ε relationship.

Work of Strain Hardening or Softening - Positive or negative gradient respectively of σ-ε relationship in the post-failure or post-yield part of the curve.

Coefficient of Work Hardening or Softening - The numerical value of the gradient, $d\sigma/d\varepsilon$.

Stick-Slip - Oscillations in σ-ε relationship.

e) Strain time (ε-t): Relationship. Stable ε-t relationships can be contrasted with unstable or episodic ε-t relationships. The shape of a strain-time (ε-t) curve, as produced in a creep experiment, also has a number of qualifying terms.

Instantaneous Elastic Strain - Immediate, recoverable strain.

Instantaneous Plastic Strain - Immediate, non-recoverable strain.

Transient or Primary Creep - Non linear ε-t relationship with negative second derivative, $d^2\varepsilon/dt^2$

Steady-state or Secondary Creep - Linear ε-t relatioship.

Accelerating or Transient Creep - Non-linear ε-t relationship with positive second derivative.

Seismic Strain Rate - Strain rate $\dot{\varepsilon}>10s^{-1}$.

Aseismic Strain Rate or Creep - Strain rate $\dot{\varepsilon}<10s^{-1}$.

These five aspects of deformation are quite independent; a part of the problem of defining brittle and ductile can be traced to the confusion caused by using one word to describe more than one different aspect of deformation with the implication that they are inevitably linked; one such prejudice is that a cataclastic deformation **mechanism** implies a localised deformation **distribution** on all scales; both are commonly referred to as

brittle behaviour.

f) Mode of failure. Rutter (1986) has greatly clarified the description of deformation by introducing the concept of 'modes of failure'. A mode of failure is a description of both the deformation mechanism and the strain distribution. Deformation mechanisms are, for simplicity, divided into two types: pressure sensitive mechanisms or cataclasis, and pressure insensitive mechanisms, including crystal plasticity and diffusive mass transfer, which are referred to loosely as plastic mechanisms. Strain distribution is either localised or non localised: a scale must be specified. From the pairs of deformation mechanisms and strain patterns, a mode of failure diagram is presented in the form of a 2x2 matrix (Figure 2.16).

2.4.2 Definitions of Brittleness and Ductility

Definitions of "brittle" can be sorted into three classes:

a) Brittle as a deformation mechanism (Lawn and Wilshaw 1975a, Logan 1978).

b) Brittle as a stress-strain relationship (Price 1966, Mogi 1972a, Heard 1960, Griggs and Handin 1960).

c) Brittle as a description of strain distribution (Hobbs, Means and Williams 1976).

a) By Deformation Mechanisms. The most comprehensive definition of brittle in terms of deformation mechanisms is given by Lawn and Wilshaw. "Brittle" is defined as deformation by fracture,and solids are classified according to their fracture mechanism: the brittleness of a solid depends on the degree of intracrystalline plasticity accompanying the fracture. The various classes are characterised by the ratio of Fracture Toughness Γ, to surface energy, γ, and by the numerical value of Γ. This is a precise classification, being at the same time easily quantified and measured, and based on a sound theoretical analysis. Note that ductile is

FIGURE 2.16
Rutter's Classification of Modes of Failure

FIGURE 2.17
Type A and Type B Failure in Rocks, after Mogi (1972a 1974). Curves 1-4 are differential stress ($\Delta\sigma$) vs. strain curves at increasing confining pressure. In type A, there is a significant amount of permanent strain before fracture. Therefore a curve such as 3 may be defined as ductile behaviour based on a pre-failure strain criterion, but brittle by the criterion of stress drop after failure. The two criteria coincide for Type B behaviour. Most materials have a component of both types of behaviour.

FIGURE 2.18
The Upper Transition in failure, after Rutter (1986). This occurs at the point when differential stress is no longer pressure-sensitive. The conventional Byerlee brittle-ductile transition occurs at the confining pressure given by the intersection of the frictional sliding/cataclastic faulting curves.

DEFORMATION MECHANISM	STRAIN DISTRIBUTION: LOCALISED	STRAIN DISTRIBUTION: PERVASIVE
CATACLASIS	Cataclastic Faulting	Cataclastic Flow
PLASTIC	Plastic Shear Zone	Homogenous Plastic Flow

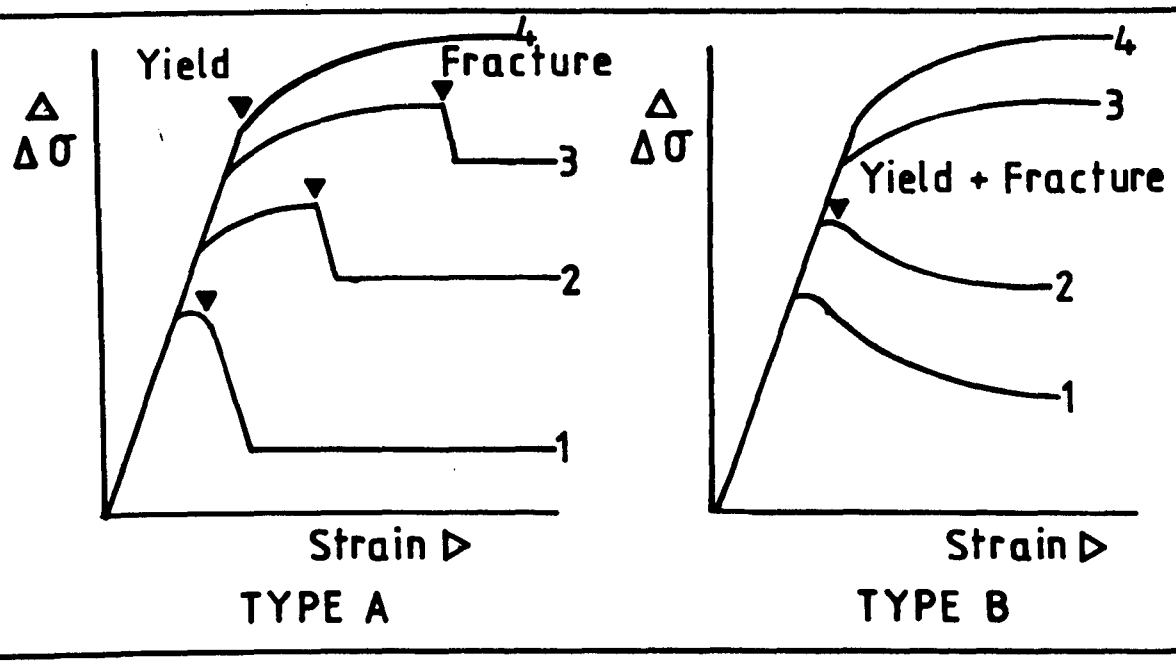

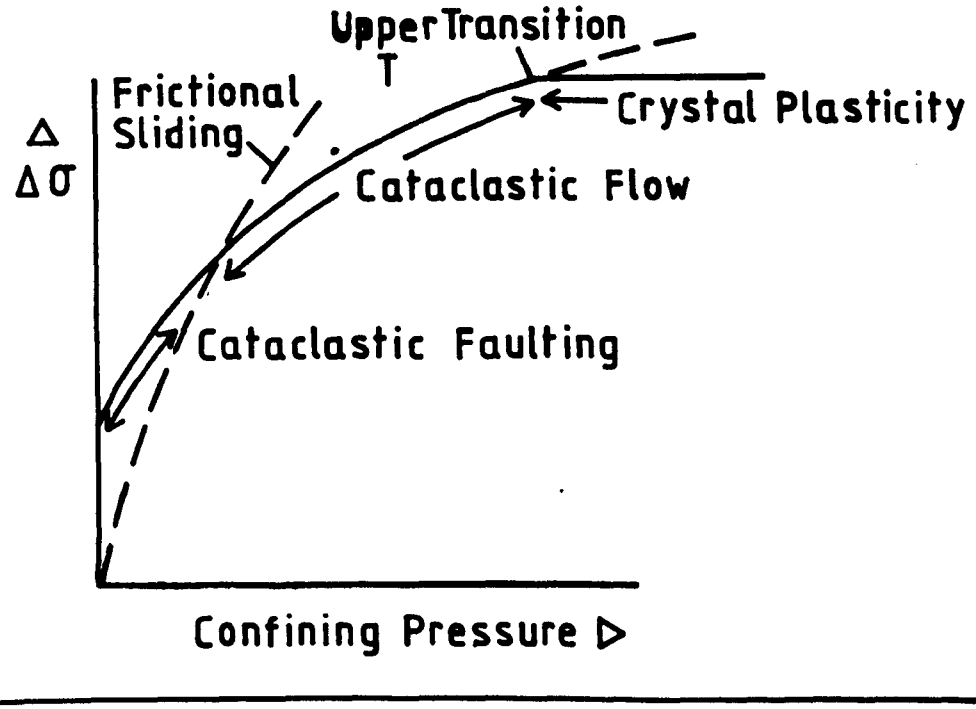

not used to mean the opposite of brittle. Although this treatment is perhaps too fundamental for widespread geological application, the basic concept can be applied successfully, e.g. Logan 1979. Brittle phenomena are: "a number of processes that are dominated by fracture as a mechanism or are controlled by the pre sence of preexisting fractures". Carter and Kirby (1978) used this approach to restrict the definition of "semi-brittle" to the combination of fracturing and intracrystalline plasticity.

b) By Stress-Strain Relationship. Brittle as a description of a rock's stress-strain relationship has been used by Price (1966), who defined brittle as linear stress-strain up to failure, semi-brittle as some non-linear behaviour up to failure, and ductile as non-linear behaviour without failure. The terms thus become synonymous with elastic and plastic (as defined above). An alternative of application of the terms to the description of the stress-strain relationship was proposed by Heard (1960) and adopted by Mogi (1972a). In brittle behaviour, the maximum permanent (non elastic) strain before failure is less than 3%; "transitional" between 3% and 5%, and ductile, over 5%. Paterson (1978) substitutes "fracture" for failure in the same definition. Griggs and Handin (1960) also adopt this definition for relative ductility: "the amount of permanent deformation achievable prior to rupture." They make the further point that "Nothing is implied about the actual mechanism involved". In all these definitions, ductile is clearly considered as the antithesis of brittle. In yet a third description of the stress-strain relationship, Byerlee (1968), followed by Rutter, defines brittle behaviour as the decrease of strength after faulting and ductile behaviour as no loss of compressive strength.

c) By Deformation State. The use of deformation state in the definitions of brittle and ductile is made explicit by Hobbs, Means and Williams (1976) and remains implicit in the application of the terms by

many others.

"This type of deformation, where rocks deform by developing marked discontinuities across which there is often a break in cohesion, is called brittle behaviour.... The opposite type of deformation, where rocks deform by distributing the strain in a smoothly varying manner throughout the deforming mass, is called ductile behaviour".

When used in this way, the terms are simply describing deformation continuity and this is particularly common in the field description of deformation as "ductile", implying continuous strain.

Other definitions may combine two or more aspects of deformation to give a hybrid of the approaches a-c outlined above. For example, Kirby (1980) uses a combination of deformation state, stress-strain relationship and deformation mechanism to characterise three regimes of rock behaviour from experiments:

Brittle. Shortening is accommodated by localized displacements on shear fractures, faults, or extension fractures, with stress drops and increasing ultimate strength with pressure.

Semi-Brittle. Strains are distributed throughout the specimen, but both brittle and ductile "processes" (i.e. deformation mechanisms) operate.

Ductile. A very small pressure effect on strength, no dilatancy and abundant evidence of mechanisms of "plastic" deformation (e.g. intracrystalline plasticity). Kirby and Kronenberg (1984) adopt a similar approach, as does Norton (pers.comm.), where brittle is defined as "Deformation proceeds by the fracturing of grains and grain aggregates followed by sliding and rolling of the fragments past each other without significant internal strain".

Rutter's (1986) discussion on brittleness and ductility uses deformation mechanisms to define brittle, and strain distribution to define ductile, emphasizing the point that they are not mutually exclusive: "Brittleness is associated with the formation of cracks in otherwise rigid

single or poly-crystals". "Ductility is the capacity for more or less homogeneous flow, and is a concept which must be defined on a macroscopic scale". These are useful definitions which can be applied to both laboratory experiments and field observations, but the definition of ductility is slightly unsatisfactory due to its vagueness: for example neither the 'ductile shear zone' referred to, nor the example of cataclastically-accommodated large-scale folding, are strictly homogeneous flow. To include these examples, the scale range must be restricted both to greater than microscopic and less than an upper limit of perhaps the outcrop.

2.4.3 The Brittle-Ductile Transition

Attempts to define the brittle-ductile transition have naturally reflected the variety of definitions used for brittle and ductile. A further problem is created by the difficulty of trying to specify a single point in what appears to be a completely continuous range of behaviour: this ideally requires quantification, which has been attempted in some cases, but means that the transition is defined arbitrarily unless some theoretical meaning can be given to the chosen values.

Following the first of the three approaches to the definitions of brittle and ductile, the transition may be defined in terms of deformation mechanism, i.e. the transition from cataclasis to crystal plasticity or diffusive mass-transfer. The difficulties of precision become most obvious in this case, especially following the work of Carter and Kirby (1978) and Kirby and Kronenburg (1984) which emphasises the importance of semi-brittle behaviour: the interaction of intracrystalline plasticity and crack formation is likely to be of such considerable geological importance that a simple binary brittle-ductile classification of deformation mechanisms with a "transition" point appears to be fairly meaningless. Even if strain could be partitioned accurately between fracture and crystal plasticity,

the continuously variable role of plasticity in crack formation would make this measurement of a "transition" of doubtful validity. There may also be further distinctions to be made within all the mechanisms that are classed together as "cataclastic".

The transition in terms of stress-strain was defined by Heard's (1960) definitions of brittle and ductile by strain before failure. Again, however, the existence of the "intermediate" class (3-5% permanent strain before failure) shows that the idea of a simple transition is not a good description.

Two alternative ways of defining the brittle-ductile transition are recognised by Tullis and Yund (1977) in their experimental treatment of granite. Their "macroscopic transition" is the change from microcracking to dislocation motion, i.e. the transition is defined by deformation mechanism. Their "microscopic" transition is a definition from stress-strain relationship, by amount of permanent strain before fracture. They argue that the "microscopic" transition is responsible for the macroscopic transition and cause the cessation of seismic activity at a certain depth on strike slip faults (as proposed by Sibson 1977, 1983).

The transition is also defined in terms of stress-strain relationships by Byerlee (1968), who produces perhaps the most complete description in his well known formulation that the transition occurs at a "pressure in rocks at room temperature both in compression and in extension ... at which the stress required to form a fault surface is equal to the stress required to cause sliding on the fault. This statement is shown to be true for a wide variety of rock types and moreover is given a physical interpretation, following Orowan (1960): the shear stress required to cause frictional sliding on a faulted surface clearly increases with normal stress and therefore confining pressure: once a fault has formed, frictional sliding will occur by asperities overriding each other until it becomes easier for the asperities to fail by fracturing: this will be at the peak strength

and, therefore, no stress drop will occur on formation of a fault at the brittle-ductile transition.

Although Byerlee's definition is very useful, there are a number of theoretical and practical problems. A careful reading of the 1968 paper reveals that the evidence produced for this statement is the result of a circular argument: having defined "brittle" as behaviour with stress drop following failure, Byerlee "proves" that the transition occurs by showing that brittle points on a $\Delta\sigma$-σ_3 diagram have higher peak than residual strengths, i.e. they fall on the high $\Delta\sigma$ side of the criterion for frictional sliding on faults ("Byerlee's Law"), which is deduced from the very rocks that showed a stress drop in the first place. The "proof" therefore amounts to no more than a re-statement of his initial definitions. Secondly, the criterion is for rocks at room temperature only: in no definition of the brittle-ductile transition is this likely to be geologically reasonable, and temperature effects are undoubtedly important in "semi-brittle" behaviour. Lastly, as in most such early experiments, no attention was paid to the role of pore-fluids.

The contradiction between these two types of definition by stress-strain is noted by Mogi (1972a,b,1974) who illustrates it in his division of rock behaviour into type A and type B (fig. 2.17). In type A, there is a discrepancy between the "pre-failure strain"-defined transition and the "stress drop"-defined transition due to the fact that a large amount of permanent strain may occur before failure (probably by cataclastic flow) at moderate to high confining pressures. The two definitions coincide for type B behaviour, where failure is not preceded by significant strain.

The distinction between types A and B behaviour is given a physical interpretation in Pat erson's (1978) discussion of the brittle-ductile transition. He suggests that type A behaviour corresponds to a simple change from fracture to plastic deformation mechanisms that are pressure

sensitive. On the other hand, type B behaviour is a change from fracture to cataclastic flow, which becomes progressively less sensitive to pressure.

Rutter (1986) introduced a second transition, the "Upper Transition", as a point on the strength vs. confining pressure diagram (Fig.2.18). This point is at the pressure where deformation becomes completely pressure-insensitive. This at least divides deformation into three rather than two fields and in a quantitative fashion that has physical significance; when the pressure sensitivity of strength is completely lost, presumably no cataclastic deformation is occurring. However, the Byerlee brittle-ductile transition, as noted by Mogi, probably does not have such a fundamental significance, since cataclastic flow may occur both before and after this point, which is at an arbitrary place on a continuum of behaviour. An alternative ternary scheme is proposed by Kirby (1980) who defined brittle, semi-brittle and ductile by a combination of deformation state and deformation mechanism, (localised displacements on shear faults, distributed fractures and some plasticity, and plastic deformation respectively). He then showed that the transitions between these mechanisms could be given for most rocks by the values of $\sigma_3/\sigma_f = 0.4$ for the first transition and $\sigma_3/\sigma_d = 0.8$ for the second transition. σ_f is the residual strength for sliding on a pre-existing fault given by the high-pressure version of Byerlee's Law ($\tau_f=0.8+0.6\sigma_n$), and σ_d is the ductile strength (differential stress at 10% strain).

In summary, the brittle-ductile transition has been defined by deformation mechanism, strain before failure, or stress drop. In all cases there is no simple transition, but rather a continuum of behaviour, and no unique relationship between the deformation mechanism, strain and stress. Significant improvements to the transition concept have been made by dividing deformation into three stages, and recognizing the importance of semi-brittle behaviour. The term "brittle-ductile transition" is rendered

largely meaningless by these observations.

2.4.4 Cataclasis, Flow, Cataclastic Flow

Cataclasis is a deformation mechanism defined above as a combination of fracture and sliding. **Flow** is a description of strain distribution implying continuous deformation (Stearns 1968b, Griggs and Handin 1960). Taking these two generally acceptable definitions, cataclastic flow can be defined quite logically; for example, Paterson (1978) "Cataclastic flow describes the permanent strain achieved by the combination of distributed fracturing whereby the material is broken into fragments and the relative movement of the fragments".

Handin & Heger 's (1957) definition restricts the scale of movement to granular displacements: "Cataclastic flow involves the displacements of constituent grains of an aggregate relative to one another, accompanied by mechanical granulation, breaking or crushing of grains". The influence of experimental work is evident in this scale restriction, and is also apparent in the discussion of Paterson (1978), Hadizadeh's (198) definition of cataclastic flow, and a highly unusual definition by Wong and Biegel (1985) who consider that cataclastic flow occurs at the pressure when microcracking becomes completely isotropic. The influence of field observations, however, led to Stearns (1968b) extending Handin's definition to include fragments of any size: "Once a rock layer loses cohesion along fractures and separates into discrete parts, no matter what their size, it can begin to flow by "displacement of constituent" parts "relative to one another, accompanied by mechanical granulation, breaking and crushing". The strain distribution is therefore mesoscopically pervasive, as in most definitions of flow; although recently Gallagher (1981) describes the tectonics of China as an example of continental-scale cataclastic flow involving fragments up to 1000km in size. Jamison and Stearns (1982) define intergranular cataclastic flow as "a type of deformation that is

both brittle and macroscopically pervasive". Definitions of **cataclastic flow** therefore agree that a deformation by a mechanism of cataclasis occurs, with continuous pervasive strain at some scale. However, since all deformation can be viewed as continuous at a sufficiently large scale, it is desirable to specify a scale in order to give the term a unique meaning.

2.4.5 Discussion and Conclusion

In spite of their evidently unresolved definition, the terms brittle, ductile, and brittle-ductile transition will continue to be used by most geologists. The original definitions based on stress-strain relationships were satisfactory and quantifiable, but the adoption of the terms by field geologists now requires a broader re-definition since stress-strain relationships are never known for rocks in the field and can only be inferred in exceptional circumstances. This is expressed by Griggs and Handin (1960) thus "... Hence it is not possible to deduce from the stress-strain curve alone the nature of the deformation. The converse is also impossible, so that a geologist may not infer the type of stress-strain curve from the nature of faults or flow". Definitions based on deformation state are possible but have the uneasy restriction of requiring scale specification. However, a generally acceptable definition of brittle based on a deformation mechanism is possible: brittleness is deformation accommodated by fracture. Likewise it is possible to use deformation mechanisms to define semi-brittleness as deformation accommodated by the interaction of fracture and crystal plastic or diffusive mass transfer process.

Rutter (1986) suggests that ductile deformation is "macroscopically homogeneous flow", thus strictly excluding shear zones and macroscopic folds. It is proposed here that it is **continuity** rather than **homogeneity** that defines ductility, and that a more satisfactory definition is "macroscopically continuous deformation", particularly because at any

scale, continuity is precisely defined but the distinction between localised and non-localised deformation is arbitrary within a range of behaviour. Although this is a substantial departure from the original experimental definitions, it has the merit of encompassing all features that the field geologist usually refers to as ductile, including shear zones and macroscopic folds. The alternative possibility of using a deformation mechanism-based definition of ductile (deformation accommodated by crystal plasticity or diffusive mass transfer) has the attraction of following logically from the preceding definitions of brittle and semi-brittle, but is probably too limited to find widespread acceptance and suffers the additional drawback that the mechanisms are not always immediately identifiable.

The above proposals suggest that the 'brittle-ductile transition' as used in both rock mechanics and lithospheric deformation studies to indicate a change from brittle to plastic deformation mechanisms is a misnomer, which should be referred to accurately as the cataclastic-plastic transitional or the "elastico-friction (E.F.) - quasi-plastic (Q.P.)" (Sibson 1977) transition. In many cases this is not a simple transition due to the progressive change from faulting to cataclastic flow to plasticity with a continuously decreasing pressure sensitivity.

The introduction of **deformation continuity** into the discussion leads to a modification of Rutter's 'Modes of Failure' diagram (Figure 2.15) for the description of deformation. The state of deformation on the horizontal axis of that figure can be specified better as continuous or discontinuous, with localised and pervasive end-members of the latter category. Furthermore, it is suggested that because 'failure' has often been used in a purely brittle context, a more suitable terminology would be 'Mode of Deformation', which means a description of the deformation **mechanism** and **continuity** at a given scale. Figure 2.19(a) shows how continuity is a function of scale: with increasing scale length, discontinuous deformation

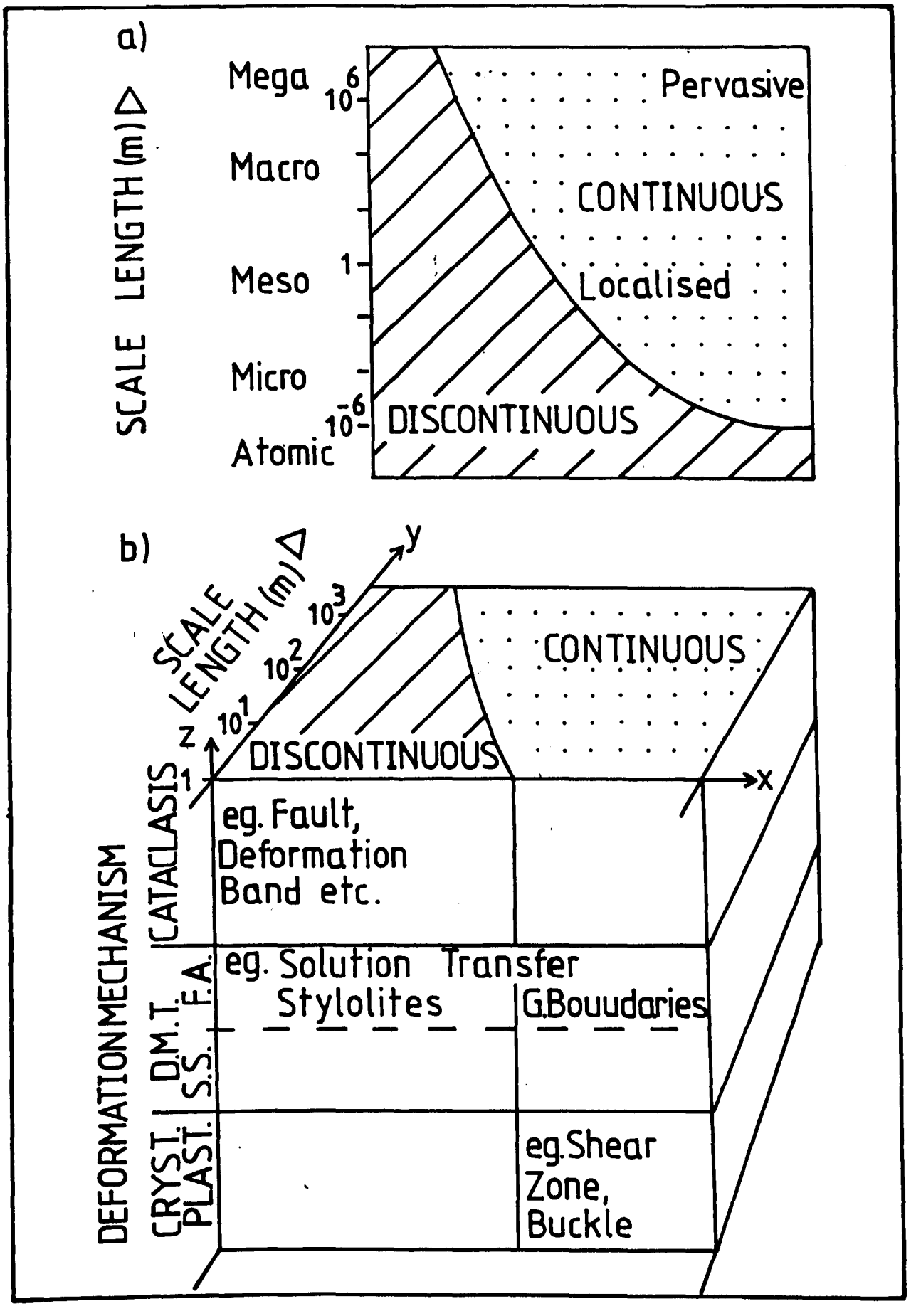

FIGURE 2.19

a) The dependence of deformation continuity on scale of observation. As the scale is increased, discontinuous deformation appears continuous and there is also a tendency for localised,continuous deformation to appear pervasive.
b) Part of the "Mode of deformation" diagram. A mode of deformation is specified by deformation mechanism (z-axis) and continuity/discontinuity (x-axis) at a given scale (y-axis). A section is shown at scale length 1m with examples of features representing different modes of deformation. Abbreviations: D.M.T. = Diffusive Mass Transfer. F.A. = Fluid Assisted. S.S. = Solid State. G.Boundaries = Grain Boundaries.

becomes continuous and there is also a trend for localised, continuous deformation to appear pervasive. The figure shows that at the atomic scale, there is no continuous deformation. An example of the discontinuous to continuous transition with scale is the accommodation of a fold by cataclastic flow: at a mesoscopic scale, the deformation is entirely by discontinuous shear on faults, but at a macroscopic scale, these discontinuities are not seen and the fold appears to be continuous. Figure 2.19(b) presents part of the 'Mode of Deformation' diagram. A mode is specified by its deformation mechanism (z-axis), continuity (x-axis) and the scale length (y-axis); alternatively, a length can be given for the discontinuous to continuous transition.

2.5 FRACTURE, FAULT AND FOLD ROCK NOMENCLATURE

2.5.1 Fracture Nomenclature

Throughout this review, a laissez-faire policy of nomenclature has been deliberately adopted in deference to the individual terms and usages of the authors referred to. However, this variety also requires the discipline of a personal scheme which is presented below, based as far as possible on three principles: that it must be as descriptive as possible, since genetic or mechanistic terms have to be justified by considered evidence, that it should primarily be applicable to the field evidence presented here but ideally encompass rock deformation studies, and that it would be scale-independent.

One common nomenclature is based on distinctions of displacement pattern. Thus a fault is defined as a surface of shear displacement, compared to a joint across which there has been no displacement. There are at least three good reasons for avoiding this usage. Firstly, displacement is well described anyway by either the terms extensional, hybrid, or shear, or modes (I, II, III or mixed); it is more useful to have definitions based

on some other character. Secondly, identical features may have more than one displacement mode, or even mixed modes, and lastly and most seriously, the appreciation of displacement is severely a function of scale of observation.

It is therefore proposed to avoid the use of the word joint altogether, and the following definitions are adopted, based on Blenkinsop (1982).

i) **Fracture.** A localised, tabular discontinuity within a rock mass at any scale. This includes all faults, joints, cracks, veins, deformation bands, slip surfaces, and granulation seams irrespective of matrix and displacement. The discontinuity may be in strain or strain rate.

ii) **Fault.** A fracture with crushed matrix on the surface, where crushed matrix is a lining or filling produced by displacement.

iii) **Crack.** A fracture without crushed matrix. Cracks may, of course, have any other sort of matrix. Neither cracks nor faults are restricted to any displacement pattern; thus it is perfectly feasible to have mode I faulting, or multimode faulting or cracking.

Cracks are further subdivided by geometry into **intragranular** (within one grain), **transgranular** (across more than one grain) and **circumgranular**, (grain boundary or intergranular cracks are equivalent around grain boundaries). Blenkinsop (1982) suggests that where grain boundary cracks encompass more than one grain, they may be called **inter-multigranular**. This classification is preferable to that of Kranz because it is entirely based on geometry (compared with the mechanistic aspect implied for example in Kranz's "cleavage crack" category).

iv) **Deformation Zone.** A zone of high fracture density. This term is introduced after Aydin and Johnson (1983) and has widespread applicability in this study. High fracture densities may develop by either or both increasing numbers of fracture sets, and/or increasing frequency of an

individual fracture set. It is clearly necessary to define a critical fracture density for the development of a deformation zone, but since this may vary depending on other factors such as lithology, no figure is included in the basic definition.

v) **Breccia Zone.** A fault in which the crushed matrix contains less than 75% fragments. This usage is after Blenkinsop (1982) to describe a common feature of cataclasis in quartzites.

2.5.2 Fault and Fold Rock Nomenclature

Fault rock nomenclature will follow that of Sibson (1977) with one important change. Otherwise clearly cataclastic fault rocks may develop a foliation. For example, House and Gray (1982) figure a cataclasite with a foliation defined both by clast shape and microscopic stylolites and Blenkinsop (1982) has described a penetrative phyllosilicate foliation in cataclasites of the Ord Thrust plane, N.W. Scotland. The existence of a crude shape fabric in thrusts could be accommodated within the Sibson classification by proposing that mylonites have a penetrative foliation, but the pervasive fabric of the Ord thrust cataclasites indicates that there is still an area of overlap between the categories, reflecting the transitional nature of the textures and processes between the two rock types. This may be an inevitable weakness of any classification scheme, and it is proposed that end-member cataclasites should therefore have no penetrative foliation, while end-member mylonites do so.

Blenkinsop (1982) introduces the terms protobreccia, breccia and ultrabreccia to describe cataclastic rocks found in folds, in order to emphasise the macroscopically ductile nature of the deformation. These terms will be used occasionally following their original definition (see also Blenkinsop and Rutter 1986).

CHAPTER 3

METHODS OF STUDY

This chapter introduces and describes all the techniques used with the exception of the Illite Crystallinity and Clay Mineralogy determinations (Chapter 4). The techniques are also evaluated for precision and error, but some discussion is left to individual chapters where the results are interpreted.

3.1 FIELD TECHNIQUES

3.1.1 Mapping and Sampling

Mapping at a variety of scales was carried out at most sampling localities. Larger scale maps were made on topographic base maps, while maps of greater detail were made by pace or tape and compass.

a) Cremenes (Figure 1.3). Samples 21-24 were collected from the Esla Nappe, 3km NNE of Cremenes and located on the I.G.M.E. 1:200,000 Mapa Geologico De Espana, Hoja 10 (Mieres), and a 1:50,000 map of the Esla Nappe by J. Rupke.

b) Bernesga Valley (Figure 1.3). A 7km x 4km section was mapped down the Bernesga Valley at a scale of 1:25,000 on a base map consisting of an enlarged copy of the 1:50,000 Edicion Militar Sheet 103 (Gordon) 1st Edition 1943. This has been used for all maps in Chapter 5. Four sub-areas were mapped in greater detail at approximate scales of 1:500, 1:1,000 and 1:5,000, and samples 1-20, 25-27 and 103-153 were collected.

c) Luna Lake (Figure 1.3). Samples 28-33 were collected from the North end of Luna Lake and located on the 1:100,000 map published in Wallace (1972).

d) Punta Vidrias (Figure 1.3). A 2x2km coastal area was mapped at a scale of 1:5,000 on enlargements of the 1:25,000 Edicion Militar Map, Hoja 13, cuadros III-IV (Cudillero) and II (Aviles). Two small areas were also mapped at 1:100 by tape and compass, and samples CVI-CV16 were collected.

e) Cabo de Peñas (Figure 1.3). Sample 102 was collected and located

on the I.G.M.E. 1:50,000 Mapa Geologico de España, Hoja 13, 12-3 (Aviles).

f) Luarca (Figure 1.7). A coastal section of 1.5km was mapped at a scale of 1:10,000 on an enlarged 1:25,000 Mapa Topografico Nacional, Hoja 11 (Luarca) as a base map. A more detailed map at 1:1,000 was made by pace and compass of a 200m section, and samples 36-45 were collected.

g) Punta Del Sol (Figure 1.4). 2km of coastal section was mapped at a scale of 1:5,000 using enlargements of the 1:25,000 Edicion Militar Map, Hoja 11 Cuadro II (Luarca), and more detailed maps at 1:500 and 1:1000 of two subareas were made by pace and compass. Samples V1-V12 were collected.

h) Navia (Figure 1.4). A small area of beach 3km West of Navia was mapped at 1:1,000 by pace and compass, from which samples N1-N4 were collected, and located on the 1:50,000 Mapa Topografico Nacional, Hoja 11 (Luarca).

i) Viavellez (Figure 1.4). Samples VZ1-VZ4 were collected from the port area of Viavellez and located on the same map.

j) Cabo Blanco (Figure 1.4). Samples CB1-CB3 were collected from 1km West of Cabo Blanco and located on the 1:500,00 Mapa Geologico Del Macizco Hesperico.

k) Tapia (Figure 1.4). A detailed map at a scale of 1:2,000 of a 1/2km coastal section was made immediately to the West of the town, and samples TA1-TA8 collected. The section was located on the 1:50,000 Edicion Militar, Hoja 10 (Ribadeo).

l) Benqerencia (Figure 1.4). A single sample (46) was collected from the Playa de Benqerencia and located on a 1:10,000 map and section from Bastida and Pulgar (1978).

3.1.2 Fracture Orientations and Number of Sets

a) Methods. As well as measuring fracture orientations over all areas mapped, certain localities were chosen for more detailed analysis. Orientated sketches of fractures on a bedding plane viewed from the dip

direction, and in a section normal to the bedding were first made, and any obvious fracture sets were labelled from F1 to F4 in order of decreasing fracture density. Two methods of collecting data were compared. In Method A, the first 50 or 100 fracture orientations were measured and classified into sets as the readings were taken. In Method B, a fixed number (3 to 25) of fracture orientations from each set were measured. The two methods can be compared in Figures 5.6 and 6.4. Generally those diagrams prepared by Method A show a broader spread of fracture orientations allowing an interpretation of more sets of fractures, while Method B yields fewer and more discrete sets. The two methods can be compared directly for the same locality at the most southerly measurement station of Figure 6.4. Method A has the advantage of complete objectivity and is appropriate for poorly defined or curved fracture sets, while Method B can be used for a rapid characterisation of a locality, where fracture sets are well defined and planar, and facilitates interpretation. Fracture orientations are represented on equal area, lower-hemisphere projections, and contoured using a Kalsbeek counting net.

b) Precision and Error. The maximum precision with the Silva compass in both dip and strike is 1^{0}. An error analysis was made for 50 fractures at Luarca by labelling and remeasuring each fracture. The results give mean error of $+/-1.2^{0}$ in strike at $+/-1.8^{0}$ in dip.

3.1.3 Fracture Density

a) Review of Methods. In spite of the importance of fracture density to cataclastic deformation mechanisms, density measurements are not a standard field technique and indeed are unknown by many geologists. Not only is there no standard method, but the several different methods used are incompatible and therefore useless for comparative purposes. One of the simplest measurements of fracture densities was by Stearns (1968) who measured the number of fractures per 100 feet (30.5m) in a number of

different lithologies. Following Wheeler and Dixon (1980), a single set of fractures can be characterised by their spacing (S), the distance between fractures measured perpendicular to the fracture surface, or its inverse, frequency (F), the number of fractures per unit length. The following comments and definitions apply to fractures on all scales, including the microfracture discussed in 3.7. These will be the true values; apparent values of S and F will be measured on any plane or in any direction not perpendicular to the fracture surface. Several measurements of S and F form a population with a mean, median and trimean, S_T, defined as

$$S_T = 1/4\ (Q_1 + S_m + Q_3)$$

where Q_1, Q_3 are the first and third quartiles, and s_m is the median. Generally, the value of the trimean lies between the median and mean, and because it is not greatly affected by extreme values, the former authors advocate it as the most reliable measure of S or F. Pohn (1981), however, adopted a more rapid and simple approach: the average of the maximum and minimum spacings was taken. For several joint sets, S or F can be measured for each set individually.

An alternative approach used with considerable effect by Jamison and Stearns (1982) and S. Dumpleton (pers.comm.), is to average the frequency of all fractures in two perpendicular directions. A very simple field method has been devised by the latter author, using a counting frame consisting of two perpendicular metre long rules placed flat on a longwall coal face, from which the frequency per metre in both directions can be counted directly. The Jamison and Stearns approach measured the number of intercepts on a 200mm length in two directions on either bedding surfaces, or cross-sectional surfaces, with four or five counts at each measurement station. The final microfault densities were calculated by giving weightings to three categories (single, thin anastomosing and thick anastomosing) based on relative cumulative gouge thicknesses.

Hudson and Priest (1983) have described a method for deriving the

dependence of discontinuity frequency on orientation in either two or three dimensions. Discontinuities are firstly subdivided into a number of sets, and frequencies are evaluated for each set along scan lines, allowing for obliquity of the scan line. From the individual set frequencies and orientations, the total frequency in any direction can be calculated. The method has importance in the field of civil and mining engineering, but is possibly too complex for widespread field application, and does not provide a single parameter to describe fracture density. For a single value to describe the combined density of all fractures, Wheeler and Dixon (1980) proposed the term Intensity, defined as the sum of the frequencies of each joint set.

However, every method so far described suffers the drawback that only one surface is used. The measured frequency is thus clearly dependent on the orientation of the fractures relative to that surface, and to overcome this problem, the method described below was devised.

b) Methods Used.

i) Fracture Densities. Fracture frequencies (F) in m^{-1} for each set were measured at each locality by counting the number of fractures of that set alone, and any others approximately parallel but of indeterminate set, along a 500mm or 250mm line perpendicular to the fracture surface. Between two and five such measurements were made on different parallel lines; these commonly showed large variations, which were averaged and the final density taken as the sum of the averages, comparable with the calculation of 'Intensity' by Wheeler and Dixon (1980). This procedure can be expressed as:

$$F_j = \frac{\sum_{i=1}^{i=n_j} F_i}{n_j}$$

$$\text{Fracture Density, } D(m^{-1}) = \sum_{j=1}^{j=N} Fj$$

where $F_{i,j}$ = frequency of fracture set i, j

n_i = number of frequency measurements of fracture set i

N = number of fracture sets.

A comparison was also made between this method and that of Dumpleton for one locality at Punta Vidri as. In this example, n_i=5, N=3, and the fracture density was calculated as 58.4m^{-1}. The Dumpleton method, also repeated five times, gave a very similar value, 60.8m^{-1}, from measurements on a bedding plane perpendicular to all three joint sets. The term Fracture Density is used in distinction to Intensity to emphasize that measurements were made along a line perpendicular to the fracture plane in three dimensions, thus giving a true value independent of a plane of observation.

ii) Fracture Logs. A second method was the 'Fracture Log', designed to reveal the variation in fracture density over a continuous area on a finer scale than the pace and compass maps. A tape measure is stretched across a flat surface perpendicular to the apparent strike of the most frequent fracture set, and the distance from the origin of every fracture intersecting the tape is recorded. The measuring surface was chosen wherever possible to be perpendicular to the fracture set; thus the fracture frequencies are approximately equal to the sum of the true fracture frequencies of the most frequent set and the apparent frequencies of all other sets. Results are represented as Bars at the distance from the origin to scale, or as histograms with various class intervals. The bar diagrams were drawn by programme FRACTLOG (Appendix A9.1), and the histograms sorted by programme SORT. (See Figure 6.7 for an example).

c) Precision and Error. Fracture frequencies being integer values, are absolutely precise. However, as mentioned above, large differences are observed in the measured values of fracture frequency for individual fracture sets. This is clearly due to the outcrop scale variation in fracture frequency, and rather limits the value of the density measures. An assessment of error for individual frequencies was made by calculating

the average error and average percentage error of all fractures measured at Punta Vidrias. The data set was subdivided into localities for which 2 and 5 measurements were made respectively.

	Average Error in Frequency (m^{-1})	Average Percentage Error in Frequency
2 Measurements/ Fracture Set (n_i=2)	+/- 4.28	+/- 27.40
5 Measurements/ Fracture Set (n_i=5)	+/- 6.65	+/- 43.85

TABLE 3.1

The results given in table 3.1 show that the average percentage error increases from 27 to 44% with the increase in number of measurements. This may at first sight seem surprising, but since the main source of error has been identified as small-scale heterogeneity, it is logical that increasing sampling will also increase the error. The implication is that fracture density measurements should be made on as fine a scale, and as densely as possible, with maximum of two measurements per fracture set at each locality.

The maximum error in fracture density measurements from summing the individual frequencies can be estimated assuming that each frequency measurement has the maximum error and that the errors are distributed randomly on either side of the true values. For two fracture sets, there is an equal probability of both errors combining, and both cancelling: the average error is thus identical to the individual frequencies. For three fracture sets, individual errors will combine to produce a threefold error with a probability of 0.25, and a single error will occur (from the combination of two like and one unlike signs) with a probability of 0.75. The average error will therefore be 1.5 times the errors of individual frequencies, or 40%. This is however a maximum value since all the individual errors were assumed to take the maximum possible value: the true value will certainly be less than this.

The fracture logs are not prone to the same errors due to small scale heterogeneities. Sources of error for the continuous fracture logs are parallax between the fracture and the tape where the taut tape is not in contact with the slightly uneven measuring surface, and the omission, or inclusion of features which may not be fractures. These errors were analysed by repeating a fracture log. The error due to parallax was negligible (+/-0.586mm for 99 fractures): of more significance was the omission of 13 fractures and inclusion of 10 others in the repeated measurements. These omissions and inclusions, however, were distributed randomly throughout the logs and produced a net imbalance of only 3 fractures. Figure 8.7 compares the repeated continuous fracture logs, and shows that a virtually identical pattern is produced by the repeated measurements in either the bar diagram from or as a histogram with 100mm class intervals.

3.2 THIN SECTION PREPARATION

Every thin section used in this study is a polished, probe sized, uncovered section mounted in epoxy resin, and all sections were prepared in the same laboratory using the same techniques to ensure as far as possible that no optically observed features were due to differences in preparation. Three mutually perpendicular sections were cut from each sample, using a variety of reference axes, as well as the field-strike mark, to orientate the section. Sections were labelled with the sample figure followed by a letter giving the orientation, as shown in Table 3.2.

EXAMPLE CV1X

Sample — Section Orientation

LETTER	REFERENCE AXES		SECTION ORIENTATION
A,B,C	None		Random
D,E,F	Fold with Axial Planar Cleavage	D	Parallel to cleavage/axial plane
		E	Perpendicular to cleavage, containing bedding/cleavage intersection
		F	Perpendicular to cleavage and bedding/cleavage intersection
R,S,T	A fracture set on the sample	R	Parallel to fracture
		S	Perpendicular to fracture
		T	Perpendicular to fracture and S.
U,V,W	A large fault	U	Parallel to fault plane
		V	Perpendicular to fault plane and containing lineation
		W	Perpendicular to fault plane and lineation
X,Y,Z	Bedding	X	Parallel to bedding
		Y	Perpendicular to bedding, and vertical
		Z	Perpendicular to bedding and Y

TABLE 3.2

3.3 GRAIN SIZE MEASUREMENTS

3.3.1 Review of Methods

An exhaustive account of methods of grain size determination is given by Exner (1972) for metallic materials, on which most geological methods, and much of this review, have been based.

a) Parameters Measured. There are two alternatives for simple size characterisation from measurements in a plane: the area of the grain, AR, (or the equivalent area diameter, = $4AR/\pi^{1/2}$), and the linear intercept, L. The measurement of grain size by area gives no information about grain shape and requires considerably more computational power than linear intercept measurements.

b) The Tomato Salad Problem. Neither areas or intercepts, however, measure the true grain size due to two effects which follow from making

measurements on a two dimensional section. Since the section generally does not cut a grain through the centre, any individual measurement is less than the true grain size: this is the Truncation Effect. Opposing this is the Sampling Effect, caused by the fact that the probability of the section intersecting large grains is greater than small grains; therefore in a population of different grain sizes, the measured distribution will exaggerate the proportion of large grains. Correcting for these two effects constitute the Tomato Salad Problem.

c) Solutions to the Tomato Salad Problem. Exner (1972) gives a formula for correcting intersect area measurements for both the truncation and sampling effects: this was used by Norton (1982) to calculate recrystallized grain sizes in quartz mylonites. The method assumes that grains can be approximated by spheres of discrete size classes. A common correction applied to linear intercept measurements is D=1.5 A.M.L. where D is taken to be the true grain diameter, and A.M.L. is the arithmetic mean linear intercept. However, this correction applies only to equisize spheres and ignores the sampling effect. Exner also gives a formula, due to Bockstiegel, for correcting the distribution of linear intercepts for both truncation and sampling effects with the same assumption as that for the correction of intersect areas: that grains are spheres of discrete size classes. A method also exists for the calculation of the true size distribution of ellipsoids of identical shape from intersect areas, and from linear intercepts (Exner 1972). The latter method requires the distribution of linear intercepts to be represented as a continuous function, which may be inaccurate except for very large sample sizes and small class intervals.

Bockstiegel's Formula for correcting linear intercept measurements (Exner 1972) is:

$$n_{i+1/2} = (4/\pi)(r_i/(l_i^2-l_{i-1}^2) - r_{i+1}/(l_{i+1}^2-l_i^2))$$

Where $n_{i+1/2}$ = Number of spheres per unit volumes in class i+1/2

r = Number of linear intercepts per unit length in class i.

l_i = Upper Class Limit of linear intercept length of class i.

i = Class Number For an arithmetic grouping of class interval C the following relations exist which can be used to simplify the formula:

$$l_{i-1} = l_i - C, \quad l_{i+1} = l_i + C$$

Bockstiegel's formula becomes:

$$n_{i+1/2} = (4/\pi)(r_i/(l_i^2-(l_i-C))^2 - r_{i+1}/((l_i+C)^2-l_i^2))$$

And since $l_i = iC$

$$= (4/C^2\pi)(r_i/(2_i-1) - r_{i+1}/(2_i+1)) \qquad 3.1$$

For a geometric grouping with the standard module $2^{1/2}$ and lowest class limit, L.C.

$$l_{i-1} = l_i/(2)^{1/2}$$

$$l_{i+1} = l_i(2)^{1/2}$$

$$n_{i+1/2} = (4/\pi)(r_i/(l_i^2(1-1/2)) - r_{i+1}/(l_i^2(2-1)))$$

$$= (4/\pi)((2r_i - r_{i+1}/l_i^2))$$

And since

$$l_i^2 = 2^i(L.C.)^2$$

$$= (4/\pi(L.C.)^2)((2r_i - r_{i+1})/2^i) \qquad 3.2$$

These two formulas (3.1 and 3.2) are easily applied in a computer programme to calculate the true size distribution of spheres corresponding to linear intercept measurements for an arithmetic or geometric grouping of linear intercept measurements respectively.

3.3.2 Method Used

A linear intercept was chosen because of its computational speed, simplicity, speed, widespread application and the additional information on grain fabric. Linear intercepts were traced onto a grid of 25 orthogonal traverses spaced at 20mm intervals directly from a 'Shadowmaster'

enlargement of the thin section at x100 magnification, corresponding to an area of approximately 10mm^2 on the thin section. The traverses were made in the visually assessed long (X) and short (Z) directions of any fabric present for each of three mutually perpendicular sections per sample. The linear coordinates of the intercepts were digitised on a Ferranti Cetec digitising board, with rogue values entered in the data to allow for areas where grain boundaries were discontinuous e.g. pores, dissolved or fractured grains. This data file was used in programme LINCEP (Appendix A9.3) to calculate and write to a second file the scaled linear intercept lengths in millimetres separately for the X and Z directions. The programme also calculates the Geometric Mean of Linear Intercept Lengths (G.M.L.), the Geometric Standard Deviation (G.S.D.L.), and counts the total number of intercepts (N). Results from files 0011AX0 and 0105AX0 are shown as histograms in Figures 3.1 and 3.2, a and b.

To allow for the truncation and sampling distortions, Bockstiegel's solution for spheres was applied since the shape of the grains is unknown, and the time required to obtain sufficient data and fit a continuous function to the distribution of linear intercepts would limit the measurements to very few samples. Programmes RLTONDA, B and C (Appendix A9.3) take the data files of linear intercept lengths, sort them respectively into class intervals of width 0.025, 0.01 and 0.1mm on an arithmetic basis, calculate the Arithmetic Mean of Linear Intercepts (A.M.L.), the Arithmetic Standard Deviation (A.S.D.L.) and then apply formula 3.1 to calculate the true size distribution of spheres, from which the Arithmetic Mean of Sphere Diameters (A.M.D.) and Arithmetic Standard Deviation (A.S.D.D.) is also calculated. Results from the same files as the Linear Intercept Measurements are shown as histograms in parts c and d of Figures 3.1 and 3.2. The same procedure is followed by RLTOND G and F (Appendix A9.3) with the difference that a geometric grouping with a module of $2^{1/2}$ is used, with lowest class limit 0.005 and 0.0003mm respectively, and

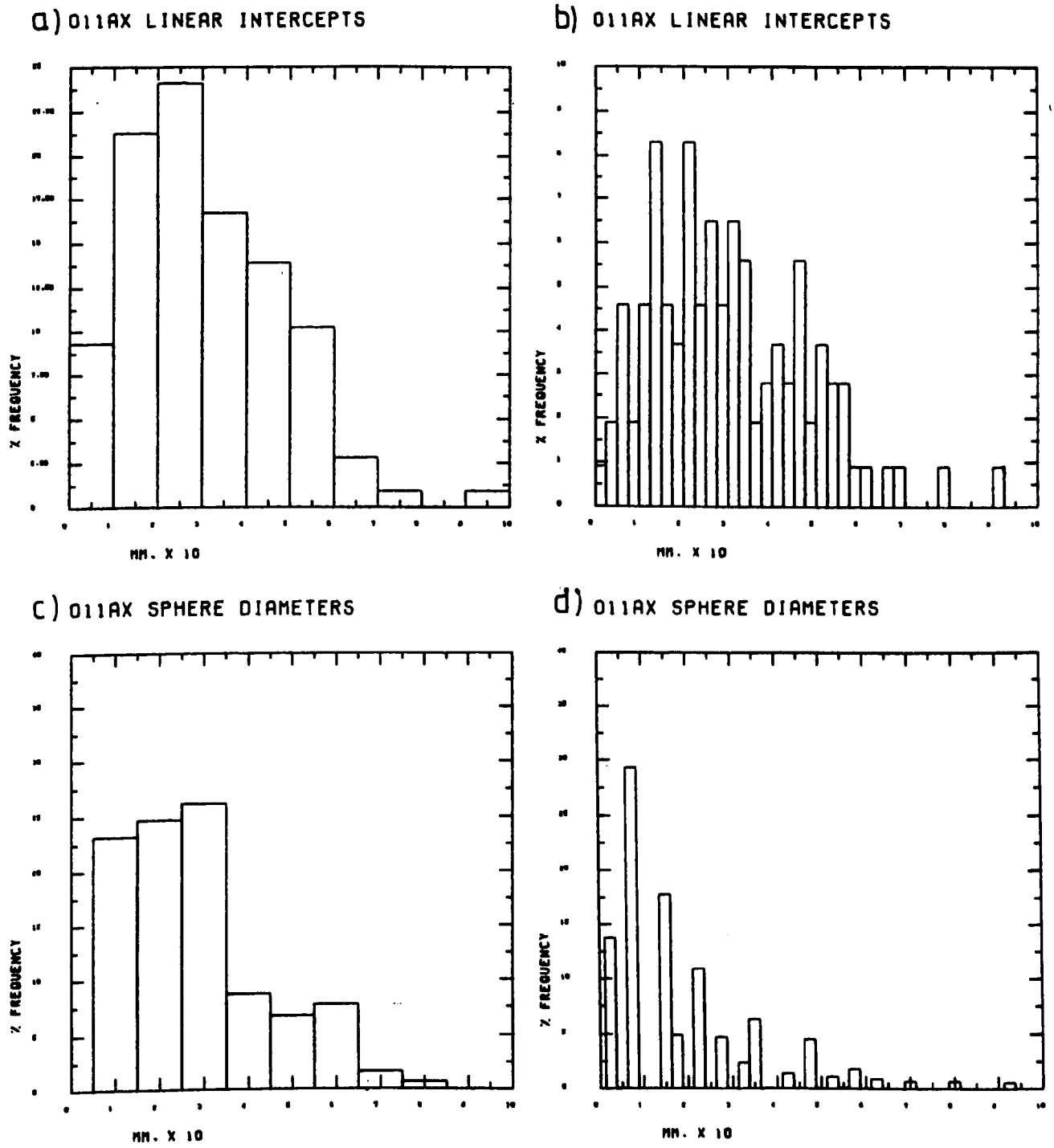

FIGURE 3.1

The distribution of linear intercepts and corresponding sphere diameters with an arithmetic grouping and class intervals (C) of 0.1 and 0.025mm, File 0011AX0.

a) Linear Intercepts, C = 0.1mm
b) Linear Intercepts, C = 0.025mm
c) Sphere Diameters, C = 0.1mm
d) Sphere Diameters, C = 0.025mm

Sphere diameters are calculated from Bocksteigel's Formula (Equation 3.1) to correct for sampling and truncation effects. Sphere diameter distributions calculated with C = 0.1mm are relatively continuous; with C = 0.025mm, the numerous blank class intervals give an unreliable average sphere diameter. These distributions are typical of large grain-size samples with compact microstructures.

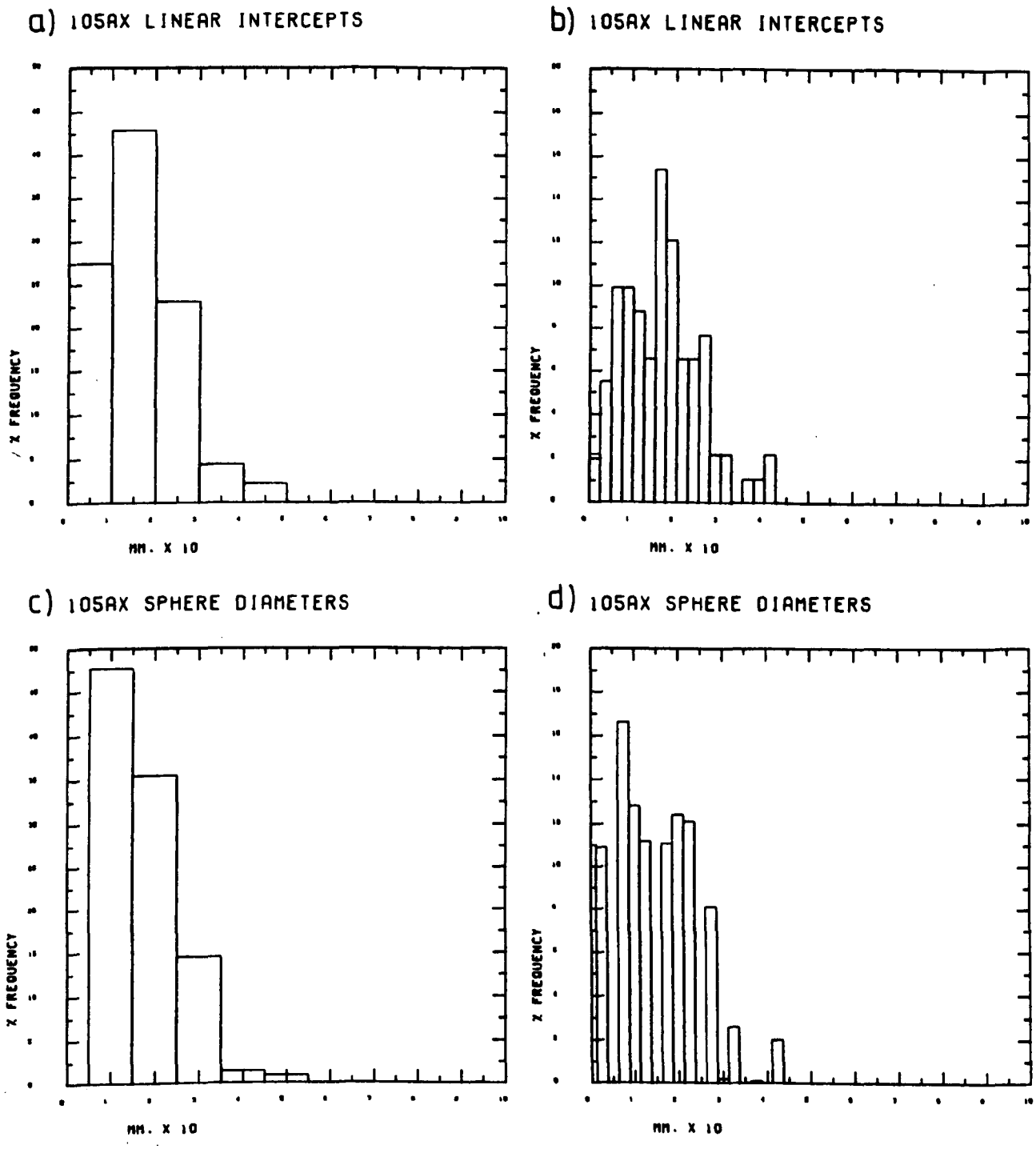

FIGURE 3.2

The distribution of linear intercepts and corresponding sphere diameters with an arithmetic grouping and class intervals (C) of 0.1 and 0.025mm. File 0105AX0.

a) Linear Intercepts, C = 0.1mm
b) Linear Intercepts, C = 0.025mm
c) Sphere Diameters, C = 0.1mm
d) Sphere Diameters, C = 0.025mm

As in Figure 3.1, the distribution of calculated sphere diameters is more continuous for C = 0.1mm than C = 0.025mm; however the discrepancy is much less than Figure 3.1. These distributions are highly positively skewed and typical of samples with grain sizes and more porous microstructures by comparison with 3.1.

then formula 3.2 is used to calculate the true size distribution of spheres, and Geometric Means of Linear Intercepts, or Sphere Diameters (G.M.L. and G.M.D.), and Geometric Standard Deviations (G.S.D.L. and G.S.D.D.). The values of G.M.L., A.M.L. and A.M.D. for arithmetic groupings with class intervals of 0.1 and 0.025 respectively are shown in Appendix A1.

A completely independent measurement of grain size was made incidentally during the course of fracture density measurements on the S.E.M., in which the number of grains/area was determined (3.7.2). A reasonable negative correlation between G.M.L. and this value was obtained for the five data points.

3.3.3 Evaluation of Methods

From Appendix A2, a clear difference between the arithmetic and geometric methods can be seen: as expected for a positively skewed population the arithmetic means of linear intercepts or sphere diameters (A.M.L., A.M.D.) is greater than the geometric mean (G.M.L. or G.M.D.) which is a more effective measure of such population mean (Davies 1929, Langley 1971, see 3.8.3.). The relationship between A.M.L. and G.M.L. is presented in Figure 3.3, which yields the following expression from regression analysis:

$$A.M.L. = 1.2324 \times G.M.L. - 0.0053$$

with a correlation coefficient of 0.994.

Appendix A1 also shows that the geometric means of sphere diameters (G.M.D.) show a much wider fluctuation in values than any of the other parameters and that the result using a lower class limit, L.C. of 0.0003 differ considerably from those with L.C. = 0.005, and in an inconsistent way. This results from the assumptions that the grains are spheres with discrete sizes. For the arithmetic method, the ratio of number of linear intercepts in class i to class i+1 must have a minimum value, depending on

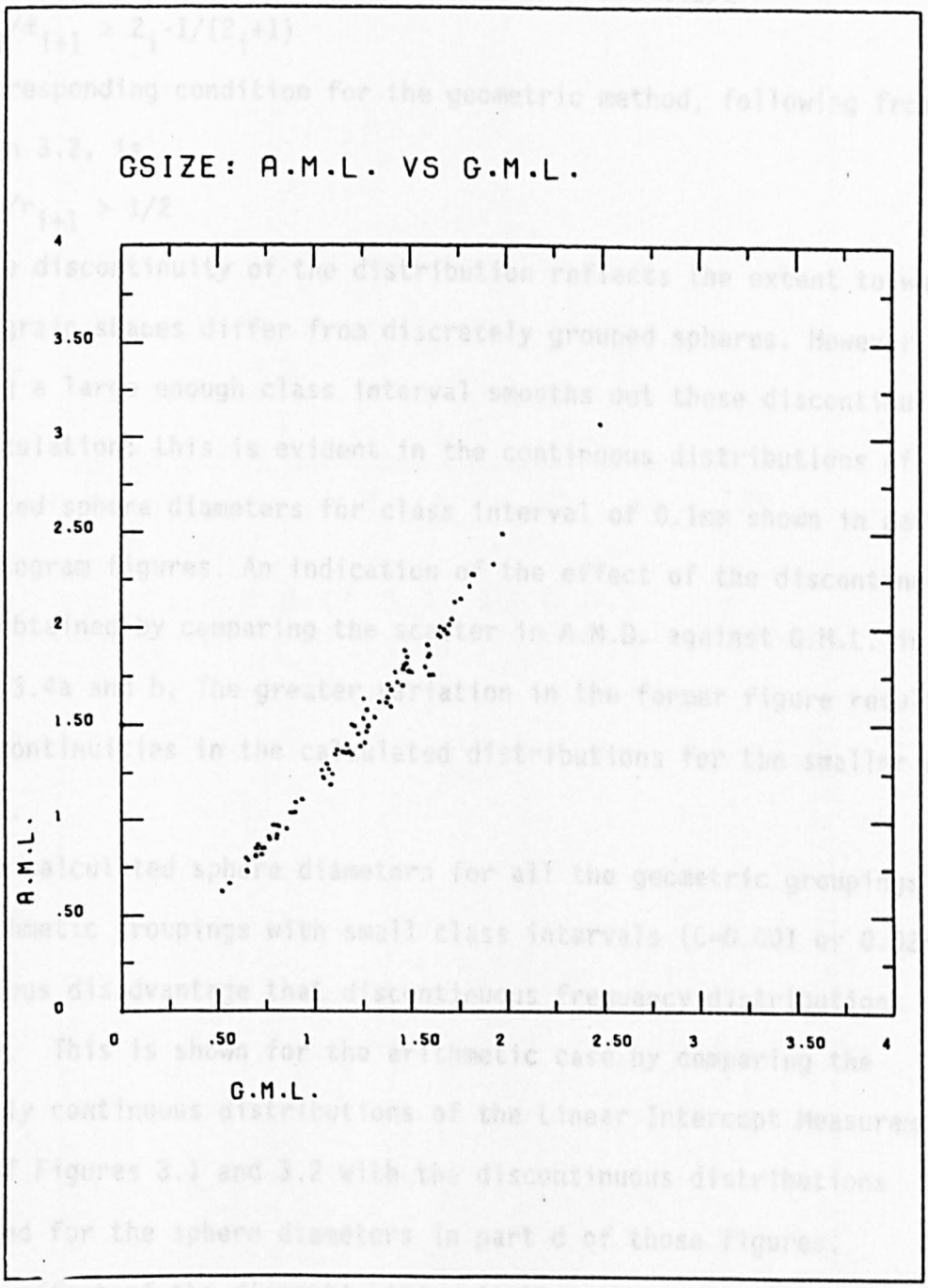

FIGURE 3.3

The relationship between Arithmetic Mean and Geometric Mean Linear Intercept (A.M.L. and G.M.L.). A.M.L. is consistently greater than G.M.L. as expected for positively skewed populations. The relationship is

$$\text{A.M.L.} = 1.2324 \times \text{G.M.L.} - 0.0053,$$

with a correlation coefficient of 0.994. Scales in mmx10.

the value of i, to generate a positive number of spheres in class i+1/2. This can be seen from Equation 3.1:

$$n_{i+1/2} = (4/\pi(L.C.)^2)(r_i/(2_i-1) - r_{i+1}/(2_i+1))$$

From which the condition for a positive value of $n_{i+1/2}$ is

$$r_i/r_{i+1} > 2_i-1/(2_i+1)$$

The corresponding condition for the geometric method, following from Equation 3.2, is

$$r_i/r_{i+1} > 1/2$$

The discontinuity of the distribution reflects the extent to which the actual grain shapes differ from discretely grouped spheres. However, choosing a large enough class interval smooths out these discontinuities in the calculation: this is evident in the continuous distributions of calculated sphere diameters for class interval of 0.1mm shown in part c of the histogram figures. An indication of the effect of the discontinuities can be obtained by comparing the scatter in A.M.D. against G.M.L. in Figures 3.4a and b. The greater variation in the former figure results from the discontinuities in the calculated distributions for the smaller class interval.

The calculated sphere diameters for all the geometric groupings and the arithmetic groupings with small class intervals (C=0.001 or 0.025) have the serious disadvantage that discontinuous frequency distributions are produced. This is shown for the arithmetic case by comparing the relatively continuous distributions of the Linear Intercept Measurements in part b of Figures 3.1 and 3.2 with the discontinuous distributions calculated for the sphere diameters in part d of those figures.

One effect of the discontinuities is that the arithmetic means of sphere diameters (A.M.D.) increase with the class interval. This is shown in Figure 3.5, which shows the relationship between A.M.D. (C=0.025mm) and A.M.D. (C=0.1mm), which yields

$$\text{A.M.D. (C=0.025mm)} = \text{A.M.D. (C=0.1mm)} \times 0.668 + 0.0219$$

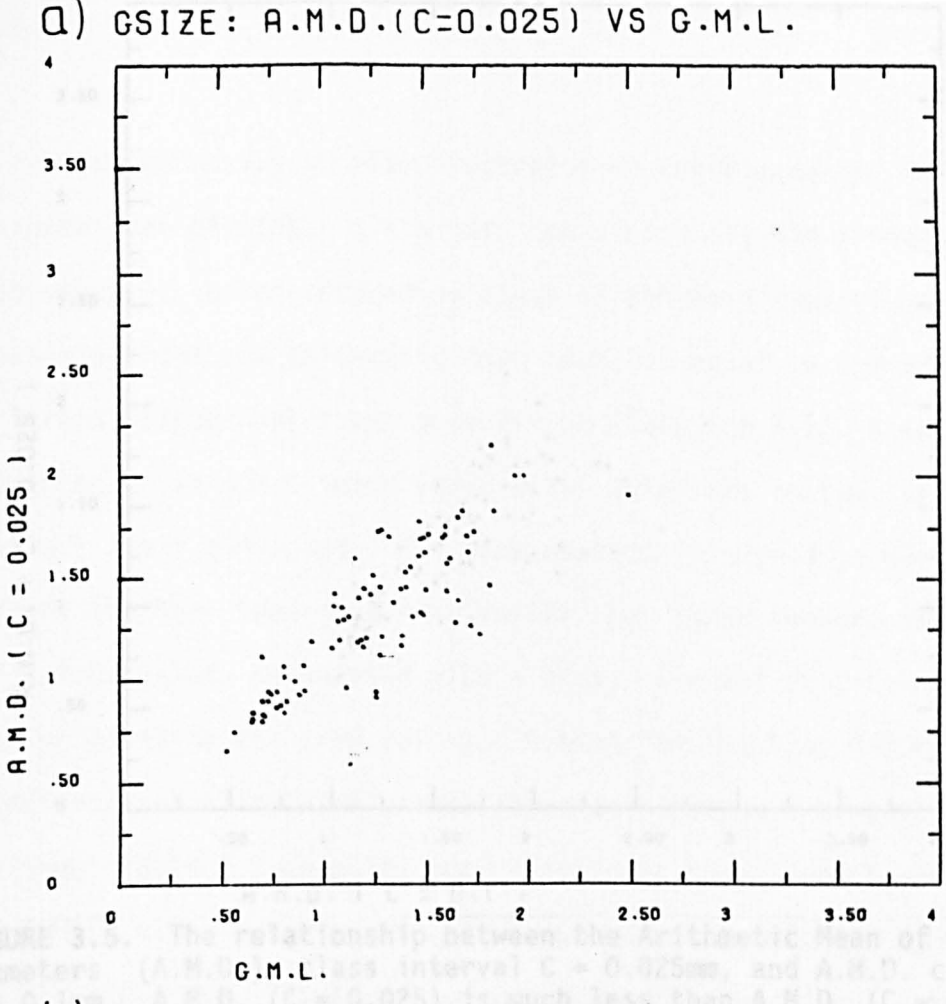

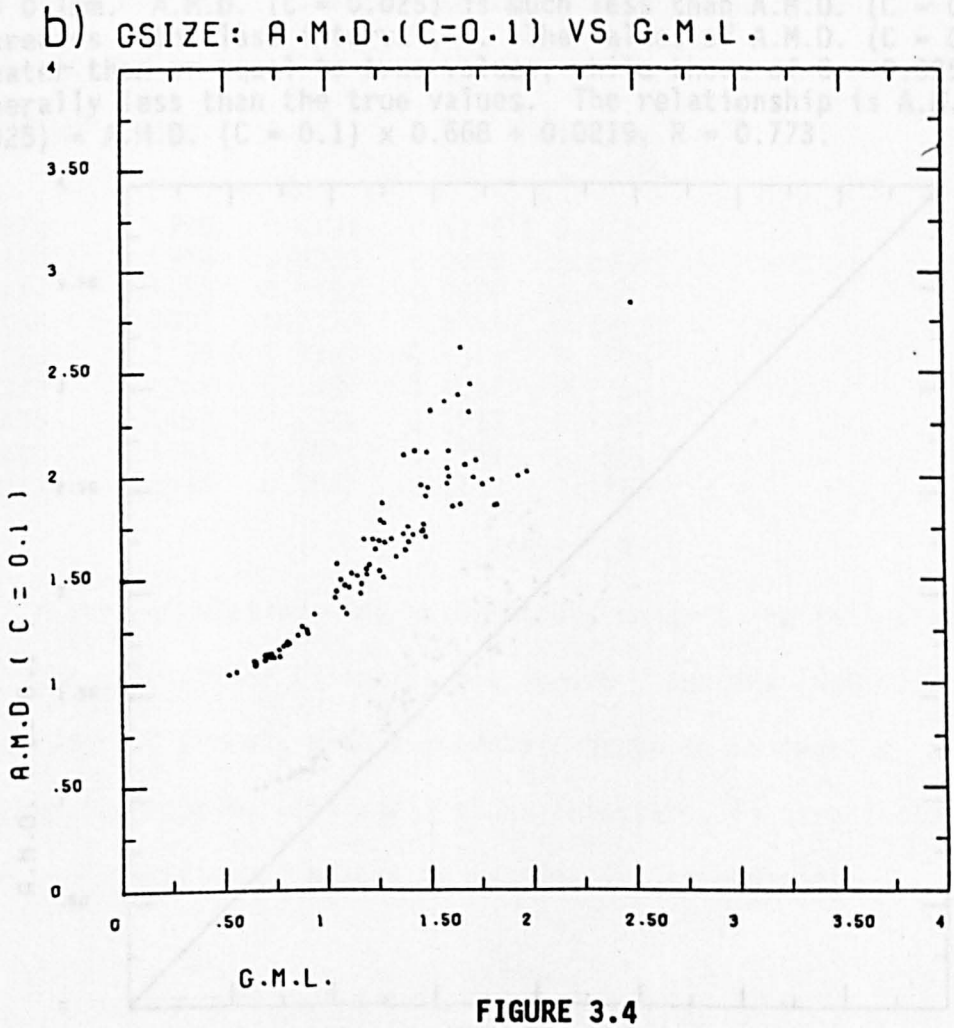

FIGURE 3.4

The relationship betwewen Arithmetic Mean of Sphere Diameters (A.M.D.) and Geometric Mean of Linear Intercepts (G.M.L.) C = Class Interval. The scatter of results in (a) is far greater than (b) due to the discontinuous distributions of sphere diameters generated by Bockstiegel's formula with small class intervals. Scales in mmx10.

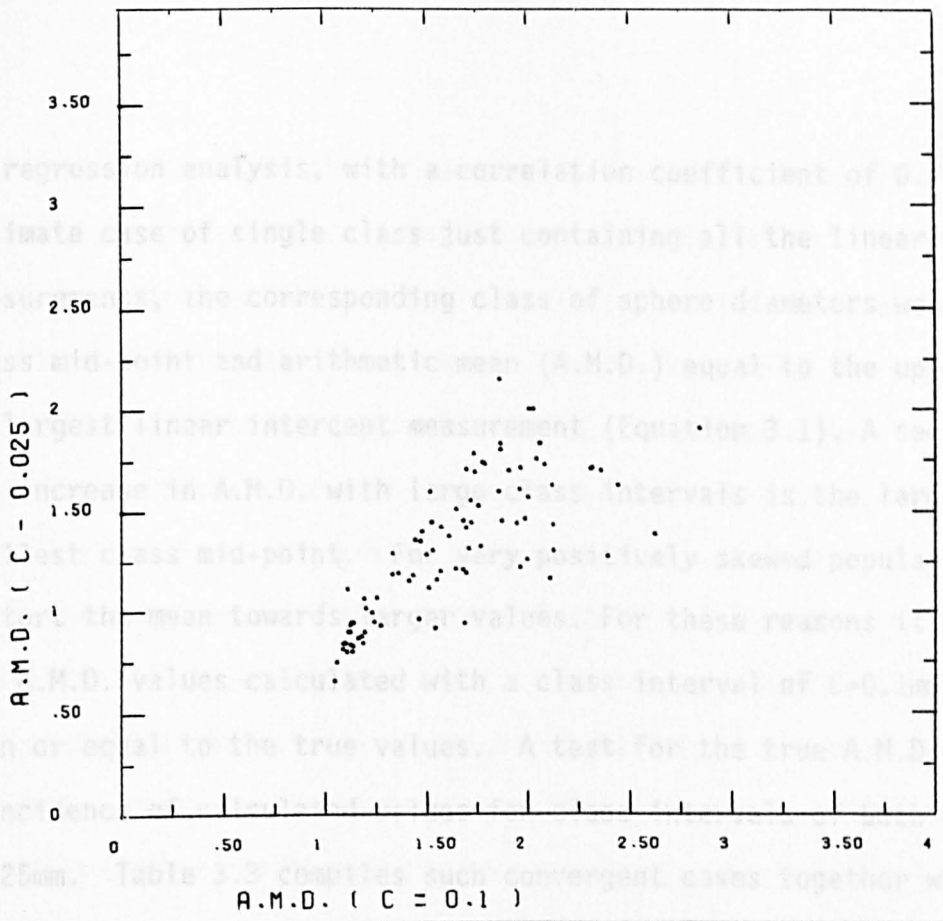

FIGURE 3.5. The relationship between the Arithmetic Mean of Sphere Diameters (A.M.D.), class interval C = 0.025mm, and A.M.D. class interval C = 0.1mm. A.M.D. (C = 0.025) is much less than A.M.D. (C = 0.1). A.M.D. increases with class interval, C. The values of A.M.D. (C = 0.1) are greater than or equal to true values, while those of C = 0.025 are generally less than the true values. The relationship is A.M.D. (C = 0.025) = A.M.D. (C = 0.1) x 0.668 + 0.0219, R = 0.773.

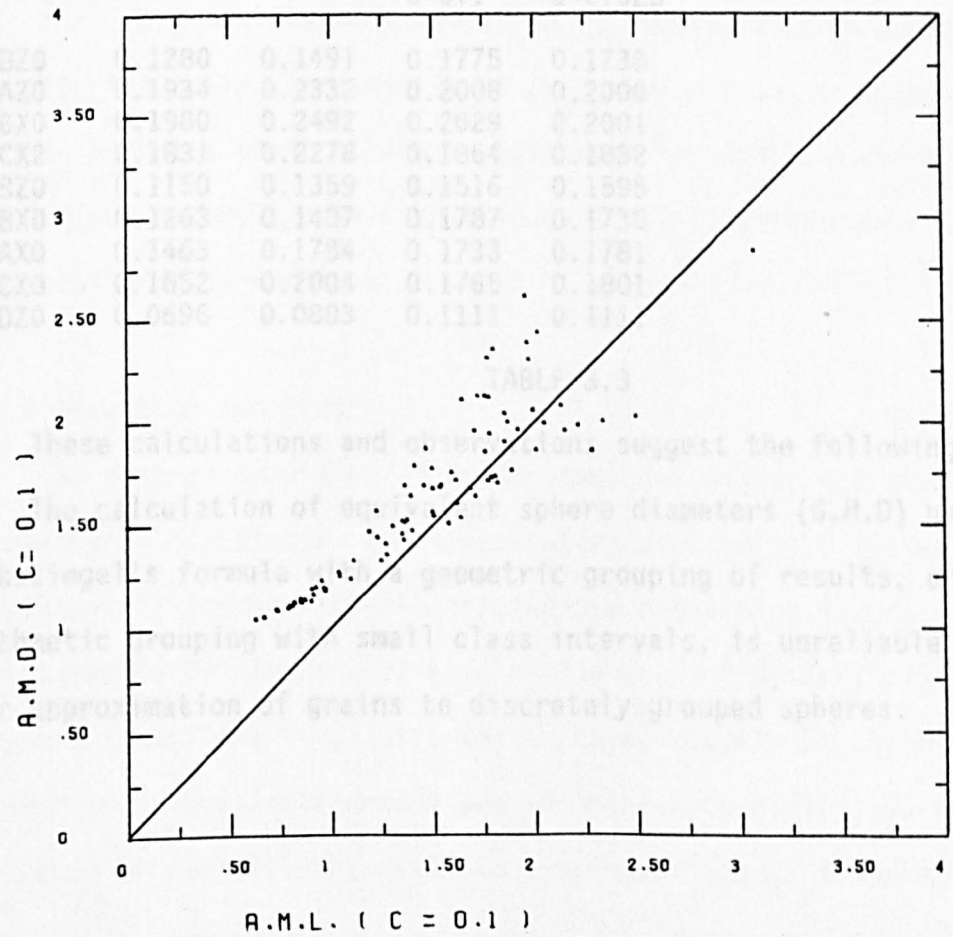

FIGURE 3.6. The relationship between Arithmetic Mean of Sphere Diameters (A.M.D.), class interval 0.1mm, and Arithmetic Mean of Linear Intercepts (A.M.L.). The A.M.D. = A.M.L. line is shown. A.M.L. is thus a good approximation to A.M.D.

on regression analysis, with a correlation coefficient of 0.773. In the ultimate case of single class just containing all the linear intercept measurements, the corresponding class of sphere diameters would have a class mid-point and arithmetic mean (A.M.D.) equal to the upper class limit or largest linear intercept measurement (Equation 3.1). A second reason for the increase in A.M.D. with large class intervals is the large size of the smallest class mid-point. For very positively skewed populations, this may distort the mean towards larger values. For these reasons it follows that the A.M.D. values calculated with a class interval of C=0.1mm are greater than or equal to the true values. A test for the true A.M.D. value is the coincidence of calculated values for class intervals of both 0.1 and 0.025mm. Table 3.3 compiles such convergent cases together with the G.M.L. and A.M.L. values, and shows that in these cases both the G.M.L. and the A.M.L. values are within maximum measurement error of the A.M.D. value, with the A.M.L. slightly closer.

SECTION	G.M.L.	A.M.L.	A.M.D. C=0.1	A.M.D. C=0.025
008BZ0	0.1280	0.1491	0.1775	0.1738
011AZ0	0.1934	0.2332	0.2008	0.2000
011BX0	0.1980	0.2492	0.2029	0.2001
011CX2	0.1831	0.2278	0.1864	0.1832
105BZ0	0.1150	0.1359	0.1516	0.1595
106BX0	0.1263	0.1407	0.1787	0.1730
109AX0	0.1463	0.1784	0.1733	0.1781
109CX0	0.1652	0.2004	0.1765	0.1801
0V1DZ0	0.0696	0.0803	0.1111	0.1111

TABLE 3.3

These calculations and observations suggest the following conclusions:

i) The calculation of equivalent sphere diameters (G.M.D) using Bockstiegel's formula with a geometric grouping of results, or with an arithmetic grouping with small class intervals, is unreliable due to the poor approximation of grains to discretely grouped spheres.

ii) The equivalent sphere diameters calculated with a class interval of 0.1mm are greater than or equal to the true values.

iii) Where true values can be identified by the convergence test, the similarity of the A.M.D. to the A.M.L. suggests that the sampling and truncation effects are approximately equal and opposite.

iv) The arithmetic mean of linear intercept measurements (A.M.L.) is potentially the most accurate measurement of grain size, taking account of both the sampling and truncation effects. This is shown in Figure 3.6, in which the A.M.D. values are scattered around the A.M.D.=A.M.L. line, but concentrating slightly on the higher side. This is because they are slightly greater than the true values (see ii above).

v) The grains can be satisfactorily approximated as spheres to allow for the sampling and truncation effects with a class interval of 0.1mm. However, more realistic models of grains, such as polyhedra, give larger numbers of small intercepts. This indicates that the A.M.L. value may be a slight underestimate of the true grain size.

vi) The G.M.L. is the most useful of all the parameters used to characterise grain size in this study because it has been calculated to a greater accuracy than the A.M.L. Although the G.M.L. is slightly less than the A.M.L. and true grain size (Figure 3.3), it allows more accurate comparative measurements.

3.3.4 Precision and Error

The maximum precision of measurement determines the precision necessary in calculation and presentation of results. The value is approximately 1mm in both the tracing and digitising stages: this is equivalent to 0.001mm on the thin section. Four decimal places for the results (in mm) are thus sufficient. Three sources of error are introduced. Very small errors due to inaccurate digitising have been evaluated by redigitising a single tracing of linear intercepts: Files

0011CX0 and 0011CX2 (Appendix A1) compare such data, and show that average individual error on 108 readings is +/-0.0028mm, while the error in the G.M.L. is +/-0.0006mm (Table 3.4). However, much larger errors result in A.M.D.: +/-0.0158mm. Errors are also introduced at the tracing stage: these are potentially more important due to the difficulty of identifying grain boundaries on the shadowmaster. Tracing and Digitising errors together are compared in files J012A2 and K012AZ by retracing and redigitising the same area of section 012AZ. The error in G.M.L. is +/-0.0014mm while again the error in A.M.D. is very much greater: +/-0.0134mm (Table 3.4). Finally, the most serious source of error is likely to be the limited area of sampling from the section, which may show marked changes in grain size due to graded bedding even on the scale of a thin section. An attempt to evaluate the combined effect of these errors was made by measuring two different areas of section 016A (Files 0016AX0 and 0016AX2, Appendix A1). Errors for the G.M.L. and A.M.D. are 0.0026 and 0.0316mm, or 2% and 17% respectively (Table 3.4). However, one of these files has an exceptionally low sample size so that these errors are likely to be a maximum estimate.

SOURCE OF ERROR	ERROR IN G.M.L. (mm)	ERROR IN A.M.L. (mm)	ERROR IN A.M.D (C=0.01) (mm)
Digitising	+/-0.0006	+/-0.0000	+/-0.0158
Digitising & Tracing	+/-0.0014	+/-0.0018	+/-0.0134
Digitising, Tracing & Sample Heterogeneity	+/-0.0026 =2%	+/-0.0023 =1.5%	+/-0.0314 =17%

TABLE 3.4

This error analysis shows that errors are lowest for A.M.L. and highest for A.M.D. The low errors in A.M.L. can be attributed to the approximation in calculation (the A.M.L. value was calculated from the grouped data, compared to the calculation from individual values used for the G.M.L.). The high errors for A.M.D. seem to be intrinsic in the

formula allowing for the sampling and truncation effects.

3.4 OPTICAL MICROSCOPY AND POINT COUNTING

The majority of optical microscopy used a Leitz binocular microscope fitted with an eyepiece micrometer for accurate length measurements. To assist the description of microstructures, classification systems were devised for grain boundaries, porosity, and components of the thin sections for point counting.

3.4.1 Grain Boundary Types

A very marked and important variation was observed in grain boundaries, which are described in this section, and illustrated by sketches in Figure 3.7. A brief interpretation is given based on observations of all thin sections.

i) Type 1. Grain boundaries are narrow and straight, generally between grains showing no optical strain features. Type 1a are distinguished from 1b by the visibility of obvious overgrowths in optical continuity with the host grain, which is marked by a line of small oxide inclusions. Quite often there may be a very slight mismatch between the orientation of the overgrowth and host grain, never more than 2^{o}. Both type 1 boundaries are interpreted as contacts between quartz cement and overgrowths.

ii) Type 2. Narrow, curved, boundaries which may truncate the original grain boundaries as marked by a line of inclusions. The curvature is invariably concave towards the grain with the smaller radius of curvature. In type 2a, the boundary is smooth, only slightly curved, and generally between two elongate grains of similar size and shape, with the type 2a boundary parallel to the long axes of the grains. The type 2b boundaries are more indented and may have patches of iron oxides at the crests and troughs of the undulations; they look like miniature stylolites. Both types

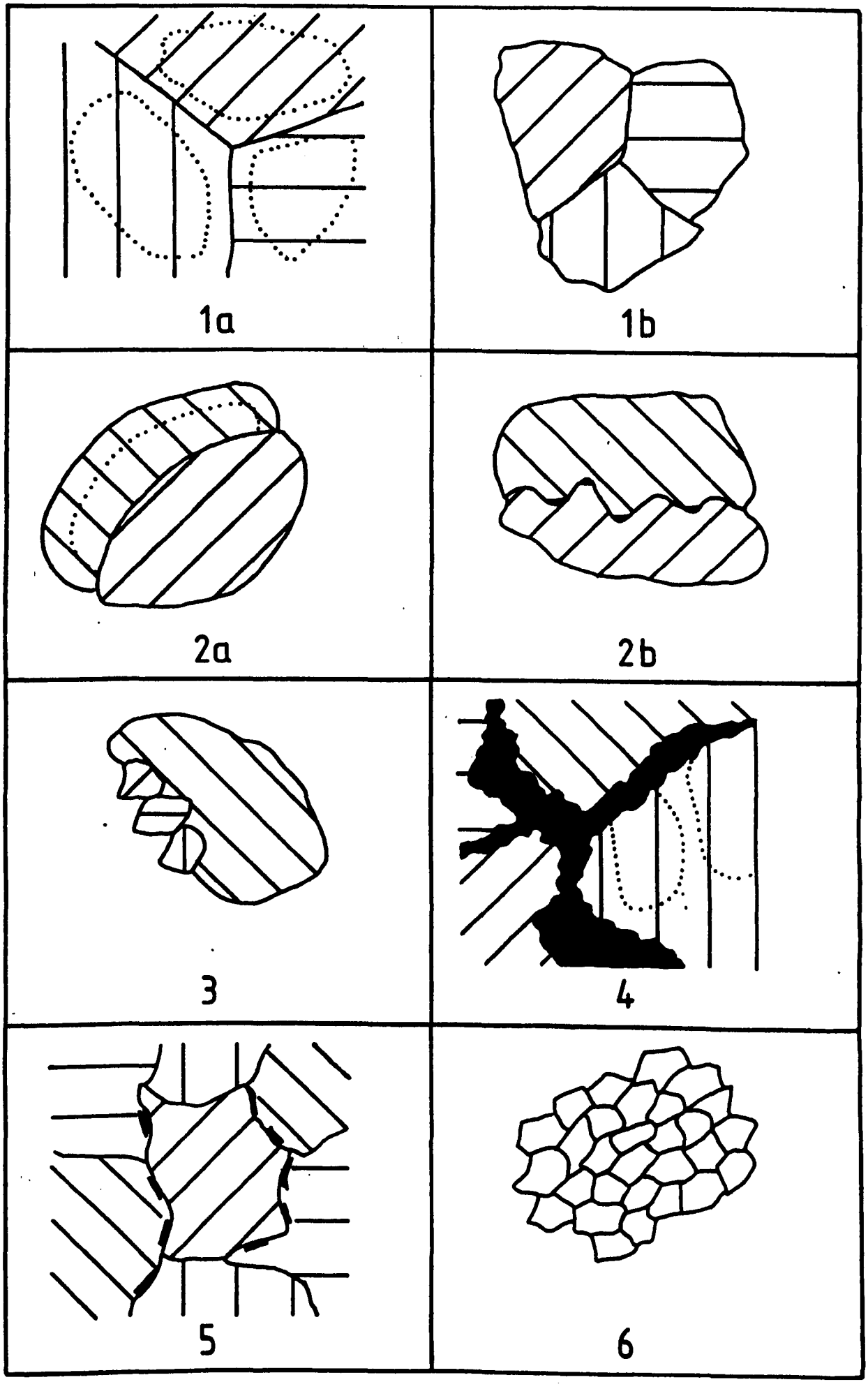

FIGURE 3.7
A classification of Grain Boundary Types. See 3.4.1.

are taken as the product of solution transfer.

iii) Type 3. Narrow, indented boundaries between one large grain and several smaller grains, usually strain-free, which may have only a small mismatch from the larger grain. The latter often has a high extinction angle, A, and possibly subgrains. These boundaries are formed by partial recrystallisation by either grain boundary migration, or sub-grain rotation.

iv) Type 4. Wide, irregular boundaries, which may truncate original grains and surround small fragments of grains. Type 4b are distinguished by the presence of iron oxides filling the wide boundary. Isotropic solution is partly responsible for this texture, but much of its primary.

v) Type 5. Narrow, straight or curved boundaries, decorated by small patches of amorphous clay or needles of white mica. This distinctive type of boundary indicates grain growth accompanied by recrystallisation of clays to mica.

vi) Type 6. Narrow, straight, undecorated boundaries, around small strain-free grains. Where these are equant, triple boundaries with 120^{0} angles are common; with a shape fabric, variable angles occur. The small size of the grains is responsible for the abundance of inclined grain boundaries which show as wide bands although the grain to grain contact on the surface of the section is still sharp. These boundaries are the result of a high proportion of dynamic recystallisation, possibly with some annealing.

3.4.2. Porosity Types

Porosity is more difficult to classify than grain boundaries due to the intermergence of all types, but four types can be classified on the basis of habit (Figure 3.8). Exactly similar types of spaces to open pores are frequently filled by iron oxides and more rarely clays: these are therefore also classified as porosity and not distinguished in the

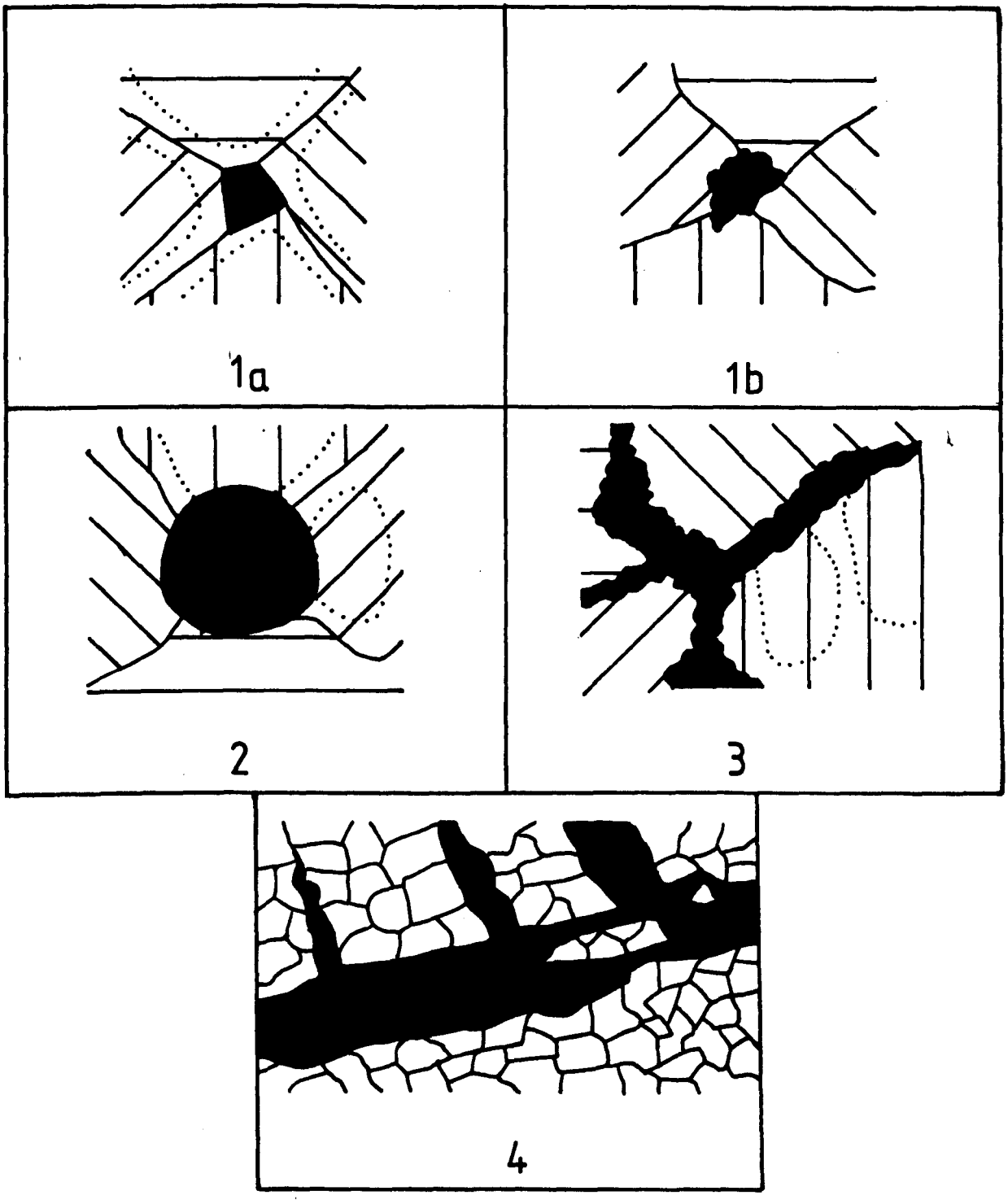

FIGURE 3.8
A classification of Porosity Types. See 3.4.2.

nomenclature from open pores.

i) Type 1. Grain Junction porosity. Type 1a is distinguished by polygonal shapes left between overgrowths; in type 1b, the shape is irregular. Type 1a is clearly primary porosity left after cementation, but type 1b may be either primary or secondary.

ii) Type 2. Large, isolated pores, which cut both grain boundaries and cement, often approximately the same size as larger grains and circular in shape occurring at well spaced intervals through intact rock. These are noticeable particularly in very well cemented rocks as the only form of porosity; in less well cemented examples, they may have irregular boundaries. They are interpreted as porosity left at the final stage of cementation as channels or isolated pores. Those with irregular boundaries may have undergone some secondary solution.

iii) Type 3. Grain Boundary porosity. Wide, irregular, type 4 grain boundaries contain this type of porosity, and grade into irregular type 1b grain junction porosity. It is found in poorly cemented rocks, and like the type 4 grain boundaries, is interpreted as the product of secondary solution.

iv) Type 4. Fracture Porosity. Fractures may contribute large amounts of porosity both as linear fractures and irregular shapes within a fracture filling.

3.4.3. Point Counting Technique and Classification

All point counting on the Leitz microscope was carried out with x10 eyepiece and objective lenses, giving a field of view of 1.39mm, and using a jump interval of 1/3mm between stops. 500 stops were made for each section along evenly spaced traverses such that more than 80% of the section was examined. The results from each of the three perpendicular thin sections/sample were averaged and are given as percentages in Appendix A3. Seven components of the quartzites were identified:

1. Quartz grains and any other obviously clastic grains, including feldspar, mica, epidote and heavy minerals.
2. Quartz overgrowths. Due to the general difficulty of identifying these, this component was abandoned and merged with the first.
3. Shear matrix. Fine grained quartz cement and fragments of grains.
4. Iron oxides in Shear Matrix. Patches, veins and fragments of dark brown and opaque oxides, and pore linings and fillings.
5. Iron oxides in intact quartzite. Patches, pore linings and fillings of oxides.
6. Authigenic clay minerals and phyllosilicates. Patches and pore fillings of clays, and needles and tablets of phyllosilicates were distinguished mainly on the basis of size from detrital layer silicates.
7. Open porosity.

3.4.4. Error

Two sources of error can be identified in the point count measurements: incorrect assignment of components and sample heterogeneity. Six sections were recounted to evaluate the accuracy of the method; the results are shown in Table 3.5. The difficulty of assigning components particularly affects categories 3 and 4 compared to 1 and 5; it is often hard to distinguish genuinely fragmented grains in category 3 from merely corroded grains which belong to category 1, and likewise to separate iron oxides in shear matrix from those in intact quartzite. This factor is responsible, for example, for the discrepancies between original and repeated measurements of categories 3 and 4 in sectios 9A and 17A. The effect of sample heterogeneity can be seen in the measured differences in porosity in any of the samples: this error is very unlikely to be due to incorrect identification. An average figure for absolute error derived from table 3.5 is +/-1.5%, although this does not include instances where

no value has been recorded in one set of readings.

	1+2	3	4	5	6	7
33C	89.8	0.8	0.0	4.4	0.2	4.8
33C Repeat	88.4	2.4	0.6	5.2	0.0	3.4
111Y	91.0	4.8	0.0	3.8	0.2	0.0
111Y Repeat	89.8	3.8	1.0	4.6	0.2	0.6
9A	69.2	18.6	3.2	7.4	0.2	1.0
9A Repeat	77.6	11.4	3.6	6.2	0.4	0.8
27A	82.2	2.0	0.6	13.4	0.4	1.4
27A Repeat	72.6	8.2	1.0	16.8	0.2	1.2
17A	77.6	0.0	0.0	5.4	5.8	11.2
17A Repeat	73.4	3.6	1.0	11.0	3.8	7.2
1A	93.0	0.0	0.0	6.2	0.0	0.8
1A Repeat	92.8	0.0	0.0	2.2	0.4	4.6

3.5 STRAIN MEASUREMENTS

3.5.1 A Classification of methods of determining the strain ellipsoid

Due to the plethora of methods that have been suggested for determining three dimensional strain, a classification of types of method, and the procedure for calculating strain, is presented in Figure 3.9 and used as the basis for the structure of this sub-section. The first distinction is between measurements which are made initially in two dimensions, and those using three-dimensional data ab initio. The second distinction is between the three types of strain marker: those for which the initial state is known, those for which it is assumed, and those for which an empirical relationship to strain is established by use of an

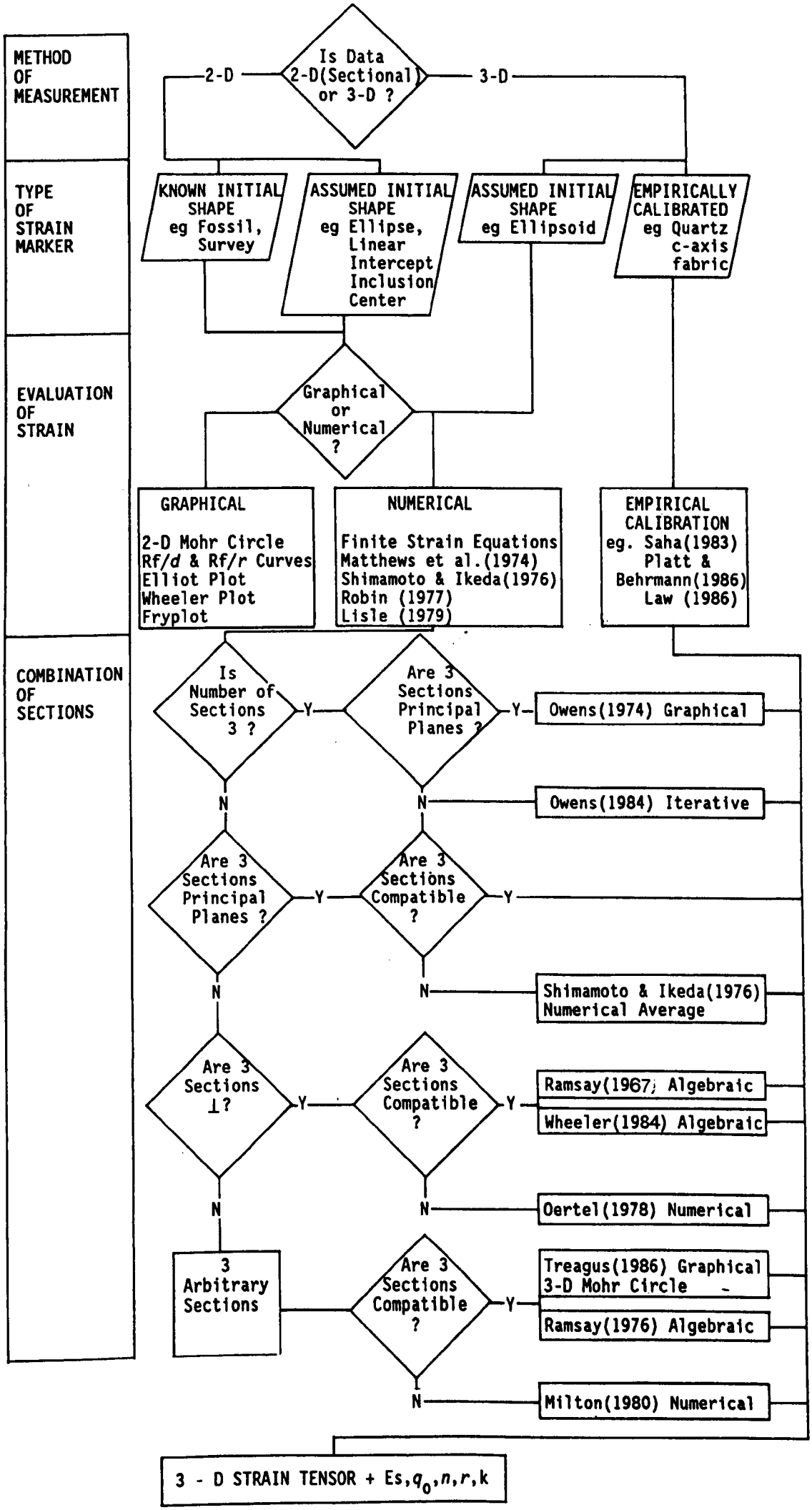

FIGURE 3.9

A classification of methods of determing strain ellipsoid.

independent method. The evaluation of strain from the measured data may be numerical or graphical (Figure 3.9). A final stage in the case of 2-dimensional measurements is the combination of at least three such measurements to give the complete three dimensional strain tensor. After stating the basic assumptions common to all strain determination, this sub-section reviews most of the methods of calculating 2-dimensional strains, their combination into three dimensions, and methods of calculating strain from measurements in three dimensions. Each method is described briefly and referenced before additional limitations and advantages are discussed. Finally the method used for this study is given in more detail and justified.

3.5.2 Basic Assumptions

All methods reviewed here make the assumption that strain is continuous (penetrative) on the scale of the measurements. Strain discontinuities on the scale of observation (e.g. faults, stylolites or shear zones) can usually be observed; in these cases strain measurements will give only the penetrative component of strain. Many examples of polymict conglomerates are known which clearly violate this assumption, while quartz anisotropy is considered to have distorted Rf/ϕ distributions in some cases (Lisle, 1985 p.25). Lisle and Freeman (1985) have also shown the influence of anisotropy in different clasts from the same conglomerate. Additionally it may be stated that all methods using axial ratios of deformed objects assume constant volume, and that all methods with the exception of the treatment of inclusions by Gay (1968), Bilby et al. (1975), Cobbold and Gapais (1983) and Lisle et al. (1983) assume homogeneous strain. This has two important implications: firstly that strain markers forming a significant volume fraction of the rock have no ductility contrast with the matrix, and secondly that they deform isotropically. Given these assumptions and certain others in specific

cases, the strain measured by any of the methods is the total finite strain.

3.5.3 Reviews of Methods

a) 2-Dimensional Data

i) Strain Markers with known initial state. The ideal strain marker is one which can be accurately described in the undeformed state. This can apply to fossils and to cartographic data from surveying. In this case, a very few measurements can give the accurate two dimensional strain: for example change in two angles and a measurement of the λ_1 direction or change in the length of three lines and their orientations can give the strain. Strain can be calculated from equations or evaluated graphically by the two dimensional Mohr circle construction. (Useful procedures are summarised in Ramsay 1967, Ramsay and Huber 1984.) There are no additional assumptions, but such ideal strain markers are not common so that the method is limited.

ii) Strain Markers with assumed initial state. Strain markers are regarded as inclusions in a deforming matrix. When these are taken as ellipses, the axial ratio (Rf) and orientation with respect to a reference line (ϕ) is measured, giving the Rf/ϕ method, various derivatives and numerical solutions. Regarding markers as points is the basis of the centre-to-centre techniques. All methods based on ellipses assume that a valid approximation of markers to this shape can be made. Problems of defining the ellipse in deformed ooids were encountered by Cloos (1947) because the ends of the ooids fray. Robin (1977) has given a method for the use of markers of any shape in certain circumstances.

The Rf/ϕ method was formalised first by Ramsay (1967) from the work of Cloos (1947). The basis of the technique is graphical: a plot of Rf against ϕ allows the determination of the tectonic strain (Rs) and the initial fabric (Ri) for some further assumptions about the initial fabric.

The Rf/ϕ method (sensu stricto) refers here only to graphical treatment including the method of estimating Rs and Ri from intercepts on the axis of symmetry, and both the Ri and θi curve fitting methods. The current use of, and limitations of the Rf/ϕ technique are comprehensively summarised by Lisle (1985).

A general limitation on the Rf/ϕ method is that the initial fabric must be assumed to be random. However Lisle (1985) has shown that it is possible to obtain reasonable Rs values for an initial orientation by using only the particles with low Ri. This assumes that particles with low Ri have effectively a random distribution, and requires a larger data set. It is also possible to make the assumption that the initial fabric was symmetrical about bedding, or even more generally, simply symmetrical. All these additional assumptions can be tested for the Rf/ϕ plot.

The major advantage of the Rf/ϕ method is accuracy for a given sample size. Paterson (1983) compared most of the techniques reviewed here on data from conglomerates. He concluded that the Rf/ϕ technique needed the fewest clasts to achieve a precision of 10% of all the graphical methods. His Table 7 also shows that the θ curve method gave the lowest Rs values: this can be taken to indicate the most accurate result since the less accurate methods tend to give higher Rs values. Of almost equal benefit from using the Rf/ϕ procedure is the fact that it is now very well established and a comprehensive standard procedure has been published (Lisle 1985).

Elliot (1972) proposed an alternative graphical treatment of ellipsoidal object data. In his polar plot, natural strain (Ef=1/2 ln Rf) is plotted against twice the angle to the reference direction, 2ϕ. Superimposing his "shape factor grid" on such a plot gives Es, Ei and θ directly. Random initial shape fabrics plot in the deformed state as egg shapes; unimodal distributions as delta or heart shapes, and bimodal symmetric initial fabrics as cigars and bananas. The Elliot polar plot

technique has exactly the same limitations as the Rf/ϕ technique since it is based on the same data. The comparative advantage of the polar plot is that the presence and type of initial fabric is easily visible.

The third graphical technique, also based on ellipsoidal object data is due to Wheeler (1984). A polar plot with a radial co-ordinate 1/2 (Rf-1/Rf) instead of Ef is made. Similar characterisations of deformed initial fabrics can be made; for example an initial unimodal fabric will deform into an ellipse.

The Wheeler equivalent of the Shape Factor Grid has only hyperbolic and straight lines, and families of ellipses of constant Ri for various values of Rs can be fitted in a similar way to onion curves on a conventional Rf/ϕ plot. Unstraining deformed Rf and ϕ values on the grid is done simply by moving points along straight lines parallel to the ellipse long axis which lies in the same direction as $\lambda 1$, since coaxial deformation paths plot as straight parallel lines rather than the curved lines of the Elliot grid. The Wheeler plot is clearly also subject to the same limitations as the Elliot plot and shares its strength in identifying initial fabrics. However the Wheeler plot has a major advantage over the former in the simple geometry of ellipses that can be used to find Ri and Rs, and the representation of coaxial deformation by straight lines. A lesser advantage is that the radial co-ordinate is also a parameter used in the Shimamoto and Ikeda numerical method to describe the strain (see below). Due to its recent invention, there has not been sufficient time for the Wheeler plot to become as widely appreciated or used than either Rf/ϕ or Elliot plots.

The first numerical method of 2-D strain calculation described here due to Matthews et al (1974), is also based on Rf/ϕ data, and requires in addition a measured value for the angle between cleavage and bedding, $\phi c = \phi s$, observed in the plane of section. The bedding trace is chosen as the x reference axis. The method factorises strain into a stretch parallel to

the x-axis, α, and a shear γ in this direction. It is shown that the average γf values ($\bar{\gamma}f$) and ϕs give the strain ratio by the following formulae:

$$\bar{\gamma}f = 1/n\sum_{1}^{n}((Rf^2 - 1)\tan\phi/(1 + Rf^2\tan^2\phi))$$

$$Rs = \frac{(\sin\phi s \cos\phi s + \gamma f \cos^2\phi s)^2}{(\sin\phi s \cos\phi s - \gamma f \cos^2\phi s)}$$

Secondly, statistical tests are presented that discriminate

-initial random or symmetric fabrics from asymmetric fabrics based on a χ^2 test and

-initial random from initial symmetric fabrics.

This test is based on the fact that the calculated value of Rs will be independent of ϕs for initially random fabrics (which has the additional implication that the reference direction for these fabrics is not confined to the bedding trace and may in fact be arbitrarily chosen). Thirdly, the fractional error, ER, in the strain determination is given in terms of the observed standard deviation of the mean γf values.

Fourthly, the converse problem of relating the minimum sample size required to achieve a given accuracy is solved for the general case of random or symmetric fabrics:

$$n_m = 4\ V\gamma i/ER$$

where $V\ \gamma i$ = Variance of γi

and for the specific cases of initial random fabrics and for initial symmetric fabrics (in which case the minimum sample size will depend on the value of ϕs as well as Rs). Lastly a procedure is described for destraining the final fabric to give the initial fabric. The Matthews method is based on all the usual assumptions for inclusion type strain markers which are approximated to ellipses, including the initially random or symmetrical fabric assumption, although tests for this are described. There is however one additional important assumption that is not mentioned

by the authors: that the cleavage trace represents the direction of the $\lambda 1$ axis. Two further limitations for practical application of the method are that bedding and cleavage must be clearly visible. In spite of the mathematical rigour of the analysis, it is a fairly complex procedure. Shimamoto and Ikeda (1976) present a greatly simplified and equally rigorous numerical method, which also treats deformation of ellipses and ellipsoids by matrix algebra. The initial fabric and the strain are both represented by the same simple matrix representation of an ellipse, which combine to give the final shape matrix.

They prove that the average components of the final shape matrix give the strain matrix for an infinite sample. The lengths of the principle axes are obtained by solving for the eigenvalue of the shape matrix, from which the principle direction can also obtained:

Final Shape Matrix: $[x \quad y] \begin{bmatrix} \bar{f} & \bar{h} \\ \bar{h} & \bar{g} \end{bmatrix} \begin{bmatrix} x \\ y \end{bmatrix} = 1$

where $\bar{f} = \frac{1}{n} \sum_{i=1}^{h} fi$ etc

$$f = \frac{1}{R} \cos^2\phi + R\sin^2\phi$$

$$g = \frac{1}{R} \sin^2\phi + R\cos^2\phi$$

$$h = \left(\frac{1}{R} - R\right) \sin\phi \cos\phi$$

The values of λ_1 and λ_2 are the eigenvalues of the Final Shape Matrix, obtained by solving the quadratic:

$$\begin{vmatrix} f-\lambda & h \\ h & g-\lambda \end{vmatrix} = 0$$

and the characteristic direction is given by

$$\tan 2\phi = \frac{2h}{f-g}$$

Error analysis is treated by modelling initial samples of 50 randomly orientated ellipses with various normally distributed axial ratios subjected to pure shear. A rotational component of strain does not significantly affect the errors. The results, which confirm those of the Matthews analysis, are intuitively obvious:

i) The percentage error in Rs, ER, increases with Ri.

ii) ER decreases with Rs.

iii) The percentage error in ϕs increases with the difference between the average initial shape orientation, ϕi, and the final strain ellipse orientation, ϕs.

iv) For a sample size of 50, ER is always less than 10% for values of Ri up to 2.8.

v) For sample sizes ranging between 10 and 300 ER is always less than 16.7 x A.M.Ri for Rs = 1.5, where AMRi is the arithmetic mean of Ri: there seems to be an upper limit to ER for a given value of Ri. In a comparison of 2-D strain measurements made from quartzites, limestones and polymict conglomerates from the Main Coastal Belt, Paterson (1983) found that this method gave the most precise results, with sample sizes as low as 10.

The Shimamoto and Ikeda analysis is severely constrained by all the limitations of ellipsoidal inclusion-type strain analysis and the assumption of an initially random fabric. No tests are suggested for this assumption. However the method is extremely simple, can produce accurate results with sample sizes as low as 10, and the Wheeler graphical method is based on the same matrix approach.

Robin (1977) proposed a simple method for measuring Rs and ϕ from linear intercepts and proved that the method was theoretically correct given the additional assumption that the linear intercepts were measured in the λ_1 and λ_3 directions. The elegant proof is worth giving, for it has some important consequences. In the unstrained state, with the usual assumptions of initially random orientations and shapes of strain markers,

$$\prod_{j=1}^{n} a_j/c_j = (a_1/c_1)\ (a_2/c_2)\ (a_3/c_3)\ldots\ (a_n/c_n) = 1$$

where a,c = linear intercepts in λ_1 and λ_2 directions, and since a, c are measured in the λ_1 and λ_2 directions in the strained state, represented by ′,

$$a'_j = (\lambda_1)^{1/2}\ a_j \text{ and } c'_j = (\lambda_3)^{1/2} c_j$$

$$\prod_{j=1}^{n} a'_j/c'_j = (\lambda_1/\lambda_3)^{n/2} \prod_{j=1}^{n} a_j/c_j$$

$$= (\lambda_1/\lambda_3)^{n/2}$$

From this it is shown here that the strain ratio is the Geometric Mean of the ratio of linear intercepts; G.M.a/G.M.c;

$$(\lambda_1)^{1/2}/(\lambda_3)^{1/2} = Rs = (\prod_{j=1}^{n} a'/c')^{1/n}$$

$$= G.M.Rf$$

$$= \prod_{j=1}^{n} (a'_j)^{1/n}/(c'_j)^{1/n}$$

$$= \frac{G.M.a}{G.M.c} \quad Q.E.D$$

Where G.M.Rf etc. are the geometric means.

If the λ_1 direction is unknown, it can be found by maximising λ_1/λ_3 as a function of ϕ. One of the main benefits of Robin's contribution lies in his insight that the linear intercept measurements can be made on strain markers of any shape: not only are the usual constraints of assuming an ellipsoidal approximation avoided, but there is potential for using larger variety of objects as strain markers. The chief limitation is the necessity of identifying the λ_1 direction.

The final numerical method is the simplest of all. Lisle (1977a) has shown that the harmonic mean of Rf and the Vector Mean of ϕs can provide a useful quick estimate of Rs and ϕs.

$$\text{Harmonic mean, } HMRf = N/\prod_{i=1}^{N} 1/Rf_i$$

$$\text{Vector mean, } VMRf = 1/2 \tan^{-1}\left(\prod_{i=1}^{N} \sin 2\phi i / \prod_{i=1}^{N} \cos 2\phi i\right)$$

This method gives an overestimate of Rf which increases with Ri. The overestimate can be allowed for by making an estimate of Ri or assuming a typical value from published data on the type of strain marker in use: Lisle (1985) gives a graph of how HMRf relates to Rs for various values of Ri. Siddans (1980) reported an overestimate of 12.6% for the harmonic mean.

Although the method is subject to the theoretical limitations of a random initial fabric, experience suggests that errors are not much greater than for any of the other methods. The great simplicity of the method, lending itself readily to evaluation on a pocket or programmable calculator, and allowing its use in the field, is its major attraction.

The final two dimensional strain analyses to be considered are the graphical "centre-to-centre" techniques. Plots are prepared by choosing each strain marker in turn as the origin and showing the positions of other strain markers around. The distribution of markers with distance along any azimuth of the plot will reflect the spacing of markers in this direction in the deformed rock. Thus a strain ratio and azimuth can be measured from the maximum and minimum mean (or modal) distance of markers from the origin, i.e. the axis of the ellipse formed by the markers. The original method used only "nearest neighbours", but Fry (1979) pointed out that clustered distributions of markers will not be accurately represented and introduced the "all object" separation plot in which all other markers are plotted, thus sampling both clustered and anticlustered space equally. An important misconception about the Fryplot is that the central area which contains no points represents the final sh ape ellipse. This central area delineates only minimum object-object separations, which may have a significantly different shape from the shape ellipse for two reasons:

firstly, if combinations of strain markers with different initial shapes are used, the central clear area is then defined by the superimposition of two shape fabrics, and thus corresponds to neither of them individually. This effect has been demonstrated and modelled by Lacassin and Van Den Driesche (1983). Secondly, shape fabrics with an initial orientation will be reflected in the central area: this effect is shown in Figure 3.10. The figure also shows that the mean final shape fabric defined by the Fryplot will only correspond to the strain ellipse for an initially isotropic distribution of strain markers. This is the most important additional limitation on the use of the method. It can, however, be tested by identifying the initial shape fabrics from the type of pattern shown in the Figure. The major advantage of the Fry method is that large amounts of data can be collected extremely quickly by digitising, and that the Fryplot gives a direct measurement of strain without the need for further calculation. It also has the advantage of all the graphical methods that initial fabrics can be identified.

b) Combination of 2-Dimensional Strain Data to give the Strain Ellipsoid. Methods for combining planar section data to give the strain ellipsoid have been given for data on three sections parallel to the principal planes of the ellipsoid (Ramsay 1967, Shimamoto and Ikeda 1976), for data on three arbitrary but mutually perpendicular planes (Ramsay 1967, Helm and Siddans 1971, Oertel 1978 and Siddans 1980), for three completely arbitrary planes (Milton 1980, Gendzwill and Stauffer 1981, and Owens 1984). Both graphical and numerical methods have been proposed.

Any of these methods are subject to the difficulty that the measured section ellipses may not fit together along their mutual line of intersection due to measurement errors.

The following reviews the available methods for determining the strain ellipsoid, and how the problem of arriving at a "best fit" solution, due to incompatible section measurements, has been approached, depending on the

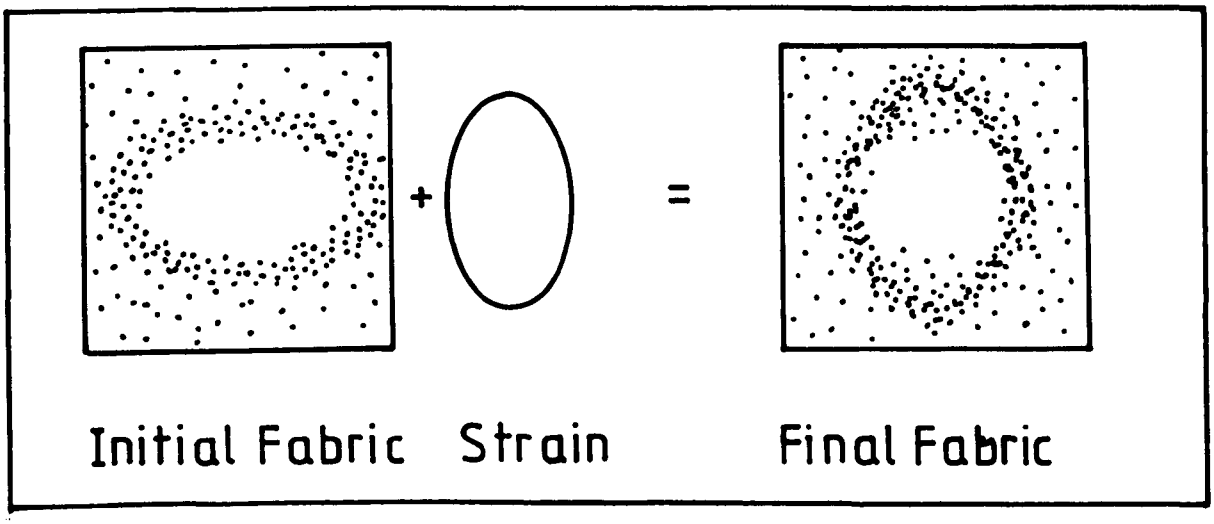

FIGURE 3.10
A Fryplot showing an initial fabric: the presence of an initial fabric means that the central clear area does not define the imposed strain; this is more accurately reflected in the strongest concentration of points.

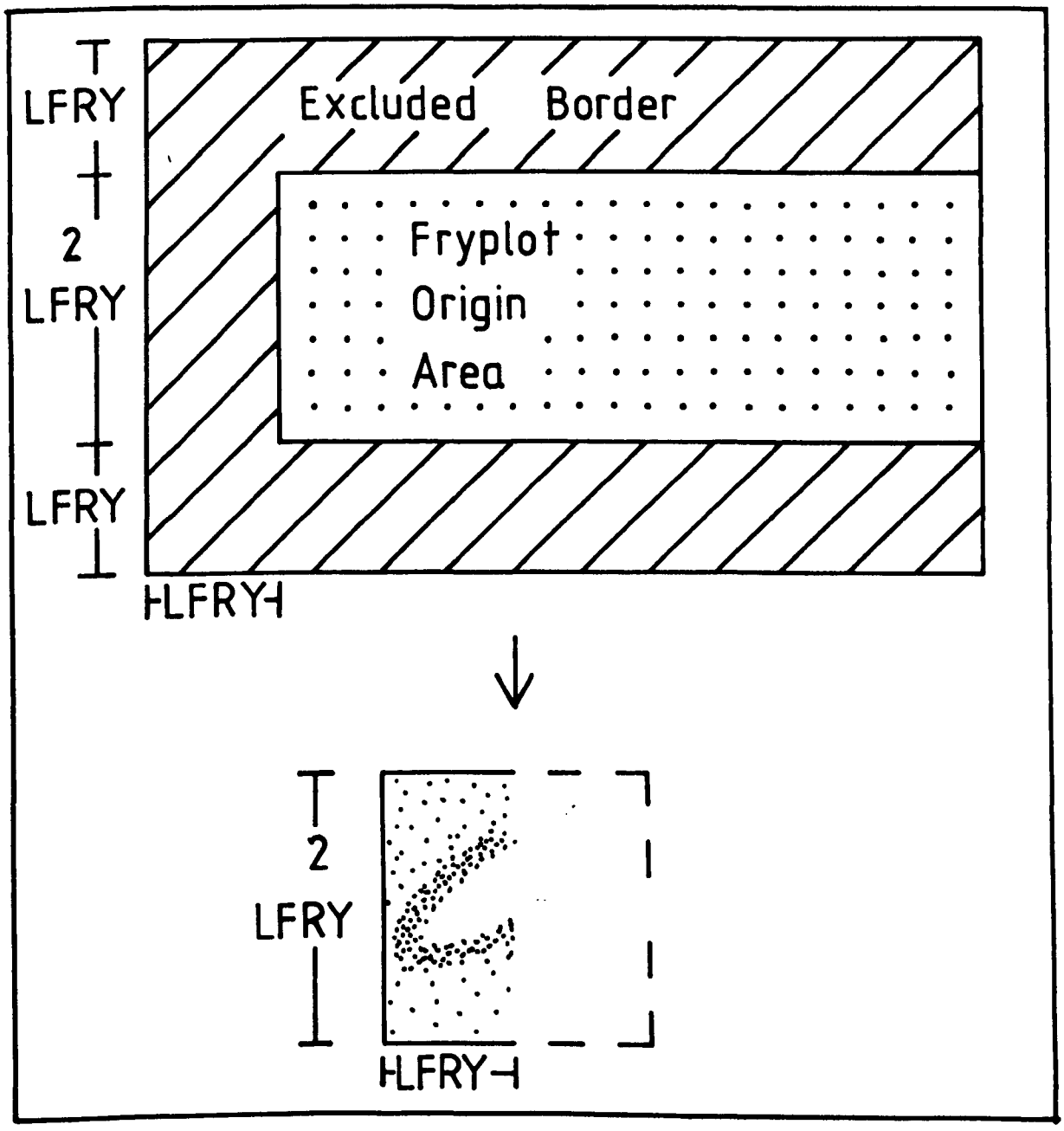

FIGURE 3.11
The Fryplot Origin Area. A border of half the dimension of the Fryplot dimension, LFRY, is omitted around three sides of the sample area in order to avoid distortions due to edge effects. The fourth side may be sampled because of the symmetry of the Fryplot.

type of measurements made.

i) Three sections parallel to the principal planes of the ellipsoid. In the simplest ideal case, compatible measurements give the strain ellipsoid directly. The orientation of the principal planes may be known from supplementary data, or, more commonly assumptions can be made, for example, that cleavage is perpendicular to λ_3 or that a lineation is parallel to λ_1. From non-compatible measurements, Owens (1974) proposed a graphical method in which a plot of E1, VS E2 VS E3 on a triangular diagram could be used to give a visual best fit. This approach has the advantage of great simplicity and rapidity, though not necessarily of high accuracy. A numerical approach is given by Shimamoto and Ikeda (1976). The strain ellipsoid is specified by five independent components:

$$[x\ y\ z]\begin{bmatrix} C_{11} & C_{12} & C_{13} \\ C_{21} & C_{22} & C_{23} \\ C_{31} & C_{32} & C_{33} \end{bmatrix}\begin{bmatrix} x \\ y \\ x \end{bmatrix} = 1$$

Since $C_{ij} = C_{ji}$ and $C_{22} = 1$ (size is arbitrary). However, strain ellipses measured on the three principal planes give six quantities (3 x axial ratio and orientation) specified in matrix terms by:

$$[x\ y]\begin{bmatrix} f_{xy} & h_{xy} \\ h_{xy} & y_{xy} \end{bmatrix}\begin{bmatrix} x \\ y \end{bmatrix} = 1 \quad [y\ z]\begin{bmatrix} f_{yz} & h_{yz} \\ h_{xz} & g_{yz} \end{bmatrix}\begin{bmatrix} y \\ z \end{bmatrix} = 1 \quad [x\ z]\begin{bmatrix} f_{xz} & h_{xz} \\ h_{xz} & g_{xz} \end{bmatrix}\begin{bmatrix} x \\ z \end{bmatrix} = 1$$

Incompatible section measurements mean that the ellipse components will not give the strain components, which are overdetermined. The f, h and g components can be related to the C_{ij} components in six possible ways depending on which components are assumed to be equal initially. Shimamoto and Ikeda proposed that the best fit ellipsoid will be a simple arithmetic average of the six possibilities. This is mathematically very simple and could be usefully applied when errors in determination of each of the section ellipses are equal.

ii) Three mutually perpendicular, arbitrary sections. The basic method for determining the ellipsoid in this case is given by Ramsay (1967, pp.142-147). Siddans (1980) proved that the method was justified by modelling deformation of a randomly orientated ellipsoid. The ellipse shapes on any three sections in the deformed state were calculated and then unstrained. The unstrained ellipses, measured on planes which became the section planes, were calculated and shown to be identical to the ellipses of the original ellipsoid on these planes.

Oertel (1978) has given a method for obtaining a best fit for incompatible data. The errors from the determination of the section ellipses are assumed to have a normal distribution, and they are used to give a weighting in the adjustment of the section ellipses to give a best-fit ellipsoid. It is mathematically rather complex.

iii) Three arbitrary sections. From data on arbitrary sections, Ramsay 1967 (pp.147-149) gave a method to construct the ellipsoid by first determining the ellipses on three orthogonal planes. Milton (1980) proposed to deal with incompatible strain ellipses on three arbitrary planes by superimposing an "adjustment ellipse" on each of the strain ellipses. These adjustment ellipses are weighted by a factor proportional to the size of the angle between the sections. A weighting for errors in determining each section ellipse can also be introduced. A method is also suggested to reduce the axial ratios of the adjustment ellipse to a minimum. The method is attractively simple.

A graphical method for determining the ellipsoid has also been proposed by Treagus (1986), using the Mohr Strain diagram for three dimensions. It appears to be complex, although has the advantage of not requiring any computation.

iv) Three or more arbitrary sections. The most recent and comprehensive method is due to Owens (1984). Two stages are followed: in the first, each element of the tensor of reciprocal quadratic elongations is arbitrarily set to unity. Treating each of the six elements of this matrix in this way gives six possible solutions for the strain ellipse. One of these solutions is used as the basis to obtain a best-fit solution by linear least squares. The sum of squares of the differences between observed and predicted values of a quantity related to the observed section ellipse axial ratios and orientations is minimised. These error vectors are used to adjust the tensor of reciprocal quadratic elongations to the best fit values, from which the principal axes and orientations of the strain ellipsoid can be obtained.

The program also produces the axial ratios and orientations on the observed section planes that would be predicted by the best fit solution. These can be compared to the actual data to indicate how well the solution fits the data. This is quantified by applying the reciprocal strain to the observed ellipse on each section plane. The axial ratios of these undeformed ellipses can give a measure of the goodness of fit of the solution: a parameter ρ, the weighted log mean of the undeformed axial ratios, approaches unity as the solution provides a better fit to the observed data.

The interpretation of ρ values is complicated by two factors: the number of sections used and the presence of an initial fabric. The fewer the sections, the greater chance of the ellipsoid fitting the data well. As the number of sections is increased, Owens shows how the ρ values progressively more towards a ρ value that characterises the initial fabric ("ρi"). The stronger the initial fabric, the greater the value of ρi and the further the ρ values will depart from unity for a given number of section planes. When these factors are taken into account, ρ is a useful parameter for evaluating the success of the solution, but not its accuracy.

The results of simulation runs of the method on synthetic data show that accuracy increases with sample size, with decreasing initial axial ratio, and with sections that are orthogonal rather than randomly orientated. Although the method is complex, it is the most comprehensive approach yet, and the only method given so far for using more than three sections.

c) Three-Dimensional Data

i) Strain markers with assumed initial shape. Measurements of strain markers in three dimensions could give the strain tensor directly if they can be assumed to have an originally spherical shape in addition to the other basic assumptions mentioned previously. However, for the more realistic case of an initial fabric, Shimamoto and Ikeda (1976) prove that, if the fabric is random in three dimensions, an infinite sample will give the strain ellipsoid by the arithmetic mean of each component of all the final shape matrices. The method cannot determine volumetric strain, but is of importance where strain markers are large enough to be measured accurately in three dimensions, for example, in conglomerates.

ii) Empirically calibrated strain markers. Quartz c-axis fabrics can be used in two ways as a strain-sensitive parameter. Lister and Williams (1979) have divided shear zone fabrics into those which rotate with the foliation, and those which remain fixed with respect to the flow plane. Numerous examples of rotational fabrics have been recorded (e.g. Carreras et al. 1977, Burg and Laurent 1978, Simpson 1980, 1982), which can therefore be used in the same way as the foliation to deduce the amount of simple shear, assuming no additional component of pure shear. Platt and Behrmann (1986) used measurements of fabric obliquities in conjunction with maximum principal elongations to show that tectonites in the Betic Cordillera, Spain, had a deformation history of essentially simple shear along mylonite zones, but variable amounts of pure shear in the nappes between mylonites. Intensity is the second aspect of fabrics that can be

related to strain: this was first proved by Saha (1983), who evaluated the intensity of c-axis preferred orientation by comparing the observed distribution to a random orientation. Using the coefficient of skewness as a measure of preferred orientation, he proved that it was directly proportional to natural strain, Es, for $0.65<Es<2.04$. This has also been shown qualitatively by Law et al (1984), and a direct proportionality between intensity of detrital grain c-axis fabrics and strain magnitude was established by Law (1986).

iii) Direct measurement of 3-Dimensional data. Direct measurements of fabrics are only practical for objects of sufficient size, e.g. pebbles, but this technique has been successfully applied to pebbles from the Laksefjord Nappe, Norway (Chapman et al. 1979) and to felsic aggregates in amphibolite dykes by Niamatullah (1983).

3.5.4 Methods Used.

a) **Measuring the 2-dimensional data.** Quartz grain-shape fabrics are observed in thin sections of most specimens of quartzites in the present study. The fabrics can therefore be measured in three dimensions by combining 2-dimensional data from both elliptical and centre-to-centre techniques. The exceptional purity of the quartzites makes them particularly suitable for centre-to-centre measurement; of these techniques, the Fry method is preferred because, as referred to above, clustering and anticlustering can be allowed for. The main reason for choosing centre-to-centre method is speed of data collection: a typical Fryplot can be prepared, for one section, within a hour and a half compared to double that time for collecting Rf/ϕ data. The basic assumptions of both methods (penetrative and homogeneous strain, no volume loss) are clearly justified by the relatively homogeneous fabric development over the whole of a thin section.

A more contentious assumption is that of random initial fabric. There

is clear evidence (see below) for a depositional fabric in some cases. The complications introduced by this initial preferred orientation are the major drawbacks of the method, but apply equally to any of the other methods, since cleavage is defined well only for a few samples. (The Matthews et al. method allows for an initial preferred orientation if the cleavage is known). The existence of an initial fabric was tested for by examining the Fryplot for the characteristic pattern shown in Figure 3.10.

The Fryplots were prepared by marking the positions of grain centres onto acetate sheet directly from a 'Shadowmaster' enlargement of the thin section at x100 magnification, corresponding to an area of approximately $10mm^2$ on the thin section, as for the method of measuring linear intercepts. The coordinates of the grain centres were digitised on the Ferranti Cetec digitising board, and used in programmes FRYCIC, FRYDOT, and FRYCOL, FRY26, and FRY50 (Appendices 9.4, 9.5) to produce various representations of the Fryplot.

All the FRY programmes begin by obtaining coordinates of other grain centres relative to each grain in turn ("Frycoordinates"). However, two subtleties are introduced to maximise the number of Frycoordinates without allowing errors to be introduced by edge effects. These arise because not every grain centre can be used to generate Frycoordinates: grains at the edge of the sample area would generate frycoordinates only towards the centre of the sample area, creating a biased fryplot. The permissible Fryplot origin area is therefore confined to the sample area reduced by a border of half the dimension of the Fryplot (LFRY) (Figure 3.11). The programmes accept a variable value of the Fryplot dimension LFRY, and automatically exclude points outside this plot origin area for a rectangular sample area of 375x300mm. However, it is possible to exploit the symmetry of the Fryplot so that this border is reduced to three of the four sides of the sample area by choosing Frycoordinates from only points to the right of the Fryplot origin. The resultant plot shows half of the

total fabric, and includes as many plot origins without edge distortions as possible. The remaining, symmetric half of the Fryplot is completed in the programmes by operating a rotation of 180^{o} about the Fryplot centre on every point. The programmes also count and print values of three useful variables: L, the number of Fryplot origins used, M, the total number of points on the plot, and N, the number of coordinates in the original data file.

In order to evaluate the accuracy of the Fry technique several other methods were applied to a few samples. Programme RSAVPHI (Appendix A9.6) was written to apply the Shimamoto and Ikeda formula to measurements of Rf and ϕ made using the eyepiece micrometer and rotating stage of the Leitz microscope at x100 magnification on 040W. Tracings of grain boundaries from sections 038R and 041 were made on the Shadowmaster under the same conditions as the linear intercept and grain centre measurements. Coordinates of grain long and short axes were digitised and used in programme RSAVPHI to calculate Rs and ϕ, by the Shimamoto and Ikeda method.

Long and short axes of irregularly shaped grains can be defined in a number of ways. In this study, the long axis was chosen first by eye and the short axis taken as the distance between grain boundaries along the perpendicular bisector of the long axis. Programme LISLE was written to evaluate the geometric, harmonic, and arithmetic means of ellipse ratios and the vector mean of ellipse long axis directions, allowing a further numerical evaluation of strain by the method of Lisle (1977a). The overestimate of R_s by the harmonic mean was corrected for from Lisle's curves assuming 1.4 for the mean value of Ri (typical for quartz grains in sandstones). The three samples of Rf/ϕ data were also analysed by the graphical Rf/ϕ data following the procedure given in Lisle (1985): a symmetry test was applied, before curve fitting from the Rf/θ curves. Success in the symmetry test generally indicates the absence of an initial fabric with a probability of 0.05 (certain initial fabrics may still

satisfy the symmetry test; see Lisle (1985)).

The extension of Robin's method of linear intercepts derived in section 3.5.3ii allows a further numerical strain calculation to be made from the linear intercept measurements of grain size. It was shown that the ratio of geometric means of intercepts in the λ_1 and λ_3 directions gives the strain ratio. The linear intercept measurements were made in the (visually assessed) λ_1 and λ_3 directions, and geometric means were accurately calculated for the grain size determinations. These were used as another strain estimate for sections D and E of samples V1, V5, V8, V10 and V12.

b) Representation of the Fryplot. For the almost isotropic fabrics of most of the samples, it is very difficult to make an accurate measurement of the axial ratios. A variety of techniques were developed to discover the best method of presenting the data.

i) Windowed Plots. Fryplots are conventionally represented on a grid system in which the number of points within each square is printed at the centre of the square (Fry 1979). In this study the raw data divided into grids of 26 x 26 or 50 x 50 square elements (Programmes FRY26, FRY50 Appendix A9.4). An example is shown in Figure 3.12. The 26 x 26 grid was preferred to the smaller spacing between grid elements on the 50 x 50 plots because these contained too much detail. Fabrics were then measured by taking the axial ratios of the central, point free area. Two major problems arose. Firstly, this area may have given a completely false impression of the actual fabric simply by the inclusion of just one or two points at atypical co-ordinates close to the centre of the plot. The same difficulty arises even if the measured area includes grid squares with one, two, or any number of points: the windowed data does not define any shape that can be successfully approximated to an ellipse. The real fabric is accurately reflected in the most dense concentration of points. This is not easily assessed from presentation of the data numerically. A second problem

C039RXX 278 999 315

```
 2 2 1 2     1 2 3 2   3 4 3   2 2 2 1 1     2 1 1 2
 1 3 5 4 1 7 1 3 2 3 2 1 2 6 2 4 5 2 6 1 2 4 2 3 3 3
 2 5 1 2 4 3 2 5 4 2 1 6   4 2 2 5 5 6 5 5 3 5 4 4 1
 3 3 3 4 6   3 9 3 2 1 3 2 5 4 2 5 1 2 2 1 5 6   4 2
 1 1 4 6 1 6 1 4 4 4 7 5 4 4 2 2 8 3 3 3 4 2 1 3 1 2
 2 4 6 4 3 4 3 2 4 4 6 3 4 4 3 4 6 6 2 4 3 4 3 1 5 1
 2 3 3 5 5 3 1 1 5 2 2 6 5 5 5 3 1 6 2 2 5 6 9 1 4
   2 1 4 3 7 3 2 3 3 1 5 4 4 4 4 2 4 7 5 4 4 8 2 7 4
 1 1 3 3 4 1 3 2 6 2 2 3 1   1 1 5 2 1 7 2 7 2 1 6 4 1
 2 6 5 1 2 6 6 4 2   2   2   1 4 1 2 6 1 3 4 7   2 4
 2 5 1 4 9 5 4   1 3             1   1 2 8 5 5 1 3 2 1
 1 3   3 2 1   3 2 1             1 1 3 4 5 4 5 5 3 4
 5 4 7 8 10 6 6 2   2       1       1 3 3 4 4 4 1 1 1
 1 1 1 4 4 4 3 3 1       1       2   2 6 6 10 8 7 4 5
   4 3 5 5 4 5 4 3 1 1               1 2 3   1 2 3   3 1
 1 2 3 1 5 5 8 2 1   1               3 1   4 5 9 4 1 5 2
 4 2   7 4 3 1 6 2 1 4 1   2   2     2 4 8 6 2 1 5 6 2
 1 4 6 1 2 7 2 7 1 2 5 1   1   1 3 2 2 6 2 3 1 4 3 3 1 1
 4 7 2 8 4 4 5 7 4 2 4 4 4 4 5 1 3 3 2 3 7 3 4 1 2
   4 1 9 6 5 2 2 6 1 3 5 5 5 6 2 2 5 1 1 3 5 5 3 3 2
 1 5 1 3 4 3 4 2 6 6 4 3 4 4 3 6 4 4 2 3 4 3 4 6 4 2
 2 1 3 1 2 4 3 3 3 8 2 2 4 4 5 7 4 4 4 1 6 1 6 4 1 1
 2 4   6 5 1 2 2 1 5 2 4 5 2 3 1 2 3 9 3   6 4 3 3 3
 1 4 4 5 3 5 5 6 5 5 2 2 4   6 1 2 4 5 2 3 4 2 1 5 2
 3 3 3 2 4 2 1 6 2 5 4 2 6 2 1 2 3 2 3 1 7 1 4 5 3 1
 2 1 1 2     1 1 2 2 2   3 4 3   2 3 2 1     2 1 2 2
```

FIGURE 3.12

Examles of a Windowed Fryplot, 26x26 grid. Sample 39, section R. Each integer gives the number of points within the square. Figures on the top of the plot are: L - The number of Fryplot Origins, M - The total number of points plotted, N - The number of points in the data file from which the plot has been made. Assessment of the fabric, defined by the greatest concentration of points, is clearly difficult from this representation.

a) C039RXX 278 1007 315

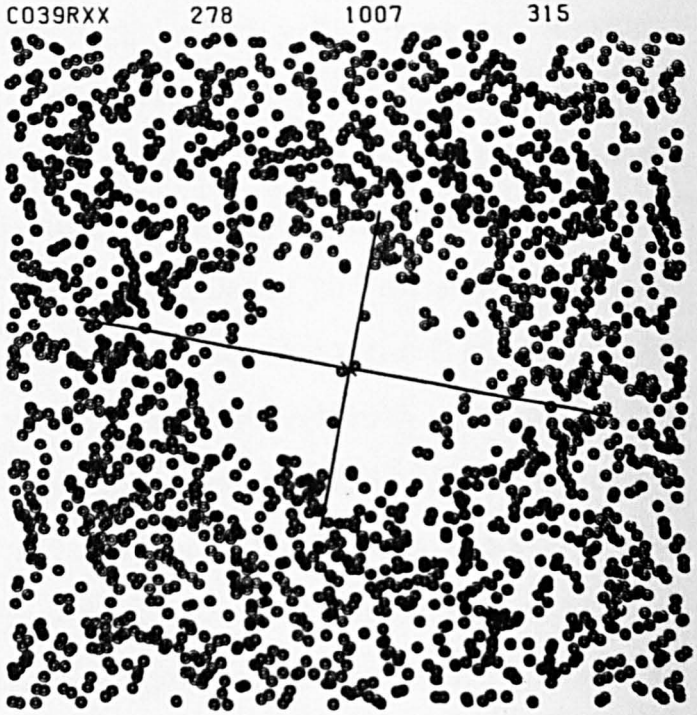

b) C039RXX 278 1007 315

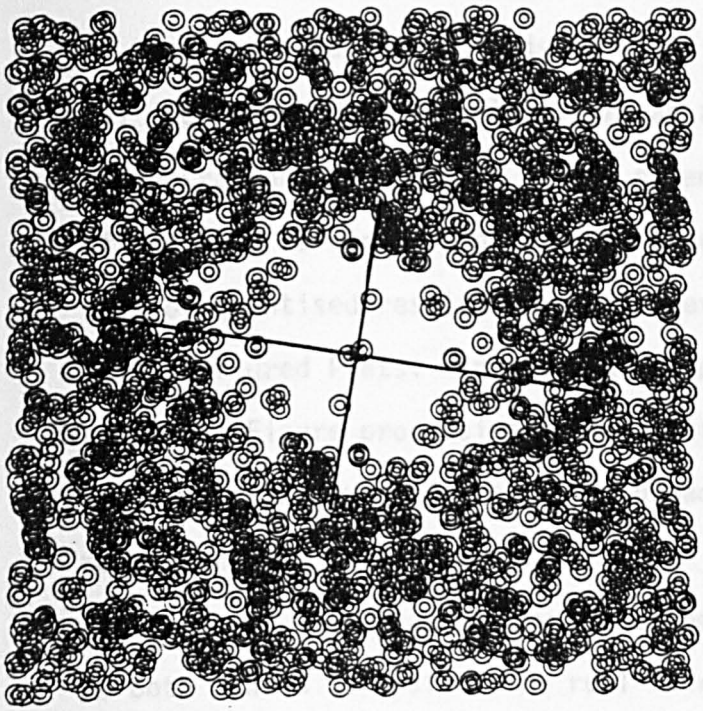

C) N039RXX 373 1742 435

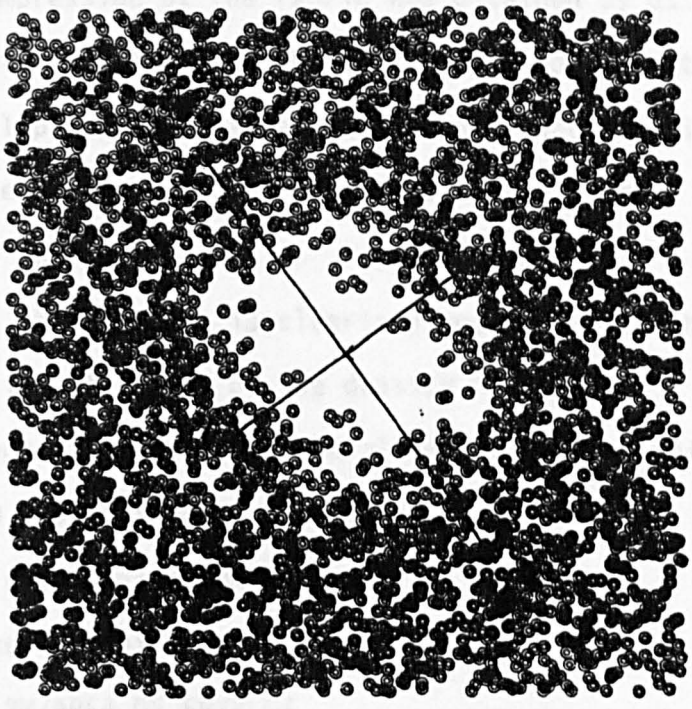

FIGURE 3.13

Development of the best Fryplot representation. Sample 39, section R (as in Figure 3.12). L, M, N are defined as in Figure 3.12.
a) O = 0.13 Measured axial ratio, Rf = 1.67, ϕ = 101
b) O = 0.25 Measured axial ratio, Rf = 1.68, ϕ = 111
c) O = 0.25 Measured axial ratio, Rf = 1.78, ϕ = 144.
The Figures show how increasing O (the overlap betwen circles) improves definition of the fabric ellipse (compare a and b) and how increasing L brings a further improvement, and gives a different orientation (compare b, L = 278 and c, L = 373).

is that any grid system leads to quantisation of results.

ii) Coloured, Windowed Plots. In an attempt to emphasize the most dense concentration of points, a colour scheme was given to the numerical values of the 26 x 26 windowed plots. Unfortunately, the second problem above, that of quantised results, is still severe.

iii) Contoured Plots. An attempt was made to contour the windowed data using the Figure processing facility at Keele. However, the windowed data is too discontinuous for even the broadest contour spacing to define representative axial ratios.

iv) Symbols. The raw data was plotted using various symbols. Crosses and Xs both tended to distort the real fabric towards the directions of the straight elements of the symbol. Finally circular symbols were chosen. Although solid circles (dots) offer some advantages, the CALCOMP plotter is incapable of superimposing several dots with identical or near co-ordinates.

v) Open Circles. The best impression of the fabric was obtained by using circles to represent each point. The radii of the circles was adjusted to give an optimum amount of overlap: at this value, the densest concentration of points, which represents the fabric, becomes clear due to the overlap of circles creating an ellipse of ink.

The overlap of circles in this ellipse is clearly proportional to the circle radius, R, and the Density of Points D. The density of points defining the ellipse may be approximately proportional to the average point density. Therefore parameter O was defined:

$$O = R \times D$$

R - Circle Radius, mm

D - Average Point Density,

= 2M/AREA OF FRYPLOT

(Programs FRYC1C1,2,3)

Plots for several values of O were produced. The optimum was found by visual assessment of the fabric to be 0.25. With larger values, the

increase overlap merely blurred the ink ellipse, while lower values did not give enhancement to the elliptical area. A further improvement was made by drawing two circles, one with a radius R/2, at each point (Programs FRYCIC D,E,F). Figure 3.13, a and b, compares two Fryplots from identical data, in which O has been increased to an optimum value to enhance the fabric ellipsed, and c shows how a further improvement occurs by increasing the number of Fryplot origins, L. A minimum value of 300 was used, but increasing the value of L did not define the fabric more clearly in all cases. In some instances, however, it did alter the orientation of the ellipse considerably; the fryplot from the largest value of L is probably the most reliable even if there is a slight loss of definition.

c) Combining the 2-Dimensional Data. Of the methods for combining the 2-dimensional data, only those treating three arbitrarily orientated planes are suitable since the difficulty of preparing exactly orthogonal sections introduced significant deviations from this condition. The methods of Ramsay and Treagus do not allow for incompatibilities between the measured ellipses. Owen's 1984 Method is preferred to Milton's because of the linear least-squares fitting procedure used, and because of the useful parameter ρ.

The data input required for Owen's programme requires the axial ratio and orientation of the measured two dimensional ellipses. The orientation of the sections was measured most accurately from the one block of the sample which preserved cut faces parallel to all three sections: the use of this gave the section orientation data in . cooordinates relative to this block. The output of Owen's programme gives, for both trial and best fit solutions, the strain, natural strain, and orientation of the principal planes of the strain ellipsoid, from which the natural octahedral unit shear γ_o, the natural shear strain E_s, Lodes parameter ν and the ellipsoid shape factor, k, have been calculated (Hossack 1968) (Appendix A5). The final step necessary for the effective presentation of the data was to

rotate the relative orientations of the principal planes and other microstructures to their true orientations. A two stage procedure using Programmes Plinter and Rotator by D. Sanderson was used in conjunction with the field strike mark. In the first rotation, the strike mark is rotated to its correct horizontal position from its position in relative coordinates. The pole and amount of rotation is found from the pole to the great circle joining the strike mark in the two positions, and then operated on all other data. The second rotation, using the strike mark itself as an axis, rotates the specimen until the marked surface has the correct dip. The results were checked to establish that the handedness of the strain axes was preserved by the rotations. The various methods of strain analysis and procedures used are summarised in Figure 3.14.

3.5.5 Comparison of Methods

The results of the Fry method, Shimamoto and Ikeda's method, Lisle's method of harmonic means and the Rf/ϕ analysis are given for the three samples 038R, 040W, and 041 in Table 3.6.

	Fryplot		Shimamoto & Ikeda		Lisle				Rf/ϕ		
	Rs	ϕ	Rs	ϕ	HMRf	GMRf	AMRf	VMϕ	HMRf	Rs	ISYMM
038R	1.60	100	1.61	109	2.07	2.23	2.44	109.4	1.90	1.60	0.93
040W	1.85	128	1.57	117	1.76	1.88	2.01	112	1.63	1.35	0.82
041	-	-	1.40	88	1.77	1.90	2.10	90	1.63	1.35	0.79
			Lincep								
V1D	1.06	153	1.30	89							
V1F	2.11		1.02	90							
V5D	1.00		1.09								
V5F	1.27	92	1.37	90							
V8D	1.00		1.04								
V8F	1.6	90	1.26	79							
V10D	1.22	82	1.17								
V10F	1.82	6	1.18	101							
V12D	1.08	89	1.08								
V12F	1.44	178	1.14								

TABLE 3.6

Also shown are comparisons between the Fry method and the extended Robins method (measured from linear intercepts in Program Lincep) for the other

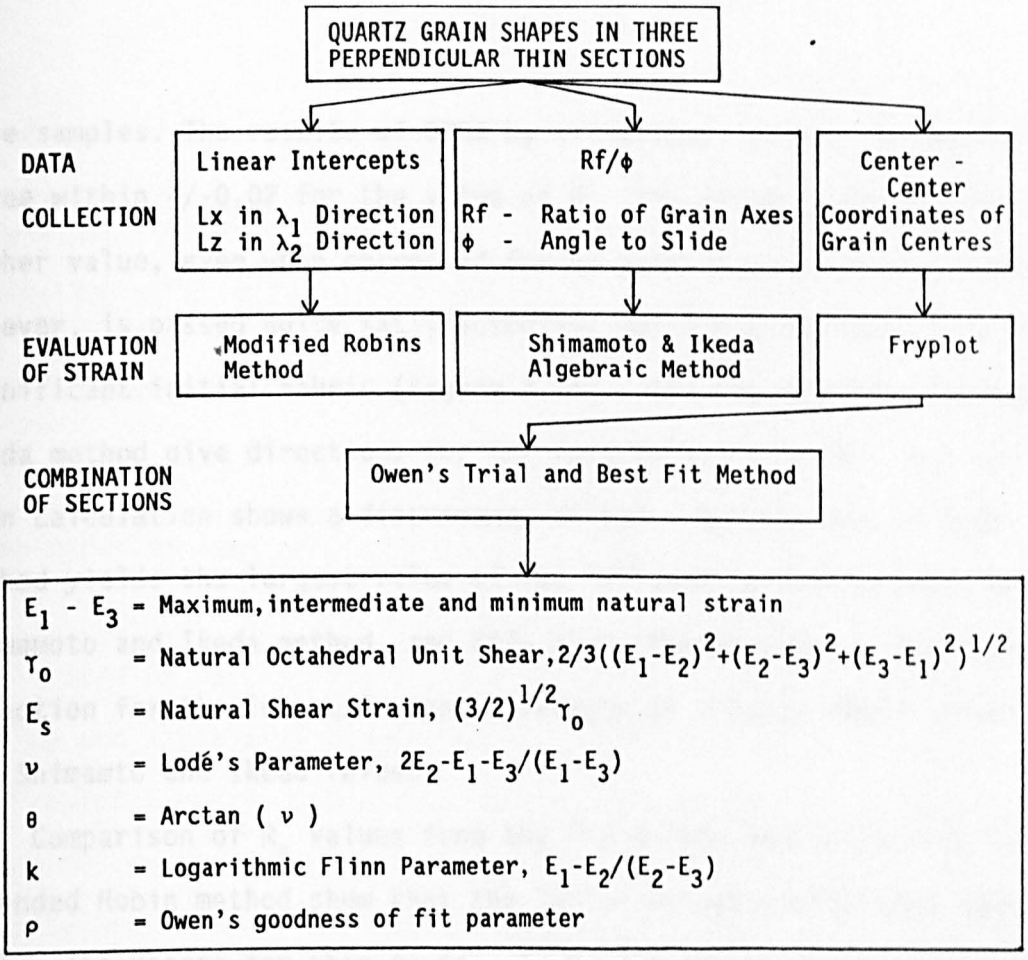

FIGURE 3.14

Summary of methods and procedure used to determine the fabric ellipsoid.

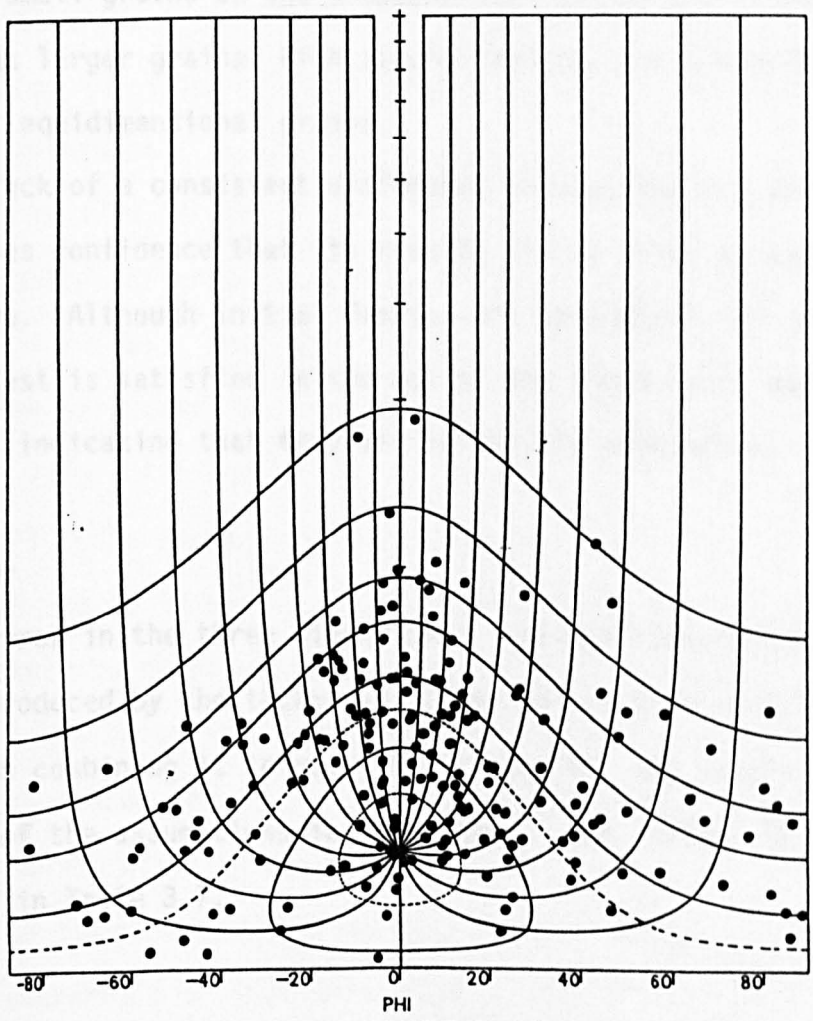

Rs-1.60

FIGURE 3.15

Rf/ϕ plot, Sample 38, section R. The plot has been made symmetrically about the vector mean ϕ value determined by the Shimamoto and Ikeda Method, and the θ curves fitted from Lisle (1985). Programs RFPHI plots Rf, ϕ data

five samples. The results of 038R by all methods except the harmonic mean agree within +/-0.02 for the value of R_s. The harmonic mean gives a much higher value, even when corrected for an initial fabric; the symmetry test, however, is passed quite satisfactorily, which may indicate lack of a significant initial fabric (Figure 3.15). The Fry method and Shimamoto and Ikeda method give directions for the long axis within 10^0, but the vector mean calculation shows a discrepancy of 60^0. In the case of 040W, the Fry method yields the largest value of Rs, followed by the harmonic mean, Shimamoto and Ikeda method, and Rf/ϕ plot respectively. The vector mean direction for the long axis again diverges by a large amount from the Fry and Shimamto and Ikeda values.

Comparison of R_s values from the Fry method and those from the extended Robin method show that the latter are generally much lower (Table 3.6). The reason for this is not clear, but may be due to the difficulty of seeing small grains on the shadowmaster; during the Fryplot tracing it may be that larger grains, with strong fabrics, are preferentially selected over small equidimensional grains.

The lack of a consistent difference between the Fry method and the others gives confidence that its results are at least as accurate as any alternative. Although initial fabrics are undoubtedly present, the symmetry test is satisfied in two out of the three cases and very nearly by the third, indicating that they are relatively unimportant.

3.5.6 Error

The error in the three dimensional strain ellipsoid has two components errors introduced by the techniques (both in measuring the two dimensional data and in combining it to give the ellipsoid), and errors due to the violation of the assumptions in the method. The former component is summarised in Table 3.7.

Source of Error	Error in R_f	Error in ϕ
Digitising, tracing & sample heterogeneity	+/-0.002mm =2%	
Estimation of Ellipse from Fryplot	+/-0.03 =1.3%	+/-0.9^0
Combined Errors of Ellipse	+/-0.17 =12.9%	+/-17^0
	Error in Strike	Error in Dip
Orientation of Section	+/-1.2^0	+/-3.3^0

TABLE 3.7

Errors in determining the two dimensional strain ellipse arise at the tracing and digitising stages, in estimating the ellipse axial ratios from the Fryplots, and in determining the orientation of the sections. The former two errors can be taken from the evaluation of the linear intercept measurements, made by the same technique. Including also the effect of sample heterogeneity, Table 3.4 indicates a combined contribution of +/-2% in the relative positions of two grain centres.

The error in estimating the ellipse axial ratio has been evaluated by repeating measurements on the same Fryplots for seven cases. The average error in Rf is +/-0.03, or +/-1.3%, and +/- 0.9^0 in ϕ. The error includes all other sources of error (tracing and digitising, and estimating the ellipse axial ratio). Much more important errors arose when sample heterogeneity was taken into account, by repeated measurements on redigitised data. Average errors are +/-0.17 in Rf (12.9%), and +/-17^0 in ϕ (Table 3.7). The largest of these errors arise through failing to identify any fabric in one of the pair of repeated measurements. However, they are likely to be overestimates of the true error because some measurements are based on Fryplots with L (the number of origins used for the Fryplot) less than 300. In practice, all Fryplots used were made with L>300, which will improve accuracy.

Error in measuring the orientation of the section can be evaluated by repeated measurements of fracture orientations on laboratory samples.

These give values of +/-1.2^{0} in strike measurements and +/-3.3^{0} in dip measurements, but they do not include an estimate of the error in reorientating the sample in the laboratory.

Errors in the combination of the three sections can be evaluated by comparing the observed section ellipse data with the values calculated for the orientation of the section, from the best fit ellipsoid. The parameter ρ indicates the success of the solution, given in Appendix A5 for the strain measurements, and varies from 1.01 for the best fit solution to 1.42 in the worst case. High internal consistenty of the results implied by low values of ρ, is more probable with few sections, as used here; so that ρ can only be interpreted as a relative measure of the goodness of fit and not as an estimate of the accuracy of the strain estimate. Individual values of ρ are discussed in the context of the relevant chapters.

No absolute error can be estimated for the final solutions because of this difficulty.

The assumption of random initial fabrics is clearly one of the weaknesses of the strain measurements. However, the Rf/ϕ plots indicate that the influence of the initial fabric may not be too great for those samples at least. The other basic assumption that the quartz grains are deforming homogeneously with the rock is born out by microstructural evidence, although any grain boundary sliding will not be recorded in the strain measurement. It is concluded that the errors are sufficiently low to allow meaningful comparison of the results in terms of the intracrystalline plastic strain for those samples which show evidence of this deformation mechanism. The absolute accuracy of the measurements is uncertain.

3.6 CATHODOLUMINESCENCE

3.6.1 Recent advances in Cathodoluminescence studies.

Cathodoluminescence (C.L.) theory, technique and applications have been discussed by Blenkinsop (1982), but recent advances make a current review necessary.

a) Cause of Luminescence in Quartz. Although it has been appreciated for a decade that 'lattice luminescence' can provide an explanation of quartz (and feldspar) luminescence (compared to activator luminescence for carbonates), the details of the defects responsible are still unresolved (e.g. Zinkernagel 1978, Walker pers.comm.).

At least four models have been proposed. The 'E' centre, of which there are several types, is due simply to a missing oxygen from an SiO4 tetrahedron, which can act as a hole trap. A similar spare oxygen bond can be formed and act in a similar way if two hydrolised tetrahedra ($SiO_3.OH$) are joined across the OH groups, and one hydrogen atom is displaced. This is the 'wet OHC centre', which traps a hole in the same way as the 'E' centre. The 'O-Oπ bond' (Hanusiak and White 1975) may function in a similar way, and the latest model, that of the 'self trapped exciton' also focusses on the O-O bond between tetrahedra: in this case, an 'exciton', consisting of a tightly bound electron-hole pair with the electron not quite promoted to the conduction band, is self trapped at the site of oxygen-oxygen bond, where the release of the electron to the valence bond generates the luminescence. Spectral analysis of quartz luminescence reveals that there are two separate sources of light at 650nm (the blue peak) and 450nm (the red peak). Temperature of observation is known to affect the blue peak luminescence dramatically; both persistence and intensity increase as the temperature decreases. These characteristics fit the self-trapped exciton model well. Optically detected magnetic resonance characteristics of synthetic quartz (Hayes et al. 1984) cannot be explained

by any of the E′ centres, but match the self trapped exciton model for blue band luminescence, also favoured by Grinfelds et al. (1984). However, all silicates have the blue band in common, for example Forsterite, so Walker (pers.comm.) has argued that a defect centre related to O-O bonding between SiO_4 tetrahedra cannot be responsible; (since Fosterite has no O-O bonds between SiO_4 tetrahedra); rather it must be generated by an inherent structure within the tetrahedron (such as an E′ centre).

Furthermore, at least one component of the luminescence appears to be independent of the crystalline state of the solid, since fused silica also luminesces. All that can be firmly concluded at present is that quartz luminescence is defect related.

Although the explanation of luminescence at the level of electron orbitals is enigmatic, there is more information about the major geological factors affecting luminescence. The role of thermal history in determining colour and intensity of luminescence was investigated in detail by Zinkernagel (1978), and Sprunt et al. (1978) and more recently by Dietrich and Grant (1985). The latter authors compared spectra from quartz fibres and veins of different thermal and strain histories. Their main conclusions were that the red emission peak intensifies with temperature of metamorphism, measured by illite crystallinity, from a comparison of samples from the uppermost Helvetic Nappes, and the root zone, while the decrease in blue band intensity from early to late parts of fibres, which are assumed to have formed under similar conditions of temperature and strain rate, are deformation induced. While it is shown in this study that at the diagenetic grades of metamorphism reported for the Helvetic Nappes, lithology may have the dominant effect on illite crystallinity even within a single lithological type and therefore that crystallinity should be used as a temperature index only with extreme caution, the temperature dependence of red peak intensity is corroborated by a change in deformation mechanism in adjacent carbonates from grain boundary sliding to crystal

plasticity and by the observations of the earlier authors. The change in blue peak intensity may be deformation-related in the case of the fibres investigated, but there is clear evidence that the blue peak is also temperature dependent for temperatures of observation above -110^{o}c: the blue band intensity also increases with temperature of formation (Figure 7 in Dietrich and Grant, 1985). Strain or stress dependence of C.L. has been documented by Zinkernagel (1978), who reported that C.L. contrasts could be observed at contacts between grains (in Dietrich and Grant 1985) and by Sprunt et al. 1978, who contrasted the homogeneous, red luminescence of strained samples with heterogeneously red and blue luminescing adjacent samples with the same thermal history. However, there has been disagreement over the effect of lattice orientation on luminescence: Zinkernagel clearly considered the strain effects visible in C.L. to reflect directly optical strain features such as undulatory extinction and strain bands. Stel (1981) observed bands of luminescence contrast parallel to crystallographic planes, which he attributed to lattice misorienttion. Sprunt et al however found no relationship between C.L. colour and dislocation density or lattice orientation, and this is confirmed by Grant (pers.comm.), and accords with the above conclusions that luminescence is defect related, so that lattice orientation per se could have no effect. Strain may affect luminescence through the distribution of lattice defects; this could explain some of the above apparent contradictions.

b) Techniques. A much greater variety of techniques have recently become available enabling the use of C.L. in several specialised ways. The various possible configurations of electron source, luminescence collection, detection, analysis and applications are outlined in Table 3.8. It is principally through the addition of the monochromator to the C.L. system in the S.E.M. for spectral analysis that the major advances in understanding the causes of luminescence have been made.

ELECTRON SOURCE		LUMINESCENCE			SAMPLES	PRINCIPAL APPLICATIONS
		COLLECTION	DETECTION	ANALYSING		
COLD CATHODE			Optical		Small Chamber; Polished Thin Sections, Slabs Small solids Large Chamber; Bulk Specimens Cores	Carbonates
HOT CATHODE	S.E.M.	Flat Mirror & Lens	Optical		Polished Thin Sections	Quartz, Carbonates
	S.E.M.	Lens	Photo Multiplier	Mono-Chromator		Quartz, Spectra from Quartz, Carbonates (with mono-chromator)
	S.E.M.	Parabolic/ Ellipsoidal Mirror +/-Lens		Image And Micro Analysis System	Slabs Small Solids	
	T.E.M.	Mirror + Lens			Ultra-thin Sections	

TABLE 3.8

3.6.2 Method Used, Advantages, Limitations and Potential

Table 3.8 shows that quartz may be examined by the simplest C.L. system available on the S.E.M. In this study, samples consisting of polished, uncovered probe sized thin sections were firstly coated with a thin layer of carbon on a Biorad Polaron coater. These were earthed by adhesive aluminium foil and silver paint, and mounted at 45^{o} to the electron beam in a Cambridge Instruments S4.10 S.E.M. C.L. detection was by a Cambridge Instruments Photomultiplier Tube, connected through an Image and Micro Analysis System to the monitor of the S.E.M.

As reported in Blenkinsop (1982), such a system reveals many features in quartz which are invisible optically. The most important of these are trans- and intra-granular extension microcracks, revealed as crack fills of non-luminescing quartz. Although some of these may be seen optically as lines of inclusions, many are totally invisible, and it is the study of these that was the main application of the C.L. technique here. The matrix of larger fractures also shows as a non-luminescing quartz including

angular fragments of brightly luminescing grains. Secondly, forms of secondary quartz such as overgrowths, cements and veins are seen clearly as similar dark quartz. The luminescence of quartz grains themselves can provide some information about their provenance, and finally, other minerals can be rapidly identified in C.L. The addition of the IMAS system allows many of these features to be viewed selectively by imposing windows of variable intensity (height) and wavelength range (width) on the images, and to perform modal analyses of constituents by area. All these images can be photographed. Table 3.9 is a qualitative description of the C.L. of some minerals examined during the course of this study.

The main limitation of the technique is the poor focus achievable on the C.L. system. The reason for this lies in the small decay time of the luminescence once the sample has been scanned by the electron beam: the continued emission of light interferes with the light generated by the area illuminated under the current beam position. Under optimum conditions, magnification of x500 are achieveable with reasonable focus, but x200 is a general limit. The resolution of the C.L. system is therefore comparable with that of an optical microscope.

An equally severe restriction for the general user is the much longer decay time and intense luminescence of many rock forming minerals, especially iron oxides, carbonates and felspars. Specimens with more than 20% of such minerals cannot be studied.

Future potential of the system includes a calibration of luminescence intensities of various minerals, and the extension of the range to include most common rock forming minerals.

MINERAL CATHODOLUMINESCENCE IN THE S.E.M.

MINERAL	CHARACTERISTIC LUMINESCENCE	OTHER FEATURES
QUARTZ		
a) Detrital Grains, Non-Metamorphic	Complete range, non-luminescing - bright depending on provenance	Strain Features Brilliant Iron Oxide Rims Irregular, Patchy Luminescence, sometimes zoned.
b) Detrital Grains, Anchi-Epizone	Homogeneous bright luminescence	Very poor definition. Little visible.
c) Cement Microcrack Filling	Non-luminescing	Subtle contrasts can reveal different generations, well discriminated in I.M.A.S.
d) Fault Shear Matrix	Non-luminescing groundmass Bright grain fragments Brilliant patches/particles of Iron Oxide.	
FELDSPARS	Brilliant, Persistent	
CALCITE	Brilliant, Persistent	
IRON OXIDES	Bright, Persistent	
CHLORITE	Moderate	
MICA	Moderate	Cleavage visible
CLAYS	Dull	
EPIDOTE	Bright-Brilliant	Zoning visible
BARYTES	Bright	
VOLCANIC GLASS	Brilliant, Persistent	Characteristic angular shapes

N.B. Relative Luminescences only are described: Non - Dull - Moderate - Bright - Brilliant.
Absolute levels are highly sensitive to settings.

TABLE 3.9

3.7 MICROFRACTURE DENSITIES

3.7.1 Reviews of Methods.

'Microfracture Density' is a useful general term defined as any single measurement representing the total density of all fractures: such a catholic usage is found throughout the literature, and can be refined as described below. Reviews of the methods of microfracture density measurement have been given by Blenkinsop (1982) and Kranz (1983). Both accounts, however, are incomplete and require expansion due to the number of different methods that have been used. Firstly it is necessary to distinguish between microfracture density, defined in one of the four ways below, microfracture porosity, defined as the volume of microfractures per unit volume of rock, and dilatancy, the change in volume/unit volume. This review is of microfracture density definitions and measurements only.

a) Area Method. Possibly the simplest method is to count the number of discrete fractures over a known area and define the density as the number of fractures/unit area (Dmm^{-2}). Counting problems are created by bifurcating and converging fractures, and the area method is clearly sensitive to the orientation of the section plane if there is a preferred orientation of fractures. The method was used by Peng and Johnson (1972) and Hadizadeh (1980).

b) Grain Method. The density is given as the number of fractures per grain (DG^{-1}). In addition to the limitations noted above, this method contains no information about the absolute crack density unless grain size is also specified. It has been used by Conrad and Friedman (1976).

c) Intercept Methods. A number of fractures intersecting a line of known length are counted and given as the number/unit length. Measurements made along a line of a single orientation can be described as true fracture frequency, F, (or spacing, S, for the reciprocal value) if the line is perpendicular to the fracture plane, and apparent values along any other

direction. Again, some criterion is necessary to deal with fracture splits and mergers. The directional dependence of this method requires that the orientation of the intercept line is given; for triaxial specimens, the usual directions are parallel to σ_1 (axial) and perpendicular to σ_1 (radial). Other useful axes are parallel and perpendicular to a fault plane. The fracture density (Dmm^{-1}) sensu strictu is calculated from a number of such measurements, for example, by taking an average of two perpendicular directions.

A new technique for triaxial specimens, based on linear intercept measurements, has recently been applied by Wong and Biegel (1985). Microcrack frequencies are measured, as described above, in directions parallel and perpendicular to σ_1, or axial (Fa) and radial (Fr), and it is also shown that the full dependence of crack frequency (F) on θ, the angle between the crack and σ_1, is given by

$$F(\theta)=Fa+(Fr-Fa)\ \sin\theta$$

The form of $F(\theta)$ given above is such that a very simple formula can calculate S_v, the total crack surface per unit volume:

$$S_v = (\pi/2)\ Fa + (2 - \pi/2)\ Fr \qquad 3.3$$

This parameter is useful because the quantity S_v multiplied by the critical crack extension force, G_c (section 2.3.1) gives the fracture energy/unit volume for tensile cracking. By first determining the preferred orientations of the fracture with respect to the section planes, Blenkinsop (1982) was able to use a correction factor to calculate the true fracture density, defined as the number of fractures per unit length along a line perpendicular to the mean fracture orientation. This refinement would seem desirable for the case of a single set of well-orientated microfractures. The general method has also been used by Friedman and Logan (1970), Wawersik and Brace (1971), and Tapponier and Brace (1976).

d) Crack Density Parameter. The importance of microfractures in seismic velocity has earned the problem of measuring crack densities some

attention from geophysicists, who have introduced a 'crack density parameter' to take explicit account of fracture dimensions and geometry in specifying fracture density. A simplified form of O'Connell and Budiansky's analysis (1974) is given by Hadley (1976), who defined the dimensionless crack density parameter, ε, for three types of fracture:

i) Spheroidal Cavities

$$\varepsilon = \Sigma c^3/V$$

where c = crack length (crack radius in O'Connell and Badiansky)

V = volume

ii) Cracks of any identical convex shape and uniform size.

$$\varepsilon = 8Dmm^{-2}(A.M.c.)^2/\pi$$

where Dmm^{-2} = Number of cracks/unit area

A.M.c = Mean crack length

iii) Cracks of a distribution of sizes and shapes, in which size and shape are not correlated and the fracture ellipticity, b/a, is greater than 0.1.

$$\varepsilon = 3Dmm^{-2}\ (A.M.c)^2/4\pi$$

For smaller ellipticities, a correction factor given in O'Connell and Budiansky (1974) must be applied to the formula in (iii). However, most cracks, including the 'penny-shaped' crack of stress intensity factor analyses are probably satisfactorily approximated by (ii) or (iii), which both give a direct proportionality between the crack density parameter and the number of cracks/unit area. This method is the most thorough analysis of crack density, but requires the measurement of both cracks/unit area and crack lengths, together with a determination of the crack geometry, and is also section-dependent for orientated cracks.

3.7.2 Methods Used

The method described below allows the determination of both the number of fractures per unit area and per grain. These techniques were considered

appropriate for the generally low degree of fracture orientation, and enabled the most rapid accumulation of data. The measurements were made directly from the S.E.M. in cathodoluminescence because of the microfracture visibility referred to in the previous section.

The procedure for measurement begins with adjustment of condenser settings for the best possible focus: it was found that the optimum settings varied considerably from day to day and did not necessarily correspond with those that gave the most intense signal. At a magnification of x200, the number of fractures/grain was counted for every grain in the field of view. A traverse was made across the specimen, ensuring that no grain was measured twice. Areas of unsheared quartzite only were measured. Four improvements to this basic method were made after a limited number of trials:

- A minimum sample size of 250 grains was established.
- The focus was carefully readjusted at x500 for each field of view.
- Each grain was labelled with the number of fractures directly on the monitor screen, ensuring that all grains were counted and none repeated.
- All grains, even those partially in view, were measured (originally the sampling was confined to those grains entirely within the initial field view) by small adjustments in the sample position.

From the measurements of the number of microfractures in each field of view, the density/area (Dmm^{-2}) can be calculated. This calculation is complicated by the fact that the area of the field of view varies depending on the position of the section, due to the inclined specimen plane: at the edge of the section furthest from the electron beam, the field of view is three times larger than the value at the nearest point to the beam. This is shown in Figure 3.16, from which the following equation can be deduced for the variation in the diameter of the field of view (FV) with x, the position of the section, for $x>o$;

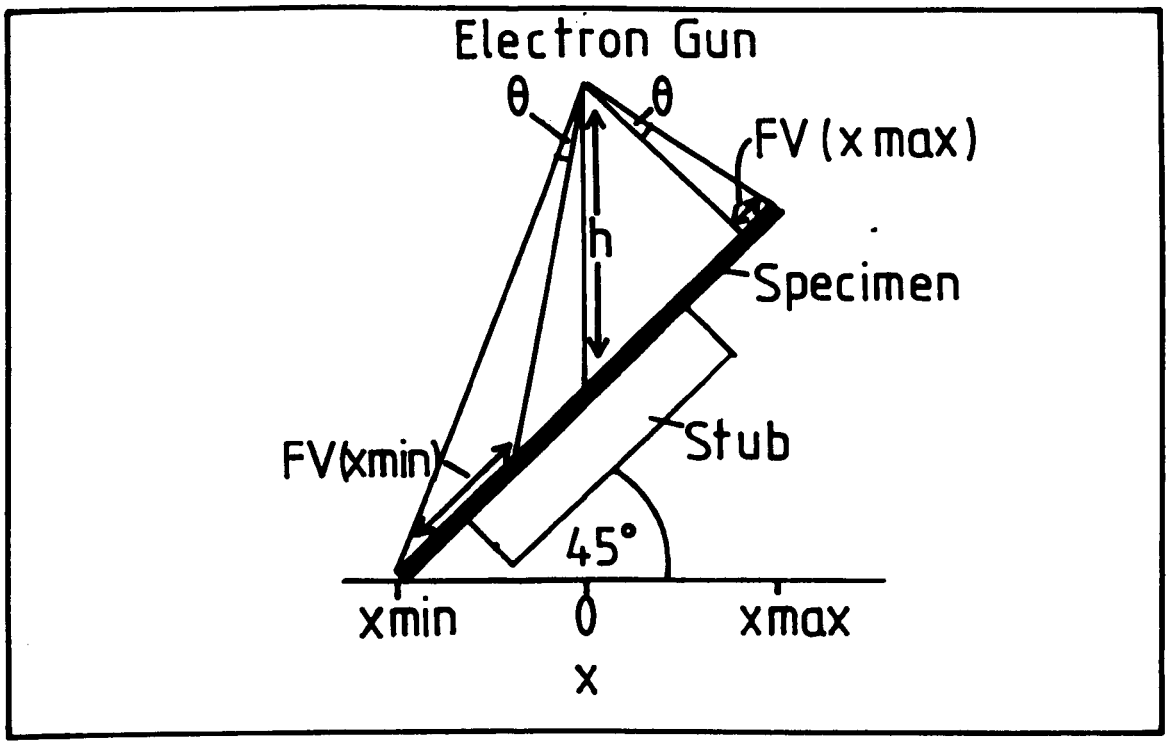

FIGURE 3.16

Variation in the field of view (FV) across a specimen inclined at 45^{o} to the beam axis in the S.E.M.

FV = Field of View (mm^2)
h = Height of beam source above centre of specimen
x = Position (x-coordinate) of specimen
θ = Angle subtended by electron beam in scan across field of view.

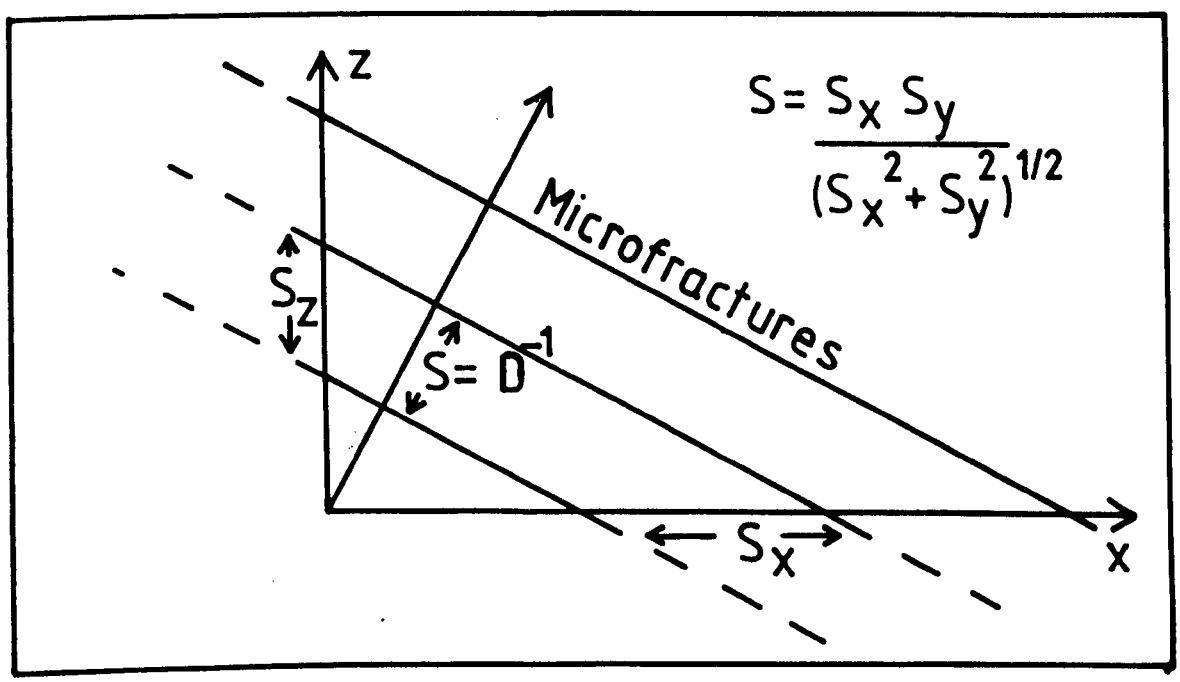

FIGURE 3.17

Calculation of microfracture density (Dmm^{-1}) from microfracture spacing(s) measured along two arbitrary but perpendicular directions, S_x and S_z.

$FV=((h-x^2)+x^2)^{1/2}\ \sin\phi/2\ (\sin(135-\tan^{-1}x+2/h-\phi/2)+\ \sin(45-\tan^{-1}\ x+2/h))$

where h = Height of the beam above the sample at x=0.

ϕ = Angle subtended by the electron beam during a scan over one complete field of view.

To allow for other complications such as the optics of the C.L. detector, rather than evaluating this expression to obtain the field of view, it was measured accurately at the maximum, zero, and minimum values of x using a 200 mesh grid.

	Field of view, FV
x max	$1.390mm^2$
x = 0	$0.806mm^2$
x min	$0.387mm^2$
Average	$0.863mm^2$

These results do indeed show a non-linear change of FV with x as predicted by the equation. The mean field of view will be slightly greater than the median (at x=0): this has been approximated by a simple arithmetic average of the three results.

In order to compare the area and intercept methods, six sections covering the complete rante of densities/mm^2 were also measured in the S.E.M. by intercepts under identical conditions to the area measurements. A grid of perpendicular intercept lines was drawn on the sections with a total minimum length of 30mm, along which the number of intercepts was counted. This method allows a correction to be made for any anisotropy in microfracture density by comparing the microfracture spacing in the two perpendicular directions (S_x, S_z), so that the fracture density (D) can be calculated along the line perpendicular to the fracture planes in the section (Figure 3.17). If S is true fracture spacing, and S_x and S_z the measured spacing along the x and z intercept lines, then:

$$(S_x^2 + S_z^2)^{1/2} = S_x\cos\phi = S_z\sin\phi$$

and $\sin\phi = S/S_X$, $\cos\phi = S/S_3$

$$(S_X^2 + S_Z^2)^{1/2} = S_Z S/S_X = S_X S/S_Z$$

$$= S\,((S_Z^2+S_X^2)/S_Z S_X)$$

$$S = S_Z S_X/(S_X^2+S_Z^2)^{1/2}$$

Since $F = 1/S$, $F_X = 1/S_X$ and $F_Z = 1/S_Z$, and $D = 1/S$,

$$D = F_X F_Z(1/F_X^2 + 1/F_Z^2)^{1/2}$$

All three microfracture densities used here (Dmm^{-2}, Dmm^{-1}, DG^{-1}) are therefore true microfracture densities within the plane of observation, but they are not equivalent to the fracture densities (Dm^{-1}) because they have not been corrected for the orientation of the section relative to any microfracture preferred orientation.

3.7.4 Error.

Comparison of the trial results with those from the final method (Appendix A6) shows that the number of fractures are consistently higher in the final method by a factor of 1.5. Most of this can be attributed to the better care taken over focussing. This dependence of fracture density on focus is also illustrated by the great sensitivity of repeated measurements to condenser settings: in some cases, the improved settings resulted in almost a 3-fold increase in measured density. One sample was remeasured under identical conditions (109CR, Appendix A6): an error of less than 1% in the area density measurements (for 72 fractures) was measured. This may give the approximate relative error for individual sections.

The effect of section orientation was evaluated during the trials on sections 109 and CV5 (Appendix A6). For the relatively high values of fractures/grain in 109, there appears to be a doubling of this parameter between the sections: the lower values of CV5 are within 50% of each other. Section dependence is the biggest weakness of the fracture density measurements, and implies that such measurements should be made in at least two perpendicular sections.

a) **Comparison of Methods.** The area density and grain density measurements are compared in Figure 3.18. The general proportionality indicates merely that there is a limited range of grain sizes among the samples, since the area density will be a function of both the grain density and grain size. A more interesting relationship is shown in Figure 3.19, that between the area and linear intercept densities. Regression analysis of the latter against the former, constrained to pass through the origin, yields the following equation, which is shown on the figure and can be used to give an approximate, empirical conversion of the area densities (Dmm^{-2}) to the linear intercept densities (Dmm^{-1}):

$$Dmm^{-1} = 0.227 \times Dmm^{-2}$$

This correlation is useful because it allows some comparison to be made between linear intercept fracture densities measured in C.L. and optically. Table 3.10 shows firstly area density measurements from polished slabs of quartzites T6-T32 from the Ord Thrust Nappe, Sleat, Isle of Skye (Blenkinsop 1982). Using the above area/linear density relation, the second column gives the equivalent fracture densities to be expected from the linear intercept method. These can be compared with the linear intercept measurements made on the optically visible microfractures, in the third column. The latter values have been adjusted in three dimensions to give the true fracture densities along a line perpendicular to the plane of the microcracks: the adjustment factor used is shown in the fourth column. In comparing these figures, it must be appreciated that the linear intercept measurements in C.L. (column 2) have been adjusted for preferred orientation of the cracks in one plane only: the true fracture density must be greater than or equal to this value by an unknown adjustment.

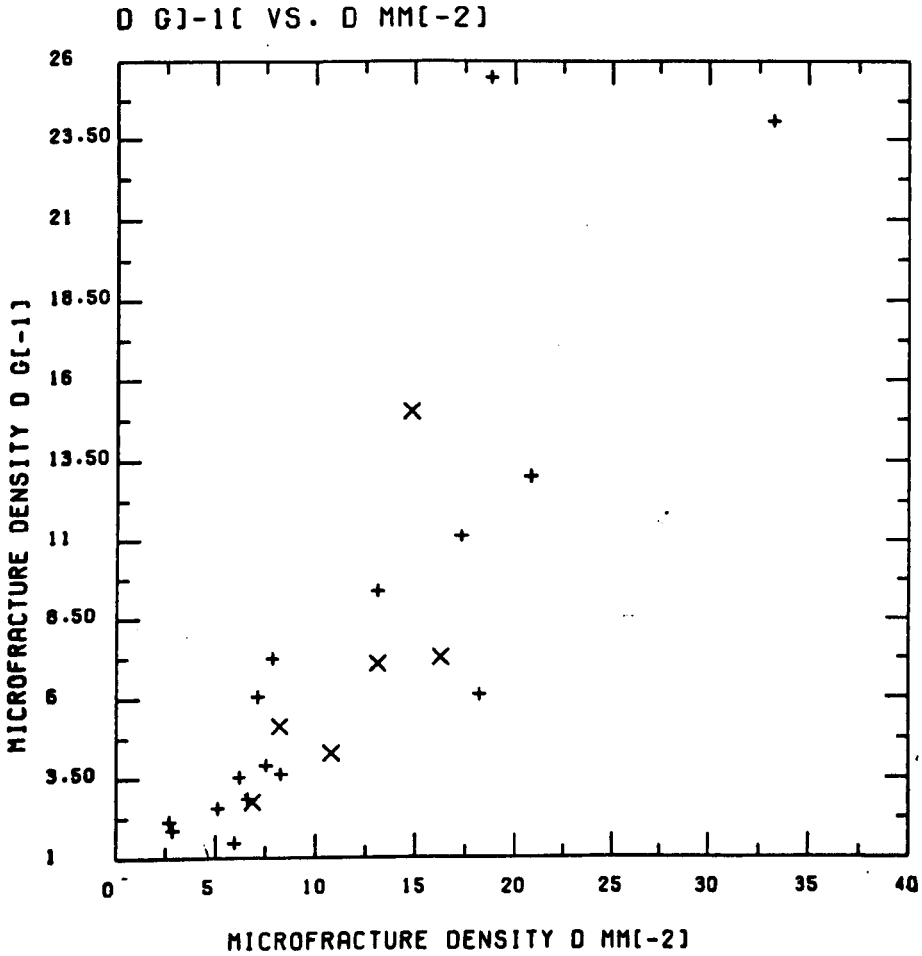

FIGURE 3.18. The relationship between microfracture density (DG^{-1} x 10) and (Dmm^{-2}). The proportionality is a consequence of a limited range of grain sizes. Plus signs - Bernesga Valley; Crosses - Punta Vidrias.

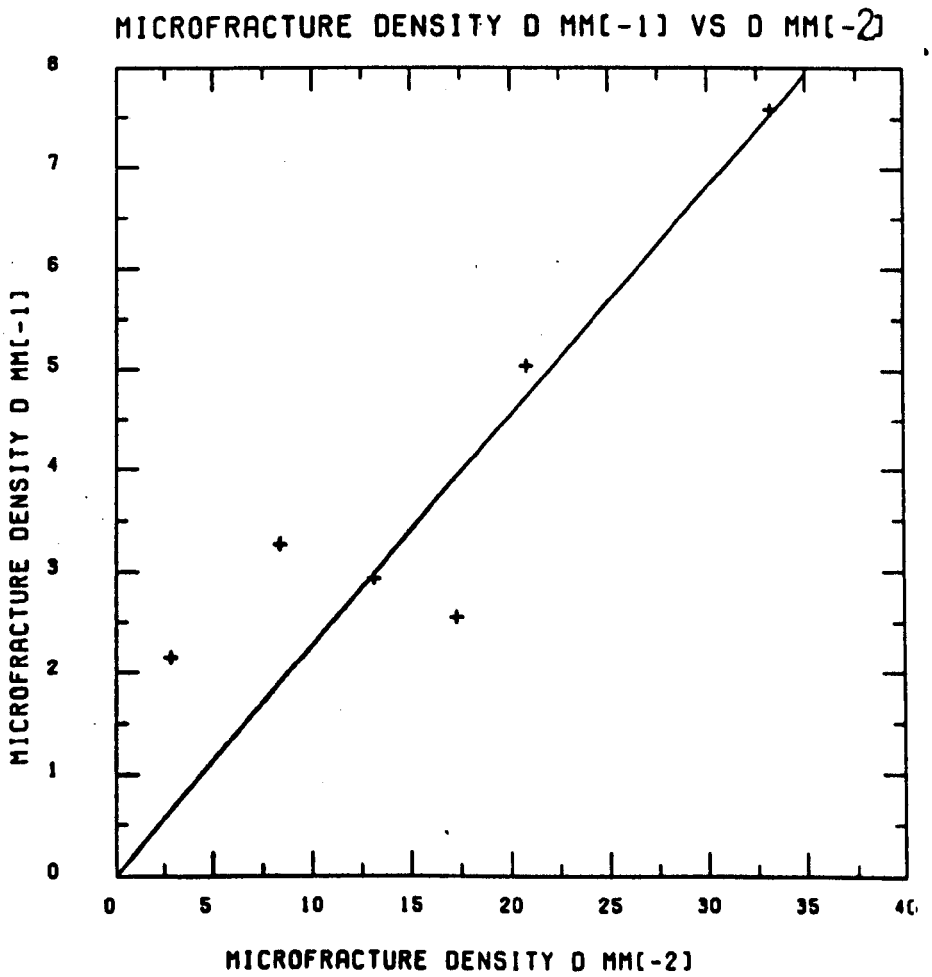

FIGURE 3.19. The relationship between microfracture density (Dmm^{-1}) and Dmm^{-2}. The relationship is shown $Dmm^{-1} = 0.227 \times Dmm^{-2}$

Section	Minimum Dmm^{-2} C.L. (Slab)	Minimum Dmm^{-1} C.L. (Slab)	True Dmm^{-1} (Optical Section)	Orientation Adjustment Factor
T6	23.6	5.3275	36.0	x2.22
T7A	28.9	6.56		
T11A	20.7	4.699	5.72	x1.0
T12A	20.9	4.744		
T32A	14.3	3.246	6.82	x1.04

TABLE 3.10

The fracture densities in C.L. are less than, but well within an order of magnitude of those determined optically. This relationship would be expected, allowing for possible orientation adjustments, if both methods are giving comparable results, and suggests that the C.L. determinations of fracture density made here can be compared with other optical determinations, by area, grain or linear intercept methods, within an order of magnitude.

The observation from Table 2 of Wong and Biegel that the parameter S_v is very close to twice the average of Fa and Fr suggests that this relationship could be analysed in more detail. In fact, the equality S_v=Fa+Fr is true to well within one standard deviation of the measurements. The difference between S_v and Fa+Fr is clearly a function of the anisotropy of frequencies in the two directions, a and r. Defining the anisotropy of frequencies, Af, as Fr/Fa, then the ratio of S_v to Fr+Fa can be derived as follows from Equation 3.3:

$$S_v/(Fr+Fa) = (\pi Fr/2 + (2-\pi/2)Fa)/(Fr+Fa)$$

Since $Af = Fr/Fa$

$$= (\pi AF/2 + 2-\pi/2)/1+AF$$

A graph of this relationship is shown in Figure 3.20, from which it can be seen that the ratio S_v/Fr+Fa is approximately one for values of Af up to 3.0. This suggests that the method of measuring fracture densities used here (an average of the frequencies in two perpendicular directions) will yield an approximate value of half the crack surface per unit volume, $S_v/2$.

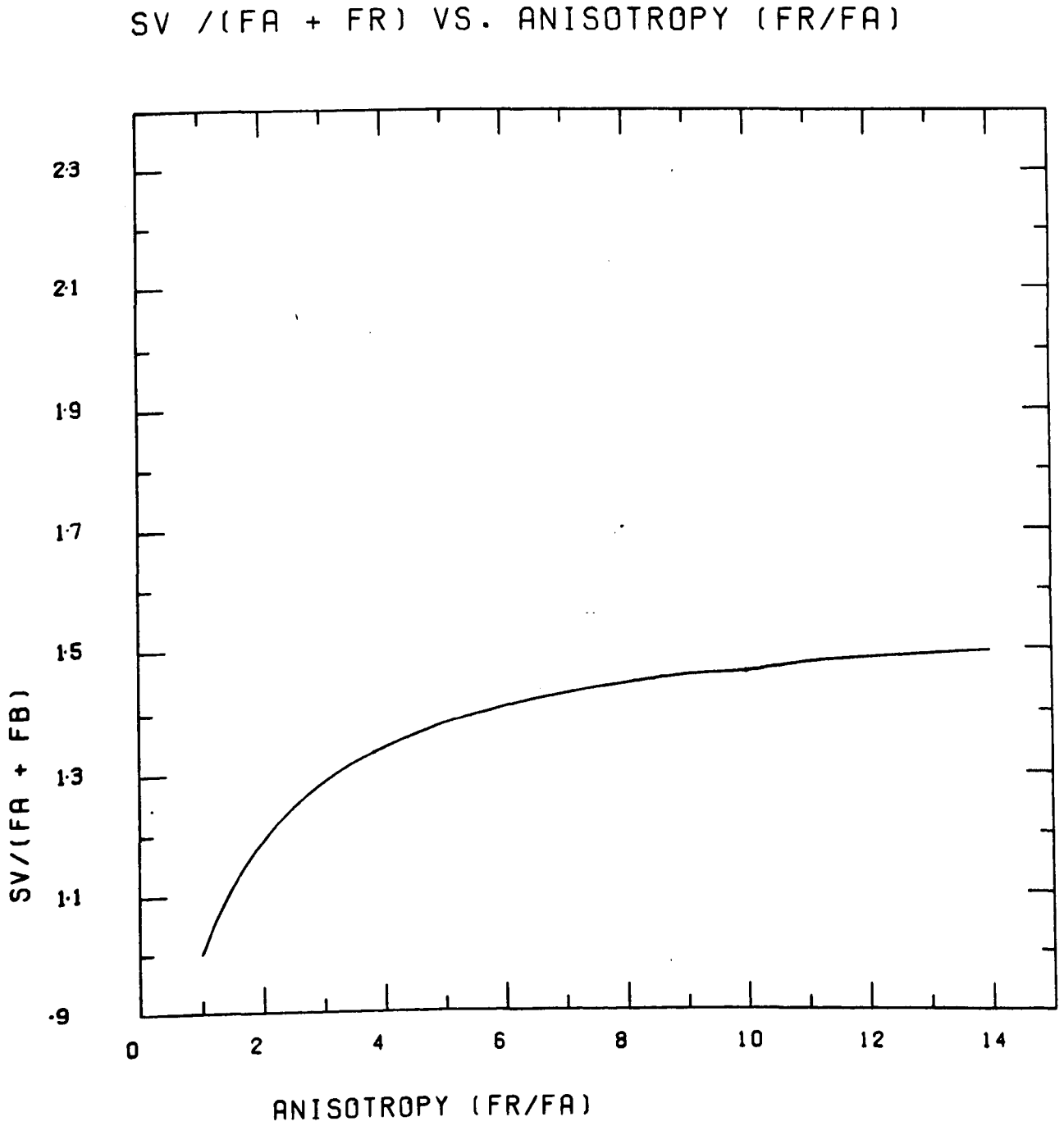

FIGURE 3.20

The relationship between the ratio of crack surface/unit volume (S_v) to the sum of microfracture frequences (Fa + Fr) and the Anisotropy of microfracture frequences (Fr/Fa) i.e. $S_v/(Fa+Fr)$ vs Fr/Fa. The relationship shows that the sum of microfracture frequences is approximately equal to the crack surface/unit volume for all anisotropies up to 3, and even for anisotropies greater than 10 is less than 1.5 times this.

3.8 OPTICAL STRAIN FEATURES

3.8.1 Review

At mid-upper greenschist facies, quartz can deform plastically to produce strong grain shape foliations and lineations, crystallographic preferred orientation and dynamic recrystallization. These features can all be quantified and used to measure strains due to crystal plasticity. However, at lower grade conditions, the operation of crystal plasticity may be difficult to detect because weak tectonic fabrics are not easily distinguished from sedimentary fabrics, little or no crystallographic preferred orientation is developed, and recrystallization is limited. The first stages of crystal plasticity involve production of geometrically necessary dislocations. Subsequently, these localise into subgrain walls, kink bands, and possible deformation lamellae, leading eventually to the formation of dynamically recrystallized new grains by dislocation climb into subgrain walls (e.g. White 1976, Nicholas and Poirier 1975, Urai et al. 1986). The net effect is to introduce a change of crystallographic orientation between different parts of the same grain, visible as undulatory extinction.

It was in order to quantify the early stages of crystal plasticity that Blenkinsop (1982) introduced the technique of measuring the intracrystalline extinction angle, A. This is defined as the maximum acute angle between extinction positions under crossed polars within a single grain. Defined in this way, A has a range of 0 to 45^{o} since extinction occurs when either of the ω or e optical directions are parallel to the polarising direction. A theoretical basis for expecting this to be related to the crystal plasticity is given by the above discussion. the technique was applied to quartzites in the Moine Thrust zone, Skye, to deduce that no increase in intracystalline plasticity occurred with strain.

The value of A measured within a single grain may be affected by five

factors:

i) The amount and nature of intracrystalline plasticity (itself a function of stress, temperature and possibly other extrinsic variables, e.g. pore fluid pressure and chemistry).

ii) Rotation of parts of grains by microfracturing.

iii) Cementation of grains (overgrowth or crack fills) by silica cement misaligned with the host grain.

iv) Inherited strain features

v) Section effects. A truncation effect due to sectioning only a small part of a grain will reduce the measured value of A, while the value will also depend on the orientation of the section with respect to the strained lattice. The orientational dependence of A may be expected to be particularly important where good crystallographic fabrics are developed. In random crystallographic fabrics, both truncation and orientation dependence of A can be allowed for by adequate sampling methods.

The application of measurements of the intracrystalline angle is a large part of this study. The relative contributions of the first four factors above is assessed in each study area, with the overall conclusion that the major variation in samples of A is due to intracrystalline plasticity. Evidence for this is presented in Chapters 5-9.

3.8.2 Method.

a) Sampling. In each section, A was measured in 50 grains (for low standard deviations) or 100 grains (for high standard deviations) along uniformly spaced traverses across the whole section. Three mutually perpendicular sections were measured from each sample, to evaluate any section orientation dependence. In addition, the following types of grain were ignored:

i) Grains containing open or healed fractures.

ii) Grains adjacent to shear faults (which may be heavily microcracked or have parts missing).

iii) Grains affected by any form of solution.

iv) Recrystallized grains. These were identified by a size criterion: only the largest grains were measured in samples showing recrystallisation. (The minimum grain long axes in samples V1,V5,V8,V9,V10,V12,N1,TA1, and TA3 is 230μ and 173μ in VZ1,VZ3 and CB1).

In practice, this means that only grains completely surrounded by other grains or SiO_2 cement were measured.

b) Data Processing. The geometric mean of extinction angles (G.M.A.) was calculated for each individual section, and the three sections from each sample combined. These results are given in Appendix A7 and presented as histograms in Appendix A10. Arithmetic means and logarithmic coefficients of skewness (SK) were also calculated for some samples. The latter is given by:

$$SK = (\log Q_1 + \log Q_3 - (2 \times \log Q_2)) / \log Q_1 - \log Q_3$$

where Q_1, Q_2, Q_3 are the upper, median and lower quart ii es respectively. repectively.

3.8.3 Evaluation of Method

The geometric mean is a more appropriate measure of positively skewed population mean than the arithmetic mean for discrete data. Langley (1971), on the basis of work by Davies (1929), suggested that a 'Davies test' could be applied to determine whether the geometric or arithmetic mean was more suitable. The conditions were that the sample size should be greater than 50 and that the logarithmic coefficient of skewness S should be less than 0.2. However, re-examining the original text reveals that Davies was concerned with deriving distribution parameters by fitting continuous population distributions to discrete data, and that a logarithmic curve was

adequate to do this job with important errors for values of S less than or equal to 0.2. This means that even for values of S>0.2, the geometric mean is more appropriate. The nine values of S calculated show that the logarithmic distribution is slightly positively skewed in three cases and slightly negatively skewed in six. This can be taken to indicate that the logarithmic distribution, and use of the geometric mean, is marginally more representative than the arithmetic mean. The correlation coefficient between A.M.A. and G.M.A. is 0.992.

The dependence of the G.M.A. on section orientation can be evaluated by comparing the individual section data for the three mutually perpendicular sections of each sample. The orientational dependence is expressed by the quantity Δ G.M.A. which is the maximum difference between an individual section G.M.A. and the sample average G.M.A. From Figure 3.21, it can be seen that the orientational dependence rises markedly with G.M.A., which is exactly as predicted for the onset of the development of crystallographic fabrics in 3.8.1. That this dependence is not simply an artefact of increasing error with G.M.A. can be established from the observation that absolute error does not increase with G.M.A.

The adequacy of the sample size was tested by evaluating the G.M.A. after 100,110,120,130,140 and 150 measurements ($G.M.A._N$). Results are shown in Figure 3.22 for the maximum, typical and minimum differences between $G.M.A._N$ and $G.M.A._{150}$. The convergence is always less than 0.125^0 by the penultimate measurement, $G.M.A._{140}$, and typically less than 0.05^0. These sample sizes evaluate G.M.A. to well within the error.

Precision of measurement on the microscope stage is 1^0. Errors were evaluated by remeasuring eleven sections with an average of $+/-0.5^0$ (8.3%). For the combined sections, the average error was $+/-0.3^0$. The comparable values of errors and precision suggest that one of the main sources of error was reading the extinction angle A on the universal stage.

iv) Other Methods. The proportion of grains with obvious subgrains or

FIGURE 3.21

The relationship between Δ G.M.A. and G.M.A. The increase in Δ G.M.A. with G.M.A. is a predicted consequence of crystallographic fabric development as crystal plasticity becomes increasingly important, and gives evidence for the fact that G.M.A. measures effect of crystal plasticity. Plus signs - Cantabrian Zone; Crosses - West Asturian Leonese Zone.

FIGURE 3.22

The convergence of G.M.A. to the ultimate value as a function of number of measurements.

a) A large difference between $G.M.A._N$ and $G.M.A._{150^\circ}$.
b) A typical difference between $G.M.A._N$ and $G.M.A._{150^\circ}$.
c) A small difference between $G.M.A._N$ and $G.M.A._{150^\circ}$.

DELTA (G.M.A.) VS. G.M.A.

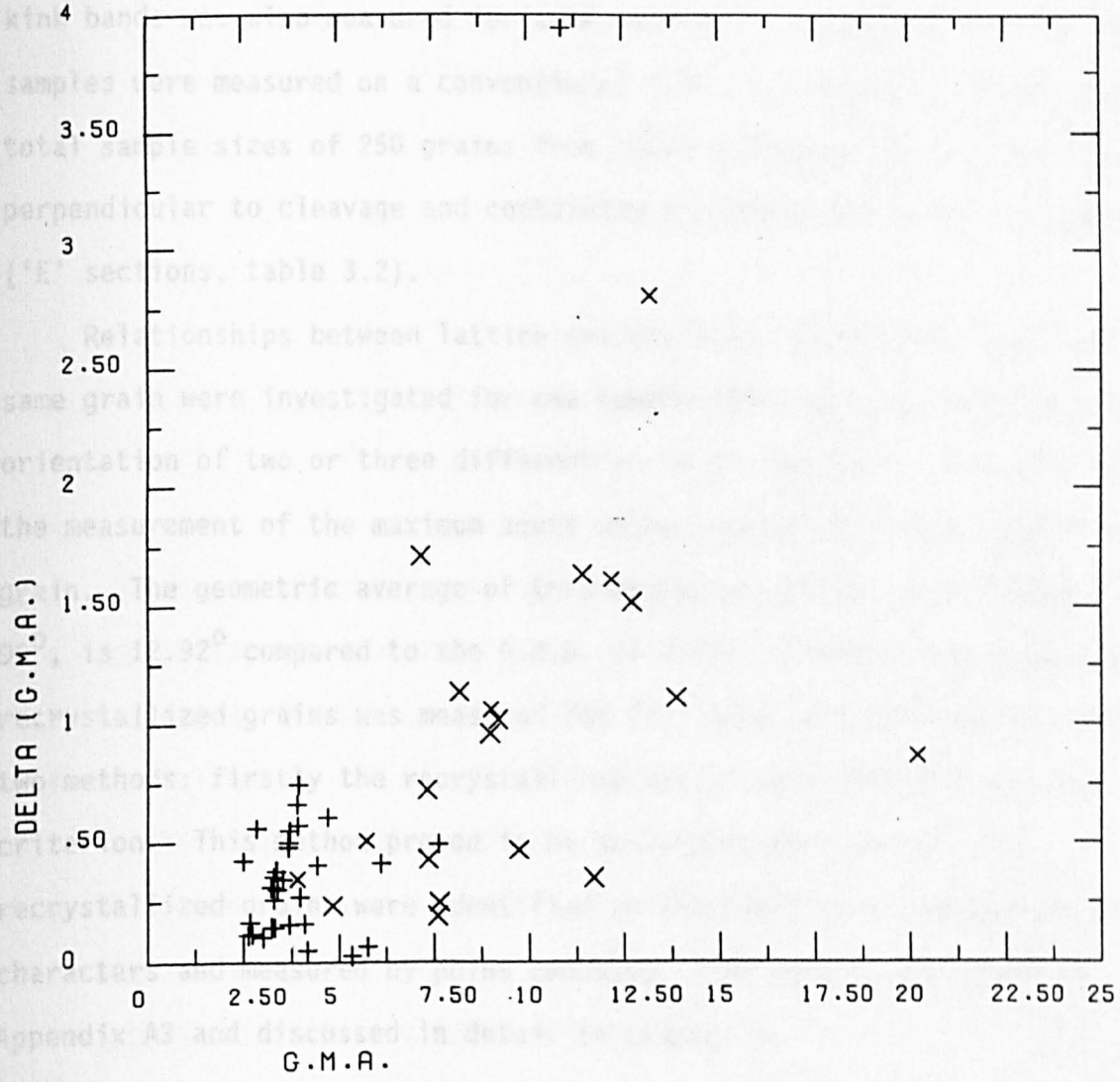

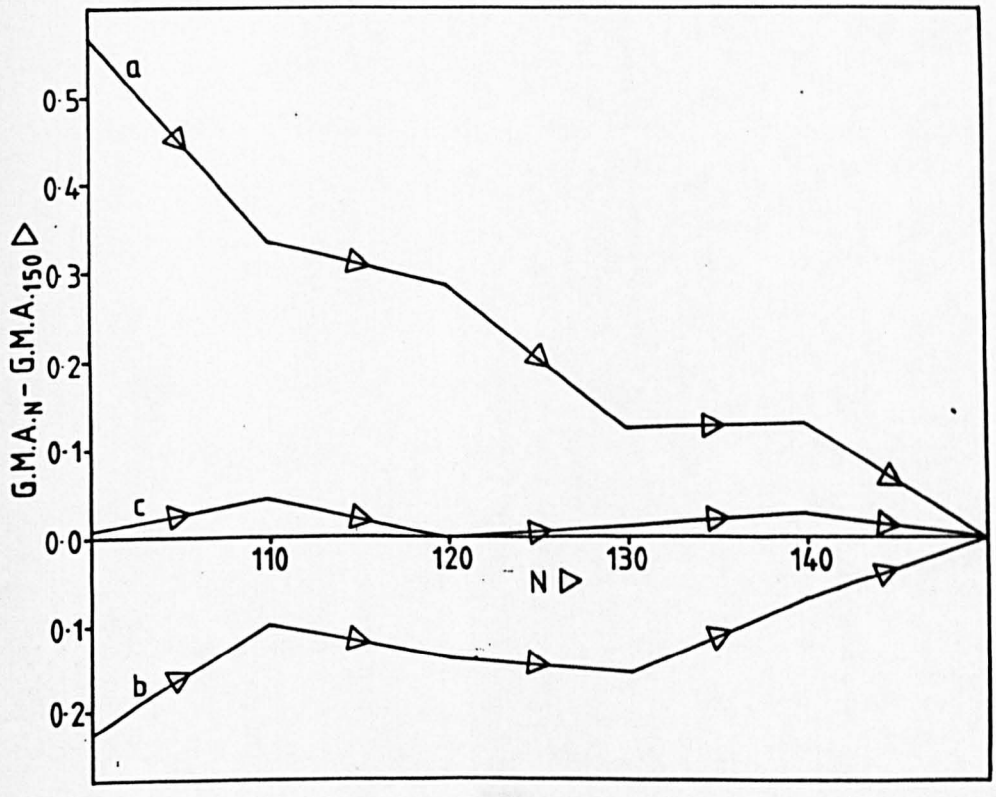

kink bands was also measured for some sections. c-axis fabrics for three samples were measured on a conventional five axis universal stage, using total sample sizes of 250 grains from three different areas of sections perpendicular to cleavage and containing the bedding-cleavage intersection ('E' sections, table 3.2).

Relationships between lattice orientations in different parts of the same grain were investigated for one sample (43V) by recording the c-axis orientation of two or three different parts of the grain. This also allowed the measurement of the maximum acute angle between the c-axes within the grain. The geometric average of this angle, which can vary between 0 and 90^{0}, is 12.92^{0} compared to the G.M.A. of 9.03^{0}. Finally, the proportion of recrystallized grains was measured for five samples from Punta del Sol, by two methods: firstly the recrystallized grains were defined by a size criterion. This method proved to be unsatisfactory, so that the recrystallized grains were identified on the basis of a combination of characters and measured by point counting. The results are given in Appendix A3 and discussed in detail in Chapter 8.

CHAPTER 4

ILLITE CRYSTALLINITY AND CLAY MINERALOGY

4.1 LOW-GRADE METAMORPHISM OF CLAY MINERALS

The precise determination of deformation conditions in the upper crust presents a major problem. For many areas of shallow crustal deformation, conventional metamorphic phase equilibria are not applicable or available. However, recent advances in the study of diagenesis and early metamorphism in sediments have supplied a number of techniques that allow at least a qualitative estimate of metamorphic grade to be made. These advances have in part derived from the realisation that the change from diagenesis to metamorphism is continuous with the same factors applying to both processes, although kinetics may play a more important role in the earlier stages, which complicates the application of the metamorphic facies concept to diagenesis.

The continuous petrographic development of a sediment can be divided into a number of stages between deposition and exposure at the present surface, based on textural criteria (such as "epigenesis" and "metagenesis" (Kossovskaya and Shutov 1963)), mineral assemblages (such as "very low stage" and "low stage" metamorphism (Winkler, 1970)), or mineral facies [such as the "Zeolite facies" (Coombs et al., 1959), prehnite-pumpellyite facies (e.g. Coombs et al., 1970)].

Since 1960 one of the most important descriptions of low grade metamorphism has been the classification into diagentic, anchi- and epizone, (DZ, AZ, EZ), now based on the increase in illite crystallinity. as defined in section 4.2. The chemical and physical changes in illite through low grade metamorphism are well known and described below, with certain other accompanying clay mineral transformations. During the first stages of metamorphism, illite and chlorite form at the expense of the expandable smectite group of clay minerals (principally montmorillorite), leading finally to a well-crystallized muscovite, as clearly summarised in Dunoyer de Segonzac (1969) or Kisch (1983). Smectite is the low

temperature phase with a unit cell of two layers of SiO_4 sheets separated by an interlayer of water and exchangeable cations. In illite, 80% of these cations (K^+ and Na^+) are fixed and in muscovite, the figure increases to 100% (Hower and Mowatt, 1966). Charge balance is maintained by increasing substitution of Al^{3+} for Si^{4+} in the tetrahedral layer, giving illite a tetrahedral charge of 0.8 (= No. of $Al^{3+}/4SiO_4$) and muscovite a tetrahedral charge of 1. Illite thus remains distinct from muscovite. The following chemical changes occur during the transition from smectite to illite and muscovite (Figure 4.1, after Dunoyer de Segonzac 1969):

1. Dehydration of interlayers.
2. Absorption of K^+ in interlayers.
3. Variable substitution of Fe^{2+}, Fe^{3+}, Mg^{2+} and Al^{3+} in the octahedral layer.
4. Replacement of Si^{4+} by Al^{3+} in the tetrahedral layer.

Three structural changes also occur. The interplanar spacing between the adjacent sheets becomes smaller as the loosely bonded water interlayers are replaced by K^+ ions bonded to both adjacent sheets. This is responsible for the increase in sharpness of the illite peak, as the proportion of expandable, water-filled layers with larger basal spacing is reduced. Secondly, when the proportion of expandable layers has reduced to less than 40%, the formerly random mixed layers show a tendency to develop a partial stacking order in a 1:1 sequence, a structure found in allevardite. The change from random to ordered interlaying has recently been examined in detail by Nadeau et al. (1985) in bentonite. They have proposed a simple model in which 'random' mixed layers consist of individual 10A units within 20A illites. Ordering consists merely of progressive diminution of the smaller units in favour of units between 20 and 50A, leading finally to illite composed of units mostly greater than 50A. Histograms of the crystal thickness thus shows a continuous increase in mean value with the smectite-illite conversion. Lastly the polymorph changes from IM_d

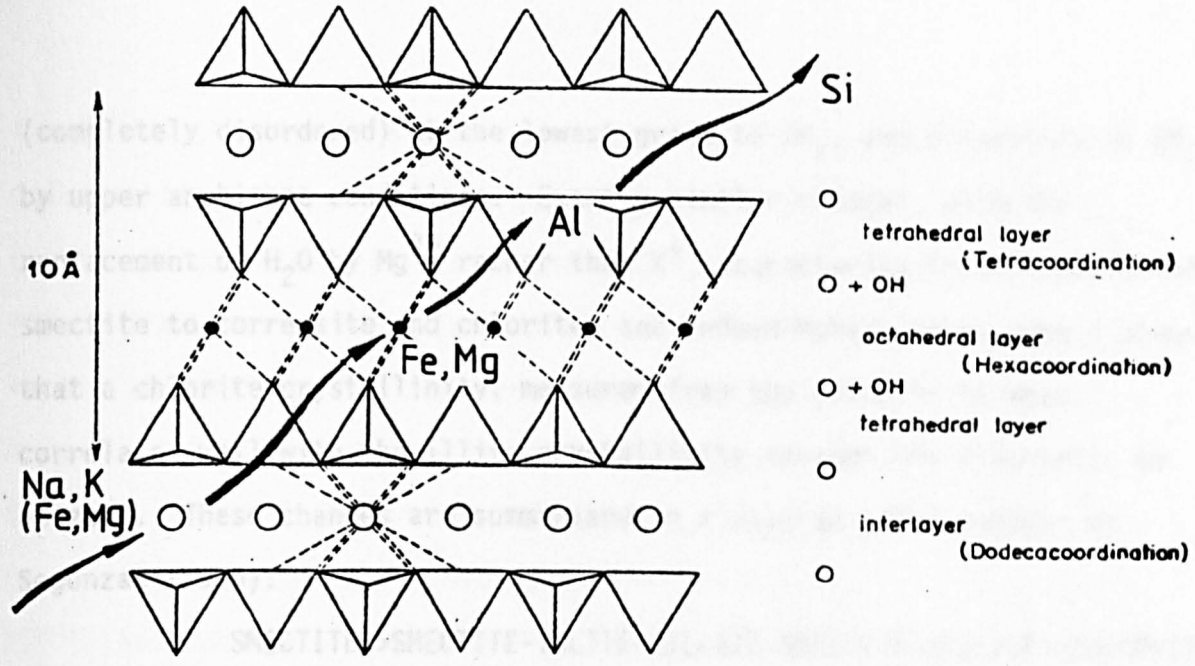

FIGURE 4.1
Chemical changes during metamorphism of smectites. (After Dunoyer de Segonzac, 1970).

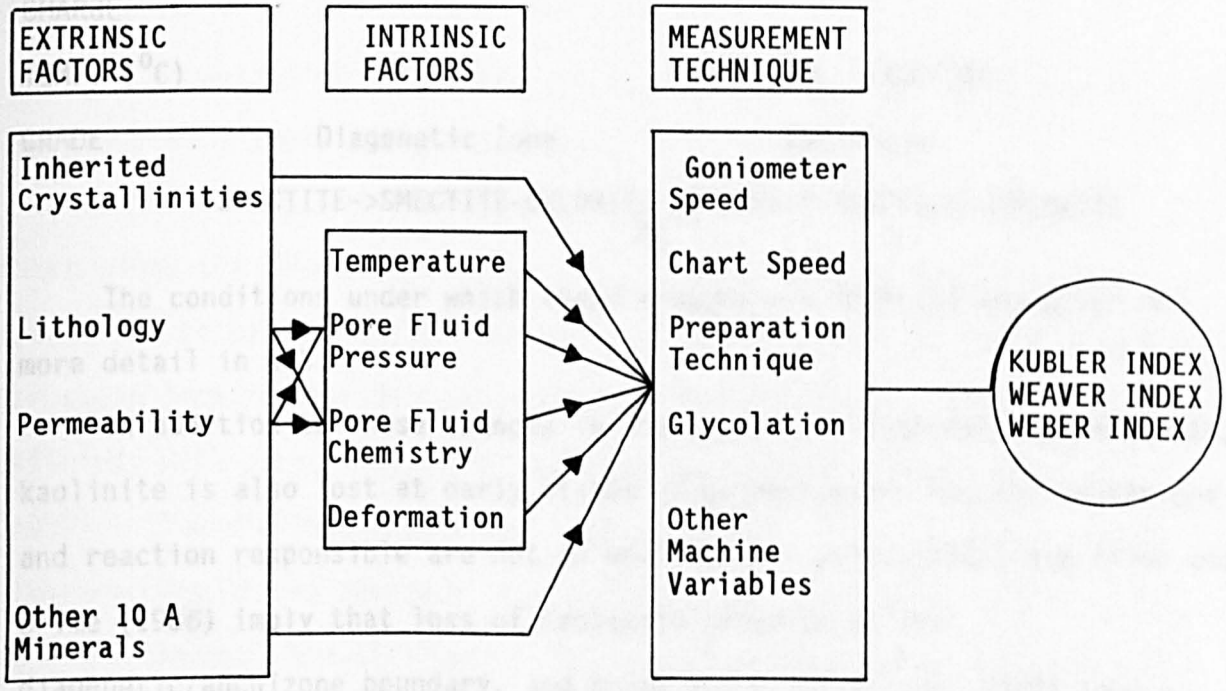

FIGURE 4.3
Factors affecting illite crystallinity.

(completely disordered) at the lowest grade to $1M_1$, and ultimately to $2M_1$ by upper anchizone conditions. Exactly similar changes, with the replacement of H_2O by Mg^{2+} rather than K^+, characterise transformation of smectite to corrensite and chlorite, and indeed Hobson (pers.comm.) shows that a chlorite crystallinity, measured from the chlorite 7A peak, correlates well with the illite crystallinity through the diagenetic to epizone. These changes are summarised in a diagram after Dunoyer de Segonzac (1970):

SMECTITE->SMECTITE-ILLITE->ILLITE-SMECTITE->ILLITE->MUSCOVITE

K^+

% ILLITE	0----------->60-65-->80-90-->100-->0				
STACKING ORDER	Random			Ordered	
POLYMORPH	$1M_d$,1M			2M	
TETRAHEDRAL CHARGE	0----------->0.6------>0.8---->1				
TEMP. (^oC)			95--->160--->200-300		
GRADE	Diagenetic Zone			Anchizone	

SMECTITE->SMECTITE-CHLORITE->CHLORITE-SMECTITE->CHLORITE

Mg^{++}

The conditions under which these changes are effected are given in more detail in 4.3.

In addition to these changes in the smectite-illite-chlorite minerals, kaolinite is also lost at early stages of metamorphism, but the conditions and reaction responsible are not so well known. Brime (1981) and Aller and Brime (1985) imply that loss of kaolinite occurred at the diagenetic/anchizone boundary, and Brime and Pérez-Estaún (1980) show a decrease from trace to negligible amounts through the anchizone. In wells from the Gulf Coast, Perry and Hower (1970) report the presence of kaolinite to a temperature of 130°C without any change in abundance with depth. Hower et al. (1976) show that potassium feldspar is completely destroyed to form kaolin over the lower-temperature part of this interval

(to 90°C). A slightly higher temperature (100-120°C) was deduced for the 'albitisation window' by Boles (1984) in which anorthite reacted with quartz and water to give albite and dickite at fluid pressures of 300-500MPa (depths of 2.5-3km) in seawater. The upper temperature of the kaolinite stability field was evaluated from wells in the Salton Trough by McDowell (1984): the kaolinite-->chlorite reaction occurred at 190°C. Sabatier (in Kisch 1983) reports the reaction of kaolinite with montmorillonite to form illite in artificial seawater at a temperature of 200°C and pressure of 1.5 MPa. The forward reaction of feldspar, kaolinite and mixed-layered montmorillonite to give chamosite/chlorite and illite occurred at 100°C, PH_2O=0.7MPa and 200°C at PH_2O=2.1MPa (Hiltabrand et al. in Kisch 1983). This indicates a pressure sensitivity which makes the other data difficult to interpret; but both experimental and in-situ observations agree on 200°C as an upper temperature limit to the stability of kaolinite.

The formation of paragonite and pyrophyllite in the anchizone is shown by Frey (1970, 1984) who gives the reaction:

Kaolinite + Quartz --> Pyrophyllite + H_2O

Kisch gives the temperature range of this reaction as 200-300°C. The appearance of paragonite in both the anchizone and epizone is attributed to formation from regular illite/smectite by Aller and Brime (1985) and detected, with pyrophyllite, in the anchizone by Brime and Pérez-Estaún (1980). It would thus appear that the loss of kaolinite at the diagenetic/anchizone boundary, and formation of paragonite and pyrophyllite in the anchizone, are also useful indicators of low-grade metamorphic facies.

Two other techniques based on the X-ray diffraction characteristics of illite-smectite have been used to study low grade metamorphism. Esquevin (1969) proposed that the Intensity Ratio of the Illite (002)/(001) peaks measured the illite chemical composition.

The use of the Intensity Ratio (I.R.) as proposed by Esquevin (1969) has been questioned by Kisch (1983), who points out that I.R. does not correlate, as suggested, with the Al/(Mg+Fe) ratio in some anchi- and epi-metamorphic zones. It is also evident that I.R. and illite crystallinity do not correlate well in general except in limited cases in the anchizone (see, for example, Gill et al. 1977, Dunoyer de Segonzac 1969, Brime and Pérez-Estaún 1980). Cronshaw (1984) shows that I.R. from individual samples of Welsh slates is too orientation dependent to be useful, and Kisch (1980) found that two regions of clearly distinguishable metamorphic grade could not be separated on the basis of I.R. The mica lattice parameter b_0 can be used as a geobarometer (Sassi and Scolari 1974) at anchi- and epizone grades; however it is not useful in the diagenetic zone so has not been applied in this study.

4.2 DEFINITION OF INDICES OF ILLITE CRYSTALLINITY

From the first use of the term 'illite crystallinity', it has referred strictly to an empirical measure of the character of the basal (001) peak of illite in X-ray diffraction. With increasing grade, the peak becomes narrower and more symmetrical, a change which can be quantified in a number of ways. However, this highly practical approach still has no established physical basis, in spite of the well known corresponding structural changes. Merriman and Roberts (1985) state that they regard crystallinity as "the fundamental thickness of mica crystallites consisting of a stack of N 10A unit cells", and give the Scherner equation relating N to half peak height width. The T.E.M. observations of Nadeau et al. (1985) certainly show that N increases with the transformation from smectite to illite, but also indicate that an interparticulate diffraction effect from water or organic molecules may generate peak broadening. Peak broadening is also well known to be caused by random mixed layering of small quantities of

smectite, as predicted by the Reynolds and Hower model (1970). Given these possible complications, Merriman and Roberts revert to an original empirical definition of crystallinity by half peak height width. Until the exact significance of illite peak broadening is successfully modelled by theory, 'crystallinity' must be regarded in this purely descriptive way.

Four methods of describing the peak have been used, leading to a regrettable difficulty in comparison of results.

4.2.1 Weaver Index

The first index, proposed by Weaver (1960), is now completely obsolete. The index measures simply the ratio of height of the (001) peak at 10A to height at 10.5A (Figure 4.2). Even this most simple index has unfortunately two variations: the majority of studies have corrected the Weaver Index for a background slope in intensity, but this has not always been the case.

4.2.2 Modified Weaver Index

To allow for the fact that the illite peak is not always exactly at 10A, a modification has been introduced so that the maximum peak height is measured and given as a ratio to the peak height at that position +0.5A (Figure 4.2) with a background correction. This recent improvement has only been made in a limited number of studies, but supercedes the original definition and will hereafter be referred to as the Weaver Index.

4.2.3 Kubler Index

By far the most commonly adopted index was introduced by Kubler (1964) to overcome difficulties of measuring Weaver indices on very narrow, high crystallinity peaks. In this case, the width of the illite peak at half peak height allowing for background changes in intensity, is measured (Figure 4.2). At first this was given a value in mm but Kisch (1980)

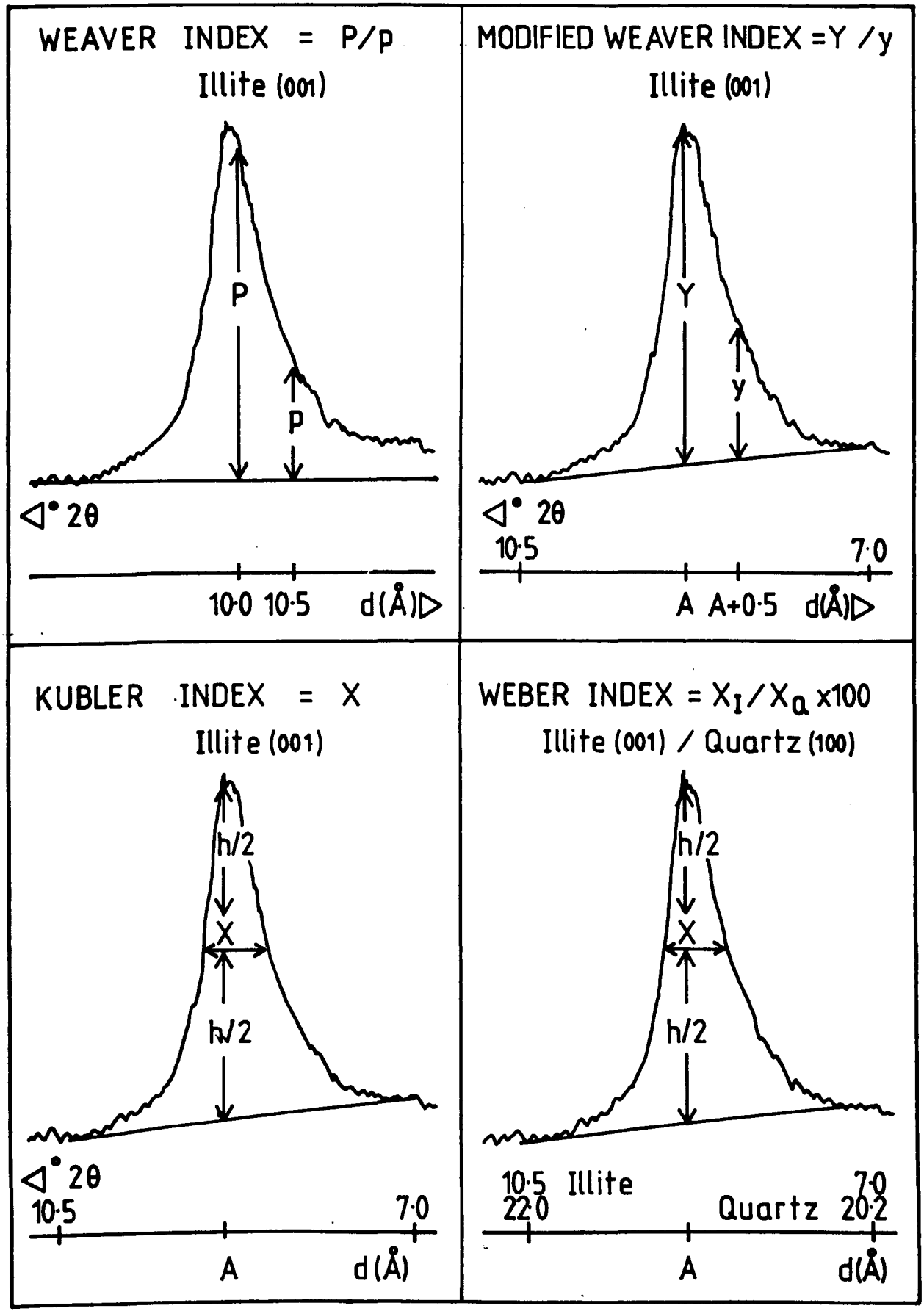

FIGURE 4.2

Indices of Illite Crystallinity
P = Height of Illite (001) peak at 10A
p = Height of Illite (001) peak at 10.5A
Y = Maximum Height of Illite (001) peak, corrected for background slope.
A = Latice spacing of maximum peak height
y = Height of Illite (001) peak at A+0.5A
X = Width of Illite (001) peak at half-peak height (h/2)

pointed out that comparison of results would be greatly facilitated if expressed in $^{o}2\theta$.

4.2.4 Weber Index

The last common index is due to Weber (1972a). This gives the half-peak height width of the illite (001) peak relative to the same measurement on the (100) peak of a quartz standard, multiplied by 100 (Figure 4.2). This is proposed in order to correct for long period and inter-laboratory machine fluctuations.

The definitions of Weaver and Modified Weaver indices are therefore such that they are dimensionless numbers that **increase** with crystallinity, while the Kubler Index, measured in units of $^{o}2\theta$, and the dimensionless Weber Index **decrease** with crystallinity. To facilitate comparisons, most diagrams have been drafted showing crystallinity increasing upwards or to the right; Kubler Indices therefore **decrease** in these directions.

In order to combine the strengths of the various indices, Cronshaw (1984) developed a composite crystallinity index (C.C.I.) from the Kubler, Weaver and Weber Indices. This expresses the value of each index as a proportion of its total range, and sums the three proportions to give a single measure of crystallinity. It enables the application of a parametric statistical test to the data because it has the effect of reducing variance between subdivisions of the data, but contains no additional information.

The relative merits of the Weaver and Kubler indices have been discussed by Kubler (1964, 1968) who suggests that errors in the Weaver Index are greater than the Kubler Index at higher crystallinities and vice-versa at lower crystallinities. This proposition is examined in greater detail on the basis of data from this study in section 4.7. There is currently a trend to measure both Kubler and Weaver indices and to display results in the form of a graph of one index relative to the other,

but few attempts have been made to question the value of this procedure. Cronshaw (1984) compares Kubler and Weber Indices and concludes that the correlation is sufficiently good to make measuring both unnecessary.

4.3 FACTORS AFFECTING ILLITE CRYSTALLINITY

The transformation of smectite to illite, and by implication illite crystallinity, is primarily determined by intrinsic factors: these govern the equilibrium crystallinity expected under a given set of conditions. However, they are in turn controlled by a number of extrinsic factors which may affect crystallinity indirectly via an intrinsic factor, and the final determination of crystallinity is also dependent on the measuring technique. The influence of the intrinsic and extrinsic factors has been elucidated from three sources: firstly, well log data in recent sediments still undergoing burial gives a direct insight into the natural process. Secondly, experiments have provided a certain amount of data but interpretations are complicated by the very slow kinetics of the reactions involved. Lastly, regional studies of eroded orogenic belts have been made with considerable success. A combination of these sources suggests that the alteration of the smectite, and illite crystallinity, must be considered as a function of the four intrinsic variables, which may be determined by some of the four extrinsic factors. The interactions between intrinsic, extrinsic and measurement factors are summarised in Figure 4.3.

4.3.1 Temperature

All studies agree that temperature is the most important parameter. A compilation of well log data showing temperatures for the reduction in percentage of expandable layers is shown in Figure 4.4. The most striking conclusion is that a dramatic reduction from 75% to 25% occurs with a remarkably coincident temperature range from approximately 80^{o}C to 100^{o}C.

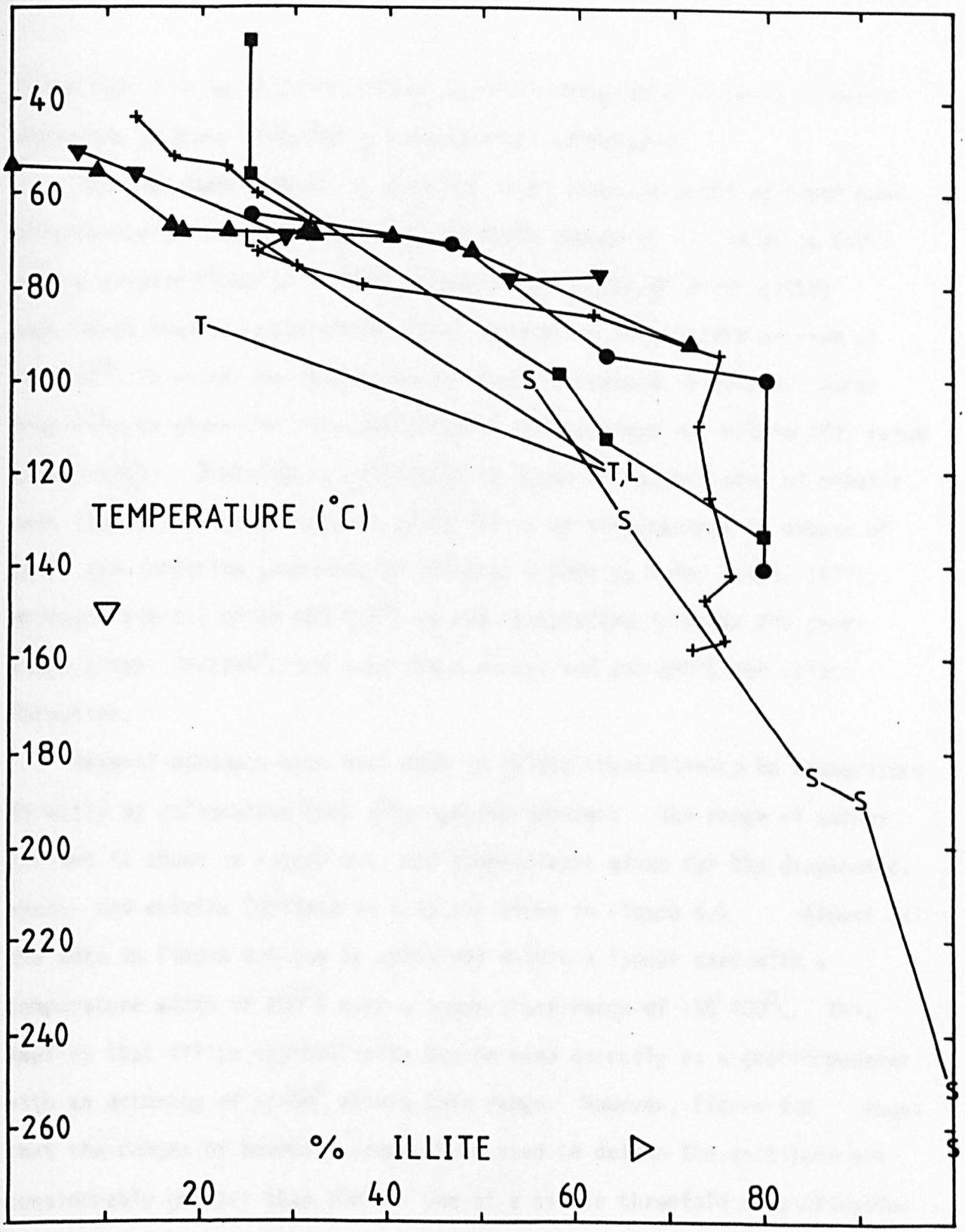

FIGURE 4.4
The Relationship between percentage of Illite Layers and Temperature

+ = Gulf Coast Well 6 (<2μ weighted average, Hower et al. 1976)
■ = Gulf Coast Well C (Perry and Hower 1970)
● = Gulf Coast Well E (Perry and Hower 1970)
▲ = Denver Basin, Dakota (minimum % illite, shales, Rettke 1981)
▼ = Denver Basin, Dakota (minimum % illite, bentonites, Rettke 1981)
S = Salton Trough, California (McDowell 1984)
T = Texas (Burst 1969)
L = Logbada, Douala Basin, Cameroun (Dunoyer de Segonzac 1969)

(Note that all the figures are not strictly comparable in terms of other variables such as lithology and measurement technique).

The subsequent reduction from 25% to 0% smectite seems to occur more progressively, reaching completion at 200°C (Hower et al. 1976) to 260°C with a crystallinity of 0.5°2θ (McDowell 1984), though Burst (1969) considered that a second temperature interval of instability existed at 120-130°C in which the proportion of smectite reduced to 10-20%. Other temperatures given for the completion of illitisation are within this range (Kisch 1983). Ordering is considered to occur at temperatures of greater than 120°C, and the appearance of 2M illite at temperatures in excess of 200°C (no confining pressure) or 125°C at 4.5MPa by Velde (1965, 1977). McDowell (ibid.) gives 100-130°C as the temperature interval for short range order, 160-190°C for long range order, and 240-280°C for illite formation.

Several attempts have been made to relate crystallinity to temperature directly by calibration with other geothermometers. The range of values derived is shown in Figure 4.5, and temperatures given for the diagenetic, anchi- and epizone (defined in 4.4) are shown in Figure 4.6 . Almost all the data in Figure 4.5 can be contained within a linear band with a temperature width of 100°C over a temperature range of 150-400°C. This implies that illite crystallinity may be used directly as a geothermometer with an accuracy of +/-50° within this range. However, Figure 4.6 shows that the ranges of boundary temperature used to define the anchizone are considerably greater than 100°C. Use of a simple threefold classification of crystallinity is less satisfactory than individual data points.

The difference in accuracy between Figure 4.5 and 4.6 is a direct reflection of the discrepancies in definition of illite crystallinity boundary values illustrated in Figure 4.7 and emphasises the need for a unified definition of absolute values together with calibration by standards.

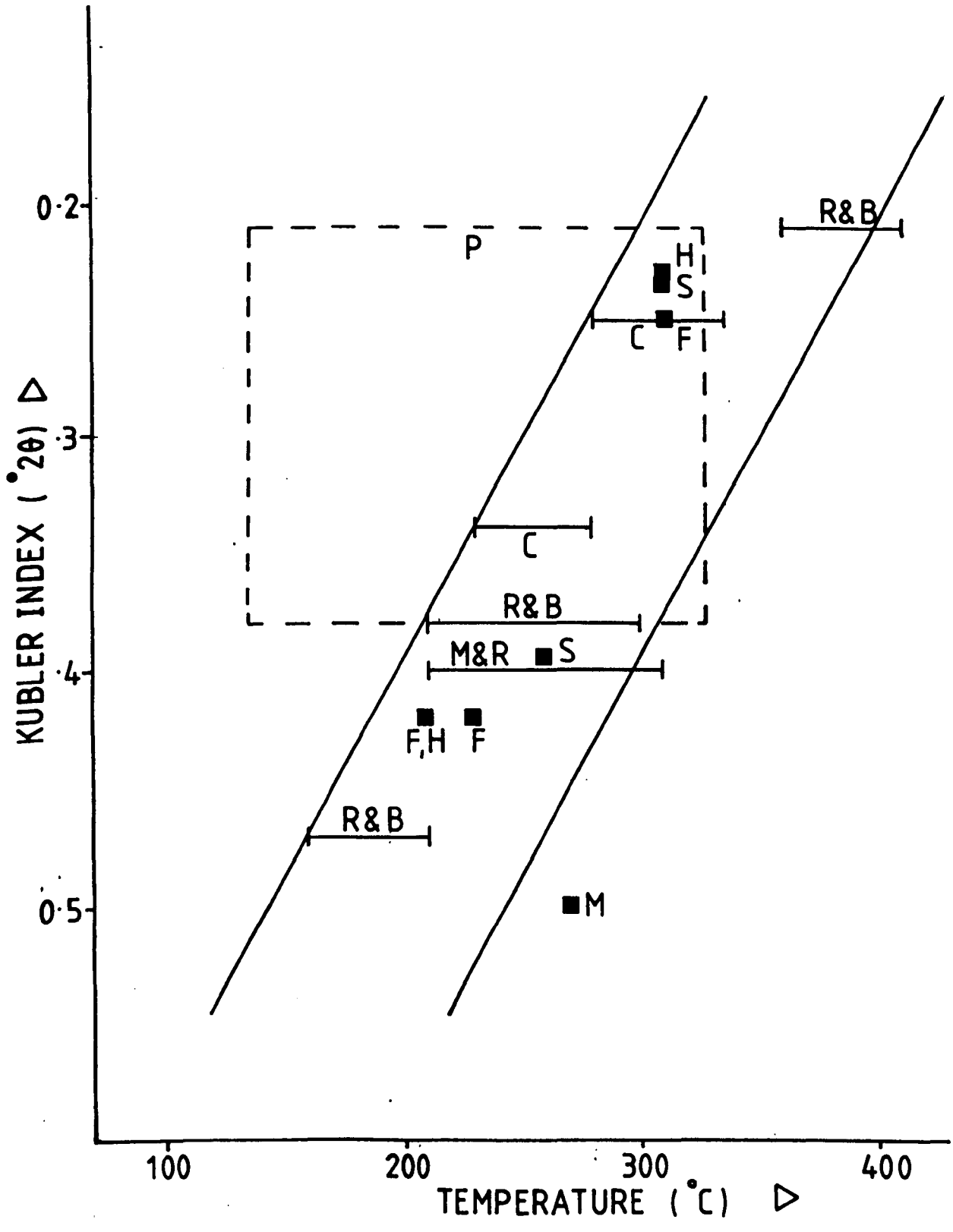

FIGURE 4.5
The Relationship between illite crystallinity and temperature, based on calibrations with other geothermometers.

R & B = Robinson and Bevins (1986)
H = Hesse (1984)
S = Stadler (1979)
F = Frey (1984)
C = Cronshaw (1984)
P = Primmer (1985)
M & R = Merriman and Roberts (1985)
M = McDowell (1984)

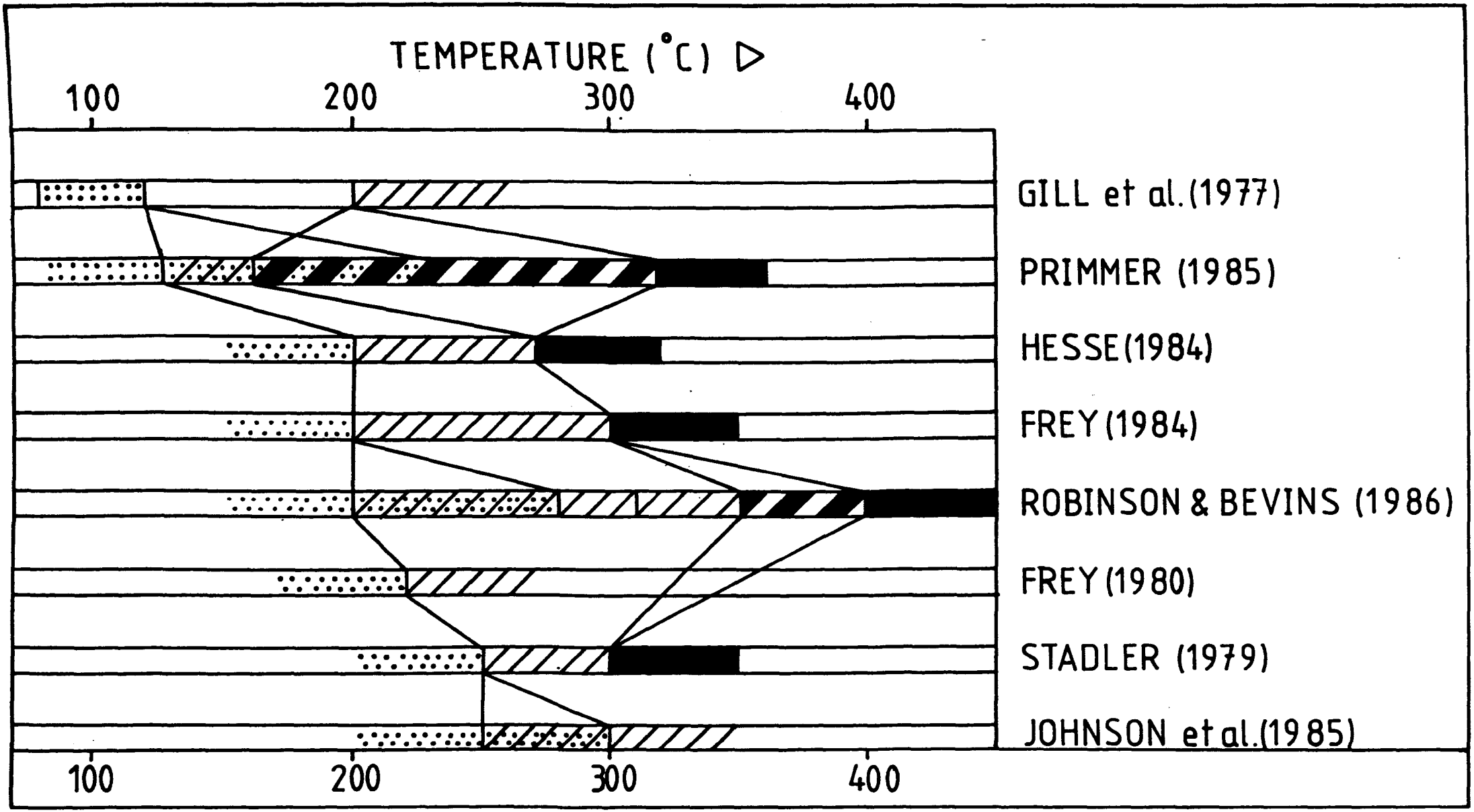

FIGURE 4.6
Temperatures given for the diagenetic, anchi- and epizones.

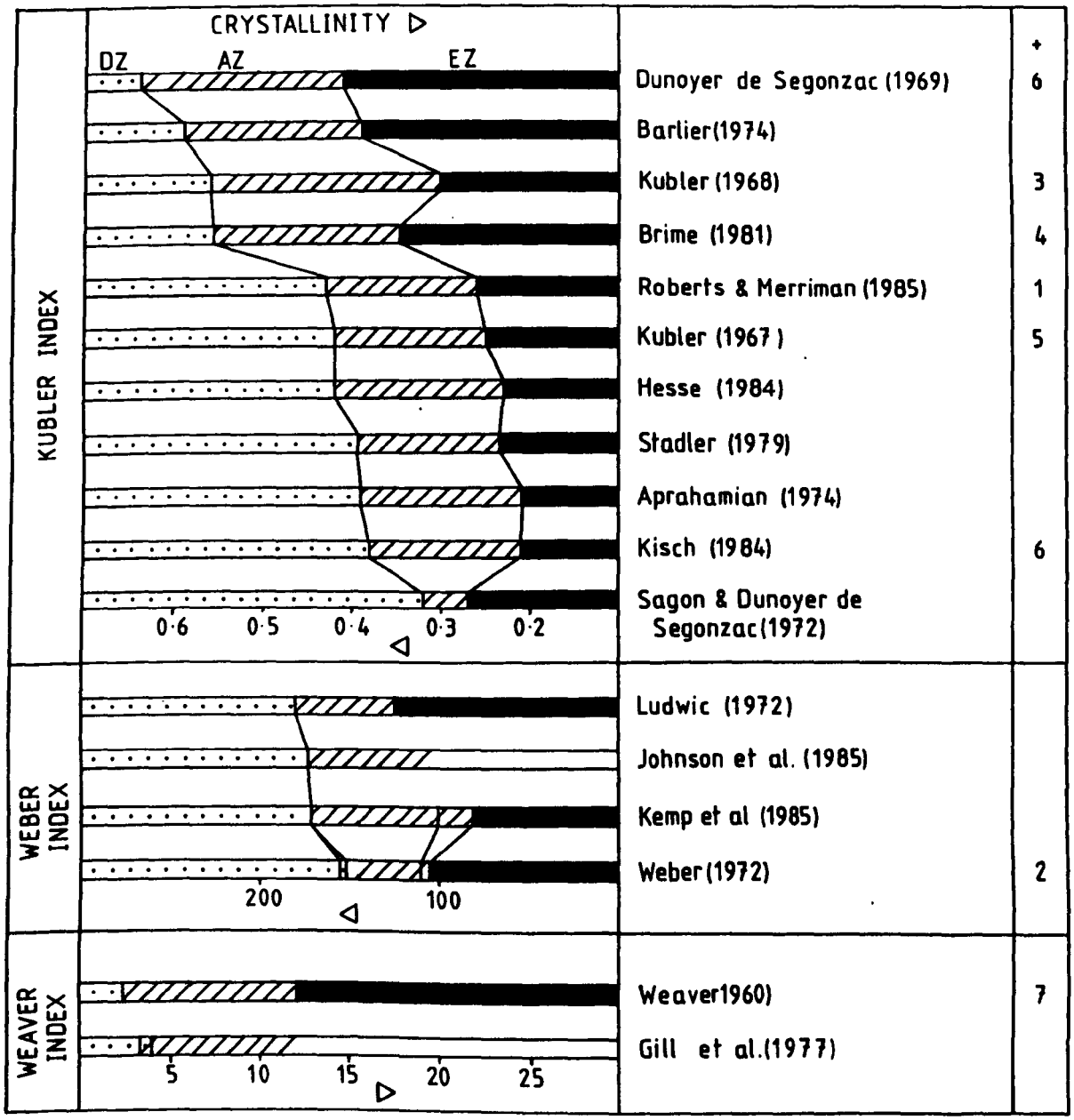

FIGURE 4.7

Definitions used for the diagenetic, anchi- and epizones (DZ, AZ, EZ). The number of other studies using the same definitions is also shown.

The range of crystallinity/temperature relationships has three important components, of which the most fundamental is the contribution of all the other factors listed in this section (4.3) to determine crystallinity. These are often unappreciated when crystallinity is used indiscriminately as a geothermometer. But permeability and lithological factors are also important influences on crystallinity in the diagenetic zone. Secondly, the range also reflects the lack of calibration between different laboratories (4.4) and lastly, the discrepancies and inaccuracies of the other two temperature geothermometers used to obtain the temperature estimates are a further source of error.

4.3.2 Pressure

A very small or complete lack of pressure dependence is implicitly or explicitly assumed by several illite crystallinity studies, and a lack of correlation between crystallinity and depth of burial has been demonstrated in South Wales (Gill et al. 1977) and South West England (Brazier et al. 1979). The almost isothermal increase in proportion of illite from 25 to 75% shown in Figure 4.4 for a range of geothermal gradients suggests that the process of illitisation is fairly pressure-independent; this is also evident from the much greater spread of depths over which this transition occurs shown in Figure 4.8a. By plotting the proportion of illite against depth at various constant temperatures for Gulf Coast Wells 6, C and E (Figure 4.8b)it is seen that there are almost equal numbers of increases and decreases of isothermal illite proportion with depth. Unfortunately the effect of pore-fluid pressure cannot be isolated from a possible lithostatic pressure effect from this data.

4.3.3 Pore Fluid Pressure

Pore fluid pressure control of illitisation is best shown by the experiments of Khitarov and Pugin (in Kisch 1983). As expected, higher

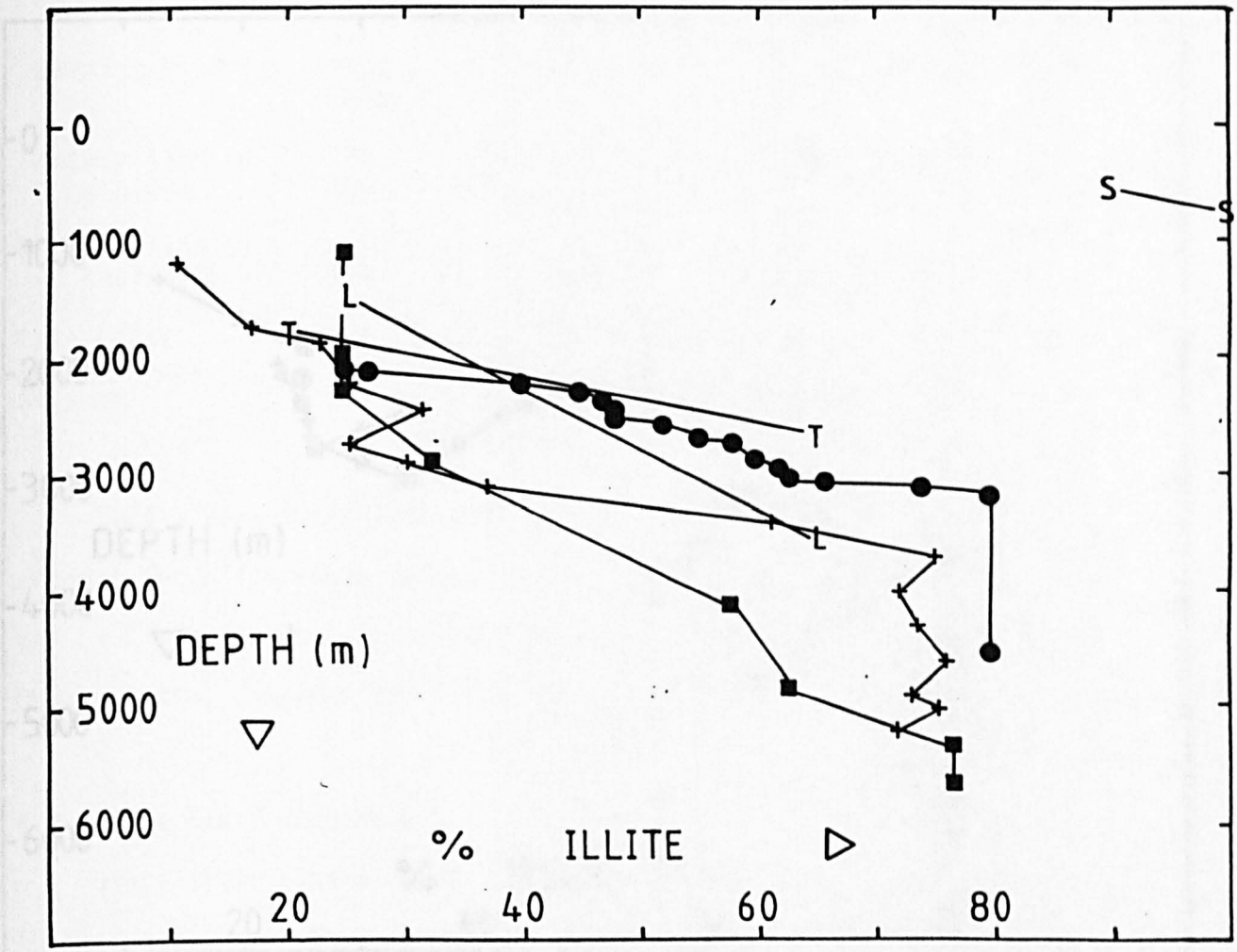

FIGURE 4.8a
The Relationship between percentage of Illite Layers and Depth

+ = Gulf Coast Well 6 (<2μ weighted average, Hower et al. 1976)
■ = Gulf Coast Well C (Perry and Hower 1970)
● = Gulf Coast Well E (Perry and Hower 1970)
S = Salton Trough, California (McDowell and Elders 1980)
T = Texas (Burst 1969)
L = Logbada, Douala Basin, Cameroun (Dunoyer de Segonzac 1969)

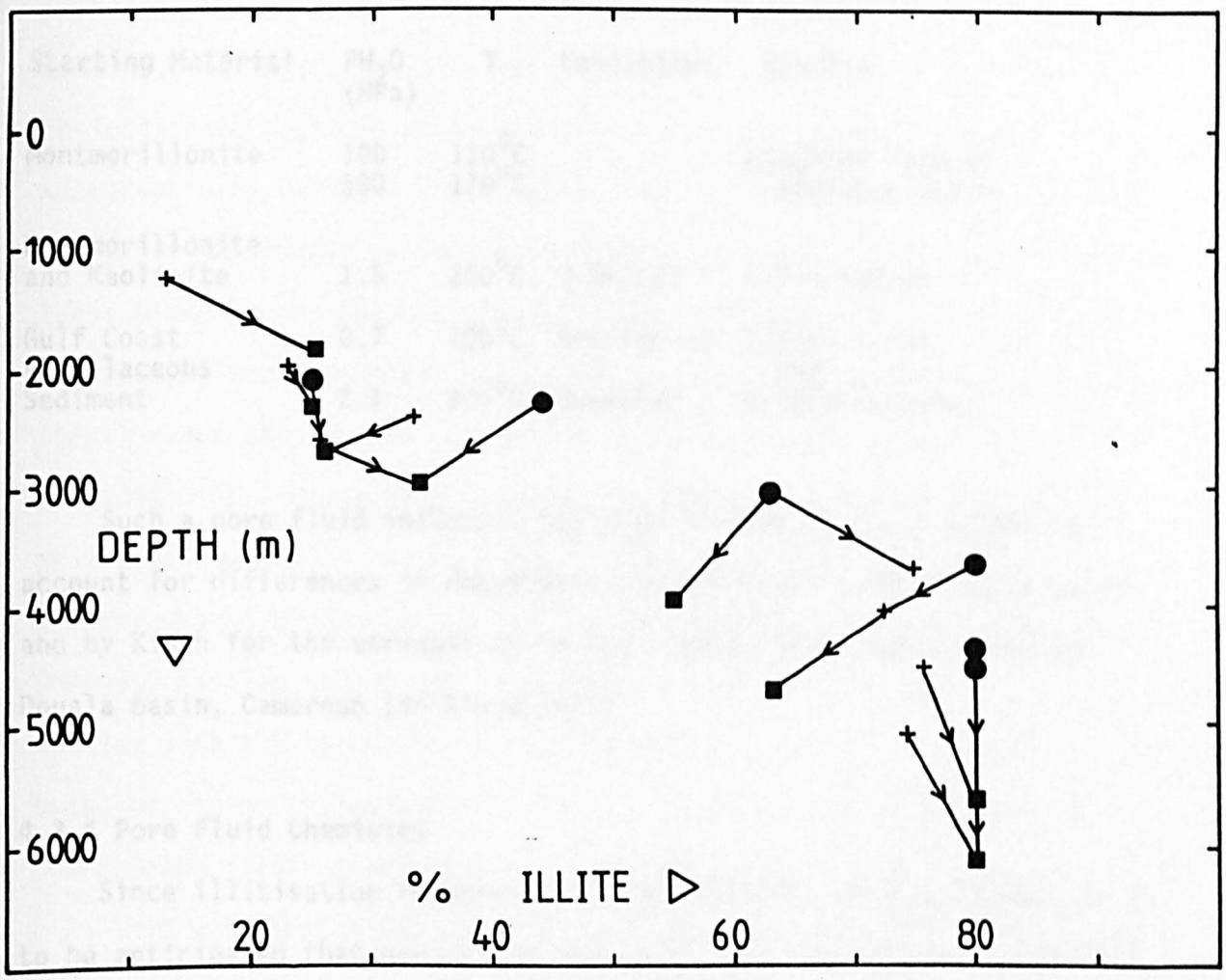

FIGURE 4.8b
The Relationship between % illite, depth at various constant temperatures.

■ = Gulf Coast Well C (Perry and Hower 1970).
● = Gulf Coast Well E (Perry and Hower 1970).
+ = Gulf Coast Well 6 (<2μ weighted average, Hower et al. 1976).

pore fluid pressures require higher temperatures to achieve dehydration. The table gives the temperatures required for complete loss of water or illitisation at various pore fluid pressures.

Starting Material	PH_2O (MPa)	T	Conditions	Results
Montmorillonite	100 500	130°C 170°C		Complete loss of interlayer water
Montmorillonite and Kaolinite	1.5	200°C	0.6KCL/1	Illitisation
Gulf Coast Argillaceous Sediment	0.7	100°C	Artificial	Illitisation and Chloritisation
	2.1	200°C	Seawater	

Such a pore fluid influence has been invoked by Burst (1959) to account for differences in dehydration temperatures in Gulf coast wells, and by Kisch for the variability in the Logbada Well samples from the Douala basin, Cameroun (in Kisch 1983).

4.3.4 Pore Fluid Chemistry

Since illitisation requires the fixation of K^+ in interlayers, it is to be anticipated that pore fluid chemistry will also affect the process. Experimental evidence reveals that illitisation of kaolinite occurs in a solution of 0.6g KCl/l at 200°C and PH_2O = 1.5MPa, but montmorillonitisation occurs in distilled water under the same conditions (Sabatier, in Kisch, 1983). Well data from Sicily and Tunisia confirms the importance of K^+ in promoting illitisation (in Kisch 1983). Host rock lithology may therefore play an important role in controlling the pore fluid chemistry, especially in K^+ deficient and impermeable rocks (Kubler 1968).

4.3.5 Deformation

Kisch (1983) has argued that the fact that schistosity develops both before and during anchizone crystallinities could mean that deviatoric and lithostatic stress are unimportant in the development of crystallinity. However, the importance of stress/strain induced recrystallisation in phylosilicate minerals at higher grades has been established and appreciated by structural geologists for at least a decade: for example, the electron microscope studies by Knipe and White (1977) and Knipe (1981). These give in considerable detail the mechanisms of formation of slaty cleavage by the initiation of Q and P domains, and the growth of P domains. The cleavage (P) domains initiate by recrystallisation and rotation and solution of pre-existing grains, and growth occurs by either bending of grains at low angles to the P domains or recrystallisation of high angle grains, driven by elastic or plastic strain energy, or interfacial free energy. Similar forces may be expected to operate throughout the evolution of clay minerals to phyllosilicates, and therefore it is not surprising that increasing evidence is coming to light suggesting that tectonic controls on illite crystallinity may be important.

This was first directly indicated by Cronshaw (1984), who suggests that local crystallinity variations around a small fold (wavelength of 100m) in North Wales slates may be due to variations in stress or strain around the fold, and in a more detailed study, Hobson (pers.comm.) has shown, from the same field area, that crystallinity of both illite and chlorite in shales increases systematically into the hinge region of a fold on a similar scale: accompanying this change is the progressive development of a more intense slaty cleavage, and a more closely spaced fracture cleavage in sandstones. Lee et al. (1986) traced the development of mudstone to slate in the classic locality of the Lehigh gap Pennsylvania, where cleavage develops with distance from the contact with an overlying quartzitic conglomerate. The absence of cleavage near the contact has been

attributed to a pressure shadow effect created by the quartzite, and the authors were able to show that the phyllosilicate orientation changed from bedding-to cleavage-parallel without intermediate stages, as the proportion of 2M:1M micas increased, as interlayering of 2M mica with kaolinite and chlorite decreased, and as a general increase in illite crystallinity occurred, although there were clearly other factors causing large variations in crystallinity. The cleavage forming mechanism was recrystallisation, possibly fluid assisted, but no rotation occurred, and the driving force was probably a combination of structural, chemical, interfacial and elastic strain energies. From this and the above studies, it is quite clear that stress and strain may both exert an intrinsic effect on crystallinity, stress contributing directly to thermodynamic driving forces for recrystallisation either with or without fluid, and the latter creating driving forces by elastic or plastic strain energy. Since the two are inevitably linked, they are treated together as a single intrinsic factor, referred to as deformation, and it is surprising that such tectonic control of crystallinity has been virtually ignored by most studies. This is probably because it is relatively unimportant in the undeformed well log data on which many earlier studies were made.

4.3.6 Permeability

Permeability probably has the most profound effect on crystallinity of all extrinsic factors because of the importance of pore fluids in three of the intrinsic controls on crystallinity. Well cores and regional studies suggest that higher crystallinities and lower percentages of expandable layers are associated with more permeable rocks: for example, in the same well core intervals, percentage of expandable layers decreased from 30% in marls to 10-20% in mudstone and 0% in siltstone (Vlasov in Kisch 1983). Stacking order likewise increases from complete absence in claystones to poor order in siltstones and good order in sandstones. (Hamilton, in Kisch

1983). Gill et al. (1977) report crystallinities in sandstones and siltstones up to 50% greater than in argillaceous rocks.

Yet the opposite effect of permeability has also been noted: Hobson (pers.comm.) for example, found lower crystallinities in sandstones than adjacent mudstones. These apparently contradictory results merely reflect the fact that permeability is an extrinsic control on crystallinity; the effect of permeability will depend on the entire pore fluid history of the rock. The prograde metamorphism may cause greater crystallinities in more permeable rocks (e.g. the well core examples) but retrogression could explain the reverse effect.

4.3.7 Host Rock Chemistry

An obvious control on local pore fluid chemistry is exerted by the host rock chemistry, which is therefore also an extrinsic factor in illite crystallinity. Gill et al. (1977) show a consistently better crystallinity in the "terrigenous" rocks throughout the South Wales coalfield than in carbonates of associated localities, reflecting access to K^+ solutions, and Offler and Prendergast (1984) also consider that crystallinity variations are due to variable K^+ concentration inherited from host rocks.

4.3.8 Inherited Crystallinities

Kisch (1980) found that diagenetic zone crystallinities of the >20μ size fraction were higher than finer size fractions, and attributed this to the presence of large grains of detrital mica. The opposite trend with size was recorded by Hower et al. (1976), in which case the finer size fractions had a greater ratio of illite to smectite, and by Offler and Prendergast (1984), in which the >2μ fraction had higher crystallinities than the whole rock, because the smaller size fraction sampled only cleavage domains, but the whole rock samples included unrecrystallised, diagenetic grade crystallinities in Q domains. All these cases can be

considered as examples of non-equilibrium, inherited crystallinity, which is another extrinsic factor that may exert an important control on the crystallinity measured.

4.3.9 Other 10A phases

Serious distortions of crystallinity may be caused by any mineral which also gives a diffraction peak around 8.8 $^{o}2\theta$ (10A), including basal reflections from paragonite (9.6-9.7A), margarite (9.7A) or pyrophyllite (9.2A). These can usually be detected by 'shoulders' on the high 2θ side of the illite peak, and lead to serious overestimates of crystallinity, shown for example by Cronshaw (1984).

4.3.10 Sample Preparation and Measurement Technique

The sensitivity of crystallinity to measurement technique was manifested very early when discrepant values from standards were measured in different laboratories. Kisch (1980) shows that one of the major sources of variation is the goniometer speed; in general, higher values of crystallinity are measured at lower rates of scan. Other variables which may have an effect are chart speed and slit aperture.

Sample preparation has not been investigated systematically as a source of variation in crystallinity except for the effects of size fraction referred to above, but this alone has important implications for the measurement of crystallinity in any samples with size dependent crystallinities.

A more subtle complication of such samples may also exist in the method by which the size fractions are isolated: it is not known how the efficiency of filtering, centrifuging and sedimentation compare, but it is unlikely that they all achieve similar results.

The type of sample used has an influence on the crystallinity because of size fraction effects. Of the two fundamental types of sample

preparation; polished slices or smear mounts, the former are restricted to whole rock samples, while the latter may be prepared for either whole rock or various size fractions. As noted above, this was the reason given by Offler and Prendergast (1984) for the source of discrepancy between their polished slice and smear mount results. The existence of domainal fabrics leading to large sample heterogeneities has been identified as a problem with polished slices (Cronshaw 1984).

Brime (1986) has suggested that ultrasonic treatment may introduce artificial crystallinity values by distorting the distribution of crystallinity with size fraction from the natural sample. In view of this problem, she recommends no ultrasonic treatment.

Finally, a major difference in sample preparation between various workers is chemical treatment with K^+ or Mg^{++} saturated fluids, or glycol. Kisch (1980) used K and Mg saturation to expand mixed layers within illite, and found that crystallinities decreased after treatment. He considered that the unsaturated values were not true crystallinities, because the mixed layers were cation-deficient and collapsed. Glycolation was used by Brime (1981) with the opposite result; crystallinities increased by as much as 30%. Since the natural process of illitisation involves the progressive reduction of proportions of mixed layers, any such pre-treatment must introduce artificial changes of crystallinity which render the results at best difficult to interpret, and at worst, meaningless.

4.4 DEFINITIONS OF DIAGENETIC/ANCH-/EPI-ZONE BOUNDARIES

The first attempt to define low-grade metamorphic zones by illite crystallinity was made by Weaver (1960), who adopted a five-fold subdivision (diagenesis-incipient metaphorphism-incipient/weak metamorphism-weak/very weak metamorphism-metamorphism). The term anchizone derives from the concept of anchimetamorphism (Von Harrasowitz, 1927), and

readopted by Kubler to refer to the three intermediate stages of Weaver's classification. The various indices of crystallinity are the fundamental basis of the resulting tripartite classification into diagenetic, anchimetamorphic and metamorphic stages, but the boundary values were also chosen to correspond to mineralogical changes. Thus in Kubler 1967a, the lower crystallinity limit of the anchizone is correlated with the upper grade limit of the existence of liquid hydrocarbons, and also the dickite-pyrophyllite transformation. The higher crystallinity limit corresponds to the appearance of greenschist-facies minerals (epidote, chlorite, stilpnomelane). Nevertheless, the definitions of the three zones are based not on these criteria, but on values of a crystallinity index.

Figure 4.7 compiles some of the values of indices of crystallinity that have been used. Two major problems are immediately apparent. Firstly, even within one index of crystallinity, an enormous variety of values have been attached to the boundaries. Some epizone crystallinities fall within the diagenetic zone of other definitions. This section examines the reasons for the discrepancies within the context of a single crystallinity index, and gives the solution adopted in this study. Secondly, there is a need to correlate values from one type of crystallinity index to the others. Section 4.5 proposes a method for correlating the three principal indices in use and applies it using the data set of this study.

It is apparent from a review of literature that there are two separate reasons for the variety of boundary values shown in Figure 4.7 . Of essential importance is the fact that different choices of absolute value have been made by different authors, and even in one case by the same author at different times. For example, the initial definitions of the anchizone boundaries in terms of the Kubler Index were given as $0.4^{o}2\theta$ and $0.25^{o}2\theta$ by Kubler (1964, 1967a, b). However, in Kubler (1968) the anchizone limits are derived at 0.56 and $0.30^{o}2\theta$ from correlating Kubler and Weaver index measurement on over 700 samples, and using Weaver's original

boundaries between diagenesis and early metamorphism, and weak to epimetamorphism. Merriman and Roberts (1985) choose a value of $0.45^{o}2\theta$ to distinguish stage I metapelites from stage II since this marks the appearance of $2M_1$ mica as a significant component, and $0.26^{o}2\theta$ to distinguish stages II and III because it also marks the disappearance of 1Md polytype.

The second reason for the variety of boundary values, which accounts for most of the differences, is the sensitivity of crystallinity to measurement technique referred to in section 4.3. This means that even when expressed in $^{o}2\theta$, the Kubler Index measured in one laboratory is unlikely to correspond to that measured in another. The correct procedure, therefore, to allow comparative measurements, is inter-laboratory calibration on standards. This has been done in a number of cases in Figure 4.7 ; for example, Kisch (1980) derived his anchizone limits of 0.38 and $0.21^{o}2\theta$ by comparing measurements on sub-standards of polished slate measured in both his and Kubler's laboratories: these suggested that the lower values of 0.38 and $0.21^{o}2\theta$ correspond to the original anchizone boundaries of 0.42 and $0.25^{o}2\theta$. Similarly, Brime (1985) derived values of 0.55 and $0.35^{o}2\theta$ from standards provided by Dunoyer de Segonzac.

The measurement of illite crystallinity is sufficiently accurate that these differences are quite significant. In this study, therefore, the problem of defining the anchizone limits has been tackled in the following stages:

i) A selection of one index has been made on which to base the definition.

ii) Absolute values of anchizone limits in this index are chosen.

iii) A set of standards are used to obtain the correct relative limits under the laboratory conditions of this study.

iv) Mathematical relationships between the various indices are derived.

v) The correct relative anchizone limits are defined in the base index and transformed into the other indices using the relationships.

i) The Kubler Index is the obvious choice as a base for three reasons: firstly, the error analysis presented later favours the Kubler Index. Secondly, it is and has been the most widespread in use and lastly, standards are available for interlaboratory calibration.

ii) Absolute values of the anchizone boundaries are logically chosen as 0.42 and $0.25^{o}2\theta$ since these were the original definitions and have been used by all subsequent studies where calibration has been made. There has been a major source of confusion in the literature over the value specified by Kubler for the anchizone/diagenetic Zone boundary. This is quoted in Kubler (1967a, b) as '4 X-Y Moseley' units. There is insufficient experimental detail to find the equivalent value in $^{o}2\theta$, but in Kisch (1980), this is given as '0.40θ'. There is, however, a misprint, since the ^{o} sign has been omitted. Kisch (1980) implies that the correct value is $0.42^{o}2\theta$, but if the equivalence of the upper anchizone limit '2.5 X-Y Moseley' units and $0.25^{o}2\theta$ is accepted, then the correct value is $0.4^{o}2\theta$. Since the value of $0.42^{o}2\theta$ has been used by a number of subsequent authors, it is accepted here with reservation.

iii) A set of four polished slate standards obtained from Kisch have been measured at Keele (Cronshaw 1984). Like Kisch, analysis of these measurements finds a consistently lower Kubler Index than that given by Kubler. The correlation is presented in Figure 4.9, yielding the following relationship on regression:

K.I. (Keele) = 1.079 K.I. (Kubler) -0.053

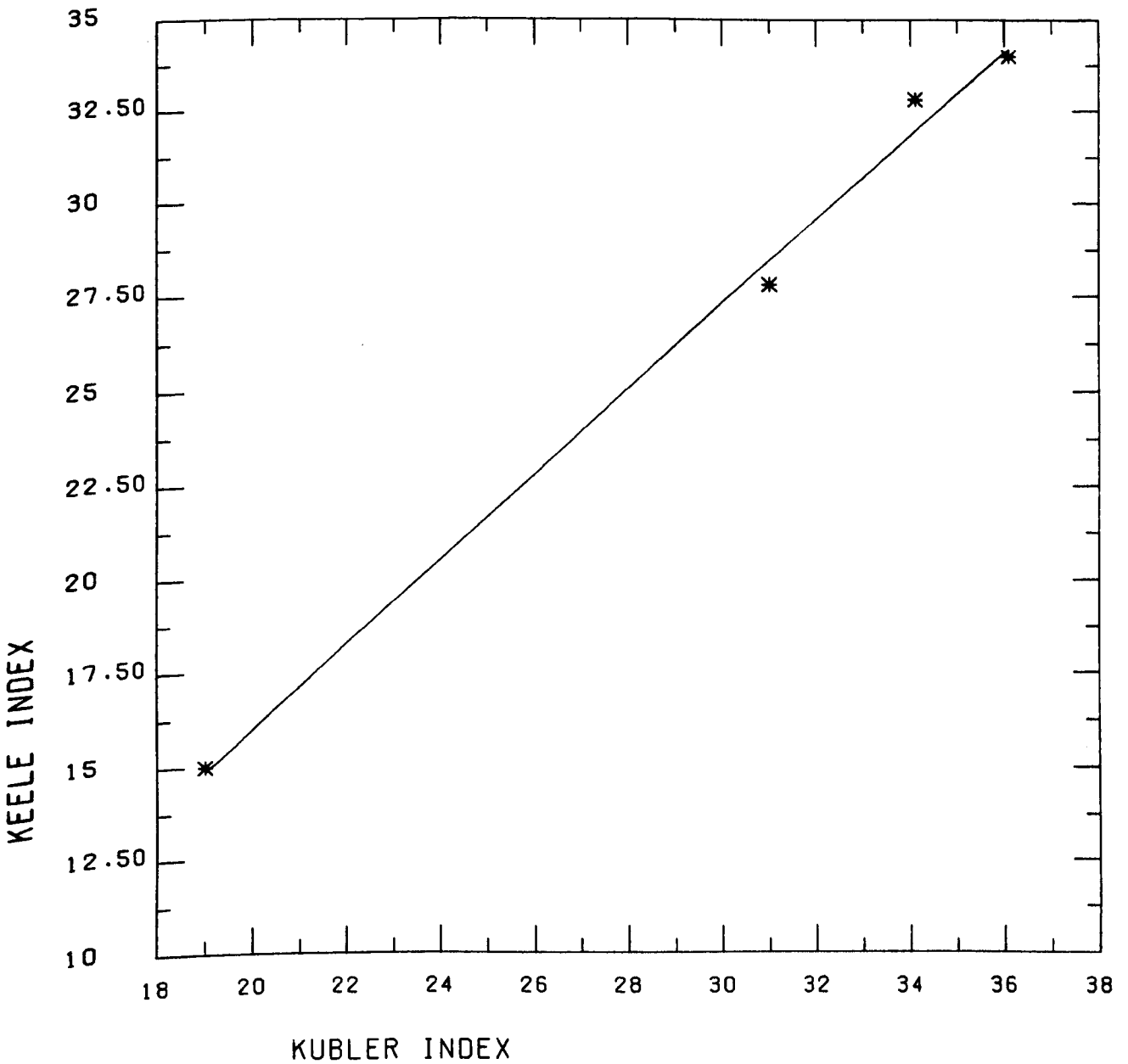

FIGURE 4.9
Calibration of Kubler Index measured at Keele (K.I. (Keele)) against Kubler Index of Kubler (K.I. Kubler), scales in $^{o}2\theta \times 100$.

where K.I. (Keele) is the Kubler Index measured at Keele and K.I. (Kubler) is the Kubler Index measured by Kubler. In practice, the standards used were a set of sub-standards which were not actually measured by Kubler, but the values of K.I. (Kubler) were estimated by Kisch from his previous correlation with Kubler and considered accurate by him.

The above relationship allows the correct relative values of the anchizone limits to be established for this study by substitution of 0.42 and $0.25^{o}2\theta$, giving 0.400 and $0.215^{o}2\theta$ as the corresponding values at Keele, as shown in Figure 4.9.

A further important conclusion to be drawn from these values is that even under the same machine conditions, there may be significant differences between crystallinities determined in different laboratories, since the goniometer and chart speeds used by Kisch and at Keele are identical, yet the anchizone limits vary. Therefore any study not based on calibration by standards will yield results which are generally not comparable. This limitation applies to several recent studies.

iv) The following relationships between the Kubler Index (K), Weaver Index (W) and Weber Index (Hb) are derived in section 4.5:

$$K = 1.05\ W^{-0.59} \qquad 4.1$$

$$K = 0.00144Hb \qquad 4.2$$

$$Hb = 1.05/0.00144W^{-0.59} \qquad 4.3$$

v) Equations 4.1 and 4.2 are used to calculate the correct relative anchizone limits in the Weaver and Weber Indices from the Kubler Index definitions for 0.4 and $0.215^{o}2\theta$:

	Kubler Index	Weber Index	Weaver Index
Diagenetic Zone			
	0.400	278	5.1
Anchizone			
	0.215	149	14.6
Epizone			

This table gives the final definitions between the diagenetic, anchi- and epizones used in this study in the three indices, and Table 4.1 gives

KUBLER INDEX			WEBER INDEX			WEAVER INDEX			
DZ	AZ	EZ	DZ	AZ	EZ	DZ	AZ	EZ	
.64	**.41**		**444**	**285**		**2.30**	**4.89**		Dunoyer de Segonzac (1969)
.59	**.39**		**410**	**271**		**2.64**	**5.32**		Barlier (1974)
.56	**.30**		**389**	**208**		**2.88**	**8.31**		Kubler (1968)
.55	**.35**		**382**	**243**		**2.97**	**6.40**		Brime (1985)
.43	**.26**		**299**	**181**		**4.51**	**10.59**		Roberts & Merriman (1985)
.42	**.25**		**292**	**174**		**4.69**	**11.32**		Kubler (1967a)
.42	**.23**		**292**	**160**		**4.69**	**13.04**		Hesse (1984)
.40	**.23**		**278**	**160**		**5.10**	**13.04**		Stadler (1979)
.39	**.21**		**271**	**146**		**5.74**	**15.21**		Aprahamian (1974)
.38	**.21**		**264**	**146**		**5.56**	**15.21**		Kisch (1984)
.32	**.27**		**222**	**187**		**7.45**	**9.93**		Sagon & Dunoyer de Segonzac (1972)
.27	. 19		181	125		9.81	18.35		Ludwig (1972)
.25			174			11.24			Johnson et al. (1985)
.25	.12 -.14		170	80 -100		11.71	42.24 -28.84		Kemp et al. (1985)
.25	.17 -.18		150 -155	105 -110		11.71 -11.10	21.55 19.94		Weber (1972a)
.64	.24		444	167		2.3	12.10		Weaver (1960)
.53 -.46			365 -320			3.20 4.00			Gill et al. (1977)

TABLE 4.1

The anchizone boundaries derived in other indices from equations 4.1-4.3. The boundary values in bold indicate the original values, those in ordinary typeface being derived values.

noted above for both to be used in conjunction.

4.5 RELATIONSHIPS BETWEEN INDICES OF ILLITE CRYSTALLINITY

The first attempt to relate indices of crystallinity was by Kubler (1968), as referred to above. Primmer (1983) illustrates the relationship between Kubler and Weaver indices on a semi-logarithmic plot, but found a considerable scatter which he attributes to distorted Weaver Indices. Cronshaw (1984) plots pairs of Kubler, Weaver and Weber Indices for all his 146 samples and deduced correlation coefficients for each pair based on linear relation between Kubler and Weber Indices, and non linear relationships between the other two pairs of indices. He uses the generally good Kubler/Weaver relationship to isolate some samples which do not fit well: these proved to have distorted Kubler Indices due to the presence of paragonite. The relationship between Kubler and Weber Indices is examined for five samples by Weber (1972b) and Ludwig (1972); this was used to find graphically the anchizone limits in the Weber Indiex from the values of Kubler.

None of these studies have attempted to relate all three indices in use. Inspired by a need to make comparisons between this study and others, mathematical relationships have been fitted to the 125 measurements of Kubler and modified Weaver indices of this study, 120 samples of Cronshaw's study and to the Kubler-Weber Indices and Weaver-Weber Indices measured by Cronshaw (1984).

4.5.1 Kubler-Weaver Index Relationship

The curved form of the data points suggests that either an exponential or power law might be used to relate these indices. Both equations were fitted as illustrated in Table 4.2. Two methods of curve fitting were used for each: linear regression on a logarithmic reformulation of the laws, and

1. KUBLER - WEAVER					
			NORTH SPAIN	NORTH WALES	COMBINED
EXP. LAW $K=Pe^{-QW}$	Regression Analysis	Number of Data	125	120	245
		P	0·662	0·410	
		Q	0·0513	0·0343	
		Average Residual	0·128	0·0283	
	Non-Linear Least Square	P	1·00	0·470	0·828
		Q	0·175	0·0463	0·107
		Average Residual	0·111	0·0297	0·0869
Average Residual $= \frac{\sum_{1}^{N} \lvert K_{obs.} - K_{calc.} \rvert}{N}$					
POWER LAW $K=AW^{-B}$	Regression Analysis	A	0·952	0·733	
		B	0·549	0·421	
		Average Residual	0·0763	0·0205	
	Non-Linear Least Square	A	1·09	0·776	1·05
		B	0·642	0·444	0·590
		Average Residual	0·0678	0·021	0·0495

TABLE 4.2
Relationships fitted and parameters derived for Kubler-Weaver Indices

2. KUBLER - WEBER				
		WEBER (1972)	LUDWIG (1972)	THIS STUDY
LINEARLAW $K = N\,Hb$	N	0·00163	0·00150	0·00144
	CORRELATION COEFFICIENT			0·995

3. WEBER - WEAVER		
POWER LAW $Hb=AW^{-B}/N$	A	1·05
	B	0·590
	N	0·00144

TABLE 4.3
Relationships fitted and parameters derived for Kubler-Weber (2) and Weber-Weaver Indices (3).

the boundary values in all indices derived from various original definitions used by other authors. These relationships reveal a very significant discrepancy between the boundary values proposed by Weaver (1960) and the original Kubler values (1964). Reference to Table 4.1 shows that Weaver's lower grade anchizone limit is a considerably lower crystallinity ($0.64^{o}2\theta$) than Kubler's ($0.42^{o}2\theta$) and that his higher grade limit ($0.24^{o}2\theta$) is at a higher crystallinity than Kubler's ($0.25^{o}2\theta$). This greater range of crystallinities in Weaver's anchizone is illustrated in Figure 4.10, which shows the four limits on a logarithmic plot of Equation 4.1. This is explored further in the pie charts of Figure 4.11, which illustrate that in all cases, a greater number of samples fall into the anchizone at the expense of numbers in the diagenetic zone as defined by the Weaver Index than by the Kubler Index. Consistent results between indices can be achieved by following the procedure (i) to (v) outlined above to deduce the correct anchizone limits in any two indices from a definition given in the third.

This problem has come to light in Kubler's 1968 attempt to relate his own results to Weaver's, causing a change of boundary value definition, and again more recently in Robinson and Bevin's study (1986), which measured both Kubler and Weaver indices and assigns samples to the three zones based on both indices and mineralogical data. They note that their mean diagenetic zone Weaver Index was 3.8, greater than the upper limit of 2.3 proposed by Weaver. This was attributed to glycolation enhancing the Weaver Index, but since this is likely to have as much effect on the Kubler Index, a more probable explanation lies in exactly the discrepancy in the low-grade anchizone boundaries shown above. Thus many samples with diagenetic zone Kubler Indices have anchizone Weaver Indices. Those which are diagenetic zone on aggregate will have Weaver Indices higher than the Weaver Index definition of the diagenetic zone. The importance of being able to correlate between the various indices increases with the trend

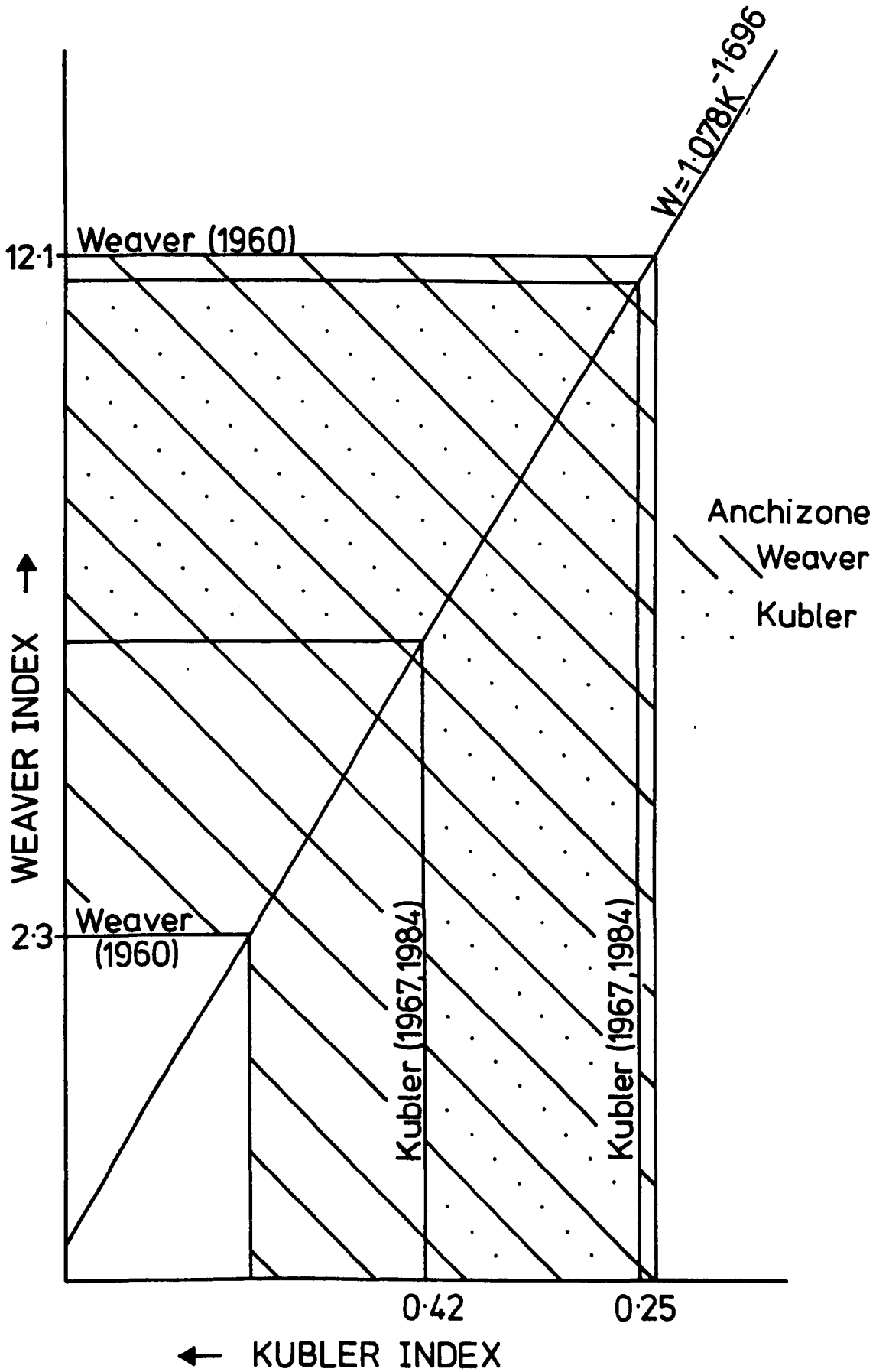

FIGURE 4.10
The relationship between anchizone limits defined by Weaver (1960) and Kubler (1964). The solid line allows a comparison between the two indices based on a logarithmic plot of the relationship $K=1.09W^{-0.642}$ It shows that Weaver's anchizone covers a larger range of crystallinites than Kubler's.

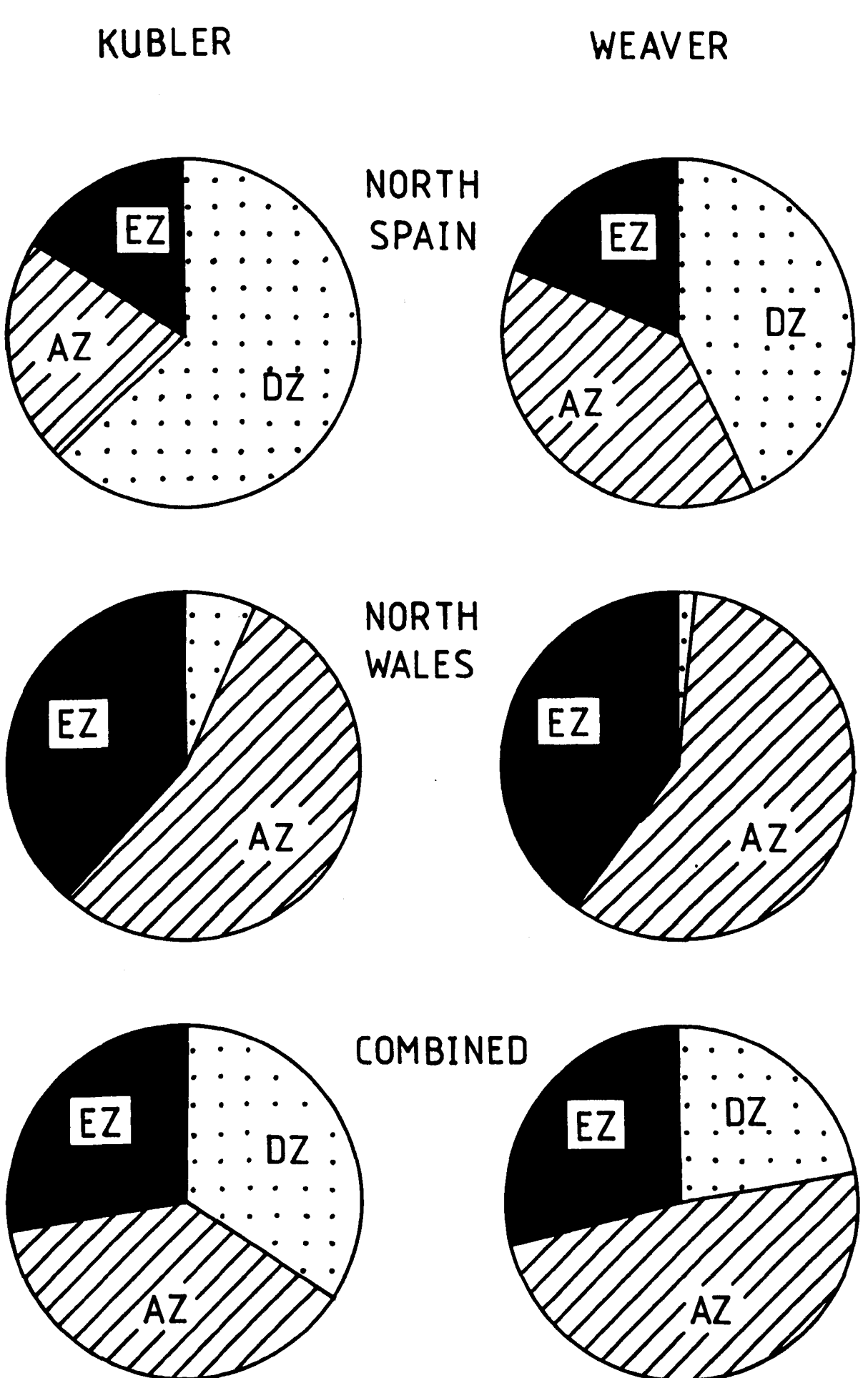

FIGURE 4.11

Pie charts illustrating proportions of samples in the diagenetic, anchi- and epizone as defined by Kubler (1964) and Weaver (1960). In all cases, the Weaver Anchizone has a higher proportion at the expense of the diagenetic zone.

a non-linear least squares fit to the laws as given (using BLIB and NLSPLOT programmes available on the Keele mainframe). The results of the curve fitting were evaluated by calculating the average residual, defined in Table 4.2 as the average difference between observed and calculated values (Programme .RESIDUAL). The power law gave a better fit in all cases, sometimes reducing the residuals by 50%. There was very little difference between the linear regression and non-linear least squares fitting procedure; the latter was marginally better (Table 4.2).

Figure 4.12 shows the data and curve fitted to the measurements of this study, from the parameters in Table 4.2. It can be seen that the fit of the curve is rather less good in the epizone: this is clearly due to the concentration of diagenetic zone crystallinities. The coincidence of the anchizone boundary values in the Kubler and Weaver indices, arrived at by the process described in section 4.5, can also be seen from the match of the dashed lines on the solid curve. Figure 4.13 is a similar plot containing the additional data from Cronshaw (1984). Because of the greater numbers of epizone crystallinities, the curve is a better all round fit. The adequacy of the power law formulation is tested further in Figure 4.14 which gives the data on a log-log plot of Kubler and Weaver Indices. The slight non-linearity of the high crystallinity results can be seen, but this figure confirms that in the anchizone, where the relationship has been used to transform the boundary values, the fit and the form of the relationship is quite satisfactory. In view of the scatter of data, fitting of a more complex polynomial was not considered necessary.

4.5.2 Kubler-Weber Index Relationship

These two indices are measured in the same way except for a normalising constant (the half-peak-height width of the quartz peak x100) multiplied to the latter. Therefore a linear relation is expected and observed, as shown in Figure 4.15. Non linear least squares analysis gives

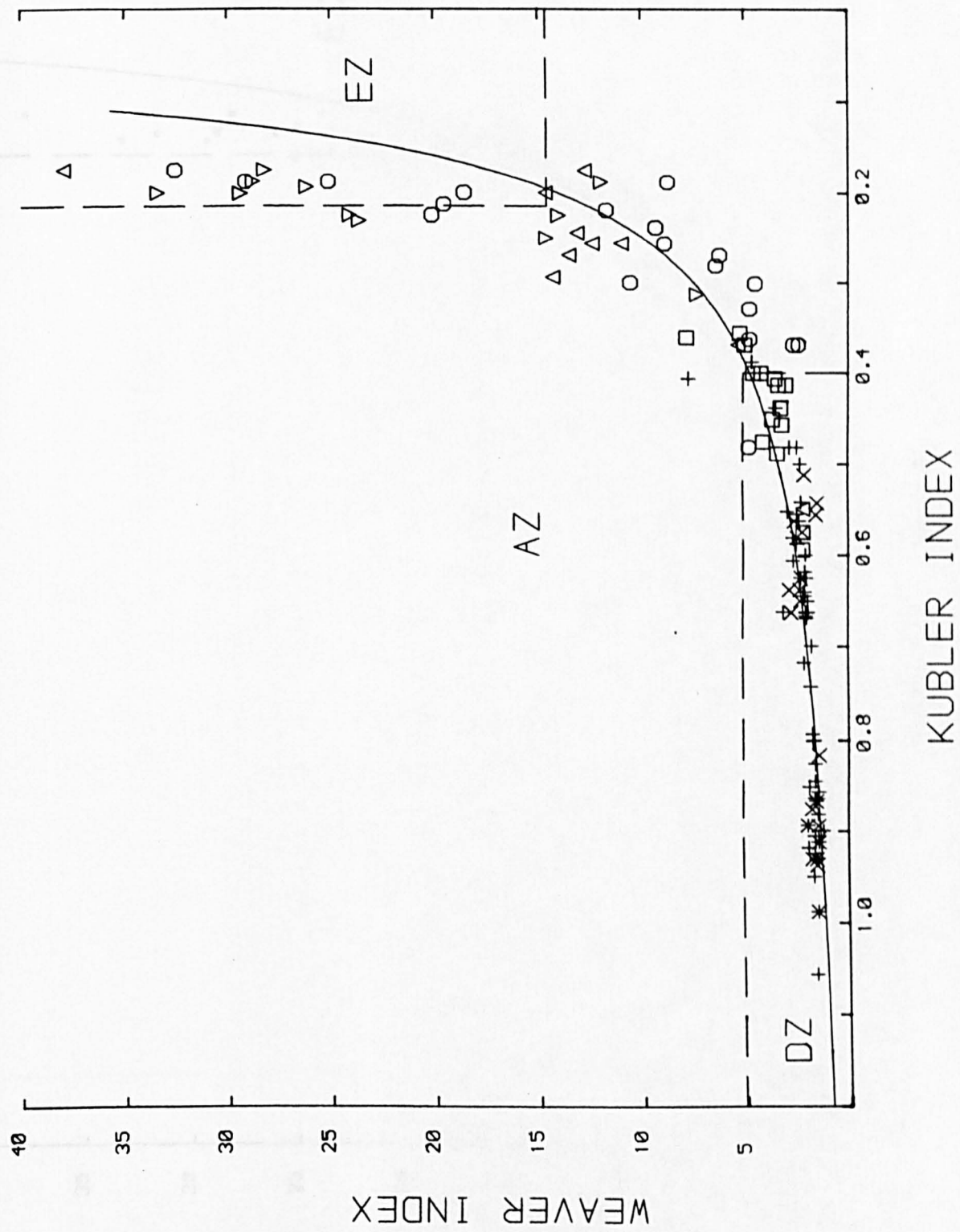

FIGURE 4.12

The Relationship between Kubler and Weaver Indices, North Spain data. The solid line gives the power law relationship from non-linear least squares analysis: $k = 1.09W^{-0.642}$

✱ = Bernesga Valley, -1.6μ fraction + = Bernesga Valley, -2.0μ fraction
× = Bernesga Valley, -20.0μ fraction
□ = Punta Vidrias, -2.0μ fraction
△ = Luarca, -2.0μ fraction ▽ = Luarca, -20.0μ fraction
○ = Punta del Sol, -2.0μ fraction

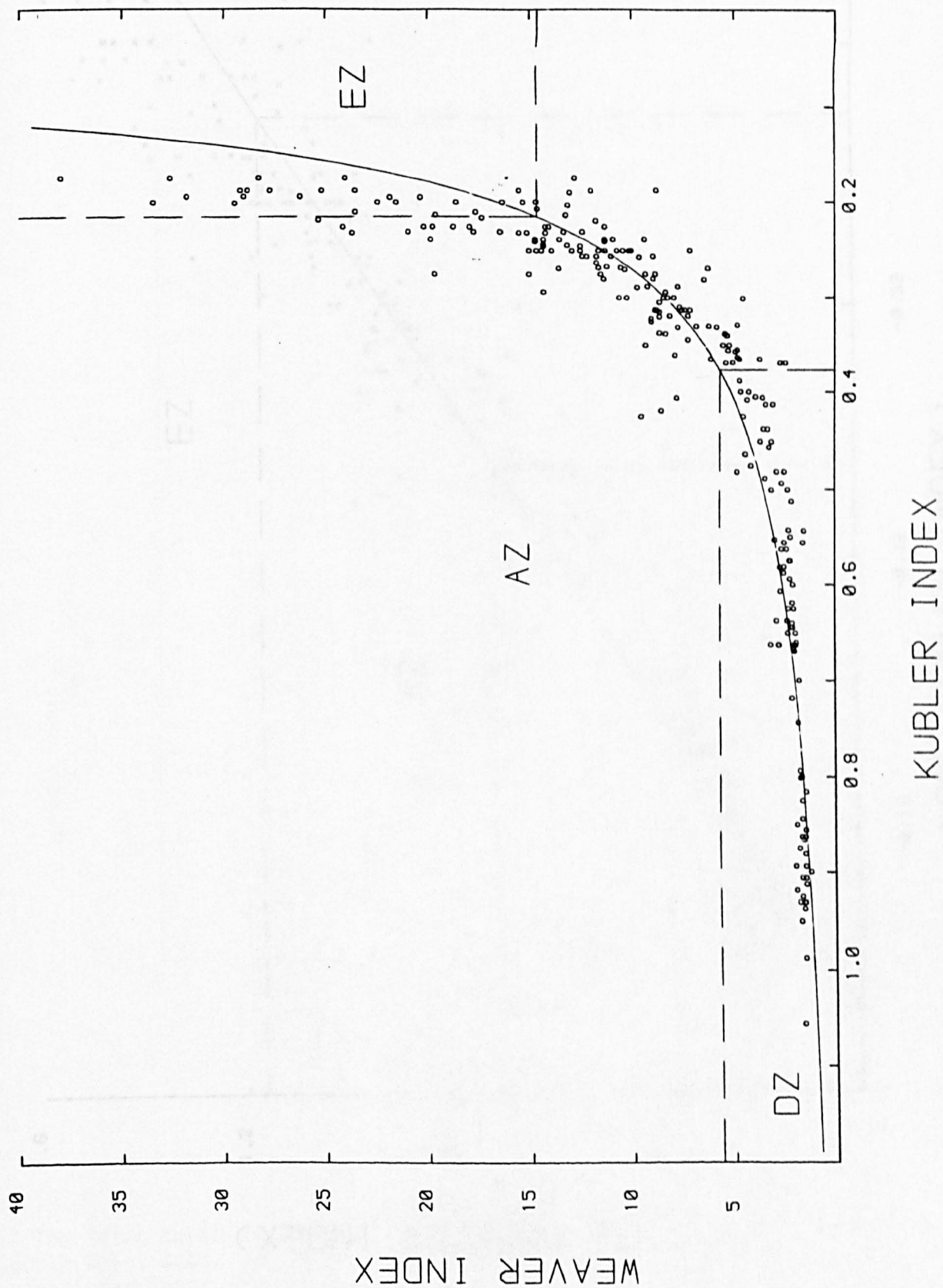

FIGURE 4.13
The Relationship between Kubler and Weaver Indices, North Spain and North Wales data. The solid line gives the power law relationship from non linear least squares analysis: $K = 1.05W^{-0.59}$

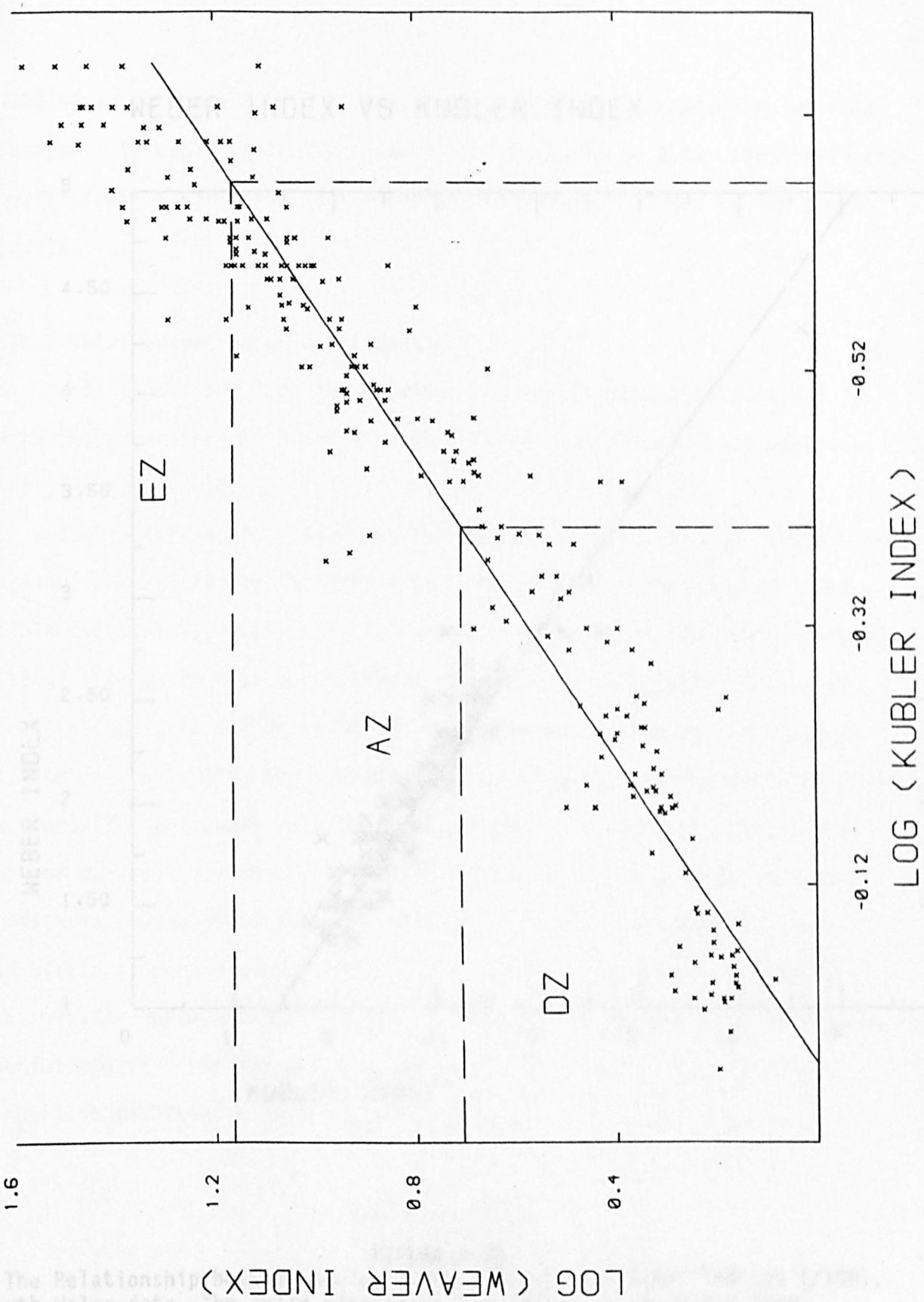

FIGURE 4.14

Relationship between logarithms of Kubler and Weaver Indices, North Spain and North Wales data. The solid line gives the logarithmic relationship from non linear least squares analysis:

$$\log K = 0.0374 - 0.59 \log W.$$

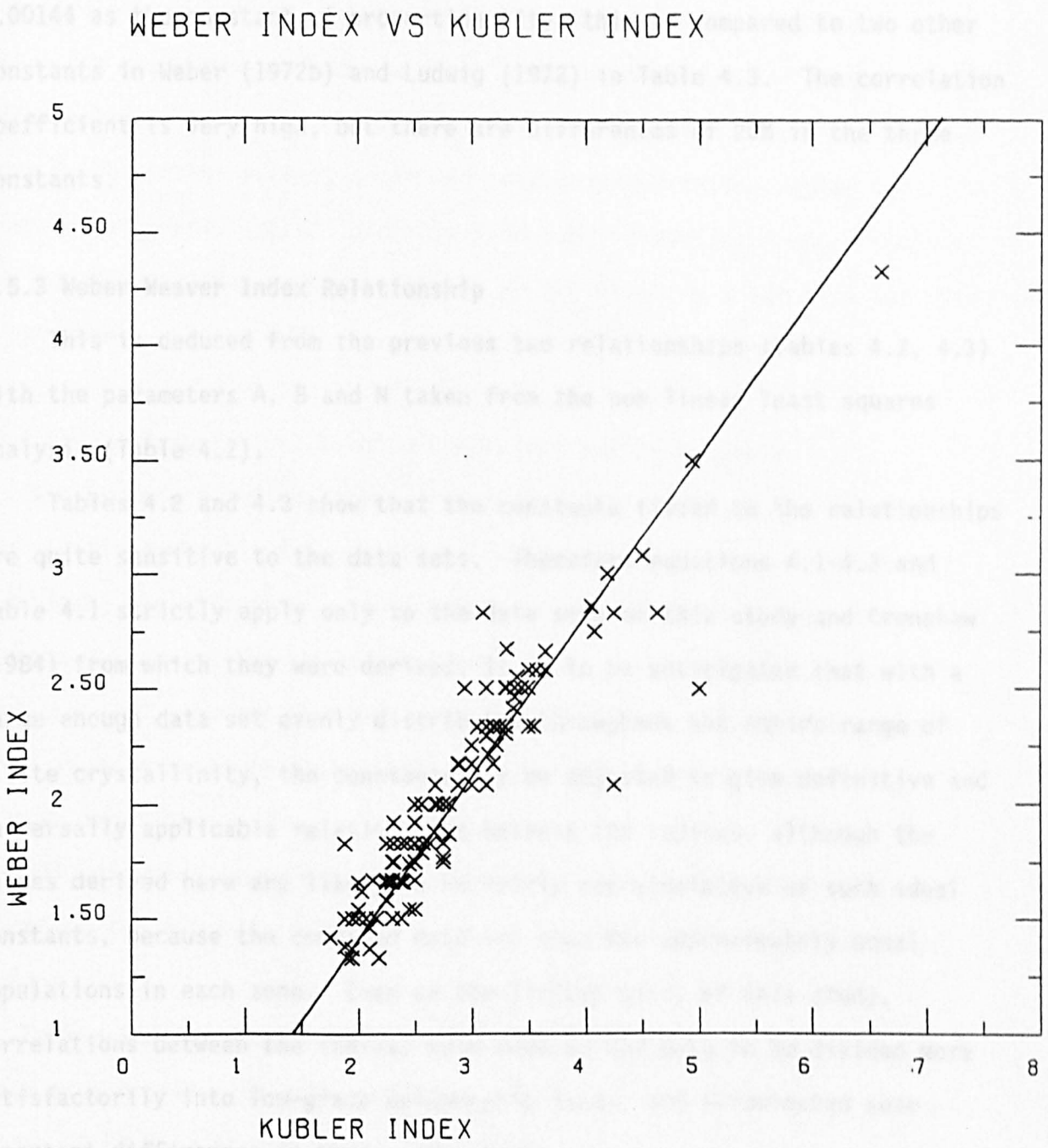

FIGURE 4.15

T The Relationship between Kubler Index (^{0}20x10) and Weber Indices (/100), North Wales data. The solid line gives the linear relationship from non-linear least squares analysis:

$$K = 0.00144\ Hb$$

0.00144 as the constant of proportionality: this is compared to two other constants in Weber (1972b) and Ludwig (1972) in Table 4.3. The correlation coefficient is very high, but there are differences of 20% in the three constants.

4.5.3 Weber-Weaver Index Relationship

This is deduced from the previous two relationships (Tables 4.2, 4.3) with the parameters A, B and N taken from the non-linear least squares analysis (Table 4.2).

Tables 4.2 and 4.3 show that the constants fitted to the relationships are quite sensitive to the data sets. Therefore equations 4.1-4.3 and Table 4.1 strictly apply only to the data sets of this study and Cronshaw (1984) from which they were derived. It is to be anticipated that with a large enough data set evenly distributed throughout the entire range of illite crystallinity, the constants may be adjusted to give definitive and universally applicable relationships between the indices, although the values derived here are likely to be fairly representative of such ideal constants, because the combined data set used has approximately equal populations in each zone. Even on the limited basis of this study, correlations between the indices have enabled the data to be divided more satisfactorily into low-grade metamorphic zones, and illuminated some important differences in their definition.

4.6 METHODS OF STUDY

4.6.1 Sampling

The illite crystallinity study aimed to investigate conditions of deformation on a regional scale over the Cantabrian and West Asturian-Leonese zones, and on a detailed scale within the thrust sheets of the Bernesga Valley. Unweathered samples (0.25kg) of two contrasting

lithologies were collected from all the field localities (Figures 1.3, 1.4). The study was confined to clastic rocks, of which the finest grained shales/pelites, and sandstones/quartzites were selected. For the detailed study in the thrust sheets, shale and sandstone/quartzite samples were collected at evenly spaced intervals from every formation along a section down the Bernesga Valley perpendicular to strike through the Rozo and Pozo Thrust Sheets (Figure 5.30).

4.6.2 Sample Preparation, Machine Conditions and Measurement

The procedure and conditions are described in Table 4.4. For all samples, smear mounts of the 0.45-2μ fraction were prepared; in order to investigate the effects of size fraction on crystallinity, samples from the Bernesga Valley and Luna Lake were also prepared in 0.45-1.6μ and 0.45-20μ fractions, and a number of whole rock smear mounts were made. Hathaway's (1956) formula based on Stoke's Law was used to obtain the correct centrifuging times.

All measurements were made on a Siemens X.R.D., fitted with a type F goniometer and a Crystalloflex 4 generator with a Kompensograph X-T chart recorder.

Kubler indices (4.2) were measured for all samples by averaging the result of a forward and reverse scan. Modified Weaver Indices (or Weaver Indices, 4.2) were also measured for most samples by the average of two results. Further details of the calculations for the Weaver Index can be found in Cronshaw (1984). These are listed on Appendix A8.

Clay mineralogy was investigated for some samples by X.R.D. profiles of both whole rock and 0.45-2μ smear mounts. For these measurements, scan rates were increased to $1^{o}2\theta$/min, and slits to 1^{o} and 0.2^{o}, and a pulse rate of 2 min. was used. Further sample treatment involved glycolation by the vapour pressure method (Brown and Farrow 1956) in which the smear mount is suspended above a bath of ethylene glycol at $60^{o}C$ for at least 1 hour,

SAMPLE PREPARATION	MACHINE CONDITIONS	
Jaw Crushing 0.25 kg ▽ Ultrasonic Bath (4 hours in 200 ml H_2O) ▽ Centrifuge (to obtain < 2 μ fraction) ▽ Vacuum Filter (To obtain 0.45 - 2 μ fraction) ▽ Smear Mount (Air Dry) ▽ ANALYSIS	Radiation	Cu Kα, Ni Filter kV = 35 mA = 20
	Slits	$1/2^0$ Divergence 1^0 Scatter 0.1mm Receiving
	Scan Speed	$1/2^0 2\theta$/min.
	Chart Speed	2cm/min.
	Time Constant	4 sec.
	Pulse Rate	$1 \times 10^2 - 1 \times 10^3 s^{-1}$

TABLE 4.4

Sample Preparation and Machine Conditions used for illite crystallinity determination.

SOURCES OF ERROR		
	METHOD	MAXIMUM CONTRIBUTION
1.Measurement	Estimate of precision	1.5%
2.Machine Fluctuation	Repeat measurements on undisturbed sample	25%
3.Sample Heterogeneities (including "orientation" and preparation effects)	Repeat measurements on reorientated sample	10%

TABLE 4.5

Sources of Error and Mean Values

and heating for at least half a hour at 400°C and then 550°C.

4.7 PRECISION AND ERROR

4.7.1 Precision

Precision of the Kubler Index is limited by measurement of the peak width on the chart (0.5mm). This gives 0.0125°2θ, or between 1.3 and 7% of the Kubler Index. The precision of the Weaver Index is much higher since it derived from a digital count of between 3 and 5 figures, giving precisions of 0.01-1.0%.

4.7.2 Error

A fairly comprehensive treatment of the errors is given in order to evaluate the relative merits of the Kubler and Weaver Indices.

Sources of error can be divided into measurement, machine fluctuations and sample heterogeneity. Measurement errors alone may be determined from the maximum precision, giving +/- 0.7 to 3.5% for the Kubler Index, and negligible errors for the Weaver Index (Table 4.5).

SOURCE OF ERROR	METHOD OF ANALYSIS	KUBLER INDEX +/- Absolute	KUBLER INDEX +/- %	WEAVER INDEX +/- Absolute	WEAVER INDEX +/- %	
Measurement	Estimate of Precision	0.0063	0.7-3.5	Negligible		
Measurement + Machine Fluctuation	Repeat Measurements on Undisturbed Samples	0.0526	3.6	0.113	4.2	DZ
		0.0401	5.2	0.404	6.2	AZ
		0.0155	7.7	2.245	9.9	EZ
Measurement + Machine Sample Heterogeneity	Repeat Measurements on Reorientated Sample	0.023	3.87			DZ
		0.003	0.98			AZ
		0.008	4.4			EZ

Table 4.5: Sources of Error with Mean Values

The combined errors due to machine fluctuations and measurement can be

derived from analysis of the differences between the pairs of readings made for each sample. This has been done by dividing the data up into zones on the basis established in 4.4 to ensure that comparable divisions are established for both indices: the mean results are given in Table 4.5, and the absolute values plotted in figure 4.16, and percentages in Figure 4.17.

The absolute value of the Kubler Index error decreases with crystallinity, while the Weaver Index error behaves in the opposite way. This was noticed by Kubler (1968), who used it to infer that the Kubler Index was more satisfactory at high crystallinities, and the Weaver at low values, a dogma which has subsequently become entrenched in the literature (e.g. Cronshaw 1984). However, a true comparison between the two indices, and of the effects of grade on error, can only be made on the basis of percentage errors, and this shows, as expected, that percentage errors in both indices increase with grade (Figure 4.17). More significantly, it also shows that the Weaver Index has higher percentage errors at all grades than the Kubler Index.

Measurement, machine and sample heterogeneity errors in total were evaluated by repeated measurements on 17 re-orientated samples (Table 4.5). These show less error than the mean results of measurement and machine error alone, from which it is concluded that sample heterogeneity is not a significant source of error on the scale of the smear mount. No samples were re-analysed through all the stages of preparation and measurement, but Cronshaw (1984) found that no greater errors were introduced after this procedure.

This section concludes that the major source of error is machine fluctuation, limiting the accuracy of the results to between 3 and 10%. It has also shown that the Kubler Index has an inherently lower error at all grades than the Weaver Index, and that proportional errors in both increase with grade. In view of the greater time taken to measure Weaver Indices, it is questionable whether any advantage is gained.

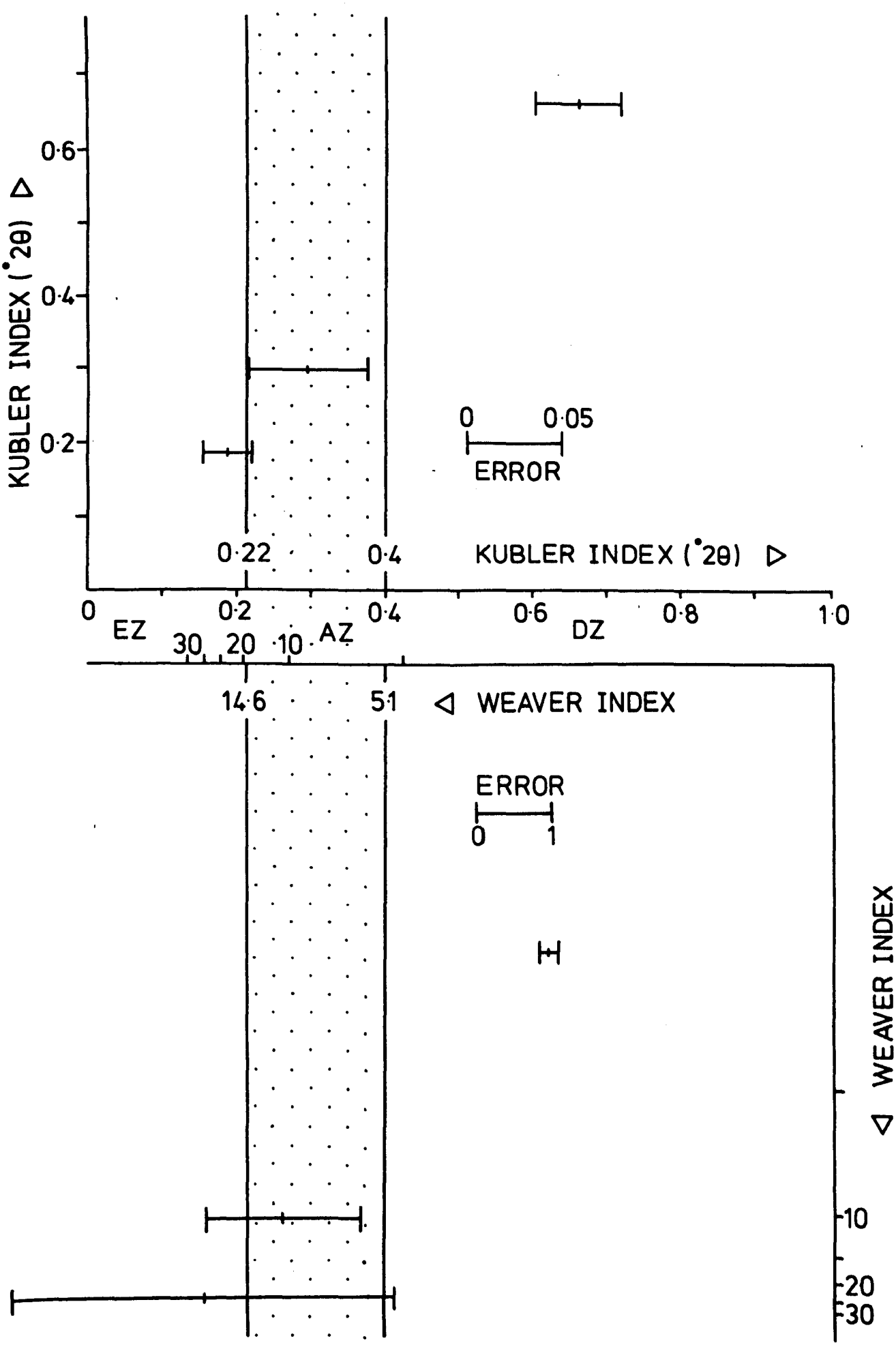

FIGURE 4.16
Mean Absolute Errors by zone, Kubler and Weaver Indices.

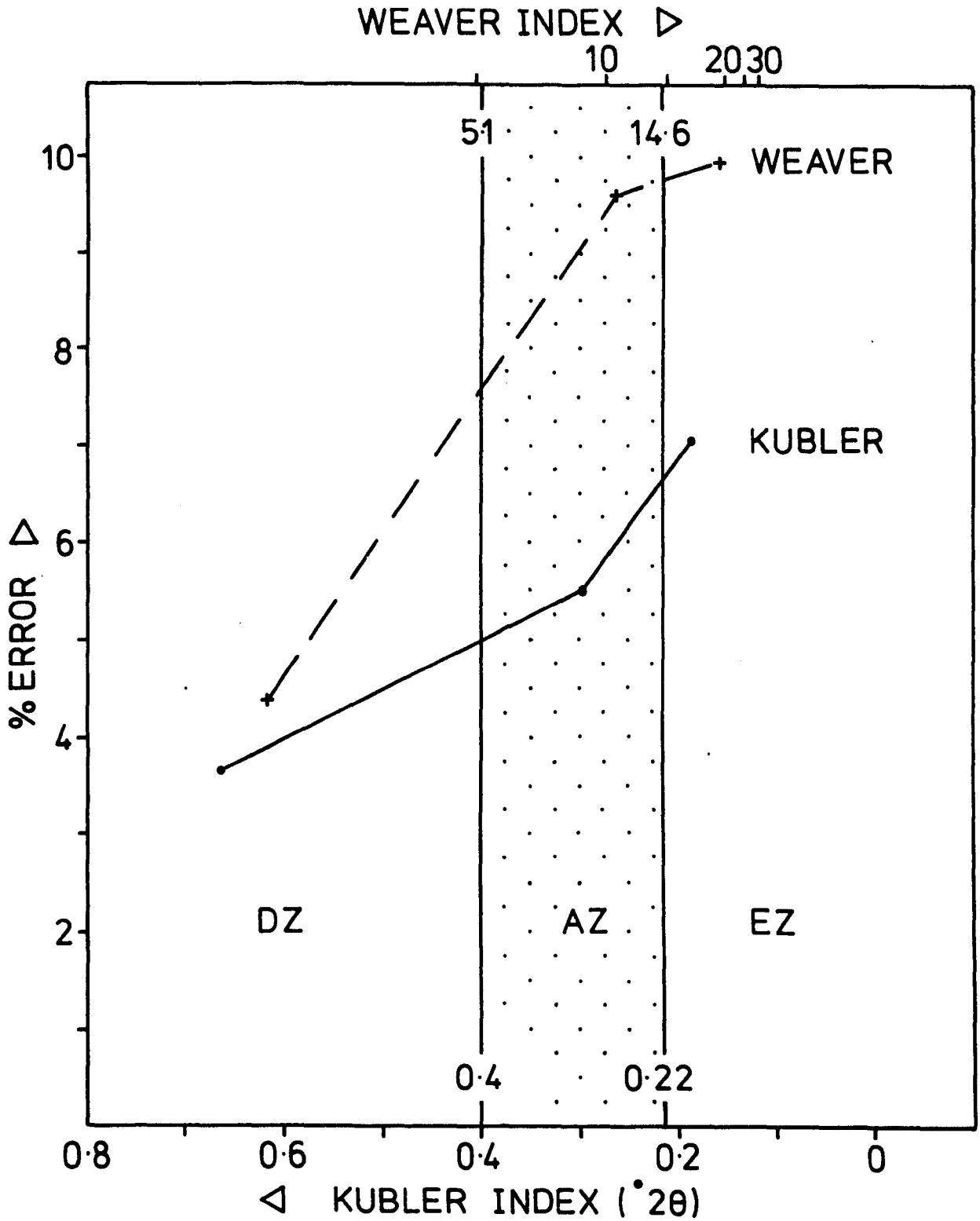

FIGURE 4.17
Mean Percentage Error by Zone, Kubler and Weaver Indices

4.8 ILLITE CRYSTALLINITY AND CLAY MINERALOGY: STUDIES IN THE CANTABRIAN ZONE, NARCEA ANTIFORM, AND WEST ASTURIAN-LEONESE ZONES

The considerable amount of excellent work on low-grade clay metamorphism accumulated over the last fifteen years from the University of Oviedo, has shown the great value of the technique in the diagenetic to anchizone conditions of the Cantabrian zone. In comparing this work to the present study, five differences of approach should be pointed out since they may have effects on illite crystallinity.

i) Samples are exclusively from shales/pelites in the Spanish case, but included sandstones and quartzites in this study.

ii) No ultrasonic treatment was given to the samples.

iii) The <2μ fraction was prepared by sedimentation as opposed to the centrifuge and filtration method of this study, which therefore samples only the 0.45-2μ fraction.

iv) Measurements of crystallinity were made in both air dried and glycolated conditions (cf air dried only here).

v) Calibration of the anchizone boundaries was made using standards of Dunoyer de Segonzac rather than Kisch.

In order to establish an interlaboratory calibration, the crystallinity of four samples kindly provided by Dr. Brime have been measured at Keele. The measurements in the anchizone showed negligible differences, but those in the diagenetic zone had appreciably higher crystallinities at Keele. The relationship obtained was:

$$\text{K.I. (Oviedo)} = 1.35\ \text{K.I. (Keele)} - 0.1077 \qquad 4.4$$

where K.I. (Oviedo) is the Kubler Index Measured at Oviedo and K.I. (Keele) is the Kubler Index measured at Keele. The anchizone boundary values used in this study (0.4 and 0.215) become 0.432 and 0.182 using equation 4.4. These are considerably different to the values of 0.55 and 0.35 used by the Spanish authors; this discrepancy requires further investigation, but

indicates that the equivalent diagenetic/anchizone boundary for the Spanish data is certainly at a lower crystallinity than 0.400. In the following discussion, the original anchizone definitions used by the authors are referred to until there is a more satisfactory calibration established.

Some of the lowest grade crystallinities are reported by Aller and Brime (1985) and Brime (1985) from the Central Coal basin (Figure 1.3). An overall southwards increase in crystallinity occurs from diagenetic to anchizone (sensu latu) and just into the epizone on the border with the structurally overlying Sobia-Gordon unit, here marked by the Leon fault and the basal thrusts of the unit in the West. Across this boundary, there is a dramatic increase in crystallinity. These changes are also recorded by the elimination of kaolinite, the increase in proportion of chlorite, the restriction of paragonite to the south of the area, the change from irregular to ordered illite-smectite and ultimately the disappearance of smectites. Together with an increasing development of cleavage, a southwards gradient of regional metamorphism is identified, postdating some longitudinal fold structures but followed by an important movement along the Leon line and related to the development of tectonic cleavage.

Brime (1985) reports crystallinities in the Sobia-Gordon unit further south and east in the footwall of the basal thrust to the overlying Someido-Correcilla unit. These low diagenetic zone values (Kubler Index greater than 0.75) contrast with the epizone values in the hangingwall of the thrusts; there is then another progressive decrease south and west to anchizone values within the Somiedo-Correcilla unit. This is recorded in great detail from sections through two thrust sheets within the unit at Luna Lake. Extremely low diagenetic zone crystallinities, with expandable mixed layers and kaolinite characterise the autochthonous Carboniferous shales in the footwall of the Somiedo-Correcilla unit; within the thrust sheets there is a clear decrease in crystallinity from the basal anchizone conditions, where chlorite is present but kaolinite and montmorillonite are

absent towards the top where low diagenetic zone crystallinities are reached. These results, from an area not 20km along strike from this detailed study made in the Bernesga Valley, are highly pertinent and discussed in more detail in 5.

The Somiedo-Correcilla unit has also been examined on the coast at Cabo de Peñas by Brime and Pérez-Estaún (1980). Here a rather different pattern is encountered. From east to west across a section only 5km long, there is a transition from lowest diagenetic zone to epizone. Kaolinite is progressively eliminated through the anchizone, in which paragonite/pyrophyllite is developed locally (a high aluminium content in the original shales is considered to be responsible for this local development), and the proportion of illite increases with crystallinity. This also corresponds to the progressive strengthening of the slatey cleavage in the shales over the section.

There appear to be two contrasting directions of increasing metamorphism in the Cantabrian zone. Increasing grades towards the geometrically exterior part of the arc (orogenically interior) are found within the Central Coal basin, and at Cabo de Peñas. These are associated with the development of cleavage. They contrast with patterns in the Sobia-Gordon and Somiedo-Correcilla thrust units, which show decreasing gradients in this direction, which is also the direction of younging within each thrust sheet. In the studies revealing the first pattern, the authors stress the increasing development of cleavage with the implication that strain has an essential role in determining the crystallinity. The second pattern is interpreted as evidence of a burial diagenetic gradient (discussed further in 5.5).

Pérez-Estaún (1973) reports crystallinities from the Narcea antiform (Figure 1.3). Precambrian rocks in the area north of the Cornombre-La Urz fault have crystallinites of upper anchizone to epizone. Deformation increases to the south of this area, and metamorphism reaches biotite grade

within 5km. This deformation can be distinguished from an earlier orogenic event, and ascribed to the Variscan tectonism. The trend of increasing metamorphism towards the interior parts of the Ibero-Armorican arc is confirmed by epizone crystallinities measured at Tapia (Figure 1.4) in the West Asturian Leonese zone by Brime (1985), and clearly relates to the regional Varican metamorphism. White mica b_o values measured in the anchizone-epizone samples of the Cantabrian and West Asturian Leonese zones establish a low pressure facies (Brime 1985) throughout these areas.